



# Bands of localised deformation in weakly cemented sands : the example of Bédoin (southern France)

Ilaria Soriano

## ► To cite this version:

Ilaria Soriano. Bands of localised deformation in weakly cemented sands : the example of Bédoin (southern France). Solid mechanics [physics.class-ph]. Université Grenoble Alpes; Heriot-Watt university (Edimbourg, GB), 2019. English. NNT : 2019GREAI047 . tel-02905470

**HAL Id: tel-02905470**

**<https://theses.hal.science/tel-02905470>**

Submitted on 23 Jul 2020

**HAL** is a multi-disciplinary open access archive for the deposit and dissemination of scientific research documents, whether they are published or not. The documents may come from teaching and research institutions in France or abroad, or from public or private research centers.

L'archive ouverte pluridisciplinaire **HAL**, est destinée au dépôt et à la diffusion de documents scientifiques de niveau recherche, publiés ou non, émanant des établissements d'enseignement et de recherche français ou étrangers, des laboratoires publics ou privés.

## THÈSE

Pour obtenir le grade de

**DOCTEUR DE LA COMMUNAUTE UNIVERSITE  
GRENOBLE ALPES**

**préparée dans le cadre d'une cotutelle entre la  
*Communauté Université Grenoble Alpes* et  
Heriot-Watt University (Royaume-Uni)**

Spécialité : **2MGE: Matériaux, Mécanique, Génie civil, Electrochimie**

Arrêté ministériel : le 6 janvier 2005 – 25 mai 2016

Présentée par

**Ilaria SORIANO**

Thèse dirigée par **Gioacchino VIGGIANI**, et codirigée par **Elli-Maria CHARALAMPIDOU** et **Helen LEWIS**

préparée au sein du **Laboratoire Sols, Solides, Structures et Risques**, dans l'**École Doctorale I-MEP2 - Ingénierie - Matériaux, Mécanique, Environnement, Energétique, Procédés, Production**

et de l'**Institute of GeoEnergy Engineering**, dans le **School of Energy, Geoscience, Infrastructure and Society (Heriot-Watt University)**

**Bandes de déformation localisée dans les  
sables faiblement cimentés: l'exemple de  
Bédoin (Sud de la France)**

**Bands of localised deformation in weakly  
cemented sands: the example of Bédoin  
(southern France)**

Thèse soutenue publiquement le **13 septembre 2019**,  
devant le jury composé de :

**Monsieur Euripides PAPAMICHOS**

Professeur, Aristotle University of Thessaloniki, Grèce, Président

**Monsieur Francois RENARD**

Professeur, University of Oslo, Norvège, Rapporteur

**Monsieur Pierre BÉSUELLE**

Professeur, CNRS Délégation Alpes, Examineur

**Monsieur Kamaljit SINGH**

Maître de Conférences, Heriot-Watt University, Royaume-Uni, Examineur





# Abstract

Weakly cemented sands from southern France exposing deformation bands were studied as a sandstone reservoir analogue. The objective was to analyse the observed localised deformation in the presence of imperfections (diagenetic or from deformation processes). 2D nano- (Scanning Electron Microscopy) and 3D micro- (X-ray Computed Tomography) image analysis techniques were employed to inspect samples of deformation bands from the outcrops and laboratory-deformed samples of undisturbed sand. Artificially cemented samples without imperfections, prepared with a novel procedure, were also tested for comparison.

Syntaxial quartz overgrowths were identified not only in compactional shear bands but also in undisturbed sand and in a dilation band. Kaolin clay was present at the time of localised deformation, since it interacted with free silica to form micro-quartz, but more clay infiltrated afterwards forming menisci bonds. Kaolinite illitization, observed in multi-strand bands and cluster, and silica cementation required temperatures  $> 70^{\circ}\text{C}$  to occur. Therefore, it is supported the hypothesis that the Bédoin sand reached a burial depth of 2 - 3 km.

The mechanical tests showed that all the samples developed localised deformation before or at the peak stress; however, peak stress was reached later in artificially prepared samples than in the natural ones. The weakly cemented sands exhibited a behaviour close to that of sands. Weaker imperfections were observed, by performing Digital Volume Correlation, to trigger localised deformation, whereas stronger imperfections shifted the bands far from them. Artificially cemented sand samples, with higher cement content than the natural ones, seemed to develop less stress concentration at grain contact, thus generating networks of shear bands, rather than fewer bands as observed in the natural samples.

Porosity and permeability analyses were performed through image processing on the samples 3D X-ray tomographies. Porosity values enabled the distinction of zones in each band type; in particular, a dilation band core reported a porosity value (30%) similar to that of the undisturbed sand. Permeability was zero in the strands of compactional shear bands, whereas the dilation band core had values closer to that of the undisturbed sand ( $10^{+4}$  mD).

# Résumé

Le sable faiblement cimenté de Bédoin (sud de la France) a été choisi comme analogue du grès réservoir pour l'étude des déformations localisées qui se développent en présence d'imperfections – soit diagénétiques, soit dues à l'histoire des déformations. Les affleurements de sable que l'on trouve à Bédoin sont recoupés par des bandes de déformation. Des techniques d'analyse d'images 2D à l'échelle nano (microscopie électronique) et 3D à l'échelle micro (tomographie à rayons x) ont été utilisées pour étudier la structure du matériau au sein de bandes de déformations, à la fois sur des échantillons prélevés du site et sur des échantillons préparés et testés au laboratoire.

L'analyse d'images au microscope électronique révèle une surcroissance syntaxiale de quartz dans les bandes de déformation localisée (qu'elles soient compactantes ou dilatantes), ainsi que dans le matériau en dehors de ces bandes. La présence de micro-quartz et l'illitisation de la kaolinite permettent d'estimer la profondeur maximum du dépôt dans son histoire à 2 à 3 km.

Les résultats des essais mécaniques de laboratoire, effectués sous tomographie x, montrent que les déformations se localisent avant le pic de résistance ; ce dernier est atteint pour des niveaux de déformation plus élevés dans le cas des échantillons préparés au laboratoire, par rapport aux échantillons prélevés du site. L'analyse des champs de déformation (par corrélation d'images 3D) montre que des imperfections “faibles” déclenchent la localisation de la déformation, tandis que des imperfections “forte” ne font qu'affecter la position des bandes de localisation – en la déviant. Le nombre de bandes de cisaillement est plus élevé dans les échantillons préparés au laboratoire que dans les échantillons naturels.

Les images 3D obtenues par tomographie x ont permis de mesurer la distribution de la porosité au sein des échantillons. Ceci permet de distinguer des régions à porosité différente pour chaque type de bande. En ce qui concerne les bandes de dilatation, la porosité dans leur partie centrale est presque la même que celle du sable naturel (30%), tandis qu'elle se réduit de la moitié (15%) vers les bords. A partir des valeurs de porosité, les valeurs de la perméabilité ont aussi été calculées. Dans le noyau des bandes dilatantes la perméabilité reste essentiellement la même que celle du sable naturel ( $10^{+4}$  mD), tandis qu'elle est fortement réduite (de 3 à 4 ordres de grandeur) dans les bandes compactantes.

*To my husband Duarte,  
the love of my life*

# Acknowledgements

*“Knowing is a process, not a product.”* (J. Bruner)

The PhD journey has been a gift to my life as student. I have significantly expanded my scientific knowledge, but more than that I have reached new horizons of my skills, thus leading to a higher level of self-awareness.

My deepest gratitude for this experience goes to my three supervisors, Dr Elma Charalampidou, Dr Helen Lewis, and Prof Cino Viggiani, for having guided me through the PhD journey. Elma has been an incredible support, a source of goodwill, and an example of enthusiasm and passion towards the world of research. Helen’s contribution made me understand the intrinsic enrichment that comes from considering different points of view. Cino, with his extensive knowledge, experience, and frankness, has represented for me not just a technical advisor but also a mentor who gave me appropriate guidance when I was needing it the most. I am also truly thankful to Dr Jim Buckman and to Prof Gary Couples (from Heriot-Watt University) and to Pascal Charrier (from Laboratoire 3SR) who have dedicated some of their time to share with me their knowledge.

I would like to thank once more my examiners, Prof Renard, Prof Papamichos, Prof Besuelle, and Dr Singh, for the constructive discussion during the viva, for the precious comments, and because they contributed to transform the scariest day of my PhD in one of the most enjoyable ones.

The person who accompanied me in every single moment of this adventure has been my husband Duarte. His devotion to me, the care, the patience, and the encouragements have been my strongest motivations to reach the end of my journey. Thank you for being always with me.

The PhD journey would have not been possible without my family support, which is irreplaceable. For this reason, my achievement is also their achievement. I am grateful to my parents and to my sister for being a constant reference of laughter and tenderness during these intense years. Duarte’s family, which has become also mine, has been equally supportive and I thank them so much for the sweetness and the happy moments.

I have shared special moments of my ordinary PhD life with many friends and colleagues. A long-lasting friendship keeps growing with the old friends from my

home town and from university in Bari: Claudia, Marilenia, Valentina, Tiziana, Stefania, Ersilia, Gabriella, Gigi, and Pasquale. We have grown up together and we keep doing it, no matter how distant we are geographically and how busy our schedules are.

In the two new “home towns”, Edinburgh and Grenoble, I have found many other friends and colleagues, and this is also the beauty of a PhD experience. In Edinburgh, I have spent pleasant time with my officemates (former and current) Wissem, Masoud, Mark, Saleh, Mohammad and Parisa. Some of them have also joined me in more fun occasions, together with my wonderful friends Mania and George, Odilla, Hydra, Mhairi and Bouja, Yasmine, Christine and Rafael, Safieh, Khosro, and Gustavo.

The Laboratoire 3SR in Grenoble has become a special place to me. It has been welcoming and productive thanks to friendly colleagues and great scientists. I am really appreciative of the cordiality that people showed in the Laboratory. Among them, an awesome group of friends was created, for the common desire of sharing the PhD adventure with each other. We have started as Seeds and we have grown into Doctors on our journey. I would like to thank you all, Jeanne, Dorjan, Marta, Mathias, Thanos, Maddi, Mohamad, Olumide, for the time spent together and for the fantastic memories that derived from it. A special thank goes to Marta... I hardly remember a moment in which we were not side by side! Finally, I am glad to have cultivated a friendship with three other friends in Grenoble, Antalya, Thibault, and Catherine, and I thank them for the kindness and the generosity they have always demonstrated towards me.

# Contents

<b>1</b>	<b>Introduction</b>	<b>1</b>
1.1	Motivations and background . . . . .	1
1.2	Objectives . . . . .	2
1.3	Structure of the thesis . . . . .	3
<b>2</b>	<b>Literature review about deformation bands in weakly cemented sands</b>	<b>5</b>
2.1	Introduction to deformation bands . . . . .	5
2.2	The theory of localised deformation . . . . .	11
2.2.1	Deformation band as localised deformation . . . . .	11
2.2.2	The bifurcation theory . . . . .	12
2.2.3	State of the art in modeling with the bifurcation theory . . . .	13
2.3	Deformation band classifications . . . . .	14
2.3.1	Compactional shear bands . . . . .	18
2.3.2	Pure dilation bands . . . . .	20
2.4	Grain properties within deformation bands . . . . .	20
2.4.1	Grain breakage . . . . .	20
2.4.2	Grain size distribution . . . . .	24
2.4.3	Grain and fragment orientation . . . . .	26
2.5	Cements within deformation bands . . . . .	27
2.5.1	Overview of cements in granular materials . . . . .	27
2.5.2	Quartz cement: occurrence and effects . . . . .	30
2.5.3	Clay cement: occurrence and effects . . . . .	32
2.6	Porosity and permeability in deformation bands . . . . .	34
2.6.1	Porosity . . . . .	34
2.6.2	Permeability . . . . .	36
2.7	Deformation bands in weakly cemented sands . . . . .	39
2.7.1	Case studies in the literature . . . . .	39
2.7.2	Bédoin and the <i>Bassin du Sud Est</i> . . . . .	40

<b>3</b>	<b>Materials</b>	<b>44</b>
3.1	Samples from Bédoin . . . . .	44
3.1.1	Collection of naturally cemented samples . . . . .	45
3.1.2	Sand characterisation . . . . .	47
3.1.3	Clay cement . . . . .	49
3.2	Artificial cementation . . . . .	49
3.2.1	Artificial cementation in the literature . . . . .	49
3.2.2	A new cementation procedure . . . . .	51
3.2.3	Sand preparation . . . . .	52
3.2.4	Cement preparation . . . . .	53
3.2.5	Cement injection . . . . .	54
<b>4</b>	<b>Experimental methods</b>	<b>55</b>
4.1	Mechanical testing . . . . .	55
4.1.1	Triaxial compression tests . . . . .	55
4.1.2	Isotropic compression test . . . . .	57
4.2	Image acquisition . . . . .	58
4.2.1	Scanning Electron Microscopy . . . . .	58
4.2.2	X-ray Computed Tomography . . . . .	62
4.3	Image processing . . . . .	65
4.3.1	Digital Volume Correlation . . . . .	65
4.3.2	Binarisation and pore space analysis . . . . .	68
<b>5</b>	<b>Assessment of Bédoin sand microstructure</b>	<b>74</b>
5.1	Introduction . . . . .	74
5.2	Grain fragmentation and packing . . . . .	74
5.3	Silica cementation . . . . .	79
5.4	Clay cementation . . . . .	82
5.5	Summary . . . . .	83
<b>6</b>	<b>Mechanical behaviour of natural and artificial samples</b>	<b>86</b>
6.1	Introduction . . . . .	86
6.2	Isotropic compression test . . . . .	87
6.2.1	Naturally cemented Bédoin sand . . . . .	87
6.3	Triaxial compression tests . . . . .	89
6.3.1	Naturally cemented Bédoin sand containing a region of en- hanced porosity . . . . .	89
6.3.2	Naturally cemented Bédoin sand containing an elongated pore	94
6.3.3	Naturally cemented Bédoin sand containing a pre-existing di- lation band . . . . .	97

6.3.4	Artificially cemented Bédoin sand with 20% clay . . . . .	100
6.3.5	Artificially cemented Bédoin sand with 15% clay . . . . .	102
6.3.6	Uncemented Bédoin sand . . . . .	106
6.4	Discussion . . . . .	109
6.4.1	Introduction . . . . .	109
6.4.2	Assessing the mechanical response of the naturally cemented samples . . . . .	112
6.4.3	Assessing the mechanical response of the artificially cemented and uncemented samples . . . . .	115
6.4.4	The effect of imperfections on natural samples in comparison with artificially cemented and uncemented samples . . . . .	120
6.4.5	The effect of clay content on natural, artificially cemented, and uncemented samples . . . . .	123
6.4.6	Properties and patterns of shear bands . . . . .	124
6.5	Further comments regarding the observed imperfections . . . . .	128
6.5.1	Behaviour of the enhanced pore . . . . .	128
6.5.2	Properties and behaviour of the elongated pore . . . . .	128
6.5.3	The non-reactivation of the pre-existing dilation band . . . . .	130
<b>7</b>	<b>Porosity and permeability calculations</b>	<b>133</b>
7.1	Introduction . . . . .	133
7.2	Porosity and permeability of Bédoin sands in the literature . . . . .	133
7.3	Selected samples for the calculations . . . . .	135
7.4	Porosity analysis . . . . .	135
7.4.1	Porosity calculations with Fiji . . . . .	135
7.4.2	Porosity calculations with PAT . . . . .	141
7.4.3	Discussion . . . . .	145
7.5	Permeability analysis . . . . .	147
7.5.1	Permeability calculations with PAT . . . . .	147
7.5.2	Discussion . . . . .	149
<b>8</b>	<b>Conclusions and Perspectives</b>	<b>152</b>
8.1	Summary of the work and conclusions . . . . .	152
8.2	Perspectives for future work . . . . .	155
<b>A</b>	<b>Sampling blocks of weakly cemented sand</b>	<b>157</b>
<b>B</b>	<b>Detailed analysis of the mechanical tests with in situ X-ray Com- puted Tomography</b>	<b>159</b>
B.1	Isotropic compression test of a natural sample from Bédoin . . . . .	159



B.2	Triaxial compression tests . . . . .	162
B.2.1	Naturally cemented Bédoin sand containing a region of enhanced porosity . . . . .	162
B.2.2	Naturally cemented Bédoin sand containing an elongated pore	166
B.2.3	Naturally cemented Bédoin sand containing a pre-existing dilation band . . . . .	169
B.2.4	Artificially cemented Bédoin sand with 20% clay . . . . .	174
B.2.5	Artificially cemented Bédoin sand with 15% clay . . . . .	176
B.2.6	Uncemented Bédoin sand . . . . .	178

# List of Tables

3.1	Sand descriptors for Bédoin 3 (values extracted from the curves in Fig. 3.6).	48
5.1	Summary of grain and cement characteristics observed in the three zones of distinct deformation band types: G = grains, C = clay cement, Q = syntaxial quartz overgrowths; *interband, in the case of deformation band cluster (for them, damage zone was not inspected).	85
6.1	Sample names and descriptions of the tests run in this doctoral work	110
6.2	Summary of the triaxial compression tests. Band angle is measured to the direction of the minor principal stress $\sigma_3$ (i.e., horizontal). Band distribution is referred to the final configuration. Signs of the angles are reported to simplify the angles identification in the 2D slices from the strain field maps, and a positive angle orientation is measured anticlockwise to the horizontal. For samples details, refer to Table 6.1.	111
6.3	Samples dimensions and bulk density (sample details in Table 6.1). Note that the bulk density values were calculated on perfect cylinders generated with the samples average measures of h and d (the real samples are irregular cylinders).	112
6.4	Details of samples tested (in this doctoral work and in previous works) with triaxial compression and analysed with Digital Volume Correlation (DVC) that enabled the measurement of $\theta_{peak}$ . $\theta_{peak}$ is measured to the direction of the minor principal stress $\sigma_3$ (i.e., horizontal) and from the DVC results published in each respective work. Note that the spatial resolution of the X-ray scans that provided DVC strain field maps is of about 15 $\mu\text{m}/\text{px}$ for all samples, except for Desrues et al. (2018), where it is 100 $\mu\text{m}/\text{px}$ .	127
7.1	Porosity $\phi$ and permeability $\kappa$ values of samples collected from Bédoin, in literature. Permeability was measured normal ( $\perp$ ) and parallel ( $//$ ) to the band.	134

7.2	Porosity calculations performed with Fiji on undisturbed sand and on deformation band samples (multi-strand, single-strand, and dilation bands) from Bédoin 3 and 4.5 (ref. to Fig. 3.1). Band zones refer to Fig. 7.4 and 7.5. . . . .	139
7.3	Porosity calculations of the dilation band OREA01 in distinct band zones identified within the sample, as shown in Figure 7.5. . . . .	140
7.4	Porosity calculation with PAT of the natural samples containing deformation bands (multi-/single-strand and dilation bands, Fig. 7.6) and 7.7 from Bédoin 3 and 4.5. . . . .	143
7.5	Porosity calculation with PAT of naturally and artificially cemented samples tested with triaxial compression (for test names, refer to Table 6.1). Sub-volumes are shown in Fig. 7.8. . . . .	144
7.6	Permeability calculations with PAT of naturally and artificially cemented samples tested in Chapter 6 and of deformation band (multi-strand, single-strand, and dilation bands) samples from Bédoin 3 and 4.5. For sample names and for sub-volumes, refer to Table 6.1 and to Fig. 7.6, Fig. 7.7, and 7.8. . . . .	150

# List of Figures

2.1	Deformation band in a Mase sandstone (Japan) sample ( $l = 39$ mm and $d = 19.5$ mm) generated at a confining pressure of 100 MPa (Hoshino and Koide, 1970). . . . .	5
2.2	Deformation bands in Aztec Sandstone in the Valley of Fire, Nevada: (a) field view, (b) back-scattered electron image of the undisturbed sandstone, and (c) back-scattered electron image of the deformation band (in b and c, black is pore) (Sternlof et al., 2006). . . . .	7
2.3	Forms and modes of localised deformation for tabular form (upper row) and for sharp form (lower row) of deformation localisation (Aydin et al., 2006). . . . .	8
2.4	Sequence of a deformation band growth: (a) single-strand band, (b) two bands, (c) cluster of bands, (d) fault (Aydin and Johnson, 1978, 1983). . . . .	10
2.5	(a) Deformation bands evolving angle of shear and becoming more numerous with increasing confining pressure (0 - 60 MPa) (Bésuelle et al., 2000); (b) From left to right: samples deformed at increasing confining pressure, showing the transition from shear to compaction bands; (1) result of isotropic compression of sample (2), $h = 80$ mm, $d = 40$ mm (Guéguen, 2005). . . . .	10
2.6	Types of deformation bands according to kinematics: PDB = pure dilation band; SEDB = shear-enhanced dilation band; DSB = dilational shear band; SSB = simple shear band; CSB = compactional shear band; SECB = shear-enhanced compaction band; PCB = pure compaction band (Fossen et al., 2017). . . . .	15
2.7	Conceptual model of deformation bands types according to four main mechanical and chemical processes: (a) disaggregation; (b) phyllosilicate inclusions; (c) cataclasis; (d) solution and cementation (Fossen et al., 2007). . . . .	16

2.8	Types of cataclastic structures (indicated by an arrow): (a) single-strand band, (b) multi-strand band; (c) cluster of deformation bands; (d - e) fault zone with indication of several slip surfaces (Philit et al., 2015). . . . .	18
2.9	Porosity measurements in a section of deformation band undergoing compaction: values in the contour zone (TZ) are intermediate between core (DB) and damage zone (HR) (Rotevatn et al., 2016). . . .	19
2.10	Force chain conceptual models and observation: (a) Conceptual models of (i) incipient and (ii) organised force chains (black) in a shear band, surrounded by grains that provide secondary support to forces (grey) and by "spectator" grains (white) (Cates et al., 1998); (b) conceptual model of force chains distribution corresponding to grain microfracture propagation (Soliva et al., 2013); (c) Microscopic observation of grain microfractures (i) and corresponding force chains (ii) inferred in the material along a deformation band (Soliva et al., 2013). . . . .	22
2.11	Rose diagrams reporting the force chain orientations in host rock (a) and corresponding cataclastic shear bands (b), and in another host rock (c) with its corresponding compaction bands (d). Note that in (b) the range $0^{\circ}$ to $20^{\circ}$ is // to the direction of maximum shortening, and in (c) the range $-20^{\circ}$ to $0^{\circ}$ is $\perp$ to the bedding direction (Cilona et al., 2012). . . . .	23
2.12	Mohr-Coulomb failure envelopes for a weakly cemented sand, showing increased internal friction in the shear band with respect to the parent material (i.e., undisturbed sand) (Kaproth et al., 2010). . . . .	24
2.13	Examples of grain size variation from undisturbed to naturally and laboratory deformed materials (a) Entrada and Navajo Sandstones and deformation bands (Aydin, 1978); (b) Locharbriggs Sandstone and samples deformed in the laboratory at different deviatoric strain levels (Mair et al., 2000). . . . .	25
2.14	Rose diagrams showing grain orientations in undisturbed material (A and C) and their respective fault (B) and deformation band (D) compared to the fault strike (crossing line): A. Flook Ranch undisturbed material, $N = 688$ ; B. Flook Ranch fault, $N = 1434$ ; C. Alder Creek undisturbed material, $N = 870$ ; D. Alder Creek deformation band, $N = 1791$ ( $N$ is the sample size) (Cashman et al., 2007). . . . .	26
2.15	Thin sections of grainstones with rose diagrams of the grain orientations within core, contour, and damage zone of two deformation bands ((a) from Rath et al. (2011), and (b) from Rotevatn et al. (2016)). . .	28

2.16	Correlation between stiffness and contact length $L$ (normalised for the grain size $D$ ), where triangles represent natural sandstones and hexagons stand for artificially cemented rocks (David et al., 1998). . . . .	29
2.17	(a) Uncemented and (b) cemented (rapid curing cement for concrete) coarse granitic sand under shear at different effective mean stresses (in both cases, the samples were saturated, $h = 14$ cm, $d = 7$ cm) (Cruz et al., 2011). . . . .	30
2.18	Porosity variations at different confining pressures in cemented and uncemented glass beads randomly packed; cement is epoxy resin (from Aydin et al. (2006), after Dvorkin and Yin (1995)). . . . .	31
2.19	Quartz cemented grains in a sandstone: (a) Back Scattered Electron image where there is no distinction between grains and overgrowths since they have the same mineralogy and (b) Cathodoluminescence image of the same area, revealing where the overgrowths are located from a comparison with (a) (see the arrows) (Fisher et al., 2000). . . . .	32
2.20	Transformation of Kaolinite with depth: (A) $< 1000$ m, mixture of vermiform and anhedral crystals; (B) 3000 m, vermiform kaolinite; (C) 3000 m, elongation of kaolin platelets and thickening of booklets; (D) 3500 m, intercalation of blocky crystals between stacks (adapted from Lanson et al. (2002)). . . . .	33
2.21	Clay type variation with the depth: at higher depth there is predominance of illite in the place of kaolinite and the temperature corresponding to this inversion is the intersection of the trending lines for the two clay forms (Kraishan et al., 2009). . . . .	34
2.22	Surface porosity (i.e., sum of pores, cements, and clays) variation in cemented sands with respect to the degree of cataclasis. Black data represent uncemented deformation bands, while yellow stands for partially cemented and red is for highly cemented structures (Philit et al., 2015). . . . .	35
2.23	Field examples (i - v) of (a) different deformation band type, (b) their texture and (c) permeability contrast. In (c) the percentage of deformation bands with a permeability reduction greater than two orders of magnitude is indicated in red (Ballas et al., 2015). . . . .	38
2.24	Field sites in the <i>Bassin du Sud Est</i> (adapted from Sallet and Wibberley (2010)). . . . .	40
2.25	Relationship between grain size (host grain is the undisturbed sand) and deformation band thickness, in comparison between three sites of the <i>Bassin du Sud Est</i> : Bédoin, Orange, and Massive d'Uchaux (Sallet and Wibberley, 2010). . . . .	43

3.1	Sand quarries explored near Bédoin (adapted from Wibberley et al. (2007)). . . . .	45
3.2	Examples of deformation bands and haematite stains on the outcrops and along the bands in Bédoin 3: the deformation bands are extended for meters in the outcrop (red tool for scale, $l = 15$ cm). . . . .	46
3.3	Field view of Bédoin 4.5: thin and almost imperceptible deformation bands are extended for meters in the outcrop. Note in (a) the haematite layer above the white sand unit (red tool for scale, $l = 15$ cm). . . . .	46
3.4	Field sampler designed to collect blocks of weakly cemented sand: (a) pieces that compose the sampler (length of longer wooden plate is $l = 40$ cm), (b) sampler during the composition in the field, and (c) assembled sampler. . . . .	47
3.5	Bédoin sand grains seen at the microscope: (a) view with Scanning Electron Microscopy and (b) element map from Energy-Dispersive X-ray Spectrometry, where blue is Silica (Si) and green is Aluminium (Al). . . . .	48
3.6	Granulometric curves of two sand types from Bédoin 3: undisturbed sand grains and sand from a multi-strand deformation band core. Principal sand descriptors extracted from the curves are reported in Table 3.1. . . . .	49
3.7	Greyscale (a and b) and correspondent trinarised images (c and d) of undisturbed cemented sands from Bédoin 3: clay (grey) binds together grains and fragments (white) (black is pore). Percentage of clay in (c) is 4% and in (d) is 10.9%. . . . .	50
3.8	Clay cement in Bédoin. Note in (b) the hexagonal shapes of the platelets, typical of the kaolin clay. . . . .	50
3.9	Aluminium mould: (a) view of the internal structure with cylindrical cavity ( $d = 11$ mm, $h = 22$ mm) and (b) setup to pour sand into the mould from the top aperture through a funnel and a pipe ( $l = 94$ mm). Note that the top mesh is not in place when the sand is poured. . . . .	53
3.10	Cylindrical sample obtained from the artificial cementation procedure. . . . .	54
4.1	(a) Vertical section of the triaxial cell created by Prof. Bésuelle and Dr. Lenoir (adapted from Andò (2013)); (b) detail of the sample setup in the cell (sample size: $h = 22$ mm, $d = 11$ mm). A flat-edged piston applies compression to the lower platen, and lubrication is applied between sample and platens to reduce contact friction. . . . .	56

4.2	Scheme of a Scanning Electron microscope: (a) Electron column and Control console, (b) zoom on the scan coils in the last lens with scheme of the beam deflection before reaching the sample ( $L$ = sample width, $W$ = working distance between sample and last lens) (adapted from Goldstein et al. (2003)). . . . .	59
4.3	Examples of BSE image of grains composed by different minerals (Qtz = quartz, Plag = Plagioclase) recognised from the greyscale variations, which reflect grain mineralogy (Exner and Tschegg, 2012). . . . .	60
4.4	Images of grain fragments in a deformation band cluster in Bédoin: a) Gaseous Secondary Electron (GSE) CCI and b) Back-Scattered Electron (BSE) SEM images. The CCI image can reveal clear edges of the grain fragments and syntaxial quartz overgrowths, with respect to the BSE image obtained simultaneously. . . . .	60
4.5	Examples of EDX histograms obtained from a specific particle indicated with an arrow in the correspondent BSE: a) brass (Cu-Zn alloy) and b) gold (adapted from Prakongkep et al. (2010)). . . . .	61
4.6	Example of X-ray CT scan of a deformation band sample from Bédoin (single-strand band ISBSC01): (a) 3D view of the sample and (b) view with vertical and horizontal sections shown in (c) and (d), respectively. . . . .	63
4.7	X-ray CT setup: X-ray console, composed by an X-ray source, an object stage, and a detector. The object stage in the Figure is composed by rotation stage; above it, a triaxial cell is installed (see sample details in Fig. 4.1); below the rotation stage, the loading apparatus is installed and reaches the sample through the piston visible in the cell. An example of output image during the acquisition (radiogram) is shown at the lower-right side of the figure (Andò et al., 2012). . . . .	64
4.8	Illustration of the DVC technique: the correlation window in the deformed image on the right moves around (see a), b) c), and d)) within the search window, searching for the target sub-volume, i.e., voxels with the same properties of the reference sub-volume defined in the reference image on the left (adapted from Charalampidou (2011)). . . . .	66
4.9	Example of results (b and c) from a DVC performed on a Bentheim sandstone sample tested with triaxial compression: horizontal and vertical sections of (a) X-ray CT image of the deformed sample, (b) maximum shear strain field, and (c) volumetric strain field (Tudisco et al., 2017). . . . .	68



4.10	Comparison of a slice from 3D strain field maps obtained with a different value of the $CW_x$ (written at the top of each figure), showing that the output obtained with $CW_x = 30$ gives a smoother image with less (or none) errors of computation, e.g., the black region in the lower part of the sample with $CW_x = 20$ . . . . .	68
4.11	Binarisation procedure of a deformation band sample (2D cross-section of single-strand band sample ISBSC01): (a) initial 16-bit image; (b) step 1: threshold application; (c) step 2: mask creation; (d) mask addition to the thresholded image obtained in (b). Voxel values in (b), (c), and (d): black = 0, grey = 128, white = 255. . . . .	70
4.12	Example of threshold Intermodes applied to the naturally cemented sample <i>Nat</i> , with histogram of the greyscale image (see the two peaks) and threshold indicated on it. . . . .	71
4.13	Example of different representations of a pore network for a sandstone sample: (a) 3D pore space; (b) pore network skeleton in black, with branches in grey; (c) nodes (spheres) and bonds (segments) network (Jiang et al., 2007). . . . .	72
5.1	Scanning Electron Microscopy (SEM) of grain fragmentation in an undisturbed sand sample (a) and in a dilation band (b, c): some grains in (a) and in the band core in (b) result fractured, but the fragments are still in their original place and they are held by cement (principally clay, see Sect. 5.4); contours in (b) are richer in cement; (c) zones that compose the dilation band: core, contour, and damage zone. . . . .	75
5.2	Grain fragmentation in multi-strand bands from Bédoin 4.5: (a) X-ray CT slice orthogonal to the direction of the deformation band plane (dashed lines) [res. $15\mu\text{m}/\text{px}$ ], where survivor grains are aligned and surrounded by a fine-grained matrix; (b) SEM image of grains and fragments in another multi-strand band from the same outcrop; (c) zoom from (b) over quartz micro-fragments, showing that their size is comparable to that of clay (elongated particles). . . . .	76
5.3	Mosaic SEM (central figure) of a strand extracted from a deformation band cluster in Bédoin 3: details of grain breakage and packing within the strand (a), in the interband (b, c) and in an iron/titanium-rich cement (d) (the mineralogy of grains and cements is shown in Fig. 5.7). . . . .	78

5.4	SEM images of grain dissolution in the deformation band cluster from Figure 5.3: the zooms on the right show detail of dissolution occurred in a zone of tightly compacted quartz micro-fragments. Note the syntaxial quartz overgrowths precipitated around the grain fragments.	79
5.5	SEM images of silica cementation in multi-strand bands and cluster: (a) and (b) syntaxial quartz overgrowths (note that in (b) it is possible to distinguish up to 25 quartz layer generations); (c) quartz fragments broken and re-cemented with quartz (see arrows); (d) micro-quartz in the pore space with flocculated clay particles. . . . .	81
5.6	SEM images of syntaxial quartz overgrowths in (a) the dilation band core (same sample as in Fig. 5.1b) and in (b) the undisturbed sand (same sample as in Fig. 5.1a). . . . .	81
5.7	Energy-Dispersive X-ray Diffraction (EDX) map (on the right) of the mosaic SEM (on the left) from Fig. 5.3: the map shows that there is less presence of clay (in green) inside the deformation band strand than in the interband (red is Fe, blue is Si, green is Al, orange is Ca).	83
5.8	Clay particles next to quartz micro-fragments in a multi-strand band from Bédoin 4.5: (a) Charged Contrast Imaging (CCI) figure of the sample, (b) Energy-Dispersive X-ray Diffraction (EDX) spectrum of the clay contained in the square reported in (c) and (d); (c) and (d) are EDX colour maps representing the clay and silica fractions, respectively, of the sample in (a). . . . .	84
5.9	(a) SEM image of a kaolinite booklet from a multi-strand band in Bédoin 4.5; (b) EDX spectrum of the illitized kaolinite shown in (a). .	84
6.1	(a) Naturally and (b) artificially cemented samples used in the mechanical tests, and (c) schematic representation of a 2D vertical slice ( $h \cong 22$ mm, $d \cong 11$ mm) extracted from 3D X-ray scans and DVC data of each sample. . . . .	87
6.2	Curve representing the evolution with the time of the confining pressure applied to the sample. Numbers 00 to 07 along the curve refer to X-ray scans acquired during the test. Step 02 - 03 is longer than the other steps because of the night break during the test, whereas the small peak after scan 02 is an anomaly due to the sample setup. .	88
6.3	Vertical 2D sections of the sample X-ray scans (a) before isotropic compression and (b) after applying 7 MPa. . . . .	88
6.4	DVC step 00-01 of the isotropic compression test: after applying 1 MPa confining pressure, the sample developed inclined layers of shear and volumetric strain. . . . .	89

6.5	Vertical 2D slices extracted from X-ray scans acquired (a) before the isotropic compression and (b) after the deviatoric loading. . . . .	90
6.6	Stress-strain curve. Numbers 00-09 along the curve refer to X-ray scans acquired during the test and stress drops next to each number represent a relaxation of the loading system when the piston is paused to acquire the X-ray scan. . . . .	91
6.7	2D vertical slice of the max shear strain field (DVC 00-01, confining pressure from 0 to 0.5 MPa) showing inclined layers characterised by higher shear, which can be related to depositional layering. . . . .	91
6.8	DVC results of the triaxial compression test on a naturally cemented sample containing a region of enhanced porosity at its lower part. . .	93
6.9	2D vertical slices from the X-ray scans acquired (a) before the isotropic compression and (b) after the deviatoric loading, showing that the elongated pore did not collapse by the end of the test. Grain breakage and pore space rearrangement is also observable at the upper part of the sample in (b). . . . .	94
6.10	Stress-strain curve . . . . .	95
6.11	DVC results of the triaxial compression test on a naturally cemented sample containing an elongated pore . . . . .	96
6.12	(a) X-ray radiography of the sample before the isotropic compression, revealing the presence of a dilation band (indicated by red lines). (b) and (c) are 2D vertical slices from the X-ray scans before the confining pressure and at the end of the deviatoric loading, respectively, showing the persistence of the dilation band, despite the deviatoric compression. The band is inclined of $32.5^\circ$ to the horizontal in (b) and of $31.5^\circ$ in (c). Note a region of enhanced porosity at the top-right of (b) and (c). . . . .	97
6.13	Stress-strain curve . . . . .	98
6.14	DVC results of the triaxial compression test on a naturally cemented sample containing a pre-existing dilation band. . . . .	99
6.15	2D vertical slices from the X-ray scan of the sample (a) before the isotropic compression and (b) after the deviatoric loading, showing details of the deformation: grain breakage, pore redistribution, and barrelling final configuration. . . . .	100
6.16	Stress-strain curve . . . . .	101
6.17	DVC results of the triaxial compression test on an artificially cemented sample with 20% of clay. . . . .	102

6.18	2D vertical slices extracted from the X-ray scans acquired (a) before the isotropic compression and (b) after the deviatoric loading, showing the initial homogeneous cement distribution and the final deformation of the sample: grain breakage, new pore distribution, and barrelling configuration. . . . .	103
6.19	Stress-strain curve . . . . .	103
6.20	DVC results of the triaxial compression test on an artificially cemented sample with 15% clay. . . . .	105
6.21	2D vertical slices extracted from the X-ray (a) before isotropic compression and (b) after deviatoric loading, showing the maximum shortening of the sample reached during the test, which provoked grain fragmentation, porosity variation, and a barrelling shape of the sample.	106
6.22	Stress-strain curve . . . . .	107
6.23	DVC results of the triaxial compression test on an uncemented Bédoin sand sample. . . . .	108
6.23	. . . . .	109
6.24	Overview of triaxial test results by combining DVC observations with peak stress values from the stress-strain curves: the range of values reported in the plot corresponds to the DVC step where each of the processes was identified. . . . .	110
6.25	Stress-strain curves of the natural samples . . . . .	113
6.26	Comparison of naturally cemented samples at the onset of localised deformation (sample details in Table 6.1) . . . . .	115
6.27	Stress-strain curves of uncemented and artificially cemented samples .	116
6.28	(a) Mohr's circles of tests on artificially cemented samples shown in Fig. 6.27 and in (b), with failure envelope inclined of $33.7^\circ$ tangent to three circles (red, brown, and orange) that represent three triaxial tests run on the three samples containing 15% of clay and confined at pressures of 0.5, 1, and 4 MPa; (b) stress-strain curves of the artificially cemented samples containing 15% of clay cement and confined with 0.5 MPa and 4 MPa (not analysed in this work). . . . .	117
6.29	Comparison of artificially cemented samples at the onset of localised deformation (sample details in Table 6.1) . . . . .	119
6.30	Comparison of naturally, artificially cemented and uncemented samples at the onset of a dominant shear band/s (sample details in Table 6.1) . . . . .	121
6.31	DVC of naturally, artificially cemented and uncemented samples at an axial strain range highlighted in yellow in the stress-strain curve (sample details in Table 6.1) . . . . .	122

6.32	Force-chain distributions in (a) uncemented and (b) 2% (Portland) cemented samples in a simulation of triaxial compression test at confining pressure of 50 kPa and axial strain of 1.76%: in the uncemented sample the force chains are fewer and thicker, where thickness represents the magnitude of contact normal forces (Wang and Leung, 2008). . . . .	123
6.33	Stress-strain curves of artificially bio-cemented and uncemented sand samples tested with triaxial compression at a confining pressure of 100 kPa: (a) deviatoric stress-strain and (b) volumetric stress-strain responses. The cemented sample showed a dilative response and a high deviatoric peak stress, differently from the contractive response of the uncemented one (Tagliaferri et al., 2011). . . . .	124
6.34	2D vertical slices of the strain field maps of uncemented sand (Hos-tun, Ottawa, and Caicos) samples tested under triaxial compression: the samples exhibit a single shear band because the ceramic platen at the lower part of the sample is free to rotate during the deviatoric compression (i.e., curve-edged piston) (Desrues and Andò, 2015). De-tails of the sands can be found in Table 6.4 with respect to the works in Alikarami and Torabi (2015) and Desrues and Andò (2015). . . . .	125
6.35	(a) and (b) are vertical slices of X-ray scan of the sample NatPore before isotropic compression and at the end of the deviatoric load-ing, respectively, showing that the elongated pore did not collapse under compression and that localised deformation occurred far from the elongated pore, at the top of the sample; (c) 3D volume of the elongated pore (in dark) extracted from (a) (3D view available at <a href="https://doi.org/10.6084/m9.figshare.10125878.v1">https://doi.org/10.6084/m9.figshare.10125878.v1</a> ), and (d) horizontal section of it (see dashed blue line in (a) for orientation) that shows the variable thickness of the cement (orange) around the pore. . . . .	129
6.36	Energy-Dispersive X-ray Spectroscopy (EDS) of a piece of the cement surrounding the elongated pore: (a) map and (b) spectrum. The map shows the clay fraction (Al = aluminium) covering the sand grains (Si = silicium) and the spectrum provides the specific composition of (a), corresponding to clay (Al - Si). . . . .	130
6.37	X-ray radiographies of the naturally cemented sample with pre-existing dilation band before isotropic compression (a) and at the end of de-viatoric loading (b): the dilation band did not collapse under com-pression. Red markers outside the sample identify the dilation band plane. . . . .	132

7.1	X-ray slices (tomography (left) and correspondent binarised image (right)) of two cylindrical samples: undisturbed (cemented) sand from Bédoin (Nat, Fig. 6.5a) and artificially cemented Bédoin sand (Artif15, Fig. 6.18a) (black = pore, white = solid). Image resolution for the two X-ray scans is 15 $\mu\text{m}/\text{px}$ . . . . .	136
7.2	X-ray slices (tomography (left) and correspondent binarised image (right)) of two deformation band samples, multi-strand bands ISBS4501 and ISBS4503, from Bédoin 4.5 (black = pore, white = solid). Image resolution for the two X-ray scans is 15 $\mu\text{m}/\text{px}$ . . . . .	137
7.3	(from left to right) Sample, X-ray tomography, and correspondent binarised slice of two deformation band samples, single-strand band ISBSC01 and dilation band OREA01 (black = pore, white = solid). Image resolution for ISBSC01 is 10.5 $\mu\text{m}/\text{px}$ , for OREA01 is 27 $\mu\text{m}/\text{px}$ .	137
7.4	X-ray binarised slices extracted from the natural samples, showing volumes and sub-volumes (contours in red and with name of the respective zone) selected for porosity calculation with Fiji: (a) undisturbed sand, (b, c, d, e) multi-strand bands, and (f) single-strand band. Image resolution is 15 $\mu\text{m}/\text{px}$ for all samples except (f), which has a resolution of 10.5 $\mu\text{m}/\text{px}$ . . . . .	138
7.5	X-ray binarised slices extracted from the dilation band OREA01 showing the sub-volumes (contours in red) selected for porosity calculation with Fiji, with indication of distinct zones: band core, contour, and damage zones, where a and b are the two sides of the dilation band (black = solid, white = pore). [Res. 27 $\mu\text{m}/\text{px}$ ]. . . . .	139
7.6	X-ray binarised slices of the deformation band samples showing the sub-volumes (contours in red) selected for porosity calculation with PAT: (a, b, c) multi-strand bands, and (d) single-strand band. . . . .	141
7.7	X-ray binarised slice of the dilation band sample OREA01, showing the sub-volumes selected for porosity calculation with PAT. . . . .	142
7.8	X-ray binarised slices of the tested samples (sample name and test described in Table 6.1) used for porosity calculation with PAT: (a - b) slices of the sample with sub-volume (contours in red), showing the central location of it within the sample, and (c - f) slices from the sub-volumes (selected with similar location) of the other tested samples. Note that only NatPore (c) contained part of the imperfection (i.e., elongated pore). . . . .	142

7.9	Image histograms of X-ray scans of the sample NatDB (a) at the beginning and (b) at the end of the test and correspondent thresholded images (c) and (d): in (a) the histogram is bimodal, and the two peaks identify the pore space (greyscale value: 13500) and the grains (greyscale value: 41500); in (b) the values between the two peak grow in frequency, therefore the peak that identifies the pores is more vague.	145
7.10	Schematic representation of porosity in the three deformation band types analysed: multi-strand, single-strand, and dilation bands. The representation reports the zonation for the three band types, according to observations: B = band core, C = contour, D = damage zone, I = interband.	146
7.11	Orientation of the reference system (x, y, z) for the dilation band sample OREA01.	148
B.1	DVC results of the isotropic compression test	160
B.1		161
B.1		162
B.2	DVC results of the triaxial compression test on a naturally cemented sample containing a region of enhanced porosity	164
B.2		165
B.2		166
B.3	DVC results of the triaxial compression test on a naturally cemented sample containing an elongated pore	168
B.3		169
B.4	DVC results of the triaxial compression test on a naturally cemented sample containing a pre-existing dilation band	171
B.4		172
B.4		173
B.4		174
B.5	DVC results of the triaxial compression test on an artificially cemented sample with 20% of clay	175
B.6	DVC results of the triaxial compression test on an artificially cemented sample with 15% clay	177
B.6		178
B.7	DVC results of the triaxial compression test on an uncemented Bédoin sand sample	180
B.7	DVC results of the triaxial compression test on an uncemented Bédoin sand sample	181
B.7		182

# Chapter 1

## Introduction

### 1.1 Motivations and background

Deformation bands are tabular structures in porous rocks where deformation localises by altering size, shape, and spatial arrangement of the rock components, i.e., grains, cements, and pore space. By altering the rock components, deformation bands can act as fluid baffle or conduit and impact the reservoir performance. Thus, numerous outcrop studies of deformation bands in the last decades (e.g., Exner et al. (2013); Rotevatn et al. (2013); Ballas et al. (2015); Griffiths et al. (2016); Fossen et al. (2017)) aimed to better understand the conditions that lead to the formation of these bands, which can occur not only in porous rocks but also in weakly cemented sands (e.g., Kaproth et al. (2010); Balsamo et al. (2013); Sallet and Wibberley (2013); Philit et al. (2015)).

This doctoral work was motivated by outcrop observations of a weakly cemented sand deposit located in the South of France (Bédoin, Provence) that presents a vast exposure of deformation bands. The sand deposit is located within an area known in the geological literature as *Bassin du Sud Est*, which was described in detail in key publications (Triat, 1982; Tempier, 1987; Dubois and Delfaud, 1894; Le Pichon et al., 2010; Schreiber et al., 2011). The specific Bédoin site was analysed in a small number of works (Wibberley et al., 2007; Sallet and Wibberley, 2010, 2013; Philit et al., 2015, 2018). These studies were focused on the outcrop scale analysis (i.e., few metres to tens of metres) and primarily commented on the frequency and spatial distribution of deformation bands, and on the petrophysics of the material altered by deformation bands. In particular, Wibberley et al. (2007) interpreted the stress state of the Bédoin deposits at the time(s) of band formation from the inspection of deformation band distribution and orientation. Sallet and Wibberley (2010) inferred the tectonic regime by reconstructing the deformation band growth, which seemed to be influenced by grain size of the undisturbed sand and by bed thickness. The same authors showed also how deformation bands affected the petrophysical



properties of weakly cemented sands (Saillet and Wibberley, 2013), concluding from their measurements that porosity reduced from about 30% to values lower than 10% in multi-strand deformation bands and faults, and that permeability decreased by one order of magnitude going from undisturbed sand to deformation band cluster. Philit et al. (2015) observed pipe-shaped structures and silicified concretions in the outcrop and silica cement using an optical microscope in the laboratory, which supported the hypothesis of groundwater networks developed in the sand deposit along deformation bands.

Several factors, among which grain size, pore size, and cement distribution (den Brok et al., 1997; Skurtveit et al., 2013; Ballas et al., 2014), could affect the mechanical processes taking place during the occurrence of deformation bands in weakly cemented sediments. Other factors, e.g., spatial density variation, hard and soft inclusions, notches, and cement content variation, were observed to influence localised deformation in laboratory prepared samples, for example in uncemented sands (Desrues and Viggiani, 2004; Borja et al., 2013), in artificially made sandstones (den Brok et al., 1997), and in natural sandstones with artificial notches (Davidsen et al., 2017). Any of the above-mentioned factors, related to natural depositional structures and/or later deformation processes, could be considered as natural *imperfections* in granular material samples. The impact of natural imperfections within granular materials collected from an outcrop and tested in their natural depositional configuration has not been widely investigated. The main challenge has been to core samples without disturbing their structure, in particular when these samples are weakly cemented sediments, as for example the Bédoin weakly cemented sands. The integrity of a weakly cemented sand can be compromised by outcrop collection and laboratory preparation because of its fragility, therefore it is difficult to investigate it at the laboratory scale. An attempt to collect weakly cemented sands was made by Skurtveit et al. (2013), where samples from Boncavaï quarry (Provence, France) were extracted after being saturated with water and frozen while in the outcrop. However, volume expansion of water under 0°C could affect the grain spatial arrangement and damage the weak cement, thus delivering to the laboratory a material that can differ in structure from that in the outcrop. Another attempt was performed in Bédoin by Saillet and Wibberley (2013), but this was addressed only to cataclastic deformation band samples, which are more compacted and resistant than the undisturbed sand.

## 1.2 Objectives

The scope of this work was to study the mechanical behaviour of the weakly cemented Bédoin sands, which were collected from outcrops that presented a vast

exposure of deformation bands. This is pursued by studying the natural material at the laboratory scale and at stress states that were allowed by selected equipments. Analysis of Bédoin samples indicated the presence of imperfections related to diagenetic structures and to deformation processes, such as depositional layers, regions of enhanced porosity and cementation, and pre-existing dilation band.

The objectives of this doctoral work are to:

- characterise the material constituents - grains, pores, cements - in the Bédoin outcrops including both undisturbed sand and sands from the deformation bands;
- identify imperfections in the Bédoin weakly cemented sand samples;
- assess the impact of the identified imperfections on the mechanical behaviour of the Bédoin sand;
- evaluate the mechanical behaviour of weakly cemented sands in the absence of imperfections.

The material was inspected at 2D nano- and 3D micro-scale through Scanning Electron Microscopy and X-ray Computed Tomography, respectively. The effects of the imperfections in the deformation band occurrence was assessed by testing mechanically the weakly cemented material collected in Bédoin. The relationship between material imperfections and occurrence of deformation bands in the samples was inferred by acquiring syn-deformation X-ray images and applying Digital Volume Correlation. In order to speculate on the behaviour of a weakly cemented sand in the absence of these imperfections, artificially cemented samples were created similarly to the natural ones but without imperfections, and they were tested mechanically at the same conditions applied to the natural samples.

### **1.3 Structure of the thesis**

The thesis is organised into seven further Chapters, which guide the reader from the background knowledge of the investigated topics, through methods and materials description, up to the presentation and discussion of the obtained results.

Chapter 2 presents an overview of definition and classification of deformation bands, and a description of their constituents (i.e., grains, pores, cements). Deformation bands in Bédoin are described in a geological framework as reported in previous works.

The tested materials, natural (from Bédoin) and artificially cemented (in the laboratory), are described in Chapter 3. The sampling procedure adopted in Bédoin

with a novel field sampler is presented. Moreover, an innovative technique for creating weakly cemented sands similar to the Bédoin natural material is described in detail.

Chapter 4 describes the methods employed in this work to study qualitatively and quantitatively the Bédoin material. Mechanical tests and image acquisition techniques selected for this work are briefly introduced. In particular, the complementarity of Scanning Electron Microscopy and X-ray Computed Tomography in resolution (i.e., nano- and micro-scale) and sample geometry (i.e., 2D vs. 3D) is explained. Several techniques used to extract data from the acquired X-ray images, are described. In particular, Digital Volume Correlation was applied to compute maximum shear and volumetric strain maps, and a manual technique and a in-house software for pore network computation were employed for porosity and permeability calculation.

The observation of the natural material from Bédoin with image acquisition is described in Chapter 5. The inspection is focused on grain fragmentation in the deformation bands and on silica and clay cementation inside the deformation bands and in the undisturbed sand.

Chapter 6 reports selected results of the mechanical tests - isotropic compression and triaxial compression - that show the effect of the imperfections within the tested samples (i.e., depositional layers, regions of enhanced porosity and cementation, and pre-existing dilation bands) during the onset of localised deformation. The mechanical behaviour of the Bédoin samples is compared with that of the artificially prepared samples that do not contain the above-mentioned imperfections but are made of Bédoin grains that were cemented with clay in the laboratory.

Porosity and permeability calculated through image processing on different deformation band types - multi-strand and single-strand compactional shear bands, dilation bands - are reported in Chapter 7. Porosity values are used to develop a graphical representation of the deformation band types in Bédoin. The results give insights into the permeability contrast between deformation bands and undisturbed sand.

Finally, the conclusions of the thesis are summarised in Chapter 8 and future work is also suggested in continuation of the gathered knowledge.

# Chapter 2

## Literature review about deformation bands in weakly cemented sands

### 2.1 Introduction to deformation bands

Deformation bands are tabular zones in (porous) rocks and sediments where grains are gradually crushed and spatially rearranged with usually increasing offset (sub-mm to dm) (Aydin, 1978; Jamison, 1979; Antonellini et al., 1994), and where porosity is typically altered with respect to the *undisturbed* material. The *undisturbed* material is the material located relatively far from the deformation band and that did not undergo localised deformation. Aydin (1977) introduced with clarity the term *deformation band* to describe this form of localised deformation. However, the term was already used by Koide and Hoshino (1967) to indicate bands where “*microcracks*” concentrate, with zigzag shape and with two conjugate directions of  $30^\circ - 40^\circ$  to the direction of maximum compression, generated in experiments under confining pressure of 147 MPa. Figure 2.1 shows one of the earliest laboratory generation of a deformation band in a cylindrical Mase sandstone sample (Japan).

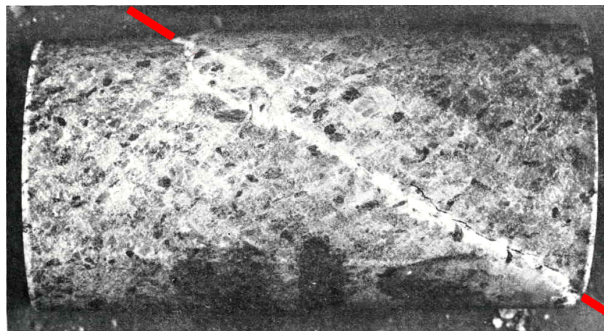


**Figure 2.1:** Deformation band in a Mase sandstone (Japan) sample ( $l = 39$  mm and  $d = 19.5$  mm) generated at a confining pressure of 100 MPa (Hoshino and Koide, 1970).

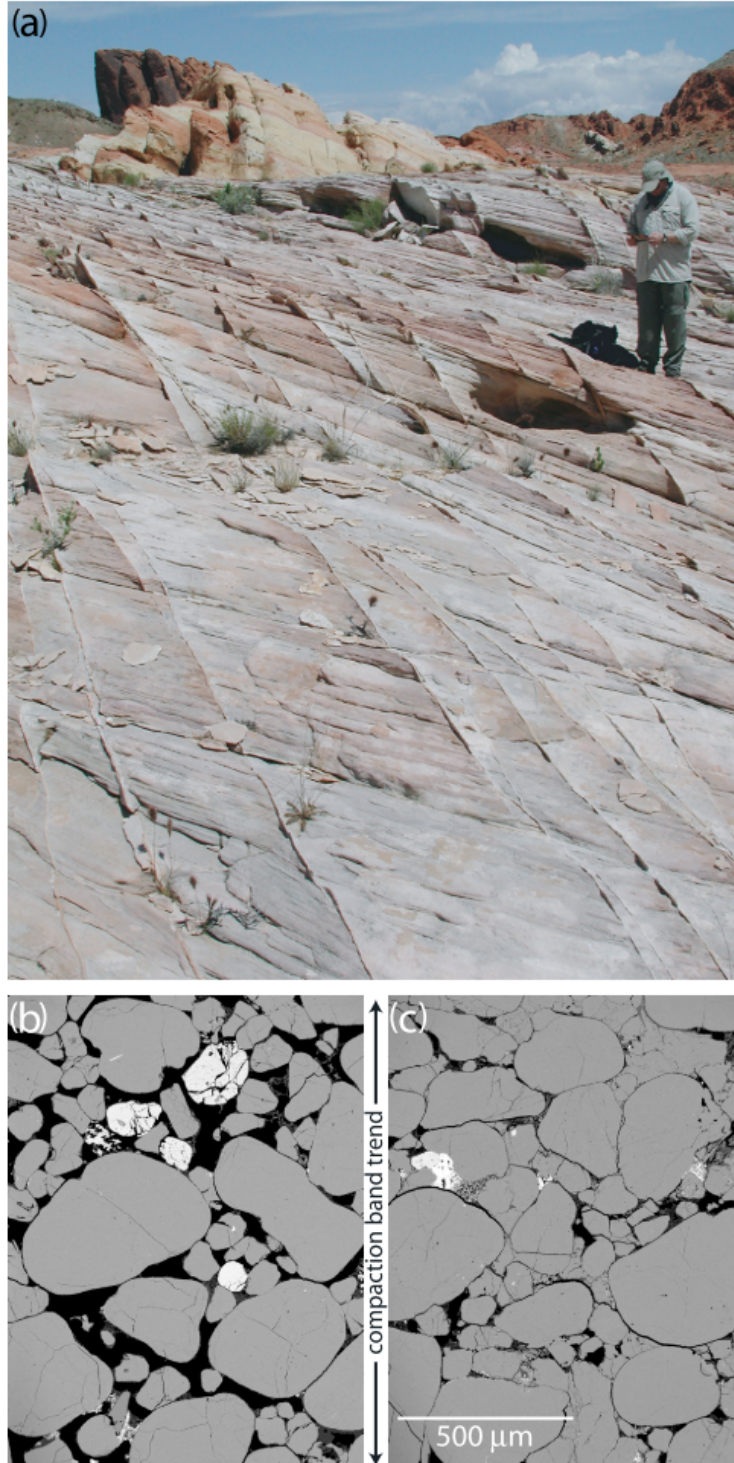
In fact, deformation bands were already object of study in the 1960s under different names, e.g., *microfaults*, *small faults*, etc. (e.g., Hara (1966); Loughran (1967)), where a *fault* is another localised deformation mode composed of deformation clusters (Knipe et al. (1998) and references therein) and characterised by surfaces across which large displacements (tens of metres to kilometres) occur (Aydin, 1978).

Figure 2.2 shows numerous sub-parallel deformation bands, which underwent pore collapse and grain crushing, as observed in the microscopic views (b and c). Typically, deformation bands:

- are the dominant tabular features in porous rocks and sediments (Shipton et al., 2005; Fossen et al., 2007);
- do not present “*discrete surface of discontinuity*”(Aydin, 1978), differently from joints or fractures where continuity is lost, at least temporarily (Griggs and Handin, 1960);
- present porosity variation, either reduction or increase, but there are also cases of grain rearrangement without porosity change (i.e., *isochoric* shear bands (Aydin et al., 2006));
- are characterised by grain rearrangement and fragmentation (Fossen et al., 2007);
- are subjected to a sequential evolution by the generation of closely spaced sub-parallel strands next to the previously formed band, thus changing from single-strand band to multi-strand band, then deformation band cluster and finally deformation band fault or slip surface (Aydin and Johnson, 1978; Jamison, 1979; Shipton et al., 2005; Fossen et al., 2007; Philit et al., 2015).

In the sequential evolution described above, the number of sub-parallel *strands* (i.e., individual deformation band) and the global displacement of the band/s grow from single-strand to fault or to slip surface. The difference between fault and slip surface is that in a slip surface there is only a single surface where the offset occurs, whereas in a fault there are numerous surfaces, which can develop in a narrow zone (Jamison, 1979).

A representation of a slip surface is shown in Figure 2.3, together with a comparison between a tabular deformation type (i.e., deformation band) and a sharp one (i.e., fracture). In the figure, three strain localisation modes are identified for the two deformation types: shear, volumetric shortening (i.e., compaction), and volumetric extension (i.e., dilation). For a deformation band, these three modes correspond to *shear band*, *compaction band*, and *dilation band*, respectively. The three deformation types are often mixed with each other in the field, and this is further described



**Figure 2.2:** Deformation bands in Aztec Sandstone in the Valley of Fire, Nevada: (a) field view, (b) back-scattered electron image of the undisturbed sandstone, and (c) back-scattered electron image of the deformation band (in b and c, black is pore) (Sternlof et al., 2006).

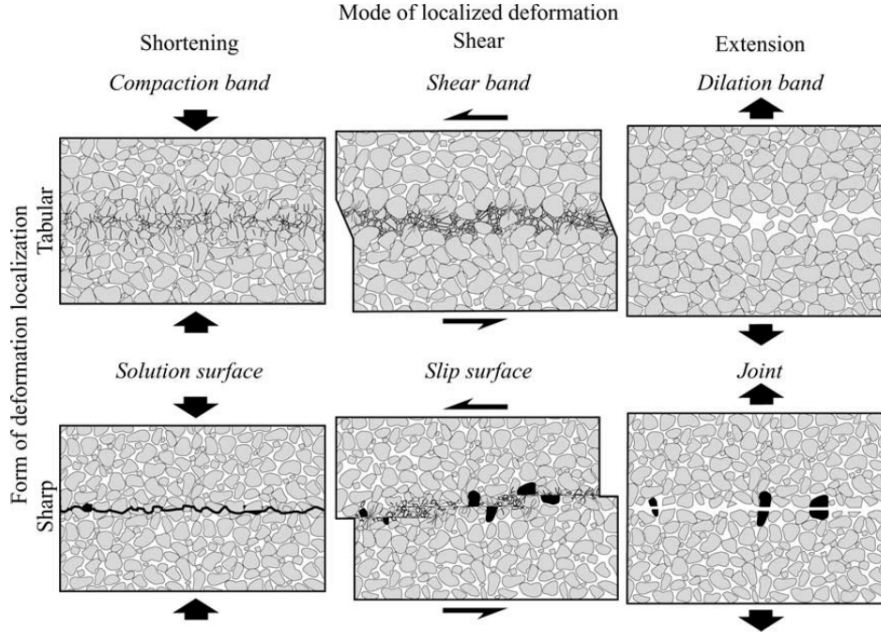


**Figure 2.3:** Forms and modes of localised deformation for tabular form (upper row) and for sharp form (lower row) of deformation localisation (Aydin et al., 2006).

below. For a sharp localised deformation (Fig. 2.3), the three modes are *slip surface* (i.e., surface where displacement occurs in two opposite directions), *solution surface* (i.e., closing fracture through pressure solution), and *joint*, (i.e., sharp discontinuity between two subparallel surfaces).

The spatial arrangement of deformation bands is influenced by natural imperfections (diagenetic or generated by later deformation) (Ballas et al., 2014; Shipton et al., 2005). In nature, sands are seldom homogeneous, they usually present variations of texture, derived from depositional structures or generated by later deformation processes. However, their influence depends on the dimension of the imperfections with respect to the scale of observation. For example, at the outcrop scale (metres to tens of metres) relevant features could be changes in lithology of surrounding sediments and rocks, burial depth, pre-existing localised deformation, whereas at the laboratory scale (millimetre to centimetre) other features could affect the texture heterogeneity, such as grain properties, presence of inclusions, regions of enhanced cementation or of enhanced porosity.

A deformation band could extend for several metres in the two directions along its plane (Fossen et al., 2007; Schultz and Soliva, 2012). However, it can be interrupted at the contact with different sand layers, as reported by Ballas et al. (2013) for shear-enhanced compaction bands that were interrupted at the contact with sand layers containing abundant clays or gravel.

According to Philit et al. (2018), deformation band and cluster thickness is affected by lithology of the sediment where deformation bands developed. For exam-

ple, coarser grains developed thicker deformation bands (Fossen et al., 2007, 2017; Sallet and Wibberley, 2010), although Antonellini et al. (1994) showed that this relation is lost if there is grain breakage. Torabi and Fossen (2009) assessed an increase in the deformation band thickness when the bands contained phyllosilicates, whereas Sallet and Wibberley (2010) observed from data coming from the South of France (Bédoin and Massif d’Uchaux) that the presence of clay may inhibit deformation band thickness growth. According to Antonellini et al. (1994), deformation band thickness is proportional to the porosity of the undisturbed material.

As deformation bands strain-harden (Jamison, 1979), there is a tendency for new or less strain-hardened bands to accommodate the next increment of displacement, where grains would require less energy to deform with respect to the existent deformation band (Aydin and Johnson, 1978). This is in agreement with observations by Mair et al. (2000) produced through laboratory experiments on sandstones.

The factors described above - i.e., length, thickness, and displacement - are related to each other. For example, Wibberley et al. (2007) observed a linear relationship between deformation band displacement and thickness. Fossen et al. (2017) reported a similar relationship, but limited to the deformation band clusters, and not valid for single-strand deformation bands. Displacement showed also a proportionality with respect to the number of strands in deformation band clusters (Aydin and Johnson, 1978; Shipton et al., 2005). The same relationship was also demonstrated in the laboratory by Mair et al. (2000), who showed that the number of deformation band strands generated in a sandstone sample is correlated with the axial strain applied to it.

Deformation band growth from single-strand band to fault (Sect. 2.1) is shown in Figure 2.4, which explains that during the sequential development there is accumulation of displacement accommodated by new bands. Therefore, a fault (d) reports the largest displacement value. Schueller et al. (2013) showed that the deformation bands growth respects a balance between the deformation bands that grow in the existing damage zone and the ones that grow adjacently to the damage zone, thus leading to a greater deformation band frequency and to a wider damage zone.

The occurrence of one type of deformation band rather than another is function of the stress state and the texture is function of the displacement/strain, e.g., a shear with more displacement has a higher degree of fragmentation. It was also shown that material imperfections can cause strain localisation and deformation banding in laboratory uncemented sand samples (Desrues and Viggiani, 2004). Other laboratory experiments showed that high confinement and high porosity can generate compaction instead of dilation, the latter one occurring at rather low porosity and low confining pressure (Antonellini et al., 1994; Alikarami and Torabi, 2015; Fossen et al., 2011; Mair et al., 2002; Menéndez et al., 1996). Other studies showed that coarse



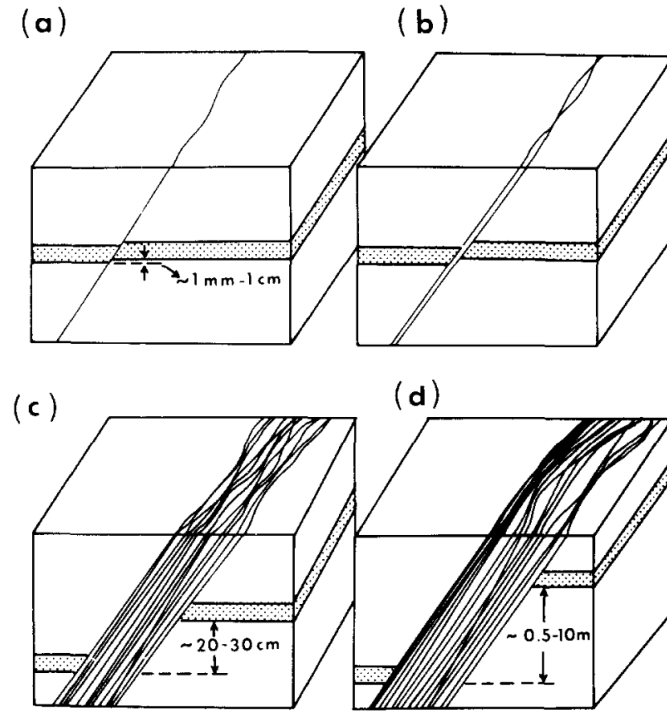
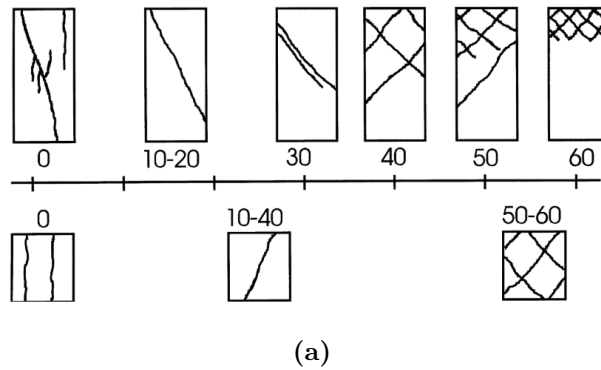
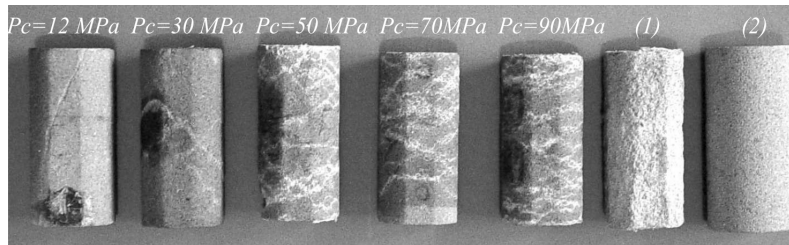


**Figure 2.4:** Sequence of a deformation band growth: (a) single-strand band, (b) two bands, (c) cluster of bands, (d) fault (Aydin and Johnson, 1978, 1983).



(a)



(b)

**Figure 2.5:** (a) Deformation bands evolving angle of shear and becoming more numerous with increasing confining pressure (0 - 60 MPa) (Bésuelle et al., 2000); (b) From left to right: samples deformed at increasing confining pressure, showing the transition from shear to compaction bands; (1) result of isotropic compression of sample (2),  $h = 80$  mm,  $d = 40$  mm (Guéguen, 2005).

grain size and high porosity in sandstone outcrops favoured compaction bands, while finer grain one and lower porosity enhanced deformation band faults (Mollema and Antonellini, 1996). Furthermore, the increase of confinement was demonstrated to generate an increase of the deformation band angle to the direction of the maximum principal stress, which can ultimately lead to horizontal compaction bands (Fig. 2.5). The following Sections provide a brief discussion of the theoretical approaches to describe localised deformation, an overview of deformation band classifications, a description of the main constituents of deformation bands - i.e., grains, cements, and pores - and a description of porosity and permeability within deformation bands.

## 2.2 The theory of localised deformation

### 2.2.1 Deformation band as localised deformation

Deformation bands belong to a class of processes generally indicated as localised deformation. As described for deformation bands in Section 2.1, localised deformation can occur in many forms (e.g., grain crushing, shear strain, pore collapse) and at all scales (from millimetre to kilometre). Its main characteristic is that it involves a limited part - generally tabular - of a material, instead of developing homogeneously in its entire volume. But why does deformation localise? Several factors can cause a divergence from homogeneous to localised deformation. For example, microstructural observations have revealed that imperfections and pre-existing cracks can evolve into a localised deformation and, usually, it is the interactions of several imperfection to start the process (Bésuelle and Rudnicki, 2004). Other factors could be mineralogy, pressure, temperature, grain shape, local pore or cement content variation, etc.

Localised deformation has attracted a great attention over the last decades because it occurs in the upper crust of Earth where it can affect human activities connected to underground structures (i.e., foundations) and infrastructures, it can trigger slope instability and seismic activity, or it can interfere with oil and gas production. Different approaches have been applied to study localised deformation at different degrees of complexity depending on the number of factors taken into account. Among the several approaches, here it is briefly described (in increasing degree of complexity): the Mohr-Colomb approach, the fracture mechanics one, and the bifurcation theory.

The Mohr-Colomb approach describes the failure in terms of stress state associated to a plane of normal  $n$  where a shear stress  $\tau_{ns}$  develops, which equals the sum of a component of cohesion  $\tau_0$  and a normal stress  $\sigma_n$  multiplied by a friction coefficient  $\mu$ :

$$\tau_{ns} = \tau_0 + \sigma_n \mu \quad (2.1)$$

With the assumption that  $\mu$  is constant, this approach to failure becomes simple and for this reason it is commonly used for a first order analysis. However, the Mohr-Colomb criterion assumes that the stress field is uniform, which is usually not the real condition for a material under deformation. Another assumption of this failure criterion is that the failure angle in case of compression and extension is the same, but experimental data have demonstrated that this angle is smaller in axisymmetric extension with respect to compression.

Fracture mechanics is another approach employed to describe the process of failure. In this case, the stress state is not considered uniform and the presence of an acute geometry (e.g., a crack) leads to high stress concentrated around it (Bésuelle and Rudnicki, 2004). This approach identifies the origin of the localised deformation in the coalescence of several imperfection, and not in a single imperfection. The limit of this approach is that it is successful in describing immediate failure, but localised deformation does not always coincide with failure, since it can correspond also to the initial stage of a deformation developing in a long interval of time.

Another approach is the bifurcation theory, which describes the possibility that a material subjected to a homogeneous deformation develops localised deformation as a planar band, instead of a further increment as homogeneous deformation (Bésuelle and Rudnicki, 2004). This theory is described in detail below.

## 2.2.2 The bifurcation theory

Rudnicki and Rice (1975), based on earlier works (Hadamard, 1903; Thomas, 1961; Hill, 1961; Mandel, 1966), formulated a model that describes localised deformation as nonuniqueness from homogeneous deformation (Issen and Rudnicki, 2000). The bifurcation approach can be applied to materials that develop a peak in the stress-strain curve at the onset of localised deformation. According to the bifurcation theory, the localisation as a planar band can occur before the peak if certain conditions are favourable, whereas it would occur after the peak for unfavourable conditions (Bésuelle and Rudnicki, 2004). These conditions are the kinematic and the equilibrium conditions. The kinematic condition needs to satisfy the continuity of the velocity field at the incipient localisation. The equilibrium condition requires the traction-rates to be continuous across the band boundary (Issen and Rudnicki, 2001). These conditions define the formulation of the bifurcation problem:

$$\{n_i L_{ijkl} n_l\} g_k = 0 \quad (2.2)$$

where  $\mathbf{n}$  is the vector normal to the plane of the planar band,  $\mathbf{g}$  is function of the distance across the band, and  $\mathbf{L}$  is the tensor that relates linearly the stress-rate with the strain-rate:

$$\dot{\sigma}_{ij} = L_{ijkl} \dot{\epsilon}_{kl} \quad (2.3)$$

Bésuelle (2001) showed that the strain localisation occurs as a shear band if  $\mathbf{g}$  has a component parallel to the plane of the band, and that the band will be compacting or dilating when the  $\mathbf{n} \cdot \mathbf{g}$  is positive or negative, respectively.

The problem in Equation 2.2 admits a non-trivial solution for  $g_k$  ( $g_k = 0$  is the trivial solution representing the continuous homogeneous deformation) only if:

$$\det |n_i L_{ijkl} n_l| = 0 \quad (2.4)$$

which constraints the possible orientations of the planar band and set their dependence on the constitutive relation that defines the tensor  $\mathbf{L}$ . The choice of the constitutive relation affects the prediction of localised deformation. For example, Equation 2.3 represents a linear law between stress rate and strain rate; other types of relation could also be chosen, e.g., bilinear, four-linear, eight-linear laws (Bésuelle and Rudnicki, 2004). Linear and bilinear laws are the simplest ones and represent the elastic (or hypo-elastic) and elasto-plastic models, respectively. In the former, the tensor  $\mathbf{L}$  is independent on the strain-rate, whereas in the latter  $\mathbf{L}$  depends on two directions of the strain-rate that are represented by two cones, one for the elastic behaviour and the other for the elasto-plastic one. In fact, materials depend continuously on the direction of the strain-rate (Bésuelle and Rudnicki, 2004). Therefore, multi-linear models would be more representative of the process. In the practise, the complex behaviours are frequently reduced to the linear law. More refined laws are chosen in special cases, e.g., the four-linear law is used to describe the behaviour of high-porosity rocks and soils. The different constitutive laws are described in detail, e.g., in Bésuelle and Rudnicki (2004) and references therein.

### 2.2.3 State of the art in modeling with the bifurcation theory

The bifurcation theory is frequently employed to predict the onset of localised deformation and this is performed through numerical modeling, especially needed in the case of multi-linear constitutive laws. This theory is able to predict the orientation and the direction of the planar band at its onset. However, the thickness of the band is not well predicted to date. The lack of this information complicates the analysis of the progression of the localised deformation and creates mesh-dependency in the numerical models (Bésuelle and Rudnicki, 2004). This is caused by the fact that the band thickness defines the energy release of the band at the onset of localisation. Other types of models, e.g., the fracture mechanics earlier introduced, are able to provide a range of values for the band thickness. For example, Tembe et al. (2008) used the fracture mechanics model to analyse field and laboratory data of sandstones and they defined an inverse proportionality between band thickness and stress level,

thus providing an order of magnitude of the energy dissipation. Differently, a study performed by Baud et al. (2006) pointed out the divergence of results obtained with the bifurcation theory and experimental data on porous sandstones at the onset of strain localisation, despite a valid qualitative prediction.

Another limit of the bifurcation theory is the assumption that the material is initially homogeneous, i.e., eventual imperfections of the material are not taken into account. In fact, natural materials (e.g., sands and sandstones) often present small imperfections due, for example, to grain rearrangement or to local variation of cement content. Pioneers of the importance of imperfections in strain localisation were Marciniak and Kuczyński (1967), who performed an analysis on a metal sheet weakened by a groove and found out that the onset of localisation may occur earlier in the groove rather than in the material without the imperfection. The current research in this topic, being aware of the limits of the bifurcation theory, is working to improve the representativeness of this theory for natural materials. The primary step towards these improvements starts from the experimental analysis of natural materials and the identification of the factors that affect localised deformation, e.g., the imperfections. In this framework, this doctoral work represents an attempt to contribute to the characterisation of the role of imperfections in the deformation band occurrence in weakly cemented sands.

## 2.3 Deformation band classifications

Deformation bands were classified in the literature according to strain mode, to mechanical and chemical processes, and to degree of deformation, among other properties and processes.

Borja and Aydin (2004) proposed a classification of band types based on the strain modes: shear and volumetric change. The first type includes *pure shear* mode and mixed modes of shear with either compaction or dilation, forming *compactive shear bands* and *dilatant shear bands*, respectively. The second type accounts only for *pure dilation* and *pure compaction*. The description in Borja and Aydin (2004) is accompanied by a schematic relationship between the three end members - i.e., shear, compaction, dilation - visualised in a triangle that reports each member in one of the three vertexes of the triangle.

The mixed modes of deformation band were named in various ways in the literature. For example, Bésuelle et al. (2000) referred to the mixed modes with the term *dilating shear band* and *compacting shear band*, whereas Schultz and Siddharthan (2005) chose the names of *dilation band with shear* and *compaction band with shear*, respectively.

Fossen et al. (2007, 2017) implemented the mixed modes in the triangle of the

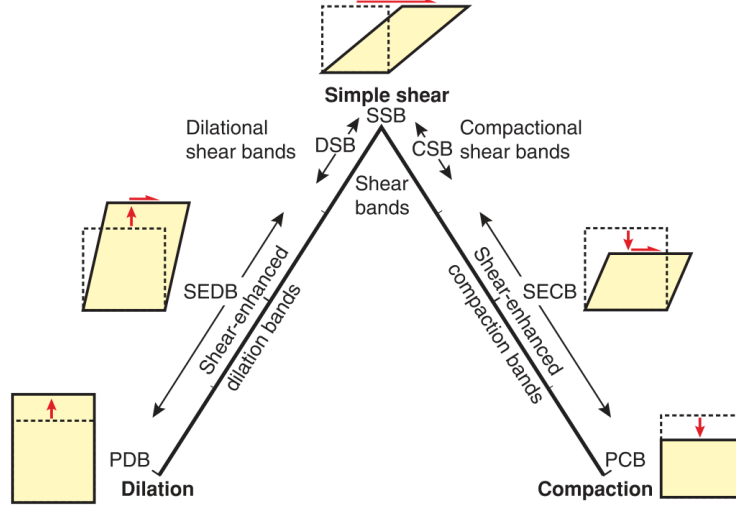


**Figure 2.6:** Types of deformation bands according to kinematics: PDB = pure dilation band; SEDB = shear-enhanced dilation band; DSB = dilational shear band; SSB = simple shear band; CSB = compactional shear band; SECB = shear-enhanced compaction band; PCB = pure compaction band (Fossen et al., 2017).

three strain modes described by Borja and Aydin (2004), thus providing a complete classification of deformation band types on a triangular scheme that is shown in Figure 2.6. The scheme in Figure 2.6 shows the three principal strain modes at the vertexes of the triangle. When simple shear is combined with modest dilation, a *dilational shear bands* is generated, whereas a higher contribution of dilation with a lower shear effect is identified as *shear-enhanced dilation band*. Similarly, a combination of shear with little compaction creates *compactional shear band*, while compaction with a small fraction of shear generates a *shear-enhanced compaction band*.

In parallel with the classification based on the strain modes, Fossen et al. (2007) proposed a classification of deformation bands according to the main mechanical and chemical processes (Fig. 2.7): *disaggregation bands*, *phyllosilicate bands*, *cataclastic bands*, *solution and cementation bands*. The band types recall the classification introduced by Antonellini et al. (1994) based on the deformation band microstructure, i.e., *cataclasis* and presence of clay within the deformation band. The term *cataclasis* derives from the greek word  $\kappa\lambda\alpha\sigma\tau\acute{o}\varsigma$ , i.e., broken in pieces, and indicates a process of grain comminution, generated by crushing when grains are sheared and/or compressed.

Each band type in Figure 2.7 depends either on the mechanical or on the chemical alteration that grains and cements undergo, but it is not rare to find two or more of these deformation processes in the same deformation band. *Phyllosilicate bands* take into account the occurrence of cements and of other inclusions. *Solution bands* include deformation bands that are affected by pressure solution, i.e., min-

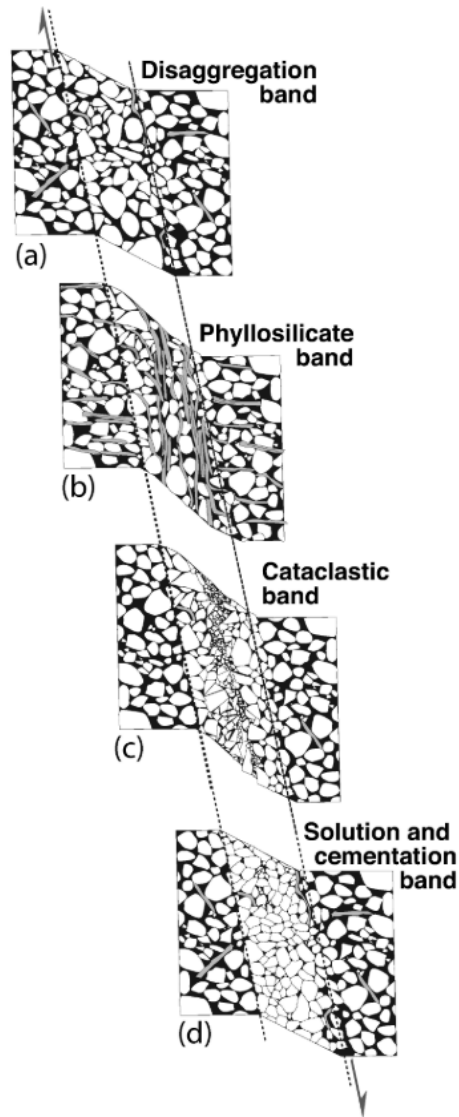


**Figure 2.7:** Conceptual model of deformation bands types according to four main mechanical and chemical processes: (a) disaggregation; (b) phyllosilicate inclusions; (c) cataclasis; (d) solution and cementation (Fossen et al., 2007).

eral dissolution at contact between grains under relative high stress. *Disaggregation* and *cataclastic bands* are principally related to mechanical processes that involve breakage of cement bonds and grain crushing, respectively.

Philit et al. (2015) proposed a classification of the cataclastic structures observed in Bédoin: cataclastic (*single-* and *multi-strand*) shear bands, *clusters* of shear bands, and *fault* zones (Fig. 2.8). The first group included single- and multi-strand bands with thickness of 1 mm to few cm, the second consisted of tens to hundreds of deformation band strands with a total thickness up to tens of cm, and faults zones consisted of clusters of shear bands with many slip surfaces.

This doctoral work followed the deformation band classification based on the strain modes proposed by Fossen et al. (2017) (Fig. 2.6) and focused on the mixed modes of shear and compaction, in particular on compactional shear bands, as well as on pure dilation bands. An overview of the structure and growth of these deformation band types is presented below. The other deformation band types identified by the classification (i.e., pure compaction band, shear-enhanced compaction band, isochoric shear band, shear-enhanced dilation band, dilational shear band) are not described because they go beyond the scope of this doctoral work.

The classification proposed by Philit et al. (2015) - which makes reference to single-, multi-strand bands, clusters and faults - is used to describe the process of cataclasis occurred in the deformation bands analysed in the following Chapters. In addition to this, the term *interband*, used in Philit et al. (2018) to refer to the granular material between deformation band strands in a cluster, is also employed.



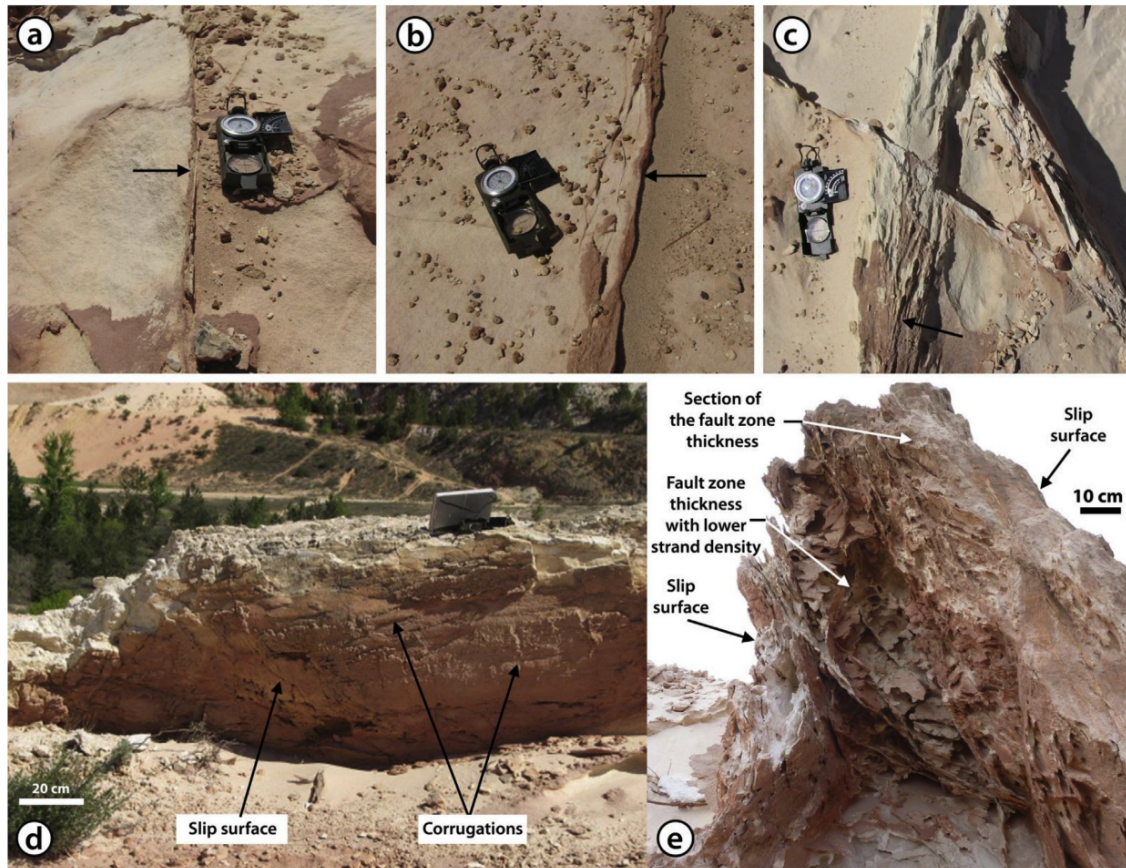


**Figure 2.8:** Types of cataclastic structures (indicated by an arrow): (a) single-strand band, (b) multi-strand band; (c) cluster of deformation bands; (d - e) fault zone with indication of several slip surfaces (Philit et al., 2015).

### 2.3.1 Compactional shear bands

Compactional shear bands are among the most common deformation bands observed in the field (e.g., Fossen et al. (2011); Ballas et al. (2012, 2013); Skurtveit et al. (2013); Cilona et al. (2014); Tavani et al. (2018)), where they usually develop in conjugate sets, intersecting with a small angle between  $20^\circ$  and  $40^\circ$  (Jamison, 1979; Skurtveit et al., 2014; Philit et al., 2015; Soliva et al., 2016).

Compactional shear bands are generally composed of three zones: the *core*, the *contour*, and the *damage* zone. The term *zonation*, used to identify the spatial distribution of cements (e.g., calcite, quartz) in geomaterials (Burley et al., 1989; Worden and Morad, 2000; Haddad et al., 2006; Molenaar et al., 2007; De Ros et al., 2009) and also to identify zones in faults and hydrocarbon reservoirs (Sibson, 1977; Jobe et al., 2017), was then used for deformation bands (Torabi et al., 2007; Alikarami and Torabi, 2015) to identify zones that differ for their micro-textural characteristics, i.e., degree of breakage and porosity. The same use of the term is made in this doctoral work, in particular to refer to the three zones of a compactional shear band.

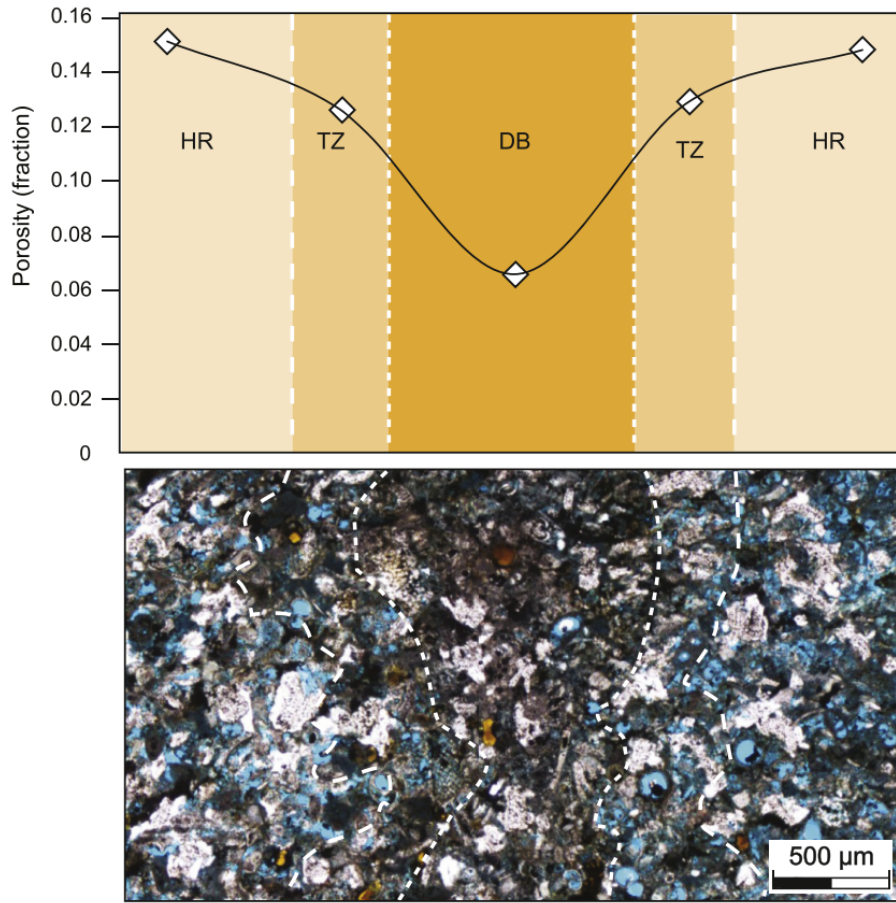


**Figure 2.9:** Porosity measurements in a section of deformation band undergoing compaction: values in the contour zone (TZ) are intermediate between core (DB) and damage zone (HR) (Rotevatn et al., 2016).

The *core* is the most characteristic zone of a compactional shear band, having the highest degree of fragmentation and the lowest porosity value (Aydin, 1978; Gabrielsen and Aarland, 1990; Torabi et al., 2007; Alikarami and Torabi, 2015). On the contrary, the *damage* zone reports the lowest degree of fragmentation and the highest porosity value of the band, which is closer to that of the undisturbed material. An accurate description of the grain properties within the core zone is provided in Section 2.4.

The *contour* zone is the intermediate zone between core zone and damage zone (Fig. 2.9), in terms of porosity and of degree of fragmentation. The contour zone was alternatively referred to in the literature as *margin* (Aydin, 1978; Milliken and Reed, 2002; Cashman et al., 2007; Rotevatn et al., 2008; Alikarami and Torabi, 2015), *transition* zone (Rotevatn et al., 2016), *outer* zone (Aydin, 1978), *boundary* zone or *rim* (Antonellini et al., 1994; Rath et al., 2011; Cilona et al., 2012; Lima et al., 2015).

The contour zone is not always identified in deformation bands. According to laboratory studies on natural samples and on laboratory created sand samples, con-

tour zones in shear bands developed under mean stress of 7 MPa (Alikarami and Torabi, 2015). Various observations within deformation band contours reported evidences of deformation and of cement-related processes, e.g., intragranular fractures that follow grain alignments called *brigdes* in Cashman et al. (2007), quartz cement filling the fractures (Milliken and Reed, 2002), calcite cementation (Cilona et al., 2012), pore alignments with preferential elongated shape (Lima et al., 2015).

### 2.3.2 Pure dilation bands

To date, only few observations of dilation bands were reported (Du Bernard et al., 2002; Kaproth et al., 2010; Exner et al., 2013). The observed bands were composed by a *core* surrounded by *damage* zone. The *core zone* of a dilation band has a higher porosity than the damage zone and the undisturbed material, and reported clay filling (Du Bernard et al., 2002; Kaproth et al., 2010) and minor grain cataclasis (Du Bernard et al., 2002; Exner et al., 2013), differently from a compactional shear band. Porosity is described in detail in Section 2.6.

Spatial arrangement and frequency of dilation bands is not well known because of the small number of observations with no band arrays identified. Displacement along the plane of pure dilation bands does not occur because of the absence of the shear component. The dilation bands were observed only as single-strand bands and their extension is not known since field observations are few and did not provide this information. Dilation band core has a thickness of about 1-2 mm (Du Bernard et al., 2002), corresponding to 5 to 10 times the average grain size. Similar thickness values were detected for single-strand dilation bands in Exner et al. (2013) of about 2-4 mm in thickness. Clay cement precipitation was observed in dilation bands by Du Bernard et al. (2002).

Exner et al. (2013) claimed that dilation bands formed at low burial. Low confining pressure (5 MPa) combined with low strain rate could generate dilation bands (dilatational shear band, according to their interpretation) in Cilona et al. (2012).

## 2.4 Grain properties within deformation bands

### 2.4.1 Grain breakage

Grain breakage occurs in deformation bands generated by shear and compaction strain modes. Degree of breakage was used as parameter to classify deformation bands (Philit et al., 2015; Ballas et al., 2015) by adapting a textural classification used for fault rocks (Sibson, 1977). For example, Ballas et al. (2015) identified the following classes of cataclasis, in increasing order: *crush microbreccia*, *protocatacla-*

*sis*, *cataclasis* and *ultracataclasis*.

Confining pressure characterises the grain breakage, principally distinguished into abrasion and splitting (Mair and Abe, 2011), depending on grain mineralogy (Aydin et al., 2006). For example, Griffiths et al. (2016) reported earlier fracturing of volcanic, carbonate, and feldspar grains with respect to quartz within deformation bands. At low confining pressure, quartz grains can reorganise spatially by rolling and translating without breaking, thus confirming that grain breakage is not a prerequisite of all shear bands (Aydin et al., 2006). Rolling and translation can generate abrasion during quartz grain rearrangement (20 MPa), thus producing flakes and less splitting than in the case of higher confining pressure (100 MPa) (Rawling and Goodwin, 2003). In similar conditions of low confinement, feldspathic poorly lithified arenites developed transgranular fractures, which is facilitated by the cleavage of feldspar (Rawling and Goodwin, 2003; Fossen et al., 2017). At high confining pressure, flaking mode in quartz grains is overcome by grain splitting (Torabi et al., 2007), whereas feldspathic and volcanic sediments are highly crushed. In addition, Mair and Abe (2011) underlined the effect of rough fault walls in enhancing grain splitting, whereas smooth fault walls promoted grain abrasion.

Grain breakage is controlled not only by confining pressure but also by contact geometry, which depends on initial grain size, roundness, sorting, and spatial arrangement. For example, coarser grains tend to break earlier than finer ones because they have fewer contact points where forces are more concentrated (Skurtveit et al., 2014; Griffiths et al., 2016). When two or more grains are aligned - average of 3 - 4 grains (Ballas et al., 2013) - chains of grains can be identified, which enable force transmission. Therefore, these structures were named *force chains* (Cates et al., 1998; Wang and Leung, 2008; Soliva et al., 2013; Ballas et al., 2014) (Fig. 2.10).

Figure 2.10 shows conceptual models of force chains (a and b), and microscopic observation (c) of microfractures (i) and corresponding force chains (ii) developed in grains along a deformation band (see also Fig. 10 and 11 in Ballas et al. (2013)). In particular, ideal spherical grains break according to the Hertzian fracture mode (Fig. 2.10b), i.e., triggering the fracture propagation from contact points between grains. The chains are interpreted as incipient strands of deformation bands (Saillet and Wibberley, 2013). The force chains in the deformation band core in Figure 2.10c are no more identifiable because grain fracturing and rearrangement already occurred.

The onset and growth of force chains depend on the grain-to-grain interaction when a granular material is loaded. This was observed in sandstones by Mair et al. (2002), who focused particular attention on the coordination number (i.e., number of contacts that a grain has with its neighbours), observing that a small coordination



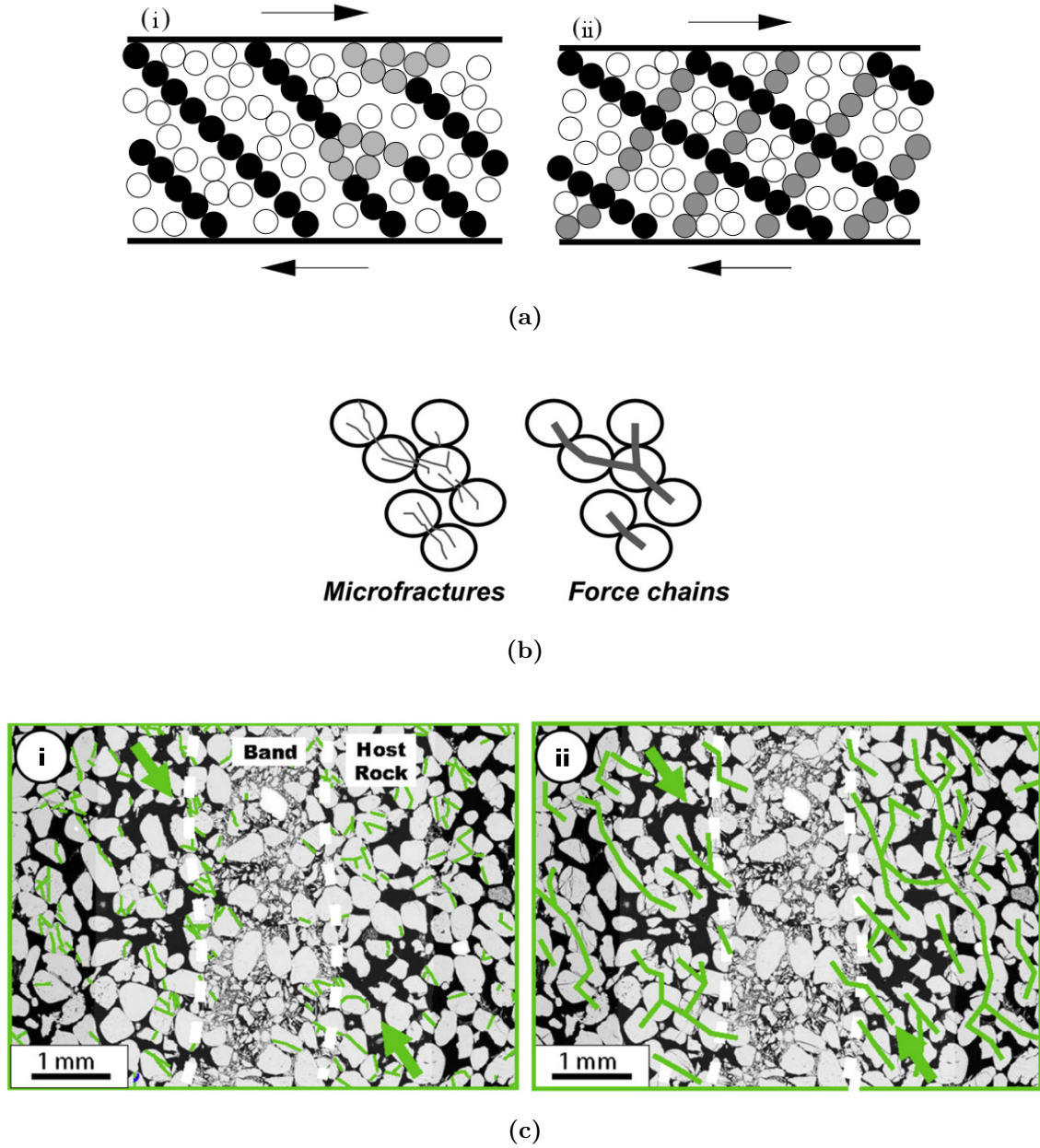


**Figure 2.10:** Force chain conceptual models and observation: (a) Conceptual models of (i) incipient and (ii) organised force chains (black) in a shear band, surrounded by grains that provide secondary support to forces (grey) and by "spectator" grains (white) (Cates et al., 1998); (b) conceptual model of force chains distribution corresponding to grain microfracture propagation (Soliva et al., 2013); (c) Microscopic observation of grain microfractures (i) and corresponding force chains (ii) inferred in the material along a deformation band (Soliva et al., 2013).

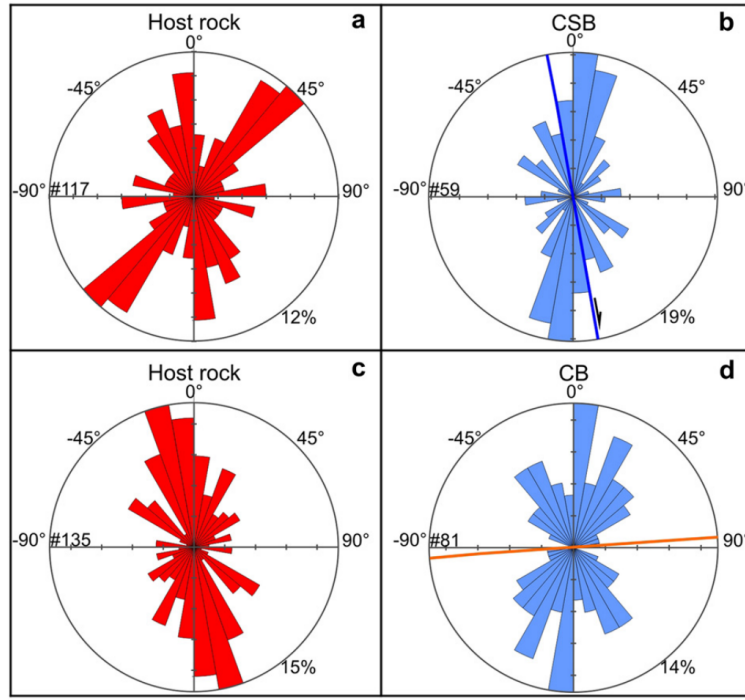


**Figure 2.11:** Rose diagrams reporting the force chain orientations in host rock (a) and corresponding cataclastic shear bands (b), and in another host rock (c) with its corresponding compaction bands (d). Note that in (b) the range  $0^\circ$  to  $20^\circ$  is  $\parallel$  to the direction of maximum shortening, and in (c) the range  $-20^\circ$  to  $0^\circ$  is  $\perp$  to the bedding direction (Cilona et al., 2012).

number would lead to a greater localization of stress chains. In granular materials under compression, force chains were reported to develop sub-parallel to the major principal stress (Wang and Leung (2008), after Oda (1972) and Ballas et al. (2013)). It is reported in Soliva et al. (2013) and also shown in Figure 2.10 that force chain direction is oblique with respect to the deformation band plane. Soliva et al. (2013) added that this direction bisects the conjugate angle in the case of conjugate pairs of deformation bands. Cilona et al. (2012) provided further analysis of the force chain orientation with comparison between undisturbed material and deformation bands (Fig. 2.11). The results of their work is shown in Figure 2.11 with a representation of preferential orientations of force chains:  $0^\circ$  to  $20^\circ$  for cataclastic shear bands as compared to  $40^\circ$  to  $50^\circ$  and  $-10^\circ$  to  $0^\circ$  for the undisturbed material, whereas two main orientations  $0^\circ$  to  $10^\circ$  and  $20^\circ$  to  $30^\circ$  for compaction bands as compared to  $-20^\circ$  to  $0^\circ$  for host rock. The wider angle range for compaction bands is explained by considering that high comminution and compaction in this band type distribute more isotropically the force chains.

In the occurrence of cement between grains, the scenario of force chains and Hertzian contact points is altered, because grain contacts are no more singular. Cemented grains need to break the cement bridges between the grains in order

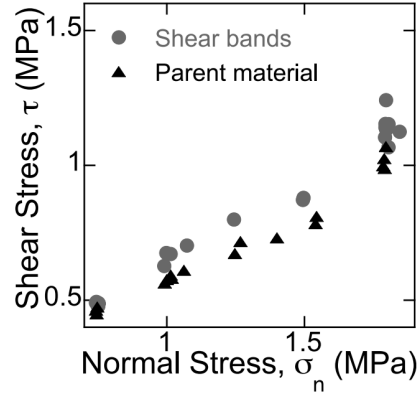


**Figure 2.12:** Mohr-Coulomb failure envelopes for a weakly cemented sand, showing increased internal friction in the shear band with respect to the parent material (i.e., undisturbed sand) (Kaproth et al., 2010).

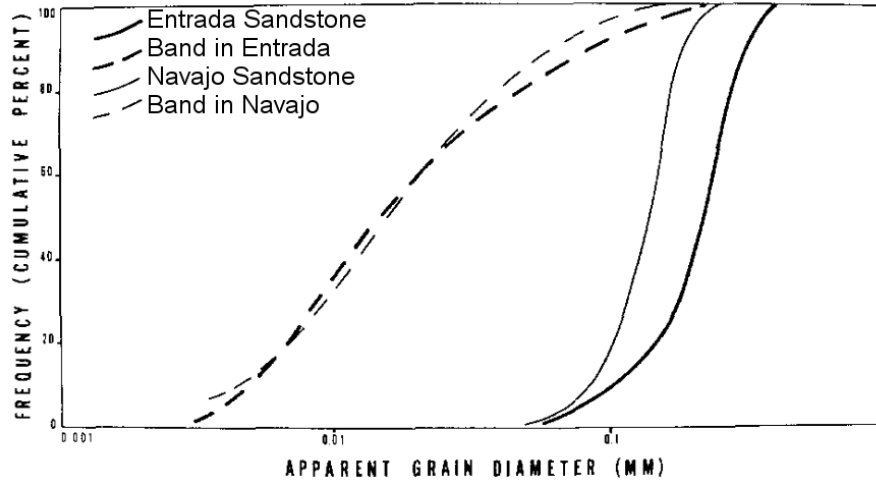
to provide freedom for grain rearrangement. Cement blocks grain rotation and translation (Wang and Leung, 2008), stabilising the force chains and producing a strong force chain network. The effects of cement is further discussed in Section 2.5.

Grain breakage provokes reduction of the average grain size and increase of the grain angularity, which create tighter packing and higher shear resistance with respect to the initial material, thus justifying the strain-hardening of a deformation band with the accumulation of displacement (Fossen et al., 2007). For example, Kaproth et al. (2010) showed in the Mohr-Coulomb plane in Figure 2.12 an increase of internal friction (for a similar cohesion) in the shear band with respect to the undisturbed material.

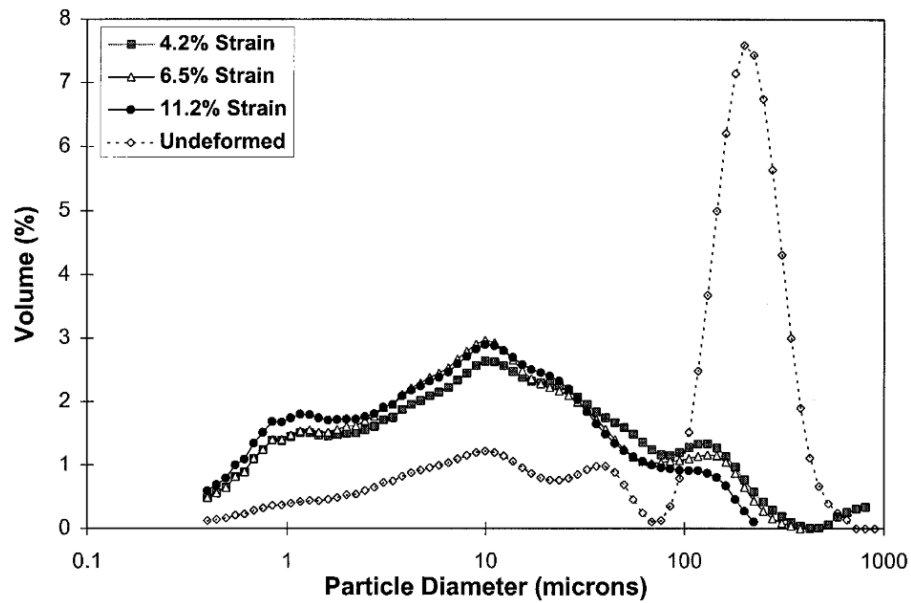
## 2.4.2 Grain size distribution

The granulometric curve of a deformation band is widened with grain comminution and with increase in the finer particles (Fig. 2.13) (Aydin, 1978; Menéndez et al., 1996; Mair et al., 2000; Shipton et al., 2005). In Shipton et al. (2005) and Wibberley et al. (2007), it is reported that finer grains are in higher quantity in fault cores rather than in single-strand deformation bands, which can be explained by the increased offset in a fault, as earlier discussed in Section 2.1.

When the fragments fill the pore space of a granular material and this reaches a porosity value near to zero, the grain or rock structure becomes matrix-supported, in contrast with grain-supported (Exner et al., 2013; Sallet and Wibberley, 2013). Philit et al. (2015) quantified the matrix as the percentage of grain fragments smaller than  $1/10$  with respect to the mean grain size of the undisturbed sand. In the matrix, the presence of *survivor* grains is observed, i.e., well-rounded (Milliken and Reed, 2002) grains of size comparable to the undisturbed ones that are found in a deformation band surrounded by great quantity (almost pore filling) of finely crushed



(a)



(b)

**Figure 2.13:** Examples of grain size variation from undisturbed to naturally and laboratory deformed materials (a) Entrada and Navajo Sandstones and deformation bands (Aydin, 1978); (b) Locharbriggs Sandstone and samples deformed in the laboratory at different deviatoric strain levels (Mair et al., 2000).



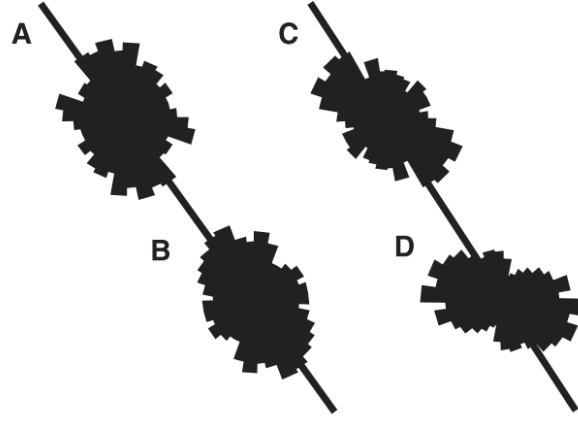


**Figure 2.14:** Rose diagrams showing grain orientations in undisturbed material (A and C) and their respective fault (B) and deformation band (D) compared to the fault strike (crossing line): A. Flook Ranch undisturbed material,  $N = 688$ ; B. Flook Ranch fault,  $N = 1434$ ; C. Alder Creek undisturbed material,  $N = 870$ ; D. Alder Creek deformation band,  $N = 1791$  ( $N$  is the sample size) (Cashman et al., 2007).

grain fragments (Engelder, 1974; Aydin, 1978; Cladouhos, 1999).

Figure 2.13 shows the grain size reduction experienced by sandstones within deformation bands (a) naturally occurred (inspected with thin sections and optical microscope) and (b) laboratory induced (measured with laser particle size analysis). The granulometric curves in (a) emphasise the change from good to poor sorting of the grains in the bands (dashed lines). Figure 2.13b shows the grain size reduction within a band at different axial strain levels.

### 2.4.3 Grain and fragment orientation

Grains and their fragments within deformation band and fault core zones are subjected to grain rearrangement, i.e., rotation and translation. This is shown for example in Figure 2.14 by the comparison of grain orientations between undisturbed material (A and C) and deformed one (B and D, respectively).

Figure 2.14 and other studies (Antonellini et al., 1994; Du Bernard et al., 2002; Philit et al., 2015) showed that grains follow an orientation parallel or subparallel to the tabular zone of localised deformation, whereas grains in the undisturbed material do not show a preferential orientation. Eventual initial orientations could primarily be related to deposition and bedding.

Grains could be preferentially oriented not only in the deformation band core zone, but also in the contour. For example, carbonate grainstones shown in Figure 2.15 affected by deformation bands showed grains oriented parallel to the deformation band plane in the core zone and an intermediate orientation in the contour zone with respect to core zone and undisturbed rock. The rose diagrams for each

deformation band zone show a wider range of angles for the contours with respect to core and also to undisturbed rock, thus representing a transition in terms of grain orientation between deformation band core and undisturbed rock.

Another type of grain fragment orientation is connected with the microfracture alignment observed in sandstone quartz grains (Aydin, 1978). The fractures of neighbouring grains are aligned and follow the direction of major principal stress (see Fig. 9 in Aydin (1978)). This microfracturing process is not originated by contact between grains, as discussed above in the case of force chains, but it occurs when grains are immersed in abundant cement whose stiffness is comparable to or higher than that of grains.

## 2.5 Cements within deformation bands

Cements are part of the structure of granular rocks and they bind the grains together. Weakly cemented sands and sandstones are typically cemented with quartz, clay, dolomite, and calcite, and occasionally by other minerals such as anhydrite, pyrite, feldspar, zeolite, haematite and Ti-rich minerals (Worden and Burley, 2003).

Literature about cementation within deformation bands in the field is not vast. Few examples of detailed characterisation of quartz cement within cataclastic deformation bands are available (Milliken and Reed, 2002; Philit et al., 2015; Griffiths et al., 2016). Clay and calcite inclusions affecting deformation bands of different types (e.g., shear-enhanced compaction bands in Ballas et al. (2013), dilation bands in Du Bernard et al. (2002), disaggregation and cataclastic bands in Fossen et al. (2007) and Skurtveit et al. (2015)) and generating *cementation bands* (Exner et al., 2013) are more frequently described.

An overview of the general reinforcing effects of cements within granular materials is provided below. Then, quartz and clay cementation are described in detail.

### 2.5.1 Overview of cements in granular materials

The strength of a cemented material depends, among other factors, on the number of contacts between the grains, on the texture, and on the thickness of the cement bonds (Molenaar and Venmans, 1993). Depending on the saturation condition of the granular material at the time of cementation, cement precipitation in a granular material can be more homogeneous or have preferential location. Cheng et al. (2013) showed that cement in a saturated material precipitates rather homogeneously around the grain surfaces, while cement in a partially saturated material precipitates preferentially where the water is retained by capillary forces, i.e., at the contact between grains and in narrow pore throats.

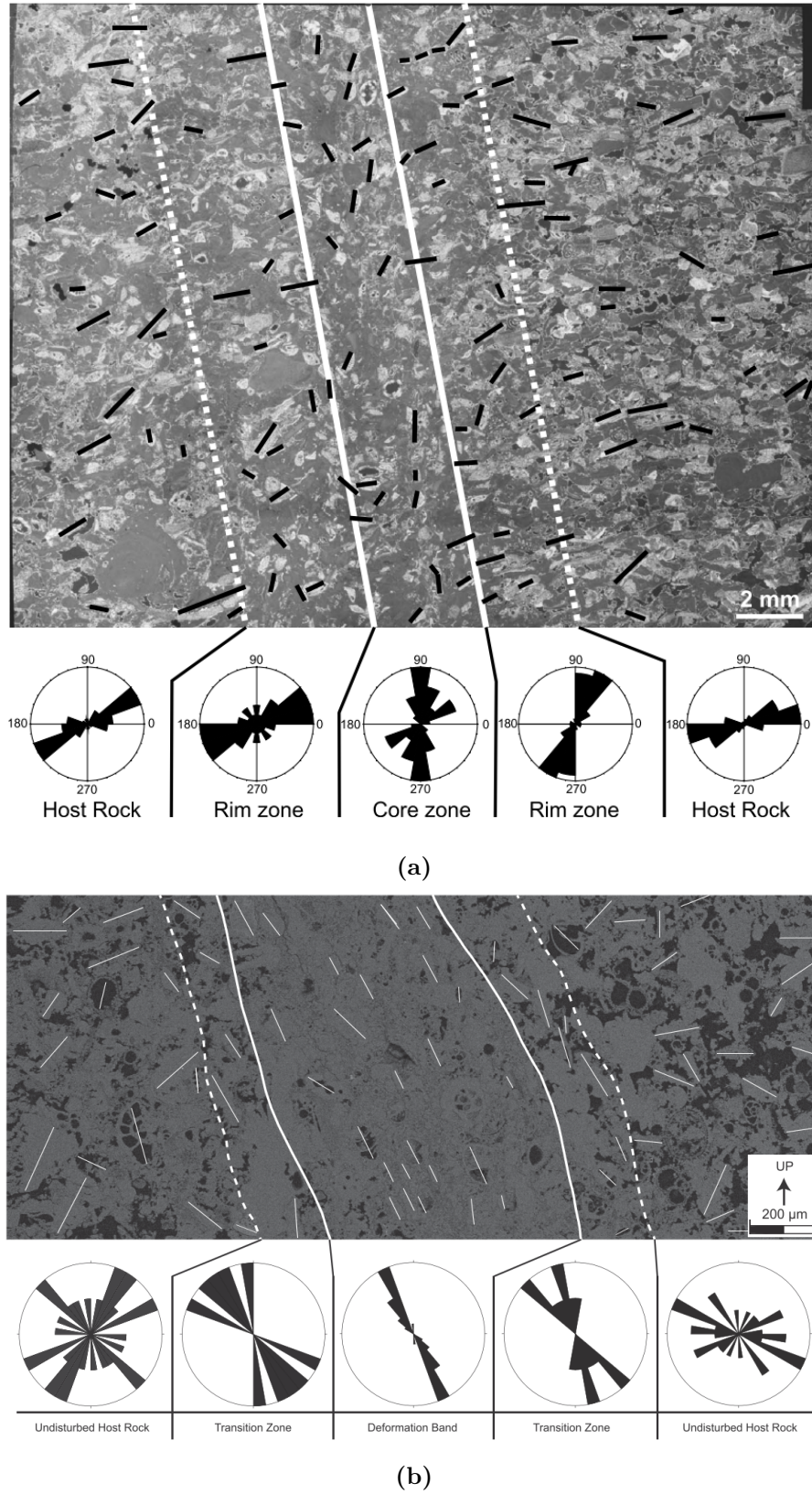


**Figure 2.15:** Thin sections of grainstones with rose diagrams of the grain orientations within core, contour, and damage zone of two deformation bands ((a) from Rath et al. (2011), and (b) from Rotevatn et al. (2016)).

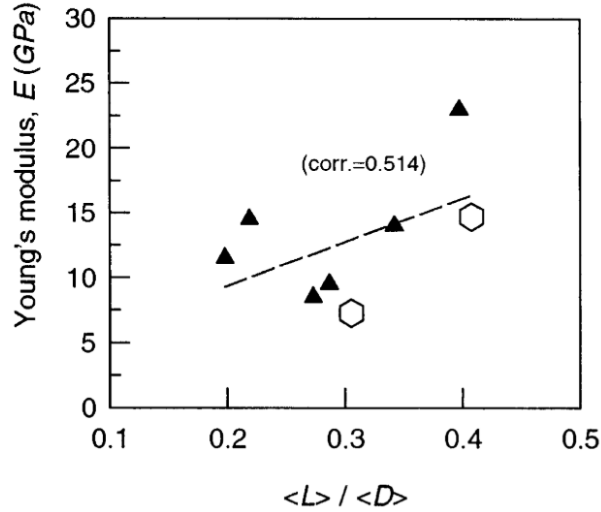


**Figure 2.16:** Correlation between stiffness and contact length  $L$  (normalised for the grain size  $D$ ), where triangles represent natural sandstones and hexagons stand for artificially cemented rocks (David et al., 1998).

When a cement deposits at the grain-to-grain contact, the contact is no more Hertzian (i.e., punctual) but it becomes larger, and when the cement deposits in narrow pore throats (i.e., small pore space that connects two larger pores between grains), it creates cements bridges or bonds that increase the number of grain contact points. Because of the grain contact increase in number and in surface, the stresses are more distributed in the overall granular material, thus leading to a more stable stress condition (Dvorkin and Yin, 1995; den Brok et al., 1997; David et al., 1998; Aydin et al., 2006) and improving the material stiffness (Fig. 2.16).

Figure 2.16 shows that the stiffness (i.e., Young's modulus) of a granular material increases with the contact length for a fixed grain size (contact length normalised for the grain size). Cement bridges increase the number of grain contacts and generate resistance to grain movement (Aydin et al., 2006; Sallet and Wibberley, 2013), i.e., rolling and sliding. Therefore, stronger and more stable force chains are generated (Wang and Leung, 2008), which prevent from grain breakage. Force chains are more uniformly distributed within a homogeneous material, considering that the lower the cement content the more heterogeneous it becomes, in agreement with observations on natural (den Brok et al., 1997) and artificially cemented samples (David et al., 1998).

Artificially cemented granular materials behave in a brittle manner when brittle cement (e.g., silica gel) is added to their volume (David et al., 1998); as a result, they show a strain-softening behaviour and the brittle-to-ductile transition is retarded. Similar results were shown in Wang and Leung (2008) by using two cement types, Portland cement and gypsum. Cruz et al. (2011) showed (Fig. 2.17a) the occurrence of brittle failure mode in cemented samples, except for the sample tested at the

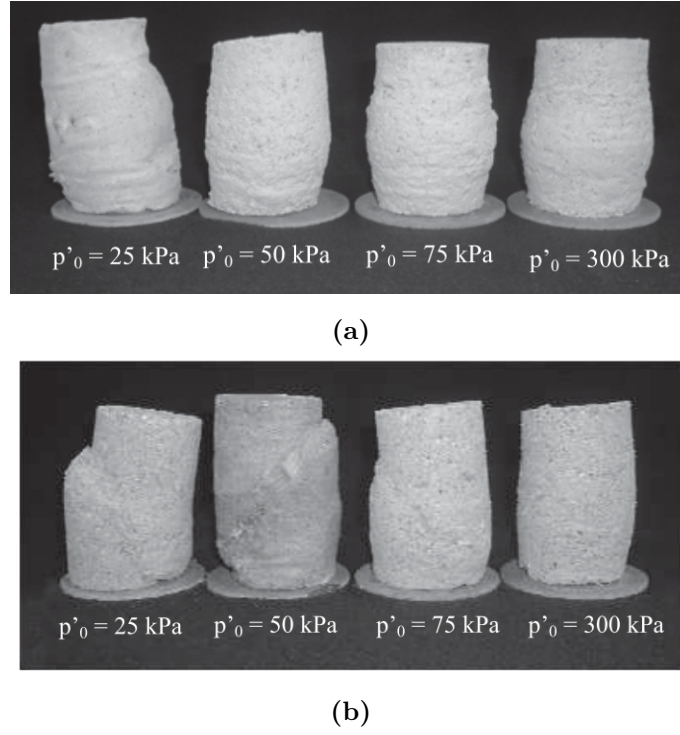


**Figure 2.17:** (a) Uncemented and (b) cemented (rapid curing cement for concrete) coarse granitic sand under shear at different effective mean stresses (in both cases, the samples were saturated,  $h = 14$  cm,  $d = 7$  cm) (Cruz et al., 2011).

highest confining pressure (300 kPa), which reported a barrelling shape. On the contrary, a ductile failure mode dominated the uncemented samples (Fig. 2.17b), which deformed in barrelling mode, with the exception of the brittle failure in the sample tested with the lowest confinement (25 kPa).

By adding cement to a granular material, even a small quantity (David et al., 1998; McBride, 1989), porosity decreases with the increase of the material resistance (Fig. 2.18). Figure 2.18 shows the porosity collapse undergone by an uncemented granular material at about 50 MPa, while the cemented material reported a little gradual porosity reduction with no collapse.

### 2.5.2 Quartz cement: occurrence and effects

The occurrence of silica precipitation (also called *silicification*) depends on a combination of factors, such as silica supply, chemistry of water (alkaline), available quartz surface for precipitation, temperature and pressure conditions (Worden and Morad, 2000).

Silica for cementation can be provided from either internal or external sources (McBride, 1989; Worden and Morad, 2000). Internal sources are quartz grain breakage, pressure solution (enhanced by the detrital clay at grain-to-grain contact, Fisher et al. (2000); Mørk and Moen (2007)), clay transformation, feldspar alteration. Ex-

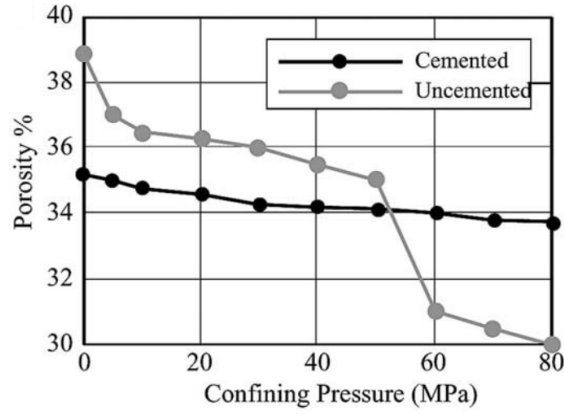


**Figure 2.18:** Porosity variations at different confining pressures in cemented and uncemented glass beads randomly packed; cement is epoxy resin (from Aydin et al. (2006), after Dvorkin and Yin (1995)).

ternal sources can be similar processes occurring in distant locations, from where silica is then transported by fluids within the rock.

Surface for quartz precipitation is provided by grain breakage because it creates new quartz surfaces that are highly reactive and preferred location for silica to precipitate (Wibberley et al., 2007; Philit et al., 2015). For this reason, quartz cementation is a recurrent process within crushed sandstones.

Temperature was described by Fisher et al. (2000) as being more relevant than pressure in the quartz cementation. The suggested temperature for quartz precipitation is of about 90° C (Fisher et al., 2000), but in some cases a lower temperature of about 60 - 70°C was estimated for continuous formation of quartz cement (Harwood et al., 2013), and even 40 - 60°C for the onset of quartz precipitation (Worden and Morad, 2000). Temperature and burial depth are parameters related by the geothermal gradient, which has a rate of about 30° C/km for rifted sedimentary basins (Worden and Burley, 2003). In field cases with low estimated burial, no quartz cementation was observed and the quartz effect on the sealing properties of deformation bands became more relevant with the depth (Saillet and Wibberley, 2013).

Quartz cementation can occur as single precipitation episode (Zhang et al., 2012) or as multiple syntaxial quartz overgrowths, i.e., in multiple layers that deposit discontinuously (Burley et al., 1989; Worden and Morad, 2000). Syntaxial quartz overgrowths follow the crystallographic orientation of the quartz grains they grow on (Fig. 2.19) (Worden and Morad, 2000). It is not a case that cataclastic deformation bands in sands and sandstones are usually quartz-cemented (Griffiths et al., 2016), since they provide both surface for cement precipitation and local source of quartz.

Philit et al. (2015) described quartz cementation within cataclastic deformation bands in weakly cemented sands. Each degree of cataclasis, following the classifica-

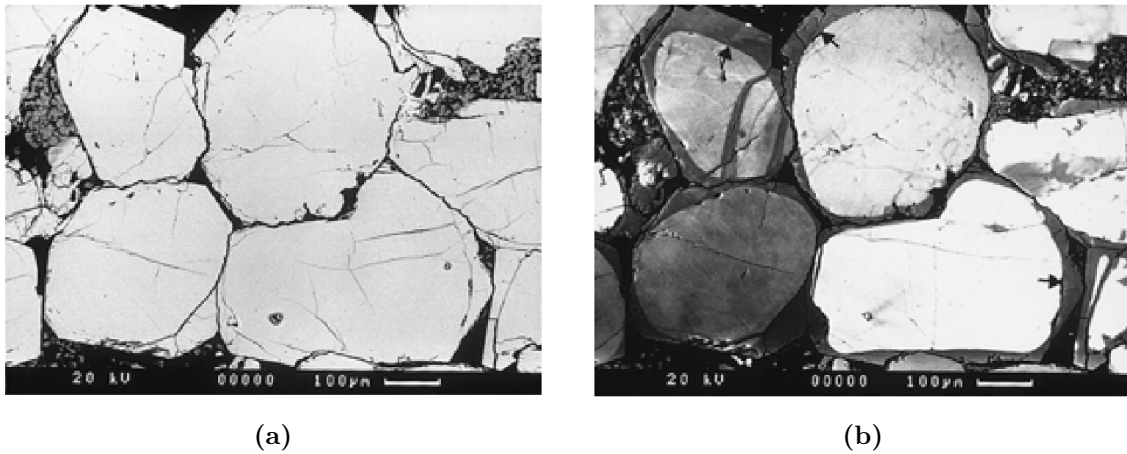


**Figure 2.19:** Quartz cemented grains in a sandstone: (a) Back Scattered Electron image where there is no distinction between grains and overgrowths since they have the same mineralogy and (b) Cathodoluminescence image of the same area, revealing where the overgrowths are located from a comparison with (a) (see the arrows) (Fisher et al., 2000).

tion of cataclastic structures discussed in Section 2.3, corresponded to a silicification degree: *crush microbreccia* and *protocataclastic zones* are uncemented or with thin cement layers, whereas intense cementation is developed in the *cataclastic* and *ultracataclastic zones*.

Quartz cement produces an increase of the rock stiffness and this effect increases with the cement content (Haeri et al., 2005). By strengthening the rock, compaction can be prevented or retarded, especially if the sediment has a low burial (Lander and Walderhaug, 1999; Worden and Morad, 2000; Mørk and Moen, 2007), for which silica precipitation can be enhanced by migration of hot fluids (Burley et al., 1989).

The reinforcement provided by silica cement is also exerted for the individual grain by healing grain fractures (Burley et al., 1989; Wibberley et al., 2007; De Ros et al., 2009). Cataclastic deformation bands enhance quartz cementation, which in turn favours cataclasis and brittle failure (i.e., microfracturing) within the stiffer rocks. On the contrary, a more ductile behaviour is generated by clays and by iron oxides (Torabi and Fossen, 2009), which lead to sliding, thus disaggregation bands and cataclastic flow (Menéndez et al., 1996; Wibberley et al., 2007).

### 2.5.3 Clay cement: occurrence and effects

Clays in sandstones can be authigenic, deriving from reactions such as alteration of feldspar at shallow burial caused by percolation of meteoric water (Worden and Morad, 2000), or it can be simply transported by fluids.

The presence of different types of clay minerals depends on the temperature which the minerals were exposed to, thus suggesting burial depth experienced by the sediment (Fig. 2.20) (Lanson et al., 2002; De Ros et al., 2009; Hartmann et al.,



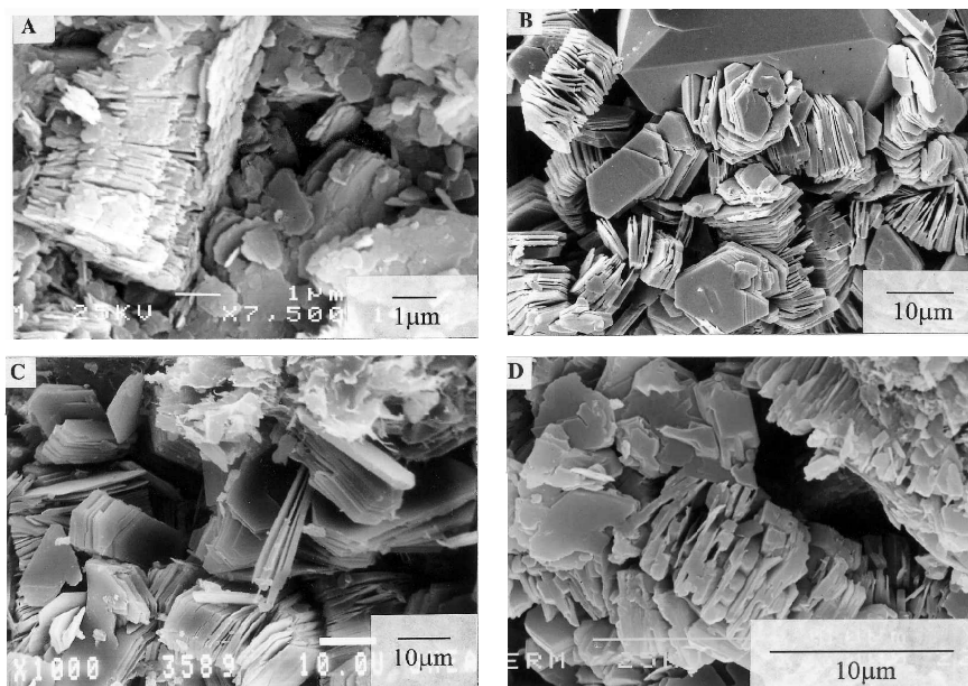


**Figure 2.20:** Transformation of Kaolinite with depth: (A) < 1000m, mixture of vermicular and anhedral crystals; (B) 3000 m, vermiform kaolinite; (C) 3000 m, elongation of kaolin platelets and thickening of booklets; (D) 3500 m, intercalation of blocky crystals between stacks (adapted from Lanson et al. (2002)).

2009; Kraishan et al., 2009).

Figure 2.20 shows the transformation of kaolin clay with the depth. A change from vermicular kaolinite to illite dominated clays was reported by Hartmann et al. (2009) in sandstones located at a present depth of about 4000 m. Kraishan et al. (2009) showed the occurrence of this transformation at a depth of about 2000 m (Fig. 2.21). Similarly, De Ros et al. (2009) documented field data of vermicular kaolinite being replaced by illite at an estimated burial between 1200 - 2200 m, which justify temperatures of up to 156° C with the permeation of hot fluids through the fractured material. Lanson et al. (2002) reported an association of the illitization of kaolinite with tectonics, i.e., intense faulting and fracturing. According to Lanson et al. (2002) and to Worden and Burley (2003), the kaolinite-to-illite transformation occurs at a temperature of about 90° C. However, kaolinite is already thermodynamically unstable at 60° C (Worden and Morad, 2000). At a temperature of about 125° C kaolinite can generate illite and quartz by reacting with K-feldspars (see eq. (3) in Worden and Morad (2000)).

The role of clays in the mechanical behaviour of cemented granular materials is ambiguous and it depends on the clay textural and spatial distribution rather than on its quantity (Fisher et al., 2000). Clay can constitute a cement itself or interact with other cements, e.g., quartz, thus generating different effects. In fact, these two



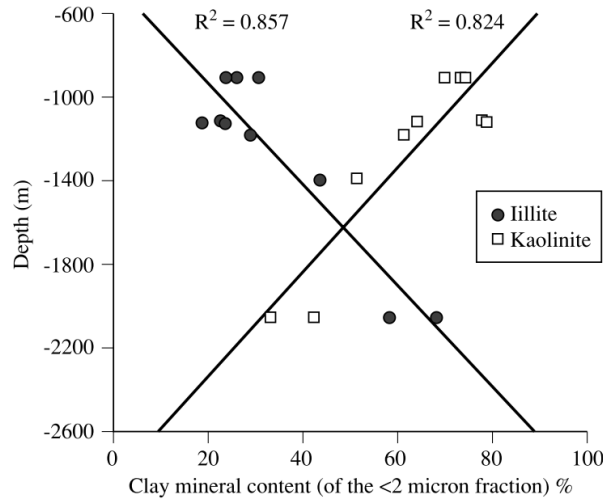


**Figure 2.21:** Clay type variation with the depth: at higher depth there is predominance of illite in the place of kaolinite and the temperature corresponding to this inversion is the intersection of the trending lines for the two clay forms (Kraishan et al., 2009).

roles can coexist in a deformation band, especially in the presence of quartz grain fragments. Clay can deposit at grain contact (Fisher et al., 2000) and create menisci bridges between adjacent grains (Du Bernard et al., 2002), thus contributing to the reinforcement of the granular rock and reducing the stress concentration at the contacts (Dvorkin and Yin, 1995; den Brok et al., 1997; David et al., 1998; Aydin et al., 2006). Alternatively, clay can coat a quartz grain fragment in a deformation band, thus inhibiting quartz precipitation on that grain (Fisher et al., 2000; Worden and Morad, 2000; Mørk and Moen, 2007) and enhancing the precipitation of quartz in a granular form, i.e., micro-quartz (McBride, 1989; Philit et al., 2015). Furthermore, clay texture can be disturbed by deformation bands, thus producing detrital clay minerals that induce quartz dissolution when they are located at the contact between quartz grain fragments (Fisher et al., 2000; Mørk and Moen, 2007).

## 2.6 Porosity and permeability in deformation bands

Porosity is a measure of the volume of pores within a rock, whereas permeability (tensor) takes into account the interconnected pores and evaluates the capacity of fluids to flow through the identified pore network. Porosity and permeability enable the comparison of petrophysical properties of distinct zones in a rock or sediment affected by localised deformation, i.e., a deformed zone from a non-deformed one.

### 2.6.1 Porosity

Porosity within deformation bands and faults have a lower value than that for the undisturbed material (Shipton et al., 2005; Aydin et al., 2006; Cashman et al.,

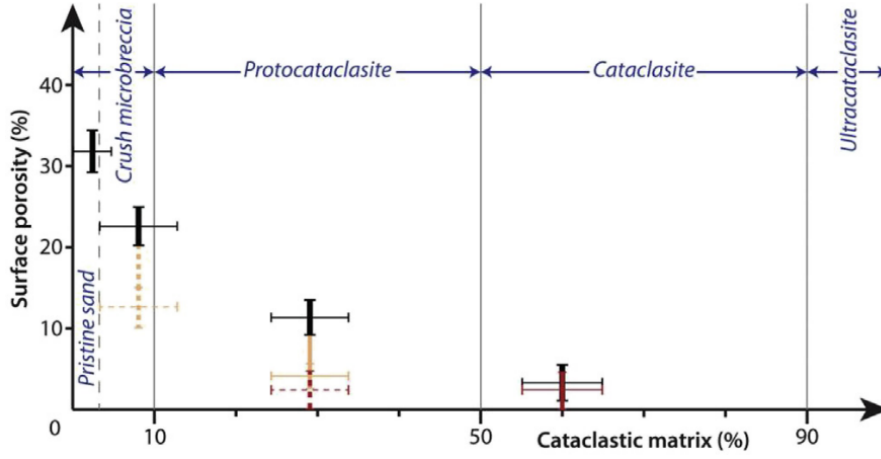


**Figure 2.22:** Surface porosity (i.e., sum of pores, cements, and clays) variation in cemented sands with respect to the degree of cataclasis. Black data represent uncemented deformation bands, while yellow stands for partially cemented and red is for highly cemented structures (Philit et al., 2015).

2007; Wibberley et al., 2007; Torabi and Fossen, 2009; Philit et al., 2015), with the exception for dilation bands that reported porosity increase (Du Bernard et al., 2002; Exner et al., 2013) and for isochoric bands obtained at laboratory scale (Wong et al., 1997; Bésuelle et al., 2000). Porosity varies with the degree of cataclasis in cataclastic bands, as shown in Figure 2.22, with a proportional reduction of the two parameters.

Figure 2.22 shows porosity values assigned to each deformation band type, described by a range of cataclastic matrix content. The porosity values gradually decrease from the undisturbed sand to the cataclastic types. In fact, porosity is more useful than the degree of cataclasis to distinguish deformation band types because porosity can be evaluated in all band types but cataclasis does not characterise all bands, e.g., dilation or disaggregation bands (see Section 2.1).

There are two principal ways to measure porosity: i) directly, by using gas (Helium, (Rath et al., 2011; Griffiths et al., 2016)) or liquid porosimetry (Mercury (Ballas et al., 2014; Skurtveit et al., 2014; Zuluaga et al., 2017)), and ii) indirectly, through digital images, either from Microscopy (Ballas et al., 2013; Griffiths et al., 2016; Zuluaga et al., 2017) or from X-ray Computed Tomography (Rath et al., 2011; Lima et al., 2015). Porosimetry is applicable to materials that can be cored into cylinders, otherwise error margin in the measure should be applied (Griffiths et al., 2016). Image Analysis with Microscopy acquisition is performed on 2D thin sections, while 3D images of a natural material can be acquired with X-Ray Computed Tomography (the two techniques are further discussed in Chapter 4). Usually, values obtained with helium porosimetry are higher than the ones obtained from digital images, because the detection of microporosity (i.e., pores with radius of few  $\mu\text{m}$ ) is

often limited by image resolution in the latter technique (Griffiths et al., 2016). If cementation is recognised to postdate a certain deformation, the porosity of that deformed material is calculated by subtracting the volume of cement from the current rock volume (which comprises the cement). This value is called *minus cement* or *pre-cement* porosity (McBride, 1989; Worden and Morad, 2000; Aydin et al., 2006).

Typical values of porosity cannot be identified, since porosity depends on several factors, e.g., undisturbed rock porosity, grain size, amount of deformation, degree of cementation, and burial depth, as discussed above. In the Southern France, two examples (Schultz and Soliva, 2012; Ballas et al., 2013) in poorly cemented sandstone showed that porosity variability can be influenced not only by the deformation band type but also by the grain size and by the initial porosity. Schultz and Soliva (2012) documented shear-enhanced compaction bands in a coarse-grained material with a porosity reduction of 5% (from 28% to 23%), while compactional shear bands in fine-grained weakly cemented sand had a porosity decrease of 8% (from 29% to 21%). Ballas et al. (2013) documented shear-enhanced compaction bands with a greater porosity reduction for more porous and fine-grained cemented sands (from 35% to 27%) than for less porous and coarse-grained ones (e.g., in Tresques quarry from 24% to 21%). Differently, compactional shear bands in Griffiths et al. (2016) determined a porosity reduction of 16% (from 26% to 10%) in coarse-grained sandstone while a reduction of only 6% (from 10% to 4%) in a fine-grained sandstone. The last two observations underline that localised deformation occurred preferentially in the material with a higher initial porosity, which was measured in the first case in the fine-grained cemented sand (35%) and in the second case in the coarse-grained sandstone (26%).

## 2.6.2 Permeability

Permeability in porous rocks can be greatly reduced if deformation bands form baffles that compartmentalise the rocks, or it can be increased by creating flow paths where the fluid can escape. In either case, the permeability variation compromises the production of a fluid in a reservoir. Deformation bands arrays, rather than single-strand bands, can affect permeability of reservoir sandstones, especially when interconnected (Rotevatn et al., 2013). The permeability contrast between undisturbed rock and deformation bands seems to control the flow dynamics within reservoirs (Shipton et al., 2005). Grain comminution within cataclastic deformation bands has high impact on permeability and grain fragments can affect the fluid flow by providing more tortuous flow paths (Zuluaga et al., 2017). For this reason, faults could report the highest permeability reduction among the localised deformation modes (Shipton et al., 2005; Torabi et al., 2013; Ballas et al., 2015).

Several techniques and devices are available to perform permeability measurement, e.g., air portable TinyPerm permeameter (Zuluaga et al., 2017), nitrogen permeameter (Ballas et al., 2012), and digital image analysis from Microscopy or X-ray Computed Tomography (Ballas et al., 2015). Permeability is a tensor, thus it can be evaluated in three directions: one across the band plane and the other two parallel to the plane and mutually orthogonal. Similarly to porosity, typical trends of permeability reduction can be found in the literature (Ballas et al., 2012; Zuluaga et al., 2017). For example, Ballas et al. (2012) reported a reduction of three to five orders of magnitude from undisturbed rock (high-porosity rocks with permeability value in the range 1000-3000 mD) to cataclastic deformation bands and clusters, where a bimodal grain size distribution was identified.

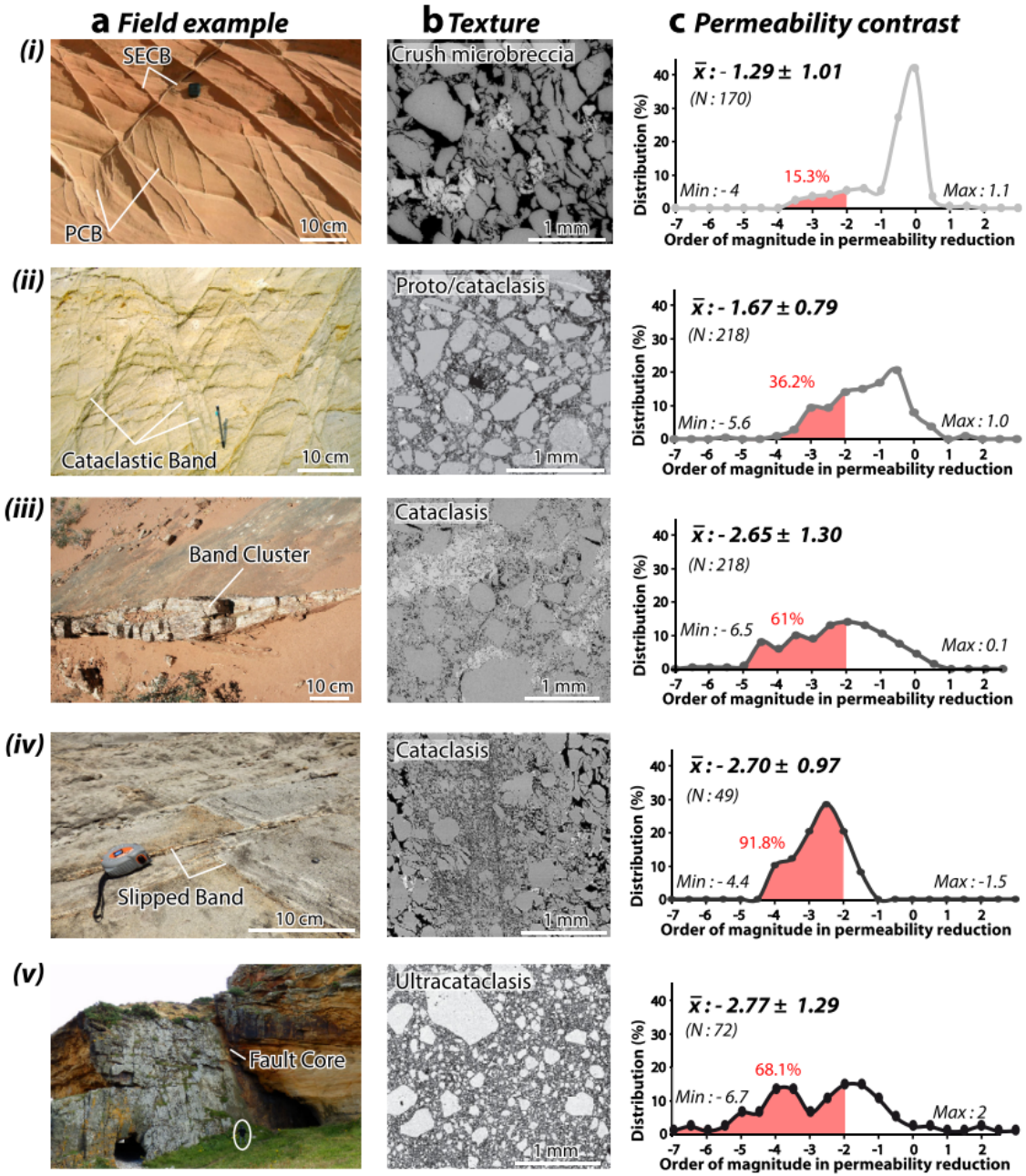
Deformation band types that involve high shear and compaction levels are generally characterised by a great permeability reduction. For example, in Zuluaga et al. (2017), thick shear-enhanced compaction bands reduce permeability of two orders of magnitude, while thinner compactional shear bands report a higher reduction, of about three orders of magnitude.

Figure 2.23 shows the relationship between permeability reduction and degree of cataclasis (i.e., texture) with respect to deformation band types identified in the field. For the different deformation band types there is an example of microscopic view and a plot of the distribution of cataclasis for each order of magnitude in permeability reduction, with the percentage (in red) of deformation bands with a permeability reduction greater than two orders of magnitude.

To the best of the author's knowledge, measurements of permeability increase within field samples of dilation bands have not been reported in the literature. According to field observations, the limited thickness and length of the identified dilation bands probably did not cause any permeability increase (Exner et al., 2013; Alikarami and Torabi, 2015).

The effect of capillary pressure arises with compaction and grain comminution and the analysis performed by Torabi et al. (2013) has demonstrated that capillarity in zones of localised deformation controls the flow properties of reservoirs. All deformation bands can offer local variation of capillary pressure. However, fault core slip zones and deformation bands clusters reported the highest capillary effect. Furthermore, Cavailhes et al. (2009) showed that capillary pressure can be altered depending on saturation level of rocks. For example, unsaturated cataclastic shear bands acted as conduits along the band due to capillary effect, whereas saturated cataclastic bands are fluid flow barriers.

Pressure, temperature, and chemical variations determine the precipitation of minerals along flow paths, i.e., of cements. Cementation (discussed in Section 2.5) can be assessed to identify flow paths within rocks, e.g., red laminations (haematite



**Figure 2.23:** Field examples (i - v) of (a) different deformation band type, (b) their texture and (c) permeability contrast. In (c) the percentage of deformation bands with a permeability reduction greater than two orders of magnitude is indicated in red (Ballas et al., 2015).

or iron hydroxides, Worden and Burley (2003); Sallet and Wibberley (2010); Ballas et al. (2012)) and in general it causes permeability reduction (Alikarami et al., 2013). In addition, it can change the nature of deformation bands from conduits to barrier (Exner et al., 2013; Skurtveit et al., 2015).

## 2.7 Deformation bands in weakly cemented sands

### 2.7.1 Case studies in the literature

Weakly cemented sands in the literature are addressed to with a variety of names, e.g., porous sandstones (Soliva et al., 2013; Ballas et al., 2014; Philit et al., 2015), unlithified sediments (Cashman et al., 2007; Kaproth et al., 2010), poorly lithified sandstones and sediments (Rawling and Goodwin, 2006; Balsamo and Storti; Skurtveit et al., 2014; Torabi et al., 2013), unconsolidated sands (Cashman and Cashman, 2000), and high-porosity sands (Wibberley et al., 2007). In this doctoral work it was chosen to name the tested material as sands, similar to the terminology followed by Wibberley et al. (2007) and Philit et al. (2015), since this material has a very low cohesion.

Grain breakage, grain rotation and/or sliding, and porosity reduction characterise deformation bands in weakly cemented sands (e.g., Cashman and Cashman (2000); Balsamo and Storti; Kaproth et al. (2010); Ballas et al. (2013)), similar to previous observations in deformation bands in sandstones. When clays are distributed in highly porous sediments, deformation bands developed narrower and more localised than in sediments less porous and with less clay content (Sallet and Wibberley, 2010). Balsamo et al. (2013) and Skurtveit et al. (2014) observed greater effects of localised deformation on coarser rather than on finer grained sand, which was explained considering the fewer grain contacts and the higher probability of intra-granular defects in the coarser one. Another frequent observation is the presence of “survivor” grains (described in Sect. 2.4) surrounded by fine-grain matrix (Kaproth et al., 2010; Balsamo et al., 2013; Sallet and Wibberley, 2013; Ballas et al., 2014). The estimated burial for weakly cemented sands that developed deformation bands is shallow, i.e.,  $\leq 1$  km, (Cashman and Cashman, 2000; Rawling and Goodwin, 2006; Balsamo and Storti; Philit et al., 2015) or even  $< 100$  m (Kaproth et al., 2010; Balsamo et al., 2013). These common observations may vary depending on the observed localised deformation mode. For example, porosity increase rather than reduction was observed in dilation bands (Du Bernard et al., 2002; Kaproth et al., 2010).

Silica cementation in weakly cemented sands was documented only where cat-aclasis was more intense, e.g., in deformation band clusters (Philit et al., 2015).

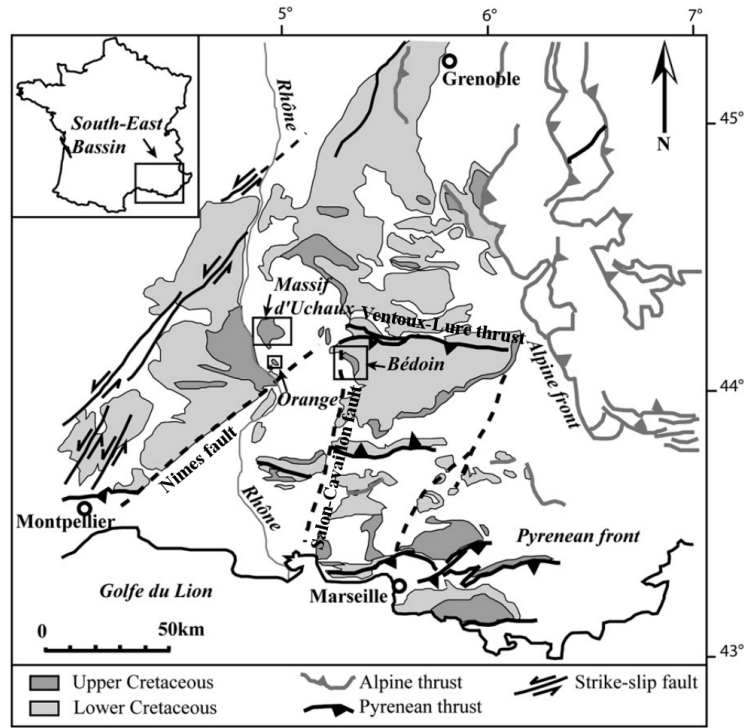


**Figure 2.24:** Field sites in the *Bassin du Sud Est* (adapted from Saillet and Wibberley (2010)).

Other types of cementation, e.g., dolomite (Exner et al., 2013), clay (Saillet and Wibberley, 2010; Ballas et al., 2013), and iron oxides (Kaproth et al., 2010), were observed in bands that behaved as pathways for fluid - usually post-deformation cementation - and where no intense cataclasis was reported.

### 2.7.2 Bédoin and the *Bassin du Sud Est*

The material tested in this work comes from a site located in Provence, southern France. The area is known in the geological literature as *Bassin du Sud Est* and it is described in detail in some key publications (Triat, 1982; Dubois and Delfaud, 1894; Tempier, 1987; Le Pichon et al., 2010; Schreiber et al., 2011). The Bédoin site was chosen for the great exposure of deformation bands in weakly cemented sands, among other sites with similar deformation band exposure in the same area (Fig. 2.24), e.g., Massif d'Uchaux (Cavailhes et al., 2009; Soliva et al., 2013; Skurtveit et al., 2014), Boncavaï (Ballas et al., 2012), and Orange (Saillet and Wibberley, 2010; Chemenda et al., 2012; Soliva et al., 2013).

Despite the fact that the *Bassin du Sud Est* was object of study in several works, there is little documentation (Skurtveit et al., 2013, 2014) about the mechanical properties of the weakly cemented sands from this area, and this limitation is attributed to the fragility of the weakly cemented granular material, which requires extra care when extracted from the outcrop, handled and carried to the laboratory.

Mechanical tests on frozen-cored samples and remoulded sands from Uchaux and Boncavaï showed compaction, porosity reduction, and strain hardening (Skurtveit et al., 2013). In addition, low-porosity material under high stress showed grain fracturing, while high-porosity material under low stress underwent grain rearrangement. Skurtveit et al. (2014) compared the mechanical behaviour of fine-grained (230  $\mu\text{m}$ ) and well sorted sand with that of coarse-grained (650  $\mu\text{m}$ ) and less well sorted sands from Uchaux. The triaxial tests at 5 MPa confining pressure showed a higher stiffness of the fine-grained sand, which was interpreted considering that higher stress concentration developed between coarser grains. The coarse-grained sand also reported a faster compaction through greater grain crushing than the fine-grained sand. These observations explained why the coarse-grained sand was the preferential location for deformation bands (shear-enhanced compaction bands) in the outcrop.

The majority of the works related to the *Bassin du Sud Est* tried to connect the deformation band characteristics (e.g., type, distribution, inclination) with the regional tectonic setting (i.e., extensional and contractional regimes). For example, Soliva et al. (2013) built a model that represented their observations in Uchaux and Orange: extensional regime favoured shear bands with small conjugate angle, whereas contractional regime favoured compactional shear bands with higher conjugate angle. Ballas et al. (2014) showed, by studying petrophysical properties of the deformation bands, that shear bands are more affected by permeability reduction than compactional shear bands. In addition, they argued that grain size, but not grain sorting or porosity, exerted influence on the band network geometry.

Other works reported quantitative evaluations of porosity and permeability (Ballas et al., 2012; Sallet and Wibberley, 2013). For example, Ballas et al. (2012) observed permeability of deformation bands in the Massif d’Uchaux and at Boncavaï quarry. The work shows that single- and multi-strand bands did not affect the petrophysical properties of the sediments; however, cataclastic multi-strand bands and cluster could have reduced the permeability of the sediment of three to five orders of magnitude. Therefore, cataclasis was identified as the principal responsible for permeability reduction.

The specific field case of Bédoin was analysed in few works (Wibberley et al., 2007; Sallet and Wibberley, 2010, 2013; Philit et al., 2015, 2018). The Bédoin site is located at the edge of the Alpine orogen, in the South of the mount Ventoux near the junction of three faults: Nîmes fault, the Ventoux-Lure thrust, and the Salon-Cavaillon fault (Fig. 2.24). The sands deposited during the Cenomanian (early Upper Cretaceous) and were interpreted to have reached a burial depth no greater than 800 m (Dubois and Delfaud, 1894) because they did not report evidences of diagenesis, i.e., they are mainly unlithified (Wibberley et al., 2007). The sands are



infilled with clays mixed with haematite, which are documented to derive from the layer that overlays the sands (Philit et al., 2015).

Wibberley et al. (2007) reported a description of the cataclastic deformation bands of Bédoin where finer grains, produced with grain breakage, filled the pore space in the deformation bands, thus making them baffles to fluid flow. Friction between grains and fragments was interpreted as cause for the growth of deformation band thickness. In addition, a linear relationship between deformation band thickness and displacement was observed. The presence of red stains on the sand deposit represents the effect of groundwater in the deposit. Finally, the critical state Soil Mechanics theory was adopted to explain patterns of network evolution in different stages of the strain localisation, following previous examples (Jones and Addis, 1986; Antonellini et al., 1994; Cruz et al., 2011).

Saillet and Wibberley (2010, 2013) observed grain crushing and compaction in the regions of localised deformation, finding out - similarly to Wibberley et al. (2007) - that deformation band thickness was linearly proportional to displacement, i.e., single-strand band with thickness of few mm with displacement  $< 10$  mm, and multi-strand bands 10 - 100 mm thick with 10 - 30 mm of displacement (Saillet and Wibberley, 2010). In addition, they discussed in detail the role played by the grain size into the band thickness by comparing sites with different grains size (Fig. 2.25) and reporting a greater thickness with coarser material and also a band thickness reduction with the presence of clays. Field exploration of Bédoin was performed through scanlines, which is detailed in Saillet and Wibberley (2010). In Saillet and Wibberley (2013), two permeability reduction trends in deformation bands were identified depending on the degree of fragmentation: i) a moderate permeability reduction (0.5 to 2 orders of magnitude) with respect to the undisturbed sand in fragment-supported deformation bands, and ii) a higher permeability reduction (up to 4 orders of magnitude) in matrix-supported deformation bands. Further details of permeability and porosity measurements are reported in Table 7.1 (Chapter 7).

Philit et al. (2015) reported an interpretation of the groundwater environment in the Bédoin porous sediment by observing the properties at microscale of quartz cementation. The cementation process is unusual - nevertheless achievable - for a shallow sediment, according to the estimated low burial (500 - 1300 m) for the Bédoin deposit. In addition, types of cataclastic structures were defined into a classification (described in Section 2.3), from the meticulous analysis performed at the microscopy, as well as other classifications of breakage and of cementation degrees within deformation bands were defined.

Philit et al. (2018) reported results of six studies (St. Michael and Boncavaï (Provence, France), Blankenburg (Germany), Cummington (Scotland), Goblin Valley and Buckskin Gulch (Utah, United States of America)) in parallel with the

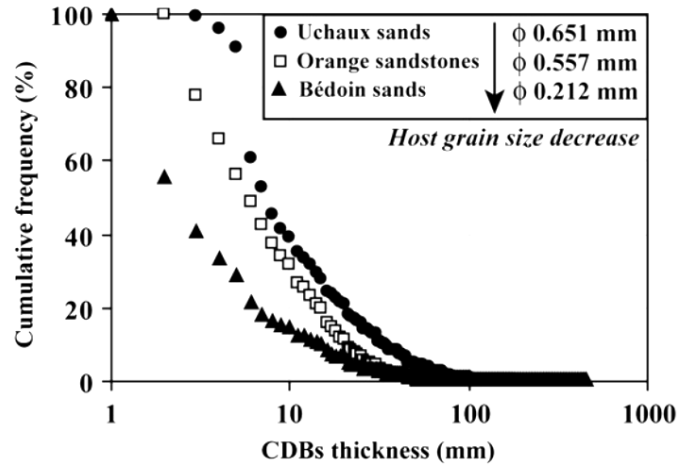


**Figure 2.25:** Relationship between grain size (host grain is the undisturbed sand) and deformation band thickness, in comparison between three sites of the *Bassin du Sud Est*: Bédoin, Orange, and Massive d’Uchaux (Saillet and Wibberley, 2010).

Bédoin outcrop. For Bédoin, as well as for all the other sites, porosity showed a negative correlation with the degree of cataclasis while poor sorting showed a positive one (and vice versa), as expected. Grain roundness decreased up to 8% of degree of cataclasis, then it showed a small increase up to 40% of cataclasis. In addition, grain breakage within the bands was reported to increase compaction and cohesion, enhanced by quartz cementation in cataclastic bands and interbands even at shallow depth ( $< 1$  km). This supported the hypothesis of strain hardening within deformation bands, which could have acted as flow baffles.

# Chapter 3

## Materials

This Chapter describes the material used in this work. Natural material was collected from the Bédoin outcrops, in the form of blocks of undisturbed sand and of deformation band samples, in small samples of deformation bands, and in uncemented sands. Sand and clay, cementing the grains in the outcrop, are characterised. The procedure to create artificially cemented material, composed by sand grains collected in Bédoin and clay acting as cement, is also described.

### 3.1 Samples from Bédoin

The material used in this work was collected from abandoned quarries of siliciclastic sands, deposited in a deltaic environment (Ford and Stahel, 1995; Sallet and Wibberley, 2010), which expose numerous deformation bands. Two outcrops were selected and they are identified as Bédoin 3 and Bédoin 4.5, since they are located near Bédoin (Provence, France). The location of Bédoin 3 is already known in the literature whereas Bédoin 4.5 was not previously analysed, therefore its location was added to an available map from Wibberley et al. (2007) of the explored Bédoin sand quarries (Fig. 3.1).

In both sites the sand is white, mixed with feldspar and iron-rich grains, and cemented with clay, with the outcrop surfaces covered by haematite oxides that infiltrated the deformation bands in Bédoin 3, thus making the bands easier to detect (Fig. 3.2 and 3.3). Clay cement enabled the exposure of sub-vertical outcrops, although the material is weakly cemented (i.e., it is crumble at touch). The haematite comes from a shallower stratigraphic unit above the white sand and it colours locally the grains with orange and red tones. A detailed stratigraphic succession of the Bédoin 3 deposit is available in Philit et al. (2015).

Bédoin 3 (Fig. 3.2) provided samples containing deformation bands and material that is undisturbed (i.e., far from localised deformation). Big blocks (some of them crossed by deformation bands, some others undisturbed) of cemented material

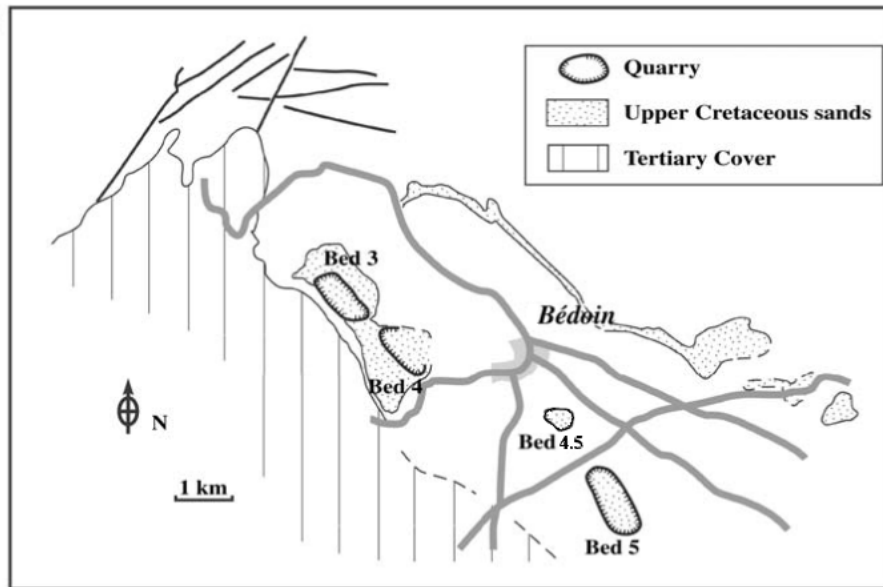


**Figure 3.1:** Sand quarries explored near Bédoin (adapted from Wibberley et al. (2007)).

were collected with an original field sampler, which is described in Appendix A. These blocks were used in the laboratory to extract samples for qualitative characterisation of the material by applying X-ray Computed Tomography and Scanning Electron Microscopy and for mechanic tests. Other small samples were extracted from deformation bands in the field to prepare polished thin sections and get a better understanding of the microstructure of natural deformation bands. Moreover, undisturbed sand was collected by disaggregating the cemented sand from an undisturbed outcrop (Section 3.1.2).

Small samples containing deformation bands were collected from Bédoin 4.5 (Fig. 3.3). Neither big blocks nor undisturbed sand grains were collected from this site. The detailed microstructural observations of the selected samples from the two sites are reported in Chapter 5.

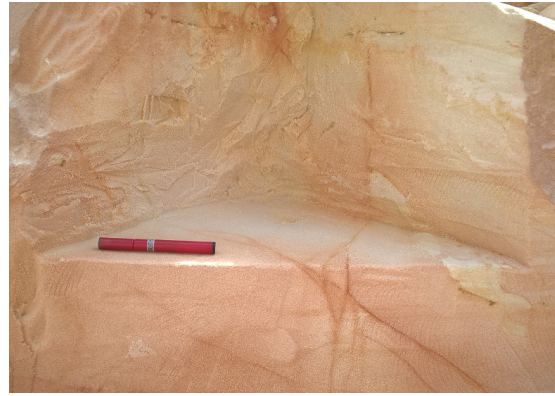
### 3.1.1 Collection of naturally cemented samples

A novel sampling technique was developed to collect samples of weakly cemented sands because ordinary sample coring was not applicable in Bédoin due to the material fragility. Even by applying a simple pressure on the material, the samples were losing their integrity.

The sampler design stems from observations on the outcrop geometry and on the material characteristics. Vertical outcrops of weakly cemented sand were chosen for the sample collection because they simplified the geometry of the sampler, which was designed to extract prismatic blocks with triangular base. The triangular shape enables to cut the outcrop by reaching its internal part with a single cut performed directly from the outside of the outcrop. The sampler is composed



(a)



(b)

**Figure 3.2:** Examples of deformation bands and haematite stains on the outcrops and along the bands in Bédoin 3: the deformation bands are extended for meters in the outcrop (red tool for scale, 1 = 15 cm).



(a)



(b)

**Figure 3.3:** Field view of Bédoin 4.5: thin and almost imperceptible deformation bands are extended for meters in the outcrop. Note in (a) the haematite layer above the white sand unit (red tool for scale, 1 = 15 cm).

of the pieces shown in Figure 3.4a, which are assembled in situ with the help of clamps and screws (Fig. 3.4b; the detailed assembling procedure is described in Appendix A). Once extracted (Fig. 3.4c), the block was carried to the laboratory, where more accurate procedures for small sample extraction were performed, as suggested by Sallet and Wibberley (2013). For the experimental work of this doctoral thesis, small cylindrical samples with dimensions of about  $d = 11$  mm and  $h = 22$  mm were required. The cylindrical shape was obtained by carefully hand-carving (procedure adopted for example by Collins and Sitar (2009)) small prismatic blocks extracted from one of the triangular blocks collected with the sampler. The obtained hand-carved samples look like the one shown in Figure 6.1a. The samples contained naturally occurring imperfections derived from diagenetic structures or later deformation processes, such as local pore size and cement content variations or pre-existing deformation bands. These imperfections were identified through non-destructive X-ray Computed Tomography and are described in Chapter 6.

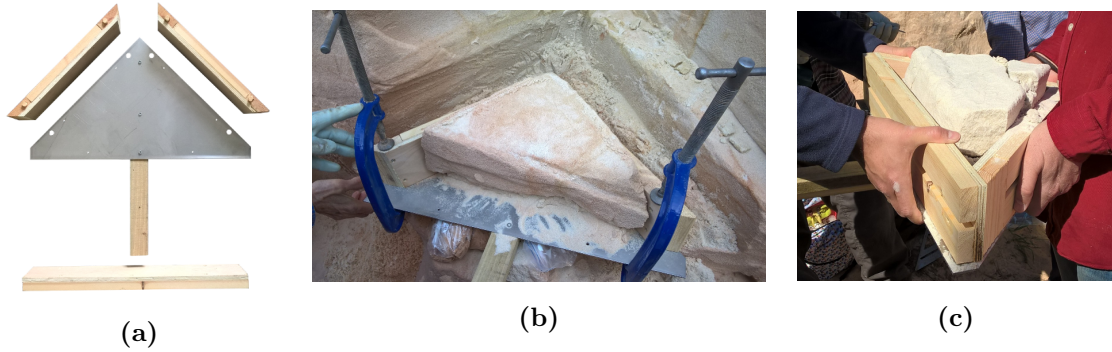


**Figure 3.4:** Field sampler designed to collect blocks of weakly cemented sand: (a) pieces that compose the sampler (length of longer wooden plate is  $l = 40$  cm), (b) sampler during the composition in the field, and (c) assembled sampler.

### 3.1.2 Sand characterisation

The material from the two sites was classified as sand, not as low-consolidated sandstone, since the material has nearly zero cohesion. The sand is weakly cemented by clays and presents minor inclusions, in particular iron-rich grains (Sect. 3.1) and feldspars.

Sand grains collected in Bédoin 3 from an undisturbed outcrop and from a multi-strand deformation band were observed at the microscopy and classified with sieve tests. The microscopic observation showed that the undisturbed grains are sub-rounded to rounded (Fig. 3.5a). The quartz mineralogy (Silica (Si) in Fig. 3.5b) controls the grain shape, which resembles prismatic and oblate. Due to the presence of clay cement (described in Section 3.1.3), it was necessary to clean the sand by washing it with a surfactant inhibitor (i.e., Sodium Hexametaphosphate) in ultra-



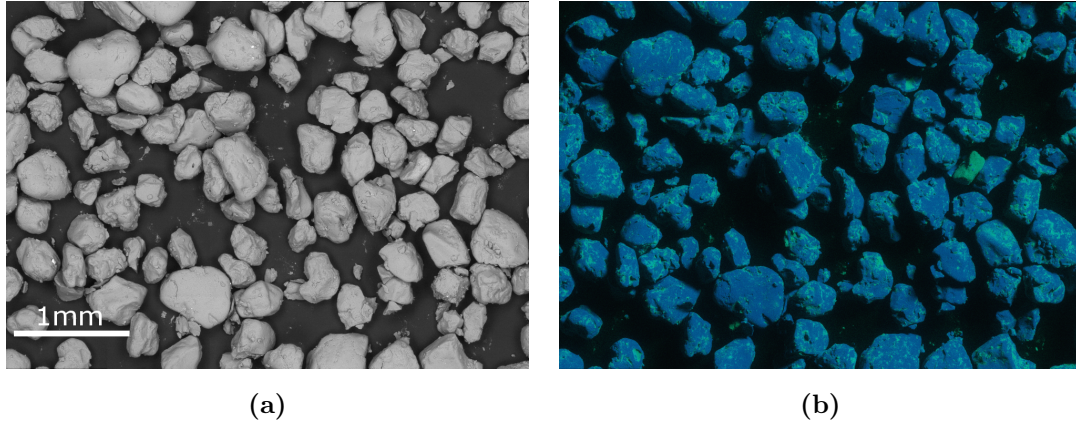


**Figure 3.5:** Bédoin sand grains seen at the microscope: (a) view with Scanning Electron Microscopy and (b) element map from Energy-Dispersive X-ray Spectrometry, where blue is Silica (Si) and green is Aluminium (Al).

sonic bath prior to sieving. The granulometric analysis (Fig. 3.6) showed that the sand is well sorted and uniform (Table 3.1), and that the average grains size ( $d_{50}$ ) is  $312 \mu\text{m}$ .

The sand grains in the deformation bands were subject to grain breakage, therefore the granulometric curve of these grains did not show any more a good sorting (Fig. 3.6). This is also confirmed by the increase of uniformity coefficient ( $C_u = d_{60}/d_{10}$ ) from 1.54 to 2.72 (Table 3.1), although the  $d_{50}$  reported a just small reduction to  $305 \mu\text{m}$ . The value  $d_{10}$  was selected as alternative grain descriptor to  $d_{50}$  for both grain types - within deformation band and undisturbed sand. By comparing the size of sands coming from the undisturbed region and from the deformation band, it was shown that the  $d_{10}$  was nearly halved (from 211 to 117, see Table 3.1).

Sand from Bédoin 4.5 was not characterised, but from intact sand grains found in the deformation bands it was deduced a higher grain size (about  $350 \mu\text{m}$ ) than the  $d_{50}$  measured in Bédoin 3.

**Table 3.1:** Sand descriptors for Bédoin 3 (values extracted from the curves in Fig. 3.6).

sample type	$d_{50} [\mu\text{m}]$	$d_{60} [\mu\text{m}]$	$d_{10} [\mu\text{m}]$	$C_u$
undisturbed	312	325	211	1.54
deformation band core	305	318	117	2.72

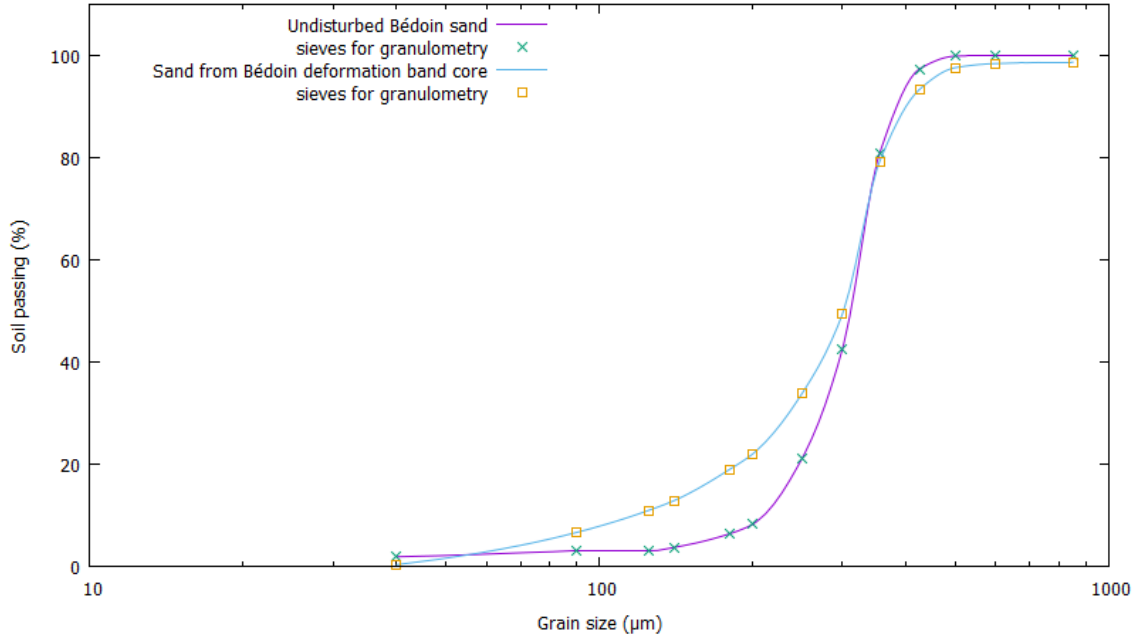


**Figure 3.6:** Granulometric curves of two sand types from Bédoin 3: undisturbed sand grains and sand from a multi-strand deformation band core. Principal sand descriptors extracted from the curves are reported in Table 3.1.

### 3.1.3 Clay cement

Clay is the bonding material between the sand grains in the Bédoin outcrops. In particular, clays infiltrated with water in the sand deposit forming menisci bonds between the grains, as consequence of water retention. This held the sands up and enabled the formation of vertical walls of cemented sand in the sites.

The clay content was measured from 2D Scanning Electron Microscopy image of undisturbed cemented sand samples (Fig. 3.7). The images were trinarised in order to separate the three phases (grains, cement, pores) and the result is a value of clay content in the range 4 - 11%. Although this value was calculated within a small surface (1465 x 974  $\mu\text{m}$  for Fig. 3.7c), it is made the assumption that the surface is representative for the tested material. From the observed dimension and shape of the clay particles, kaolin clay was identified as the predominant clay type (Fig. 3.8).

## 3.2 Artificial cementation

### 3.2.1 Artificial cementation in the literature

Artificial cementation in the literature was studied to understand the mechanical effect of cement degree (David et al., 1998; Rotta et al., 2003) and distribution (Tutuncu et al., 1997; Rotta et al., 2003; Cheng et al., 2013) in granular materials.



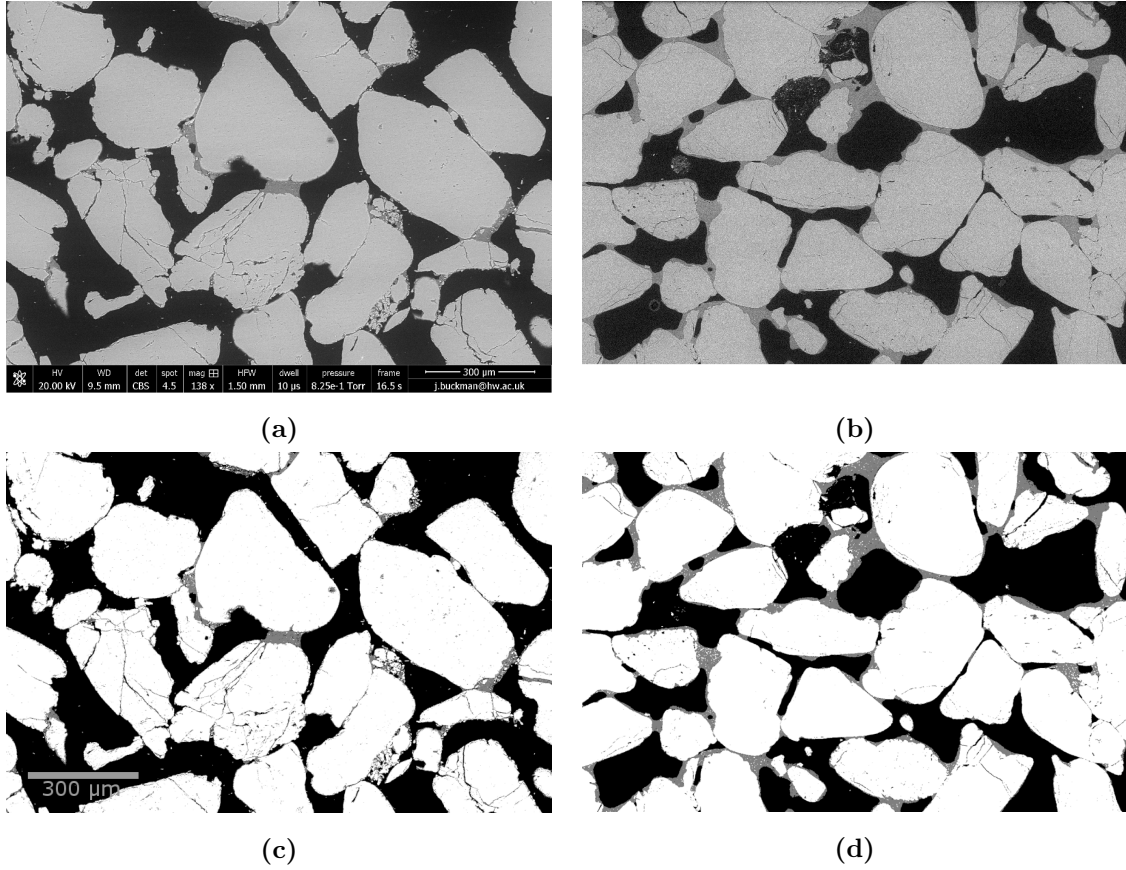


**Figure 3.7:** Greyscale (a and b) and correspondent trinarised images (c and d) of undisturbed cemented sands from Bédoin 3: clay (grey) binds together grains and fragments (white) (black is pore). Percentage of clay in (c) is 4% and in (d) is 10.9%.

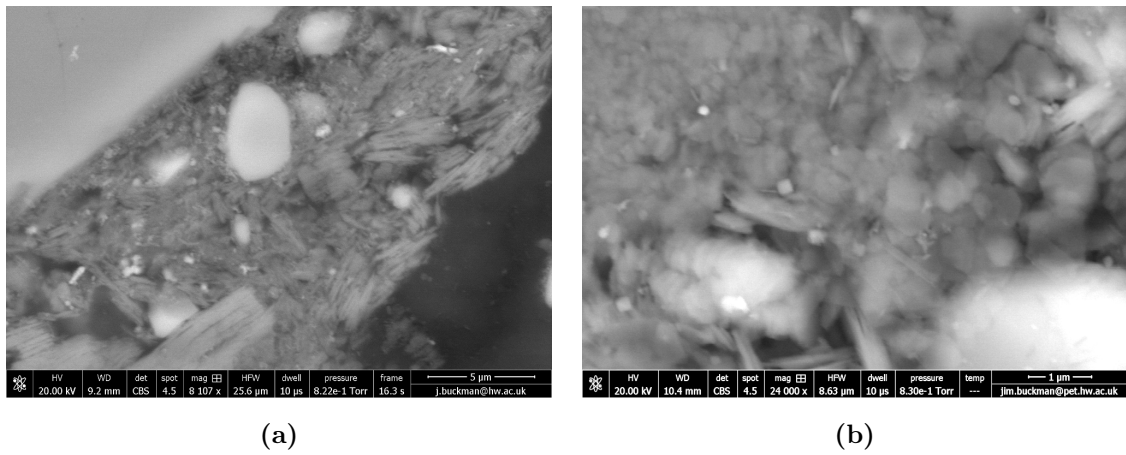


**Figure 3.8:** Clay cement in Bédoin. Note in (b) the hexagonal shapes of the platelets, typical of the kaolin clay.

These works reported beneficial effects in terms of mechanical resistance when cement is added to a granular material. In particular, absent or low cement content favours material heterogeneity (den Brok et al., 1997; David et al., 1998) and imperfections can create stress concentration which leads to strain localisation (Desrues et al., 1996; Desrues and Viggiani, 2004), whereas higher cement content favours the distribution of forces in force chain networks, thus avoiding stress concentration (Wang and Leung, 2008).

The reinforcing effect of cement depends on the type of cement that is employed. For this reason, different cement types are often compared (Ismail et al., 2002; Dejong et al., 2006; Wang and Leung, 2008). For example, in Wang and Leung (2008) the effect of Portland cement was compared to gypsum and the result was that the former transformed the mechanical behaviour from hardening to softening, whereas the same effect was not seen with the gypsum. Ismail et al. (2002) also compared gypsum and Portland plus calcite cement through triaxial tests, finding out that Portland cemented samples had ductile behaviour, while gypsum and calcite cemented ones exhibited brittle behaviour. Dejong et al. (2006) compared gypsum with bio-calcite cement and showed that the two cements exhibit similar resistance, despite a different cement texture.

The cement distribution is affected by the way the granular material is assembled in the mould and the most used procedure is the moist compaction, which consist of compacting the sand grains - previously mixed with cement - in layers into a mould (Cruz et al., 2011; Wang and Leung, 2008). The tamping technique was demonstrated to create heterogeneous porosity in a sample containing only water and polypropylene fibres (Soriano et al., 2017b). Vibration technique is an alternative procedure and it consists of vibrating the granular material when this is placed in the mould; this technique produced less heterogeneity than the tamping technique (Soriano et al., 2017b). Other techniques could be selected to place dry grains in the mould before pouring the cement, for example air pluviation or grain pluviation. Air pluviation, described by (Cavarretta, 2010), is performed through a series of deposition steps, each of them consisting of filling with dry grains a funnel in contact with the top surface of the grains in the mould for sample preparation; the funnel is then raised until emptied, then the step is repeated until the mould is filled. Grain pluviation, performed for example by Desrues et al. (1996), consists of pouring dry sand from a large funnel at constant height drop.

### **3.2.2 A new cementation procedure**

An original cementation procedure was developed to replicate in the laboratory the weakly cemented Bédoin material, which is characterised by high-porosity and is

cemented with clay. The scope of the artificial cementation was to perform mechanical tests on natural and artificially cemented samples, which would enable the identification of potential differences in terms of the occurrence of localised deformation. The natural material was characterised by local imperfections, but these were not replicated in the artificially cemented samples in order to distinguish the two material types. The artificial material was created rather clean (i.e., with no presence of similar imperfections), made by the same grains and cemented with kaolin clay. The resemblance is even closer because clay menisci were reproduced (Fig. 7.1), as observed in the natural material (Fig. 3.7). The menisci bonds were created by using a mould that prevents the sample saturation during cementation, considering that under partial saturation cement precipitates preferentially at grain contact whereas in full saturation cement would precipitate anywhere around the sand grains (Molenaar and Venmans, 1993; Cheng et al., 2013). Porosity similarity of natural and artificially cemented samples is assessed through image processing, and this is described in Chapter 7.

The cementation procedure consists of three steps, that are described in detail below: sand preparation, cement preparation, and cement injection.

### 3.2.3 Sand preparation

The sand collected from the field was washed by using a solution at 10% of Sodium Hexametaphosphate, i.e., a surfactant inhibitor, in an ultrasonic bath in order to remove the clay cement stitched to the quartz grains surface. After keeping the sand for 24 hours in the solution to enhance its action, the sand was separated from the solution through a sieve with aperture of  $125\ \mu\text{m}$ , then washed with distilled water and let dry at room temperature.

The clean sand is poured into a mould designed to create cylindrical samples with  $d = 11\ \text{mm}$  and  $h = 22\ \text{mm}$  (Fig. 3.9a). The mould is made of two aluminium cases with semi-cylindrical cavity and by two steel circular meshes placed at upper and lower ends, with mesh aperture of  $50\ \mu\text{m}$ . The upper mesh is at the top surface of the mould whereas the lower mesh is connected to the lower surface of the mould through a channel that functions as drainage, to enhance the drying of the sample and to assure that the sample is not saturated with the cement. This favours the cement distribution in menisci bonds between grains, created by effect of capillarity, thus mimicking the cement distribution in the samples from Bédoin.

The sand is poured from a distance of about  $100\ \text{mm}$  by using a funnel connected to the mould through a pipe  $94\ \text{mm}$  long (Fig. 3.9b). Note that the top mesh is removed when the sand is poured in the mould. The funnel is gradually raised during the sand pouring, in order to keep the same distance between the pouring

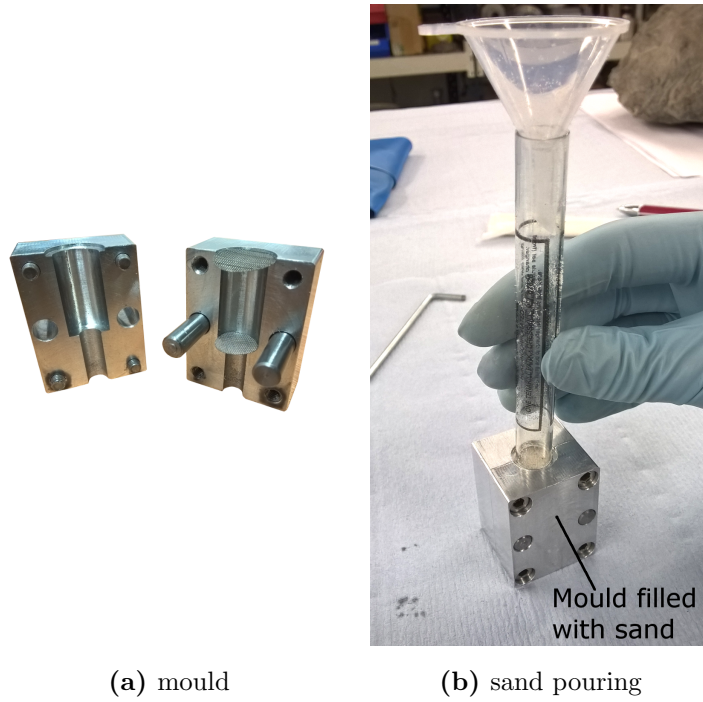


**Figure 3.9:** Aluminium mould: (a) view of the internal structure with cylindrical cavity ( $d = 11$  mm,  $h = 22$  mm) and (b) setup to pour sand into the mould from the top aperture through a funnel and a pipe ( $l = 94$  mm). Note that the top mesh is not in place when the sand is poured.

height and the sand level in the mould, so as to guarantee a homogeneous grain packing from lower to top sample. Once the mould is filled with sand, the top mesh can be put back in place.

### 3.2.4 Cement preparation

Kaolin clay was chosen to cement the sand grains, after having observed kaolin particles at the microscopy in natural samples from Bédoin (Fig. 3.8). Considering that the cement volume percentage in the analysed Bédoin samples is between 4 - 11% and knowing (by experience) the fragility of samples cemented below 10%, the cement quantity chosen for the artificial samples is of 15% with respect to the dry sand mass. Although 15% is the declared quantity, the effective cement content in the artificial sample is lower and closer to the value for the natural samples, because cement loss occurs during the preparation, i.e., residual cement in the syringe and glass beaker used for the cement preparation and cement drainage from the lower surface of the mould. Samples cemented with 20% were also prepared in order to study the influence of cement content.

The cement is prepared by mixing 1 ml of distilled water with kaolin clay in a quantity (15 or 20%) measured with respect to the sand grain mass. The water quantity was assessed by measuring the water that saturated the sand grains poured

in the mould used for the cementation, which was of about 0.9 ml. Clay and water are mixed in a glass beaker with a spatula until a homogeneous clay suspension is created by breaking apart the clay granules.

### 3.2.5 Cement injection

The prepared clay suspension is collected with a syringe and injected from the top mesh of the mould that was previously filled with dry sand grains. The suspension is injected in drops, each drop at an interval of 30 seconds so as to give time to the suspension to flow in the sample from upper to lower ends. During the injection, drainage of the suspension can occur at the lower surface of the mould, where the sample is confined by a mesh and a drainage channel. This ensures that the cement is retained in the sample only by capillarity and not by the mould (in case the mould had an impervious base). Once the cement is injected, the sample is let to dry at room temperature for 48 hours. Finally, the sample is carefully extracted from the mould (Fig. 3.10).

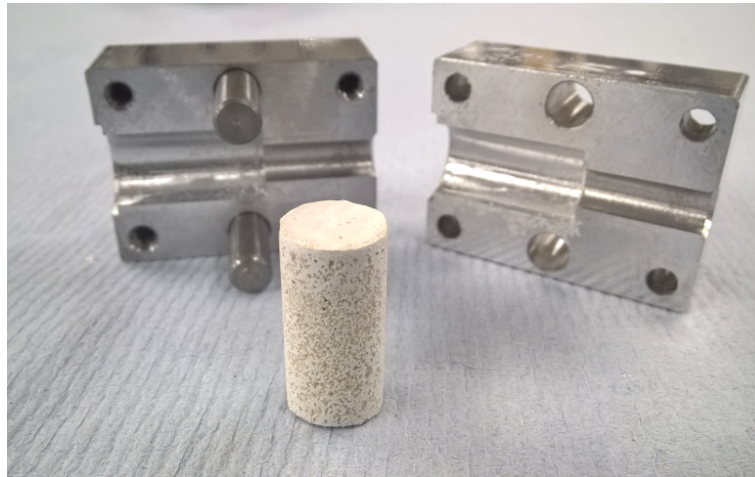


**Figure 3.10:** Cylindrical sample obtained from the artificial cementation procedure.

# Chapter 4

## Experimental methods

This Chapter presents primarily the experimental methods that were applied during this doctoral work to characterise the natural and artificially cemented sands. Moreover, a description of the mechanical tests is also provided. In particular, the Chapter presents: a) the compression experiments (lab-scale) that were carried out with in situ (i.e., syn-deformation) X-ray image acquisition; b) the Scanning Electron Microscopy (applied on 2D thin sections) and the X-ray Computed Tomography (3D), which are the two experimental methods used to extract information on the structure and on the mechanical processes of the tested material; c) the digital image processing in order to calculate the strain maps and to estimate porosity and permeability.

### 4.1 Mechanical testing

#### 4.1.1 Triaxial compression tests

In the experimental part of this work, triaxial compression test was chosen among the geotechnical tests in order to investigate failure and its related micro-processes, to potentially reproduce at the laboratory-scale deformation bands that are characterised by grain fragmentation and porosity alteration, and to compare the features and mechanisms with those observed in the deformation bands from the Bédoin outcrops.

Axi-symmetric compression tests were performed on cylindrical samples. In these tests, an isotropic compression is initially applied to the sample by increasing confining pressure to a selected value. Afterwards, during the deviatoric compression, the axial force (which coincides with the major principal stress  $\sigma_1$ ) is applied to the sample, while the intermediate principal stress  $\sigma_2$  is equal to the minor one  $\sigma_3$  and they are both equal to the radial stress  $\sigma_r$ . The isotropic compression runs in a constant confining pressure rate, while the deviatoric compression runs in a constant

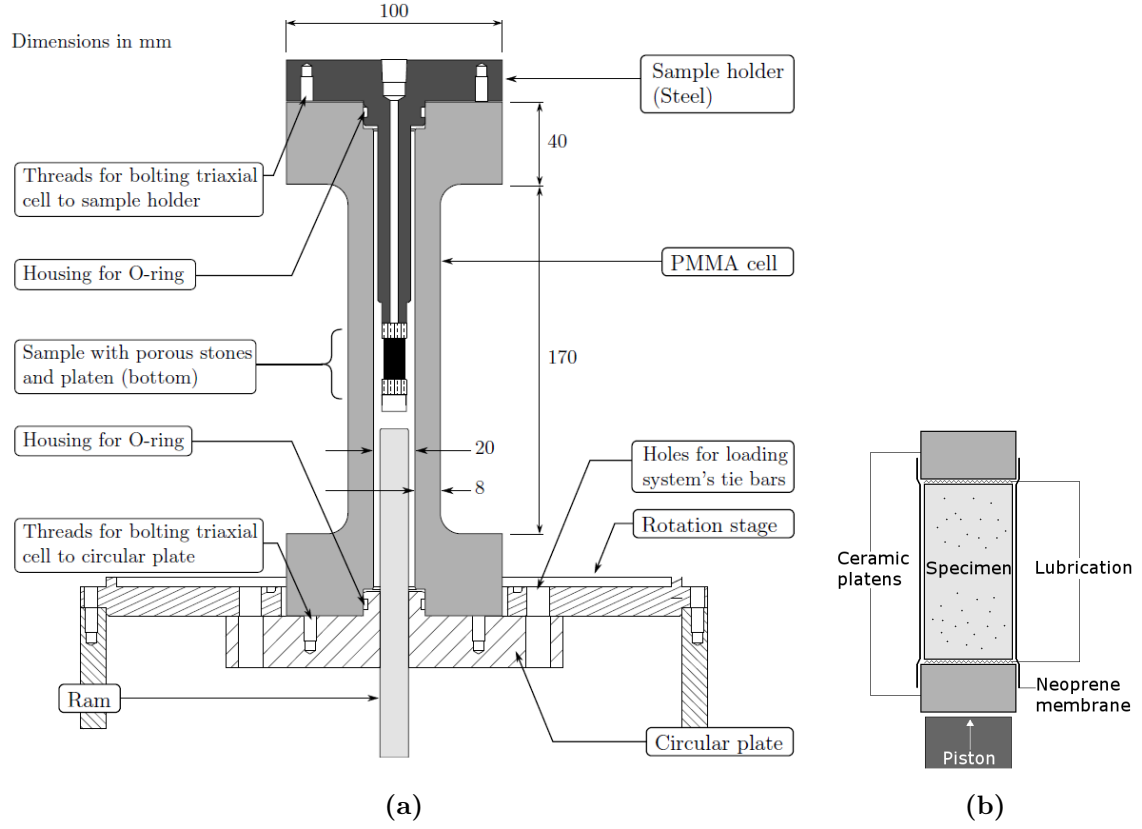


**Figure 4.1:** (a) Vertical section of the triaxial cell created by Prof. Bésuelle and Dr. Lenoir (adapted from Andò (2013)); (b) detail of the sample setup in the cell (sample size:  $h = 22$  mm,  $d = 11$  mm). A flat-edged piston applies compression to the lower platen, and lubrication is applied between sample and platens to reduce contact friction.

displacement rate. This means that the axial force is applied to the sample as the piston is displaced at a constant rate.

During the isotropic compression, a confining pressure of 1 MPa was applied to the samples. The value of 1 MPa was chosen by considering the estimated shallow burial depth (500 - 1300 m) of the Bédoin sand deposits and also considering the actual fragility of the material. The confining pressure was produced by a Gilson pump by flowing oil into the cell at a flow rate of 0.01 - 0.05 mL/min. The tests are performed at room temperature. During the test, the sample was wrapped in a Neoprene membrane (Neoprene is selected because of its high resistance to breakage when in contact with rough surfaces under relatively high pressures). The confining cell shown in Figure 4.1a (well described in Lenoir et al. (2007), Hall et al. (2010), and Andò (2013)) is made of Polymethyl methacrylate (PMMA), which makes it almost transparent to X-rays but also allows visual monitoring of the test. The 8-mm thick wall allows the cell to sustain 7 MPa confining pressure and tensile reaction force.

During the deviatoric loading, the piston is moved upwards against a non-rotating platen in contact with the lower end of the sample (Fig. 4.1) at a con-

stant velocity of  $20 \mu\text{m}/\text{min}$ , which corresponds to a strain rate of  $10^{-5}\text{s}^{-1}$  for a 22 mm high sample. The platens at the two ends of the sample (Fig. 4.1b) are made of ceramic, thus they are rigid, smooth, and impervious. The contact between sample and platens is further smoothed by adding a lubricant (i.e., Phenyl Methyl Silicone oil) in order to minimise friction at their contact. This condition guarantees that axial stress is a principal stress. The axial shortening of the sample is measured through a Linear Variable Differential Transformer (LVDT) by measuring the movement of the piston.

Global volumetric changes can be measured by using X-ray Computed Tomography images and by applying Digital Volume Correlation, either in wet or dry conditions. In this doctoral work, the samples were kept dry during the tests.

The sample size for the presented experimental work was reduced from the conventional size of  $d = 38 \text{ mm}$  and  $h = 76 \text{ mm}$  to  $d = 11 \text{ mm}$  and  $h = 22 \text{ mm}$ . The reduction of size was necessary to improve image resolution of the acquired X-ray tomographies during the test. Even though the size reduction was great, the sample was sufficiently large (about 45000 grains) so as to represent with its mechanical behaviour that of a larger volume of the same granular rock (Hall et al., 2009).

Samples tested in this work with triaxial compression tests are:

- naturally cemented samples;
- artificially cemented samples;
- uncemented sand (cleaned from natural cements).

Naturally cemented samples contained imperfections deriving from diagenetic or from later deformation processes, e.g., region of enhanced porosity and pre-existing dilation band. The tested samples were hand-carved from blocks of material collected from Bédoin. Triaxial compression experiments were performed on these samples in order to study the effect of imperfections on the occurrence of localised deformation. Artificially cemented samples were also tested with the aim of understanding the effects of cement in the localised deformation and the uncemented sand sample helped understand what would occur in the absence of cement. The comparison of the mechanical data from uncemented, naturally, and artificially cemented samples can shed light into the role of imperfections and of cement (natural vs artificial) on the mechanical behaviour of these samples. Results of the triaxial compression tests performed in this work are analysed in Chapter 6.

### 4.1.2 Isotropic compression test

An isotropic compression test was run on the naturally cemented sands of Bédoin. The test setup is similar to that of the triaxial compression test except for the piston,



which is not used in the isotropic compression test as no deviatoric loading is applied. The cylindrical sample is placed in the cell, wrapped by the Neoprene membrane and confined at its ends by lubricated ceramic platens. The value of pressure applied to the sample was chosen considering the limits of the system, which is in this case the maximum pressure of 7 MPa supported by the confining cell.

The cylindrical sample used for this test was extracted from a block of material collected in Bédoin by carefully hand-carving. The sample had dimensions of about  $d = 11$  mm and  $h = 22$  mm and it was tested in dry conditions. Results of the isotropic compression test are shown in Chapter 6.

## 4.2 Image acquisition

Sample images were acquired with two techniques: Scanning Electron Microscopy and X-ray Computed Tomography. The two techniques were complementary: the former produced images with a high (nm) 2D resolution, while the latter provided lower ( $\mu\text{m}$ ) image resolution, but with the advantage of a 3D view. An overview of the two techniques is described below.

### 4.2.1 Scanning Electron Microscopy

Scanning Electron Microscopy (SEM) is an image acquisition technique that enables the 2D observation at nano-scale of grain properties and combines this with detection of mineralogical composition. The output image is 2D in the sense that it is the scan of a surface. Thus, a granular rock sample can be either scanned along its surface or it needs to be cut in order to inspect it inside, while sand grains can be simply distributed on a flat surface.

A SEM system is schematically represented in Figure 4.2 and it is principally composed by an electron column, a control console, a chamber (for the sample) with stage, and a series of detectors (Goldstein et al., 2003). The electron column contains an electron source (gun) that accelerates an electron beam towards the sample within the sample chamber. The beam is focused during its way by a series of two or more lenses. The lenses are used to demagnify the beam to a size smaller than 10 nm. From the last lens, the beam enters the sample chamber, where it interacts with the sample and produces signals that are recorded by a series of detectors. Images are obtained by scanning the electron beam in a raster pattern across the surface of the sample. Magnification is controlled by altering the size of the area scanned. In this doctoral work, the FEI Quanta 650 FEG SEM was employed, at an operating current of 15 - 20kV, spot size 3.5 - 4.5, and at a working distance of 10 mm. The device enabled the acquisition of individual images or, using the software MAPS

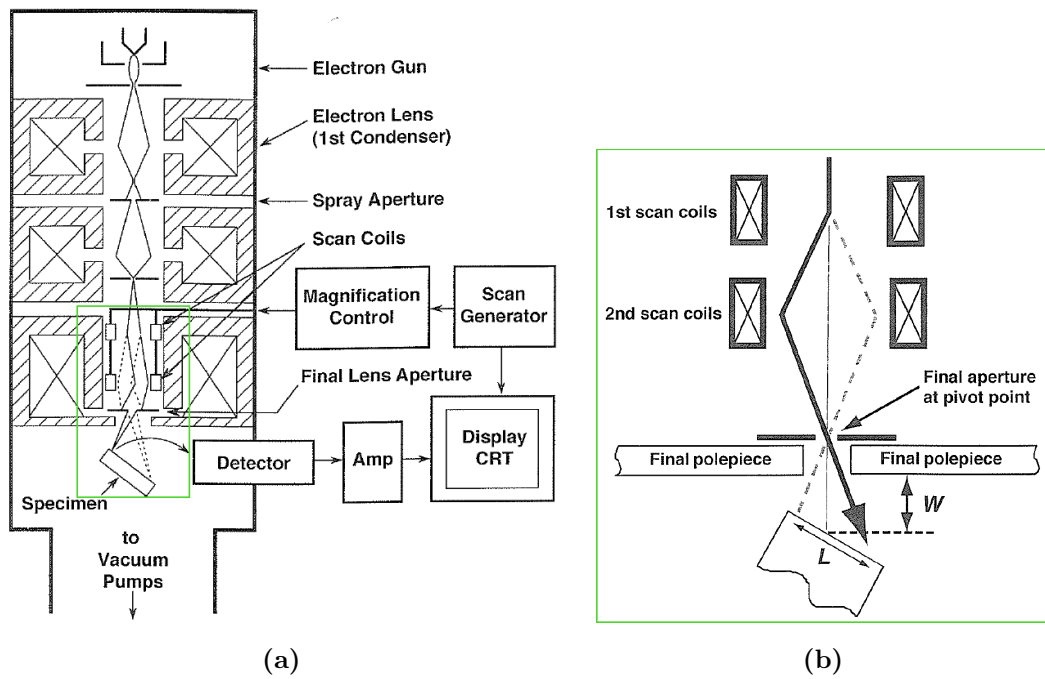


**Figure 4.2:** Scheme of a Scanning Electron microscope: (a) Electron column and Control console, (b) zoom on the scan coils in the last lens with scheme of the beam deflection before reaching the sample ( $L$  = sample width,  $W$  = working distance between sample and last lens) (adapted from Goldstein et al. (2003)).

(<https://www.fei.com/software/maps/>), a series of images (tiles) automatically scanned and stitched together to form large area high-resolution mosaics (Buckman, 2014).

Many signals are generated within the sample through interaction with the electron beam. Back-Scattered Electron (BSE) SEM images have an energy greater than 50 eV, and provide compositional information of the material scanned (Fig. 4.3) with mineral phases distinguished by texture and by greyscale level. Secondary Electron (SE) images are based on the detection of the electrons that have a low kinetic energy, arbitrarily defined as below 50 eV. SE images provide topographic information of the material scanned, and give a 2D representation of three-dimensional surfaces for broken rock surfaces. In this doctoral work, a large-field Gaseous Secondary Electron detector (LF-GSED) is used to obtain Charge Contrast Imaging (CCI) of uncoated samples in low vacuum (for more details, see Buckman et al. (2016)). Figure 4.4a shows an example of CCI image of grain fragments within a cluster of deformation bands. For comparison, a BSE image simultaneously acquired is shown in Figure 4.4b.

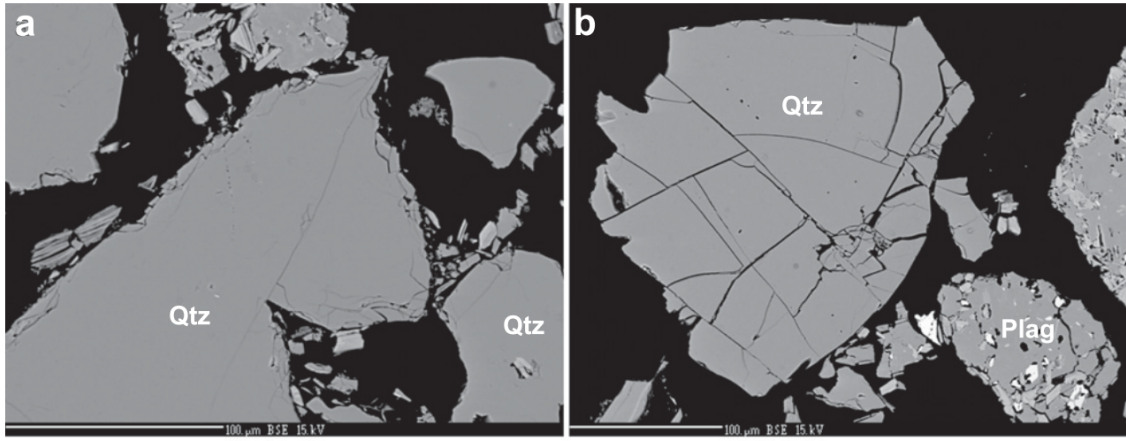


**Figure 4.3:** Examples of BSE image of grains composed by different minerals (Qtz = quartz, Plag = Plagioclase) recognised from the greyscale variations, which reflect grain mineralogy (Exner and Tschegg, 2012).

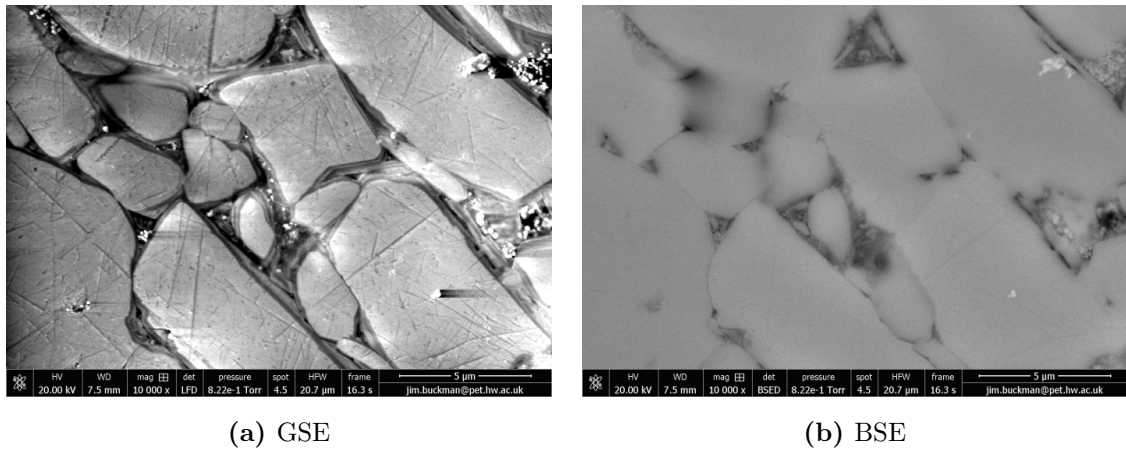


**Figure 4.4:** Images of grain fragments in a deformation band cluster in Bédoin: a) Gaseous Secondary Electron (GSE) CCI and b) Back-Scattered Electron (BSE) SEM images. The CCI image can reveal clear edges of the grain fragments and syntaxial quartz overgrowths, with respect to the BSE image obtained simultaneously.

The GSE image at high magnification in Figure 4.4a reveals the existence of quartz overgrowths surrounding the quartz grains, in a similar fashion to images that are traditionally obtained by cathodoluminescence (CL). In this case, the overgrowths are observed due to different surface charge build up in comparison to their detrital core. As it can be observed in Figure 4.4b, the BSE image is not able to distinguish quartz overgrowths from quartz grain, because the two entities are composed by the same mineral, i.e., quartz.

In addition to the two image types described above, Energy-Dispersive X-ray Spectrometry (EDX) was performed to detect chemical composition of the sample surfaces. The Energy-Dispersive X-ray Spectrometer makes use of the same electron source of the SEM and the signal is received by a (semiconductor) detector

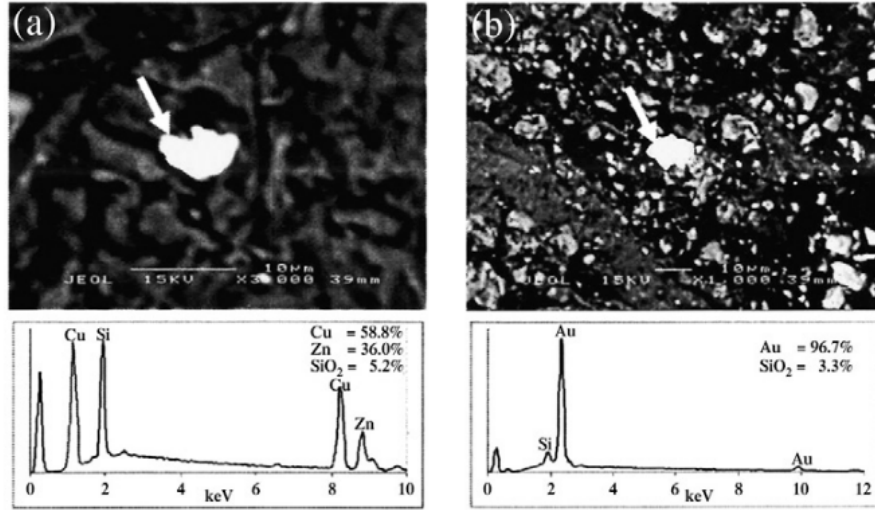


**Figure 4.5:** Examples of EDX histograms obtained from a specific particle indicated with an arrow in the correspondent BSE: a) brass (Cu-Zn alloy) and b) gold (adapted from Prakongkep et al. (2010)).

(Goldstein et al., 2003), which in this case was the  $X - Max^N$  150 mm EDX detector with AZtec Large Area Mapping (LAM) module for EDX maps, from Oxford Instruments. When the sample is hit by the electron beam, it emits X-ray photons. The X-ray photons are absorbed by the detector and emit photo-electrons, which are transformed into a charge pulse. In turn, this is converted into a voltage pulse, which is proportional to the energy of the emitted X-ray photon. The signal is finally amplified and transmitted to a computer analyser that identifies the peaks, representing specific elements, and displays them on a histogram of intensity with respect to the voltage.

Figure 4.5 shows some examples of EDX histograms about specific particles selected (see arrow) in the corresponding BSE images: a) brass (Cu-Zn alloy) and b) gold (Au). The main peak(s) in each histogram constitute the principal elements of the samples. In this doctoral work, the following sample types were inspected with SEM:

- undisturbed naturally cemented sand;
- single-strand and multi-strand compactional shear bands;
- dilation band;
- deformation band cluster.

From these samples, uncemented sand and polished blocks or polished thin sections were extracted. Uncemented grains were inspected with BSE in order to analyse their composition and texture, while polished blocks and polished thin sections were

inspected with BSE and SE for observing grain fragmentation, grain orientation, grain and cement distribution within the deformation bands. A polished block or polished thin section was prepared by encapsulating the sample with epoxy resin under vacuum, in order to coat all the granular parts of the sample and to fill the majority of the pores. Then, the sample was cut along the plane chosen for the inspection, and this surface underwent a process of polishing with abrasive material in order to show the highest quantity of details under the microscope. In addition for the polished thin section preparation, the samples were cut along the plane chosen for the inspection with a thickness of about 30  $\mu\text{m}$  and glued to a glass prior to polishing.

## 4.2.2 X-ray Computed Tomography

X-ray Computed Tomography (X-ray CT) is another image acquisition technique that produces an image of the internal structure of an object, but without the need of destructing it, as opposed to SEM. Since the image is 3D, features that are spatially distributed can be observed, for example pore space and cement distribution.

An X-ray tomography is generated from the acquisition of 2D projections of an object that is rotated by 180° or 360° (Baruchel et al., 2000). From these projections, a specific algorithm (Feldkamp algorithm, see Feldkamp et al. (1984)) is used to reconstruct the 3D image of the object. The *attenuation coefficient*  $\mu$  of the object is the parameter taken into account for the image reconstruction. The coefficient  $\mu$  is proportional to the mass density  $\rho$  [ $\text{g}/\text{cm}^3$ ] and the atomic number  $Z$  of the material, according to the relation:

$$\frac{\mu}{\rho} = K \frac{Z^4}{E^3} \quad (4.1)$$

where  $K$  is a constant and  $E$  is the photon energy. The X-ray CT technique is applied conveniently to inspect the internal structure of multi-phase materials, e.g., porous granular materials or cemented materials, where the density difference of the material components (grains, pores, cements) is inferred from the differences in the greyscale values. Each component of the scanned material is represented by a range of greyscale values, which represents the density of that component. Figure 4.6 shows an example of X-ray CT of a deformation band sample. The sample is virtually sectioned with a vertical (c) and a horizontal (d) planes to show details of the sample structure. The colours in the figure represent voxel greyscale values that vary in the range 0 - 65535 (16-bit image), as reported by the colour legends.

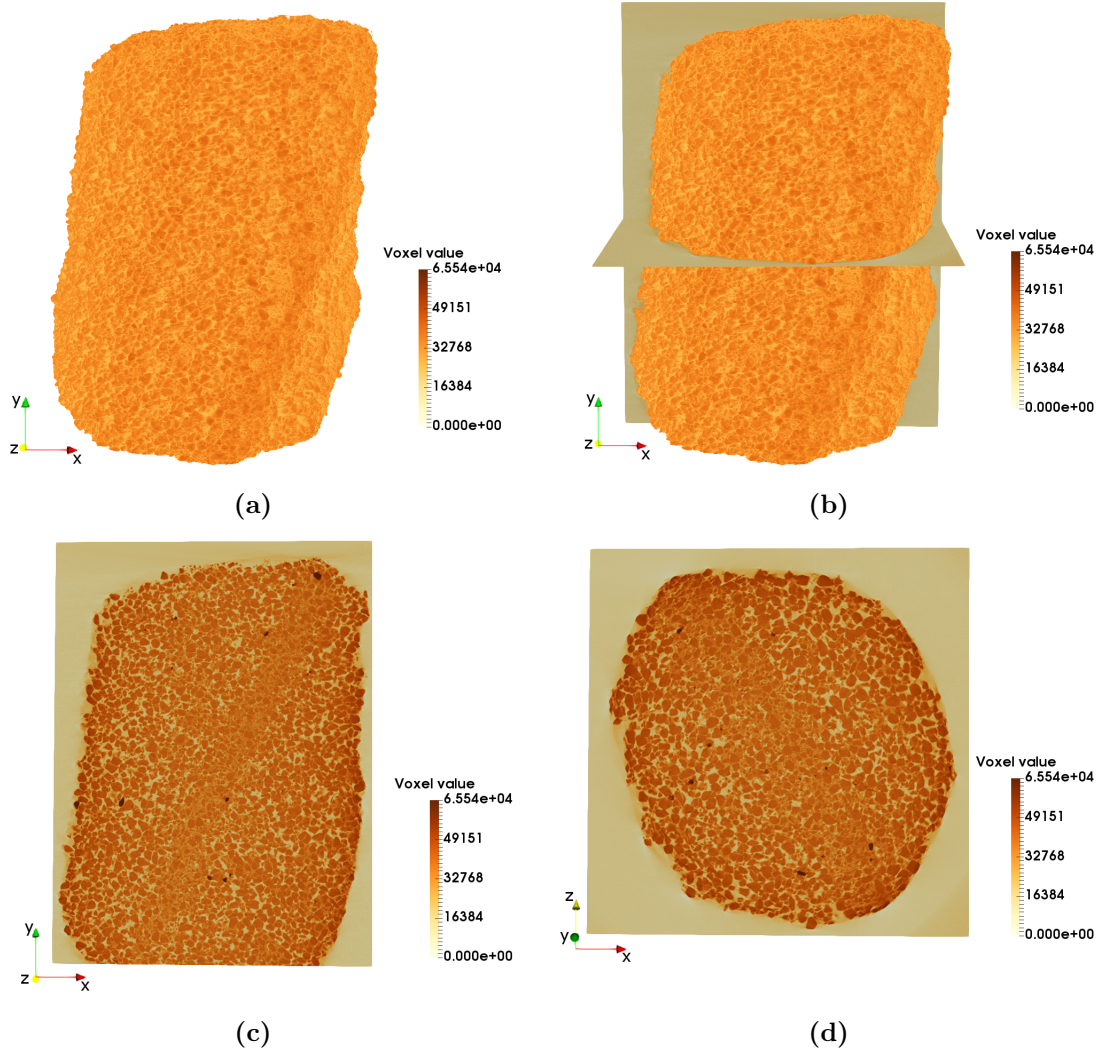


**Figure 4.6:** Example of X-ray CT scan of a deformation band sample from Bédoin (single-strand band ISBSC01): (a) 3D view of the sample and (b) view with vertical and horizontal sections shown in (c) and (d), respectively.

An X-ray CT acquisition system is essentially composed by an X-ray console and an external control console. The X-ray console is composed by an X-ray source, an object stage, and a detector (Fig. 4.7). The X-ray beam is emitted by the source and reaches the detector after going through the object placed on the stage. In order for the system to acquire projections from different angles, the object needs to rotate, thus the stage is rotational (Fig. 4.7). The control console consists of a computer connected with the X-ray console, which enables the control of position and functionality of its three main components. For example, by moving the object stage closer to the X-ray source and farther from the detector, the image resolution is improved, and vice versa. In addition, from the control console, the energy of the X-ray beam can be adjusted and some image artifacts can be corrected (Baruchel et al., 2000). For example, a low X-ray beam energy produces images with high contrast, but also with high noise. In this doctoral work, it was chosen to perform



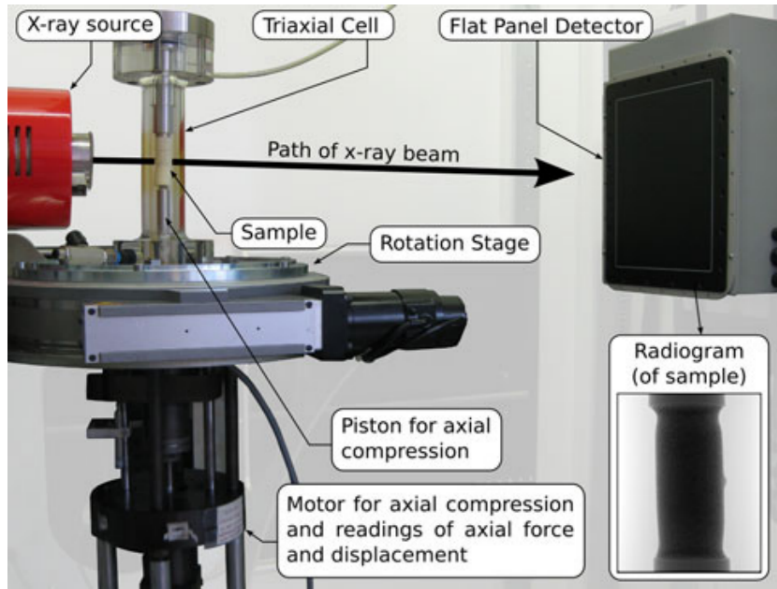


**Figure 4.7:** X-ray CT setup: X-ray console, composed by an X-ray source, an object stage, and a detector. The object stage in the Figure is composed by rotation stage; above it, a triaxial cell is installed (see sample details in Fig. 4.1); below the rotation stage, the loading apparatus is installed and reaches the sample through the piston visible in the cell. An example of output image during the acquisition (radiogram) is shown at the lower-right side of the figure (Andò et al., 2012).

scans with a voltage of 100  $kV$  and a tube current of 100  $\mu A$  (frame rate: 1), and with an image resolution of 10.5 - 27  $\mu m/px$ .

The following samples types were scanned with X-Ray CT:

- naturally cemented sand;
- single-strand and multi-strand compactional shear bands;
- dilation band;
- deformation band cluster;
- artificially cemented sand;
- uncemented sand.

Some of these samples correspond to the samples that were tested either in triaxial or in isotropic compression with *in situ* X-ray CT, and they were prepared as described in Chapter 3. The other samples from the list above were scanned to observe the 3D structure. These samples did not require any preparation.

Quantitative data were extracted from X-ray CT images of the samples listed above. In detail, maximum shear and volumetric strain fields were computed with the software Tomowarp2 (Section 4.3.1) from the *in situ* X-ray CT scans acquired

during triaxial and isotropic compression tests. Porosity and permeability were calculated for all the samples with the software Fiji (ImageJ) and Pore Analysis Tools (Section 4.3.2).

## 4.3 Image processing

### 4.3.1 Digital Volume Correlation

Digital Volume Correlation (DVC) is an image processing technique used to identify the spatial transformation (i.e., displacements) between two 3D images of the same object that are acquired at different times (Hall et al., 2010). The DVC technique described below is implemented in a Python-based open-source software called Tomowarp2 by Tudisco et al. (2017), which was applied in several published works (e.g., Tagliaferri et al. (2011); Charalampidou et al. (2014b); Ji et al. (2015); Alikarami and Torabi (2015)).

In a DVC application, two 3D images of an object are selected for the comparison: a *reference* image (i.e., initial with respect to an interval of interest) and a *deformed* one (i.e., final of that interval). The two images are compared by means of a set of user-defined parameters:

- number of nodes
- correlation window
- search window

The *node* (N in Figure 4.8) is a virtual voxel-sized point (a voxel is each prismatic element that compose a 3D image, corresponding to a pixel in a 2D image) whose coordinates are defined in the reference image. The number of nodes for a DVC is selected arbitrarily, considering that a higher number of nodes produces a more refined correlation as well as it requires a longer computational time.

The *correlation window* is a cubic volume (red square in Fig. 4.8 - i.e., section of the cube) centred around each node of the reference image and whose dimension ( $CW = CW_x$  (or  $CW_z$ )  $\times 2 + 1$ ) is defined as a function of the scale of interest in the image.

The *search window* is a volume (green dotted line in Fig. 4.8) in the deformed image around the voxel that has the coordinates N from the reference configuration. The volume of a search window is assigned arbitrarily, considering that it should contain the displacements imposed to the sample during the mechanical test.

A DVC analysis consists of finding the new coordinates of N (re-named as  $N_t$ ) in the deformed image (Fig. 4.8). In the deformed image, the node has different



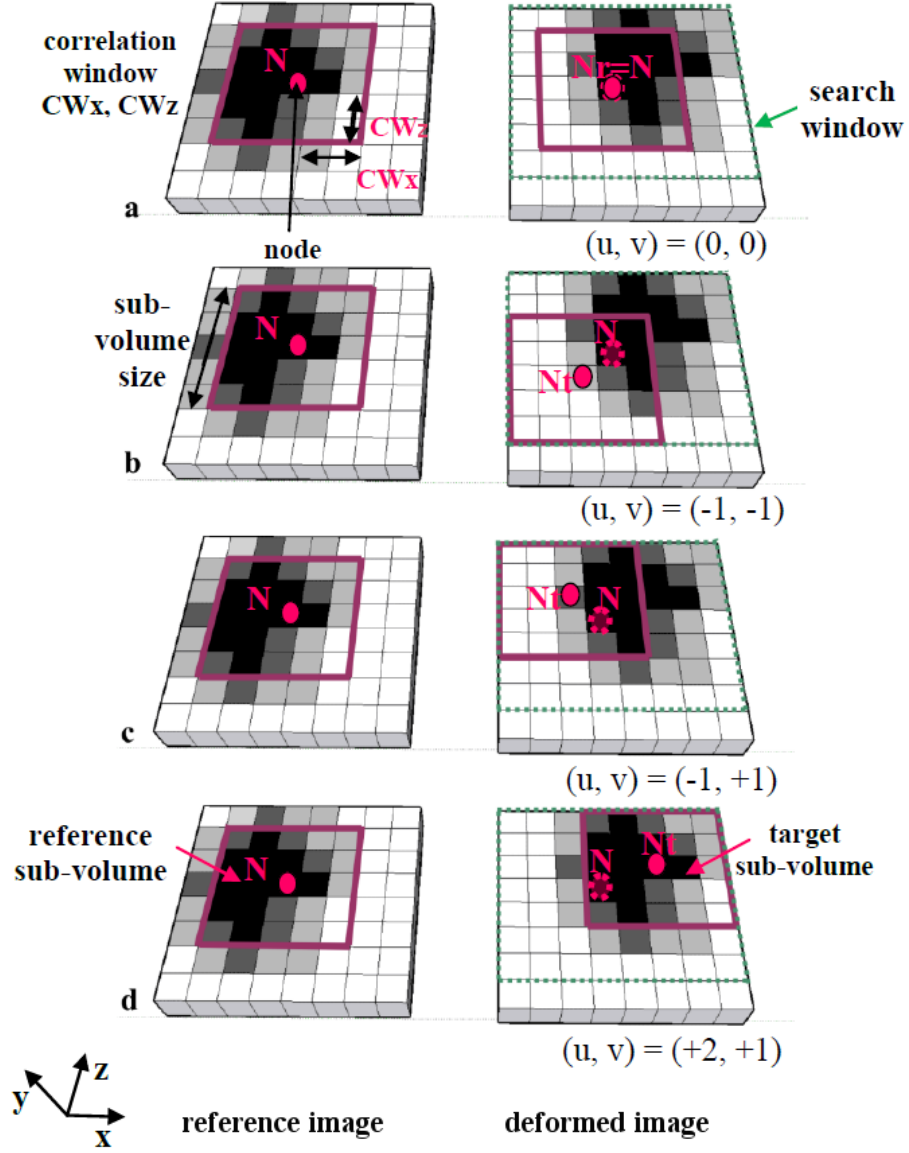


**Figure 4.8:** Illustration of the DVC technique: the correlation window in the deformed image on the right moves around (see a), b) c), and d)) within the search window, searching for the target sub-volume, i.e., voxels with the same properties of the reference sub-volume defined in the reference image on the left (adapted from Charalampidou (2011)).

coordinates since the sample represented by the image was deformed. The analysis is developed by searching the correlation window rather than the node itself, since the correlation window contains the node plus other voxels around it that can help the node identification. The computation is simplified by confining the research of each correlation window (and node) to its own search window. When the correlation window is identified in the search window, a correlation coefficient is calculated to represent the relationship between position of the node in the reference image and that in the deformed one. The searching is run independently for each node, thus each node is described by a correlation coefficient at the end of a successful computation. The correlation coefficients represent the node displacements and, from the calculation of displacements, strains can be computed.

In practice, it is suggested by Tudisco et al. (2017) to perform a DVC twice on the same pair of images (i.e., reference and deformed ones) in order to reduce significantly the computational time: at the first time, the DVC is run with low resolution parameters to get a rough estimation of displacements; at the second time, it is run by using the previous rough results and choosing high resolution parameters.

The code output is a Tab-Separated Value (TSV) file that contains correlation coefficients, coordinates, displacements, rotations and information about eventual errors occurred during the calculation. The displacement field is derived in order to compute maximum shear strain ( $\epsilon_s$ ) and volumetric strain ( $\epsilon_v$ ) fields, knowing that:

$$\epsilon_s = \frac{\sqrt{2}}{3} \sqrt{(\epsilon_1 - \epsilon_2)^2 + (\epsilon_2 - \epsilon_3)^2 + (\epsilon_1 - \epsilon_3)^2} \quad (4.2)$$

$$\epsilon_v = \epsilon_1 + \epsilon_2 + \epsilon_3 \quad (4.3)$$

where  $\epsilon_1$ ,  $\epsilon_2$ , and  $\epsilon_3$  are the maximum, intermediate, and minimum principal strains, respectively. For example, Figure 4.9 shows the maximum shear strain (b) and volumetric strain (c) fields obtained from a DVC performed on a sandstone sample (a) subjected to triaxial compression.

The samples analysed in this work with DVC are the ones that were tested mechanically with triaxial compression and isotropic compression, listed in Section 4.1. The results of DVC analyses performed in this work are shown in Chapter 6. The requirements to run a DVC are: a pair of (reference and deformed) 3D images to correlate, a value for the correlation window and for the search window, the number of nodes.

The value  $CW_x$  used for the analysis of Bédoin samples is 30 px (see Fig. 4.10), which gives a value of correlation window  $CW = 61$ . Considering that the resolution of the scans is of  $15 \mu\text{m}/\text{px}$ , the  $CW$  has a real dimension of about  $900 \mu\text{m}$ , which is

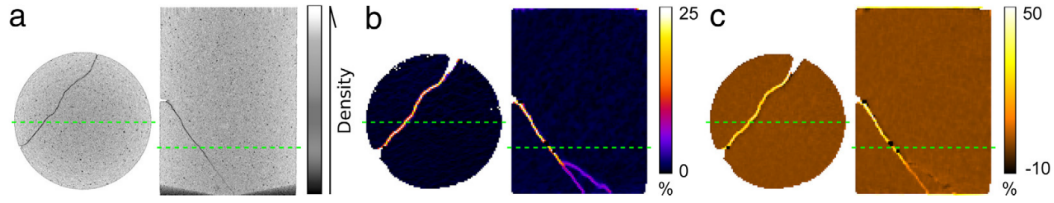


**Figure 4.9:** Example of results (b and c) from a DVC performed on a Bentheim sandstone sample tested with triaxial compression: horizontal and vertical sections of (a) X-ray CT image of the deformed sample, (b) maximum shear strain field, and (c) volumetric strain field (Tudisco et al., 2017).

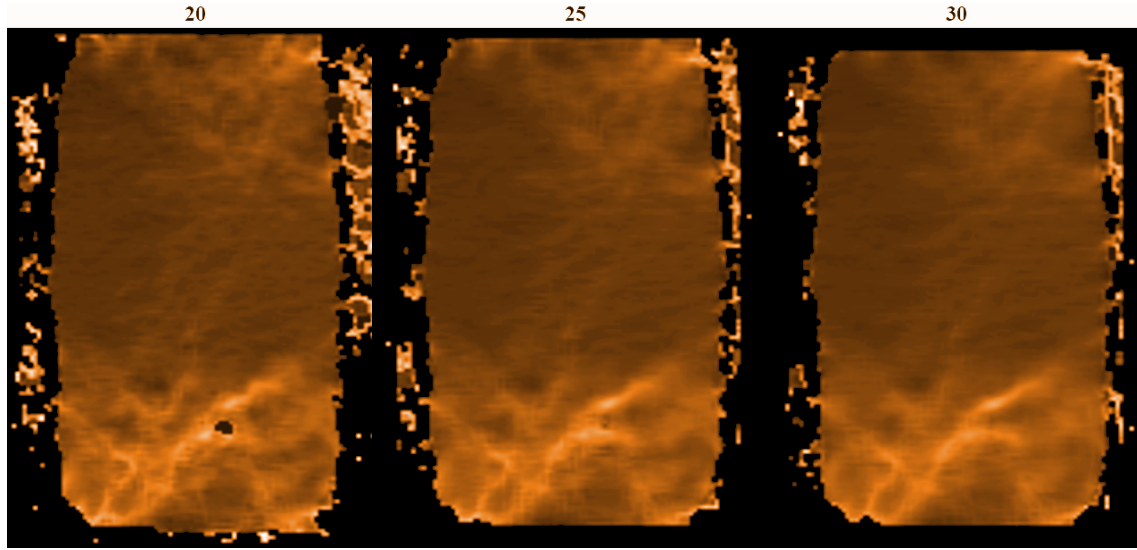


**Figure 4.10:** Comparison of a slice from 3D strain field maps obtained with a different value of the  $CW_x$  (written at the top of each figure), showing that the output obtained with  $CW_x = 30$  gives a smoother image with less (or none) errors of computation, e.g., the black region in the lower part of the sample with  $CW_x = 20$ .

three times the average grain size of the Bédoin grains. Search window and number of nodes are provided twice: the first time for the prior rough estimation DVC, the second time for the high-resolution analysis. In the prior analysis, the search window is defined by taking into account the displacement recorded through the external LVDT, measuring the movement of the piston (Section 4.1.1). The number of nodes is defined by setting the node spacing to 50 px, which corresponds to 2.5 the average Bédoin grain size. In the latter analysis, the search window is set to a suggested value of 5 px, and the node spacing is of 10 px, which corresponds to half grain size.

### 4.3.2 Binarisation and pore space analysis

Binarisation is another image processing technique that transforms a greyscale image into a binary image. The result of binarisation is an image whose pixels (or voxels)

are divided in two classes of values: 0 and 255. If the material represented in the image is a porous solid, these two values correspond to the two phases of the material, i.e., pores and solid. In this work, the solid is an assembly of grains bounded by cement, thus the voxels representing cement are included in the solid volume. Conventionally, the black (0) is assigned to the pores and the white (255) to the solid. Once the image is binarised, the two phases of the material can be processed individually, e.g., to calculate porosity and permeability of the solid phase. A binarisation procedure is proposed below to calculate porosity of the deformation band samples collected in Bédoin. Then, an in-house software that determines porosity and permeability is described below.

### **Binarisation procedure with Fiji (ImageJ)**

A binarisation procedure was defined in order to process the 16-bit X-ray CT scans (example in Fig. 4.11a) of the samples to use for porosity and permeability calculations. The procedure is developed in Fiji (ImageJ) and it consists of four steps, which were automatised into a macro:

1. Threshold application
2. Mask creation
3. Mask addition
4. Stack selection

The thresholding algorithm *Intermodes* is applied in step 1 (Fig. 4.11b), among the several thresholding methods available in Fiji (ImageJ) (Schindelin et al., 2012). Intermodes is suitable for images with bimodal histograms, i.e., histograms where two main peaks stand out (see example in Fig. 4.12). By applying this algorithm, an iterative process of smoothing the histogram is applied with a running average of size 3. The iteration stops when only two local maxima ( $j$  and  $k$ ) are identified. At this stage, the threshold is computed in the form of  $(j + k)/2$  (for further details about threshold types, see <http://imagej.net>).

A mask is created in step 2 (Fig. 4.11c) for the voxels in the image that do not represent neither pores nor solid, i.e., for the space surrounding the sample. This is necessary because the threshold (step 1) attributes to the pores inside the solid the same voxel value given to the space outside the material. Therefore, counting these voxels in the entire image would not lead to measuring the pore space. The mask is created on an inverted duplicate of the thresholded image. In this initial image, pores and space around the sample have the same voxel value (255), as explained above. The algorithm *Fill holes* is applied on the duplicate, in order to fill the pores

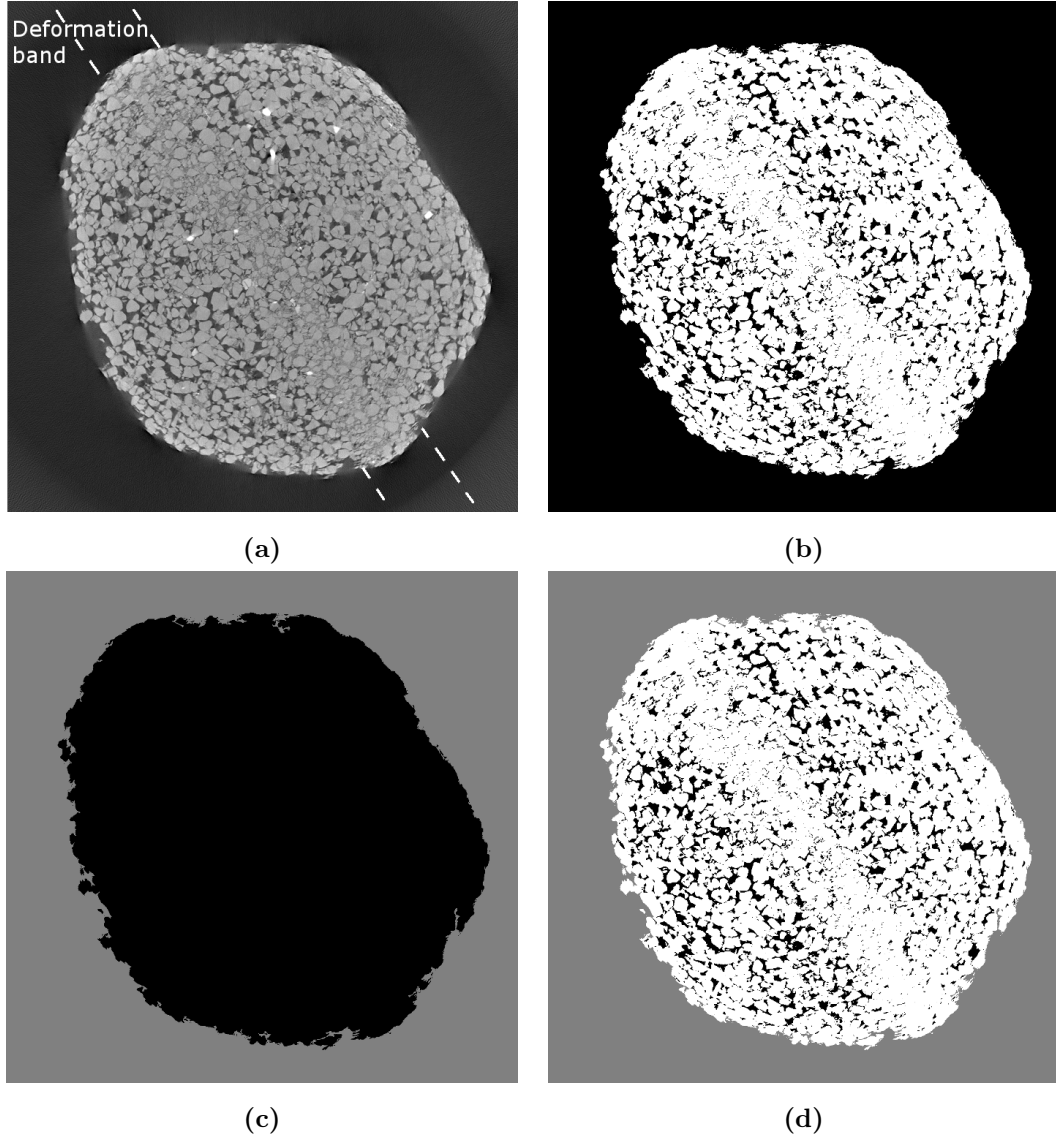


**Figure 4.11:** Binarisation procedure of a deformation band sample (2D cross-section of single-strand band sample ISBSC01): (a) initial 16-bit image; (b) step 1: threshold application; (c) step 2: mask creation; (d) mask addition to the thresholded image obtained in (b). Voxel values in (b), (c), and (d): black = 0, grey = 128, white = 255.

within the solid, thus assigning to the entire sample volume (grains + pores) the voxel value 0. The image is now divided by two, i.e., each voxel value is divided by two. The result is the mask image where the solid is still represented by voxels of value 0 and the space around the sample is identified by voxels of value 128 (i.e.,  $255/2$ ). The obtained mask is applied to the thresholded image (step 3, Fig. 4.11d) through an operation of addition between the two images.

The final step 4 consists of excluding from the entire volume the lower and top ends of the sample in 3D X-ray CT scan, which present image artifacts that cannot be corrected with the binarisation procedure. The exclusion of the slices does not affect the porosity calculation, since these slices usually do not contain sample part or they contain only a minor part of it, if compared to the entire sample volume.

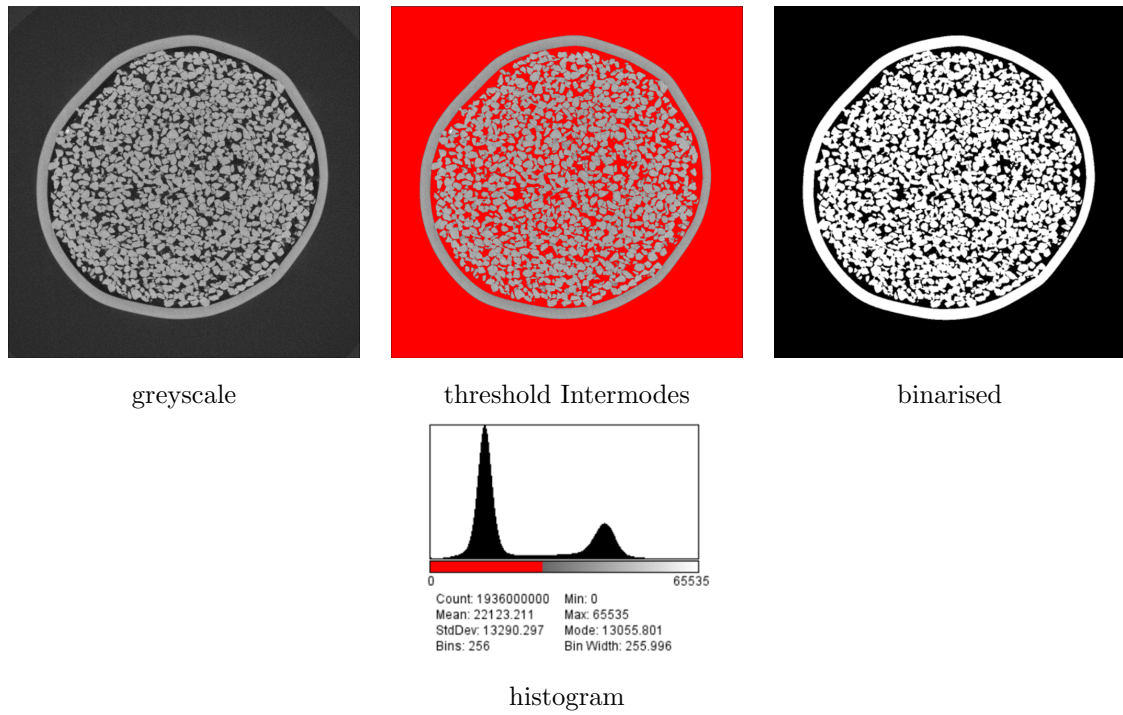


**Figure 4.12:** Example of threshold Intermodes applied to the naturally cemented sample *Nat*, with histogram of the greyscale image (see the two peaks) and threshold indicated on it.

The obtained image from the binarisation contains three voxel values, as shown in Figure 4.11d: 0 for the pores within the solid, 128 for the space outside the sample, and 255 for the solid. Therefore, by counting the number of voxels that represent the pores, the pore volume is known. The samples binarised with this procedure were the X-ray scanned ones listed in Section 4.2.2, which were used for porosity and permeability calculations described below.

### Porosity analysis

Porosity was calculated with Fiji on the entire binarised volumes of the samples mechanically tested and in selected sub-volumes of interest from the deformation band samples. The porosity analysis described here targeted especially the different zones of a deformation band, in order to characterise their porosity differences. Because these zones were in some cases narrow and of irregular shape, a manual selection (i.e., with the *Freehand selection* command) of the sub-volumes of interest was performed. By selecting irregular volumes, instead of prismatic ones, the volume could become larger, therefore the porosity value more representative.

Porosity was calculated on the selected binarised sub-volumes by simply applying the porosity definition:

$$\phi = \frac{vol_{pores}}{vol_{pores} + vol_{solid}} \quad (4.4)$$

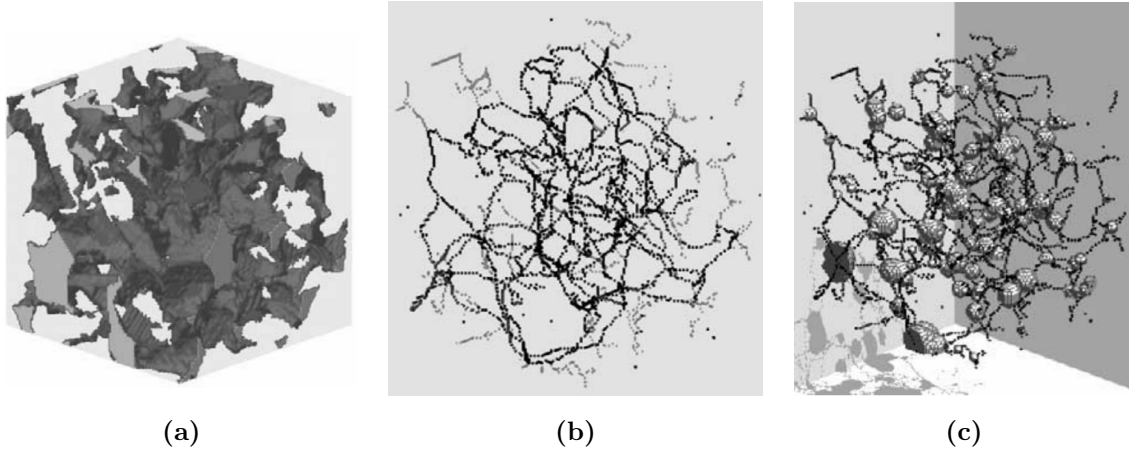


**Figure 4.13:** Example of different representations of a pore network for a sandstone sample: (a) 3D pore space; (b) pore network skeleton in black, with branches in grey; (c) nodes (spheres) and bonds (segments) network (Jiang et al., 2007).

where the pore volume ( $vol_{pores}$ ) is the number of voxels with value 0 and the solid volume ( $vol_{solid}$ ) is the sum of the pore volume with the solid volume, whose voxel value is 255. These numbers were provided by the *Histogram* command in Fiji. The porosity results obtained by analysing deformation bands, naturally and artificially cemented sands, and uncemented sands are shown in Chapter 7. The values take into account isolated pores and cavities. However, more elaborated codes can provide porosity values exclusively about connected pores, as for example the pore network analysis presented below.

### Pore network analysis with Pore Analysis Tools (PAT)

Pore Analysis Tools (PAT) by Jiang et al. (2007) is an in-house software developed at the Institute of GeoEnergy Engineering in Heriot-Watt University. The software is developed in C++ and it is used to analyse statistically pore microstructures and to generate numerical models for single-/two-phase flow simulation in porous media. Herein, the software was mainly used to extract pore network models from the pore space revealed by binary solid images, followed by directly single-phase simulation to estimate porosity and permeability.

One major function of the software PAT is to carry out a series of morphological and topological analyses based on the extracted network models. The Pore Network model (Valvatne et al., 2005) is an alternative to the numerical methods that directly solve the Navier-Stokes equations on discrete domains, e.g., Finite Elements, Finite Differences, Lattice Boltzmann. A pore network model is created to represent the pore space in porous media by partitioning the pore space into a network of pore-bodies (nodes) connected by pore-throats (bonds) (Fig. 4.13). Each element (nodes and bonds) of a pore network has a simplified geometry (e.g.,

regular cross-sections, average length, volume and surface areas, etc.) and the whole network preserves the original connectivity of the pore-solid system. For each network element, its Geometry and Topology (GT) descriptors (e.g., inscribed radius, shape factor, lengths, coordination number, volume) are calculated directly from the 3D image using well-established image analysis algorithms such as *Watershed* and *Distance Transformation*.

Furthermore, a pressure gradient is imposed on the inlet and outlet of the network, thus the pressure distribution can be calculated based on the mass conservation law. This is necessary for the onset of the flow and for the permeability calculation, considering that the fluid flow is proportional to the pressure gradient through the Darcy's law (Lambe and Whitman, 1969):

$$Q = KiA \quad (4.5)$$

where  $Q$  is the rate of flow,  $K$  is Darcy's coefficient of permeability or hydraulic conductivity,  $i$  is the hydraulic (pressure) gradient and  $A$  is the cross-sectional area from which the flow occurs. From this relation, the permeability  $\kappa$  can be computed, considering the inverse proportionality of  $K$  with respect to the viscosity  $\mu$  of the fluid (Lancellotta, 1970):

$$\kappa = K \frac{\mu}{\rho g} \quad (4.6)$$

where  $\kappa$  is the permeability of the material,  $\rho$  is the material density and  $g$  is the gravity constant.

The PAT code performs porosity  $\phi$  and permeability  $\kappa$  calculation in the three directions  $x$ ,  $y$ , and  $z$ . Isolated pores and cavities are not taken into account in this porosity calculation, differently from porosity in Eq. 4.4. This is because the code identifies a network of interconnected pores on which porosity and permeability are calculated. The input data for the calculation is a binarised raw 3D image of the material.

The principal output of the codes are the values of porosity and of permeability, the latter given in three directions ( $x$ ,  $y$ ,  $z$ ) (see Fig. 7.11). PAT also provides statistical GT information about the pore network and the corresponding pore space for further analysis. In this doctoral work, only porosity and permeability values were calculated due to time limitations. The samples selected for the permeability analysis were the ones listed in Section 4.2.2, which were binarised following the procedure described in this Section. Results of porosity and permeability analyses performed in this doctoral work are described in Chapter 7.



# Chapter 5

## Assessment of Bédoin sand microstructure

### 5.1 Introduction

The Bédoin sand was inspected at the micro-scale with the aim of identifying features that characterise deformation bands and undisturbed sand. Three major processes occurred in Bédoin - i.e., grain fragmentation, silica cementation, and clay cementation - were already discussed in previous works (Philit et al., 2015; Sallet and Wibberley, 2013; Wibberley et al., 2007). In this doctoral work, the same major processes were observed but they were distinguished within the different deformation band types - multi-strand bands, deformation band cluster, dilation band - as well as in undisturbed sand. In particular, the first observations of a dilation band from Bédoin are presented in this thesis. Scanning Electron Microscopy, Energy-Dispersive X-ray Spectroscopy, and X-ray Computed Tomography were employed for the analysis. These observations brought into light new characteristics of the mentioned processes, which were elaborated into a new interpretation of the Bédoin burial history.

### 5.2 Grain fragmentation and packing

Localised deformation affected size and shape of the Bédoin sand grains and of the pore space around them. Depending on the deformation band type (compactional or dilational, with or without shear, ref. to Fig. 2.6), the degree of grain and pore space alteration varied.

In the absence of localised deformation, the undisturbed sand (Fig. 5.1a) was reported to contain intact or lightly fractured grains and a high content of pores (porosity is discussed in Chapter 7). The few fractured grains were held by clay

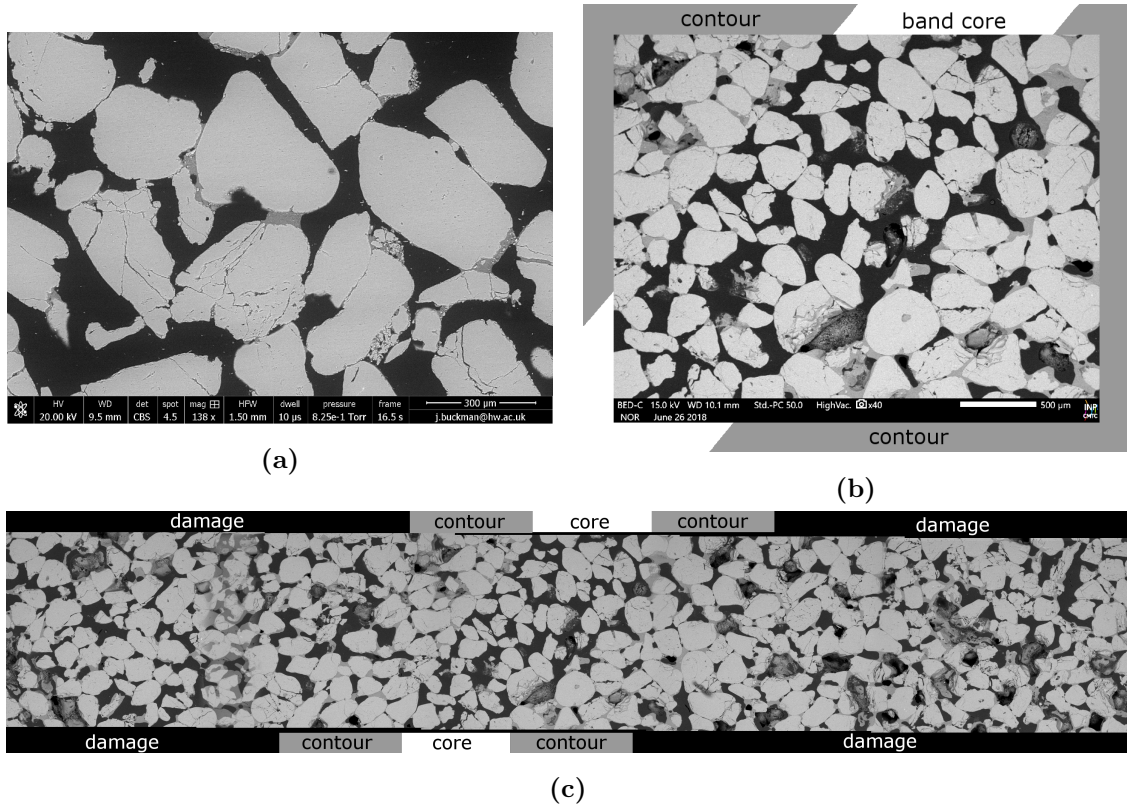


**Figure 5.1:** Scanning Electron Microscopy (SEM) of grain fragmentation in an undisturbed sand sample (a) and in a dilation band (b, c): some grains in (a) and in the band core in (b) result fractured, but the fragments are still in their original place and they are held by cement (principally clay, see Sect. 5.4); contours in (b) are richer in cement; (c) zones that compose the dilation band: core, contour, and damage zone.

menisci bonds, which kept the grain fragments in their original place as when the grains were still entire.

A sample of dilation band from Bédoin 3 (ref. to map of Bédoin outcrops in Fig. 3.1) was observed with Scanning Electron Microscopy (Fig. 5.1b-c). In the dilation band, the three zones - i.e., core, contour, and damage (defined in Section 2.3.1 for compactional shear bands) - were identified and they are indicated in Figure 5.1c. The dilation band core shared similarities with the undisturbed sand (Fig. 5.1a) in terms of grain characteristics: grains in the band core were intact or lightly fractured. In terms of cementation degree, the dilation band core reported less cement content than the undisturbed sand, with the cement still distributed in menisci between grains. The band contours were composed of grains similarly intact or lightly fractured, but the pore space was reduced by grain packing and by increase of cement content. The damage zone presented intact or lightly fractured grains and cement distributed in menisci in a similar quantity to the undisturbed sand.

The three zones - core, contour, and damage - are further described in Chapter 7, where quantitative evaluation of porosity and permeability is reported.

Several samples of multi-strand band core from Bédoin 4.5 were analysed and two of them are reported in Figure 5.2 to show the main characteristics. Due to the small dimension of the samples, contours were not identified with SEM. Few observations were made for the damage zone, such as the presence of intact grains mixed with grain fragments and a low content of clay (Table 5.1).

The sample in Figure 5.2a was extracted from a multi-strand band where it is observed the grain spatial arrangement: some survivor (or semi-fractured) grains were identified, surrounded by a fine-grained matrix that filled the pore space. The survivor grains look aligned along the deformation band plane (dashed lines).

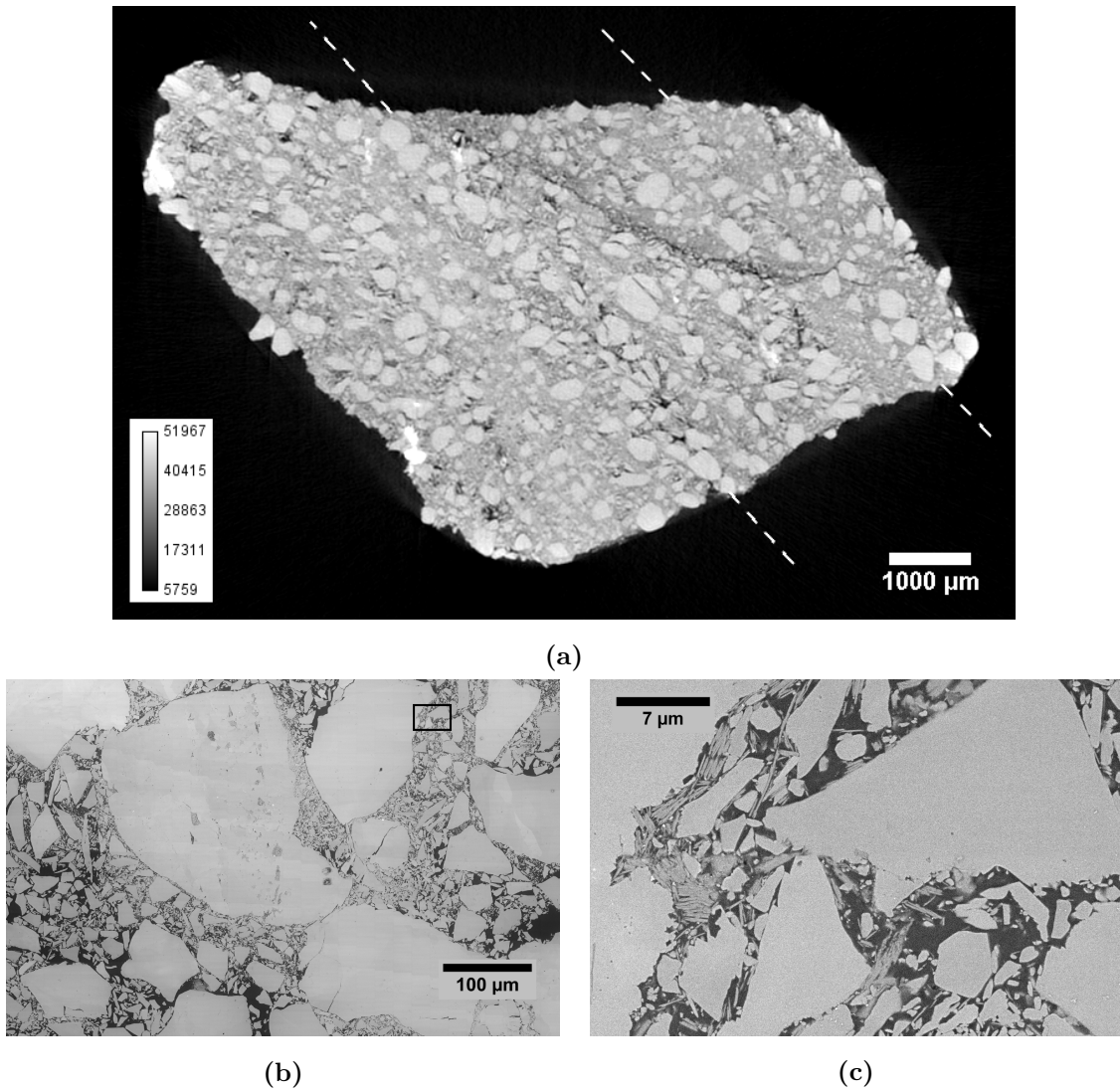


**Figure 5.2:** Grain fragmentation in multi-strand bands from Bédoin 4.5: (a) X-ray CT slice orthogonal to the direction of the deformation band plane (dashed lines) [res.  $15\mu\text{m}/\text{px}$ ], where survivor grains are aligned and surrounded by a fine-grained matrix; (b) SEM image of grains and fragments in another multi-strand band from the same outcrop; (c) zoom from (b) over quartz micro-fragments, showing that their size is comparable to that of clay (elongated particles).

The sample shown in Figure 5.2b-c showed some details at the scale of few  $\mu\text{m}$ : the fine-grained matrix is composed by quartz micro-fragments mixed with few clay particles (Fig. 5.2c). Quartz and clay particles have comparable sizes of about few  $\mu\text{m}$ , thus highlighting the high degree of comminution undergone by the sand grains.

A sample of deformation band cluster from Bédoin 3 (Fig. 5.3) showed differences of grain and pore sizes between the material inside a strand and that outside it. The strand in the polished thin section (central image in Fig. 5.3) looked blurred, but this is due to the presence of quartz micro-fragments, which are tightly embedded in the space between bigger grains so as to occupy almost the entire pore space (Fig. 5.3a).

A different condition was observed at the two sides outside the strand (i.e., interband): a greater content of intact and lightly-fractured grains were found, surrounded by a much smaller content of grain fragments with respect to the strand (Fig. 5.3b and c). Also the pore space looked greater in the interband than in the strand. In addition, cements of different mineralogy filled the pores, as for example clay in Figure 5.3c and iron/titanium-rich cement in Figure 5.3d.

Occasional grain dissolution was observed in the strand of the deformation band cluster. The two zooms on the right in Figure 5.4 show this process generated at the contact between grain fragments: the surface of the smaller fragment is either flattened by the bigger fragment, or is penetrated if the latter has a pointed shape. The silica dissolved with grain dissolution could re-precipitate on the grain surface as syntaxial quartz overgrowths. The process of silica cementation is described in the following Section 5.3.

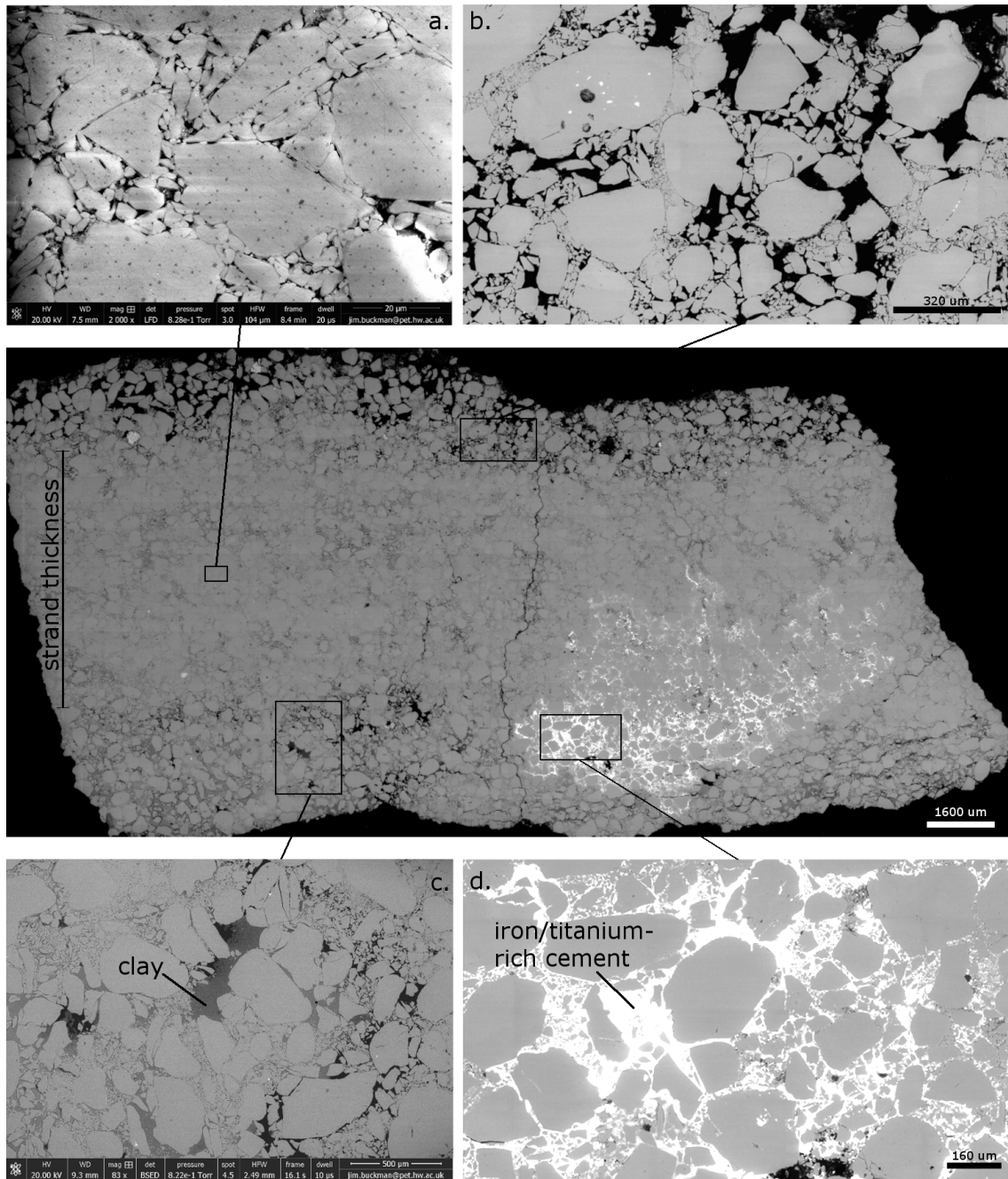


**Figure 5.3:** Mosaic SEM (central figure) of a strand extracted from a deformation band cluster in Bédoin 3: details of grain breakage and packing within the strand (a), in the interband (b, c) and in an iron/titanium-rich cement (d) (the mineralogy of grains and cements is shown in Fig. 5.7).



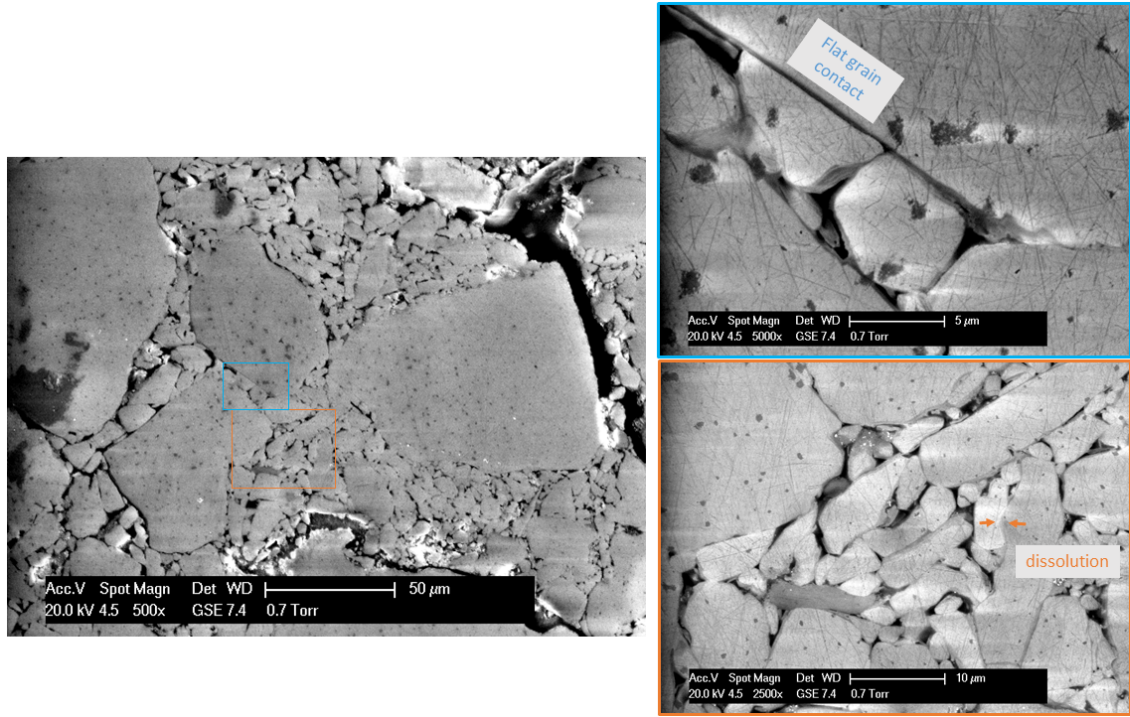


**Figure 5.4:** SEM images of grain dissolution in the deformation band cluster from Figure 5.3: the zooms on the right show detail of dissolution occurred in a zone of tightly compacted quartz micro-fragments. Note the syntaxial quartz overgrowths precipitated around the grain fragments.

### 5.3 Silica cementation

Silica cementation in Bédoin 3 was previously analysed by Philit et al. (2015), who developed an hypothesis of groundwater system, connecting in particular this type of cementation with deformation bands affected by cataclasis, i.e., multi-strand bands, clusters, and faults. In this doctoral work it was observed that quartz cementation occurred not only in the deformation bands that reported intense deformation, but also in single-strand band, in dilation bands, and even in the undisturbed sand, where intense cataclasis did not occur. In addition, further characteristics of the quartz cementation were also observed in Bédoin 3 and 4.5, for example asymmetric silica overgrowths around grains and interaction with other cements, e.g., clay.

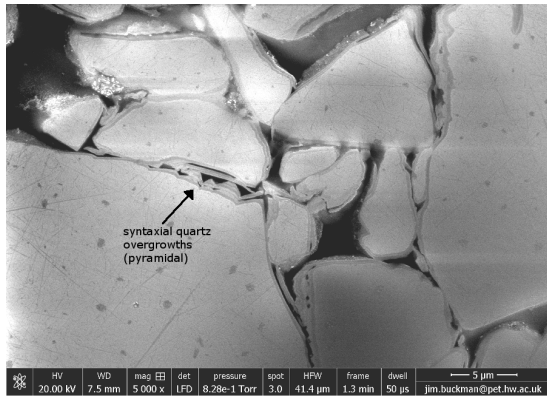
Figure 5.5a shows thin quartz overgrowths ( $\sim 1 \mu\text{m}$ ) deposited around grain fragments in the deformation band cluster of Bédoin 3. Some of the layers showed a pyramidal structure, which is typical of the quartz mineral spatial arrangement. In a multi-strand band from Bédoin 4.5 (Fig. 5.5b), silica layers precipitated as multiple syntaxial quartz overgrowths in a number of layers greater than 20. Figure 5.5b also shows that quartz overgrowths precipitated asymmetrically around grain fragments, thus implying that silica cementation occurred in different stages during and after strain localisation, when grains were crushed, thus creating new surfaces

for silica to precipitate.

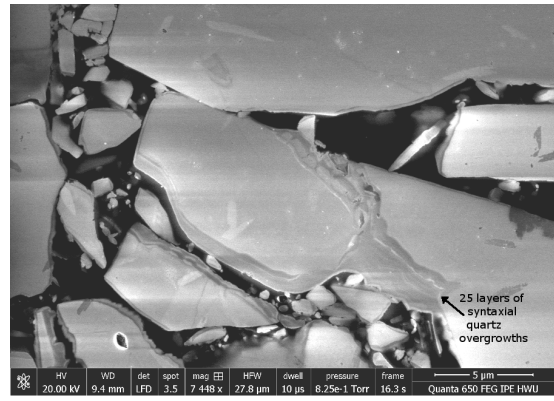
Another process involving silica cementation is the re-cementation of crushed grains so as to reconstruct the original shape of the grain. This was reported in the deformation band cluster observed in Bédoin 3 and shown in Figure 5.3. An example of the re-cementation is shown in Figure 5.5c.

Silica did not only re-precipitate as syntaxial quartz overgrowths on the grain surfaces, but it also formed granular crystals known as micro-quartz. Figure 5.5d shows micro-quartz observed in the deformation band cluster of Figure 5.3. The occurrence of micro-quartz was connected to the presence of clay floccules in the pore space together with free silica at the time of quartz precipitation. This hypothesis was discussed in Soriano et al. (2017a) and it is in agreement with Haszeldine et al. (2003) who claimed that the absence or the small content of clay coating did not prevent from silica precipitation as syntaxial quartz overgrowths in oilfields in the North Sea.

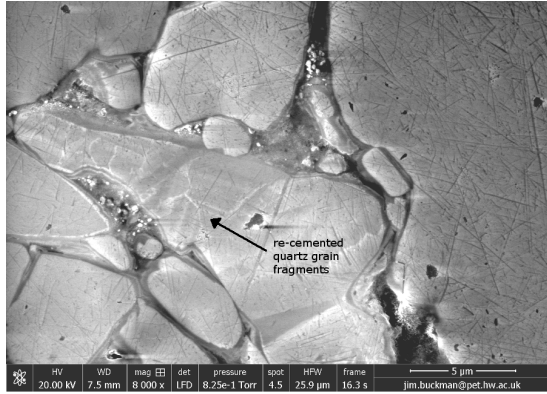
Syntaxial quartz overgrowths occurred not only in multi-strand (Bédoin 4.5) and deformation band cluster (Bédoin 3) but also in the dilation band and in the undisturbed sand from Bédoin 3 shown in Figure 5.1. In both cases, quartz re-precipitated on damaged grain surfaces (Fig. 5.6), which appear to be preferential sites for quartz overgrowths. Differently from the quartz overgrowths in deformation bands (Fig. 5.5), only few quartz layers (for a total of  $< 1 \mu\text{m}$ ) were identified in the undisturbed sand and dilation band samples. The observation of thicker (about  $5 \mu\text{m}$ ) silica overgrowths within multi-strand bands and clusters than in undisturbed sand and single-strand band supports the hypothesis that grain fragmentation in these deformation bands is the source of silica for syntaxial quartz overgrowths. In addition, the presence of quartz overgrowths outside zones of localised deformation supports a new consideration about the maximum burial depth of sand deposit before reaching the current surface location. Knowing that syntaxial quartz overgrowths generally precipitate at a temperature of  $70 - 80^\circ\text{C}$  and knowing the geothermal gradient of about  $35^\circ\text{C}/\text{km}$ , the sand deposit most likely reached a depth of at least 2 km. This hypothesis extends the maximum burial of 500 - 1300 m estimated to date (Saillet, 2009; Philit et al., 2015).



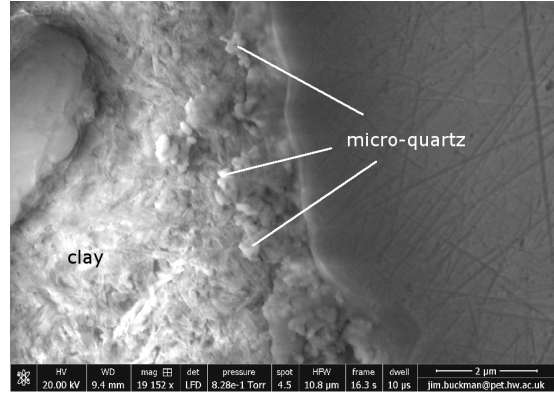
(a) quartz overgrowths



(b) overgrowths asymmetry

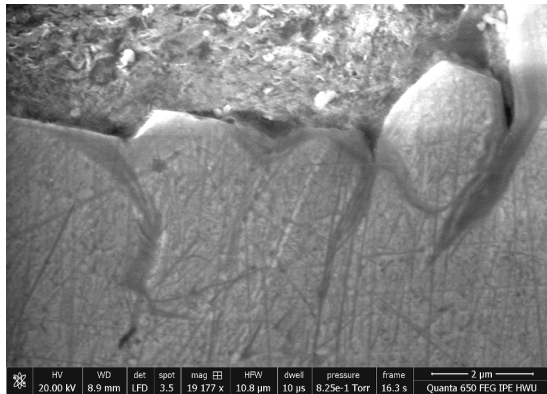


(c) re-cementation of grain

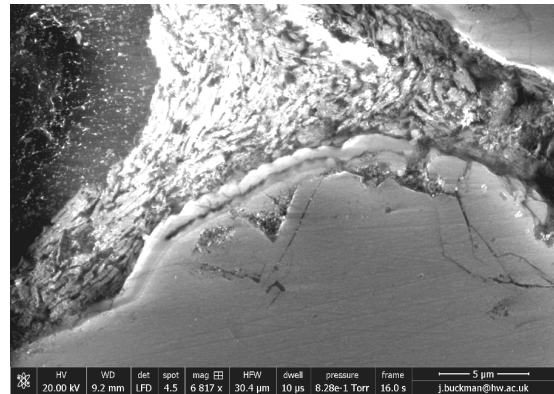


(d) micro-quartz

**Figure 5.5:** SEM images of silica cementation in multi-strand bands and cluster: (a) and (b) syntaxial quartz overgrowths (note that in (b) it is possible to distinguish up to 25 quartz layer generations); (c) quartz fragments broken and re-cemented with quartz (see arrows); (d) micro-quartz in the pore space with flocculated clay particles.



(a)



(b)

**Figure 5.6:** SEM images of syntaxial quartz overgrowths in (a) the dilation band core (same sample as in Fig. 5.1b) and in (b) the undisturbed sand (same sample as in Fig. 5.1a).



## 5.4 Clay cementation

Kaolin clay cement (introduced in Chapter 3) was observed in undisturbed sand of Bédoin 3 as well as in deformation bands of Bédoin 3 and 4.5. However, clay distribution and quantity presented differences between undisturbed sand and deformation bands. For example, in undisturbed sand (Fig. 5.1a), clay was distributed in menisci bonds between the grains. In the dilation band, clay was still distributed in menisci but in greater content along the band contours rather than in the band core, as highlighted in Figure 5.1b. In both samples, clay deposited above the syntaxial quartz overgrowths that coated the grains (Fig. 5.6). This means that clay most likely infiltrated the sand deposit at a later stage and it probably did not interact with quartz at the time of silica cementation.

Clay distribution and content in the multi-strand bands and cluster of Bédoin 3 and 4.5 showed differences with respect to the undisturbed sand and the dilation band (of Bédoin 3). The Energy-Dispersive X-ray Diffraction (EDX) map of the sample extracted from the deformation band cluster (Fig. 5.7) showed that clay is more concentrated in the interband rather than inside the strand, where a smaller clay content was detected. In the analysed sample, clay was not distributed in clay menisci but filled almost entirely the pores (e.g., Fig. 5.3c). Likewise, clay was identified in the multi-strand bands in minor content, mixed with grain micro-fragments (Fig. 5.8) and not organised in menisci bonds (Fig. 5.2a).

While clay platelets were spatially arranged in floccules in the undisturbed sand and the dilation band (e.g., Fig. 5.6), in multi-strand bands kaolin clay was distributed into booklet structures, shown for example in Figure 5.9a and represented by a characteristic EDX spectrum. In general, kaolinite booklets are the product of the illitization of kaolinite and illite is an authigenic clay produced at great burial, where the required temperature higher than 70°C for the transformation is provided (Worden and Burley, 2003), as for example the extensive kaolinite illitization occurred at a temperature of 90 - 95°C (burial depth lower than 3 km) in the Norwegian continental Shelf (Lanson et al., 2002). The fact that illitized kaolinite was found in Bédoin 3 supports the hypothesis that this sand deposit reached a depth greater than 2 km, where temperatures  $\geq 70^\circ\text{C}$  would have enabled the process. This interpretation is strengthened by the observed syntaxial quartz overgrowths, discussed in Section 5.3, for which it is claimed they developed at a minimum depth of 2 km.

The presence of kaolin clay and its alteration (i.e., illitized kaolinite) within low-porous zones of multi-strand bands and cluster justifies the hypothesis that clay was already in the deposit at the time of localised deformation. However, the greater content of clay along the dilation band contours (Fig. 5.1b), at the boundaries of the strand (i.e., interband) in the deformation band cluster (Fig. 5.7), and the well-

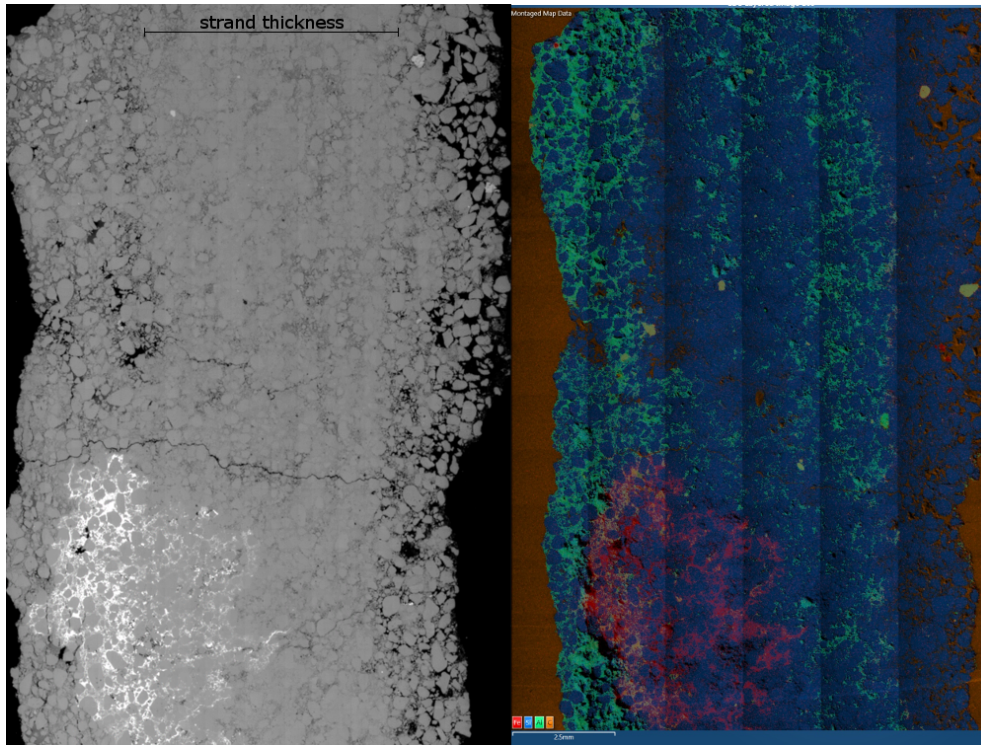


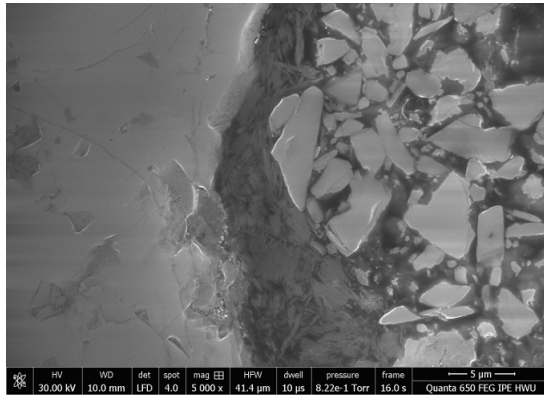
**Figure 5.7:** Energy-Dispersive X-ray Diffraction (EDX) map (on the right) of the mosaic SEM (on the left) from Fig. 5.3: the map shows that there is less presence of clay (in green) inside the deformation band strand than in the interband (red is Fe, blue is Si, green is Al, orange is Ca).

defined menisci bonds in the undisturbed sand and dilation band (Fig. 5.1a) support the idea that more clay permeated the deposit after the occurrence of localised deformation, which otherwise would have destroyed the menisci bonds.

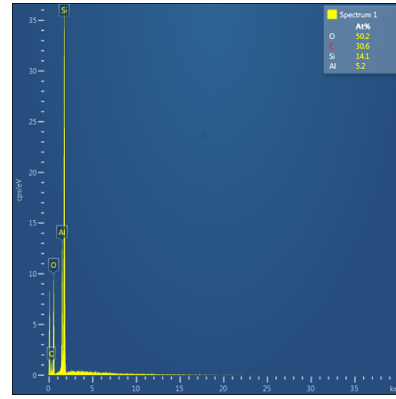
## 5.5 Summary

Observations related to grain damage and processes involving silica and clay cementation in distinct deformation band types and undisturbed material were discussed. A summary of the results is provided in Table 5.1. These observations supported the hypothesis that the Bédoin sand deposit reached a burial depth greater than the value of about 500 - 1300 m estimated by Philit et al. (2015), considering also that the presence of a geothermal source in the studied region was not reported to date.

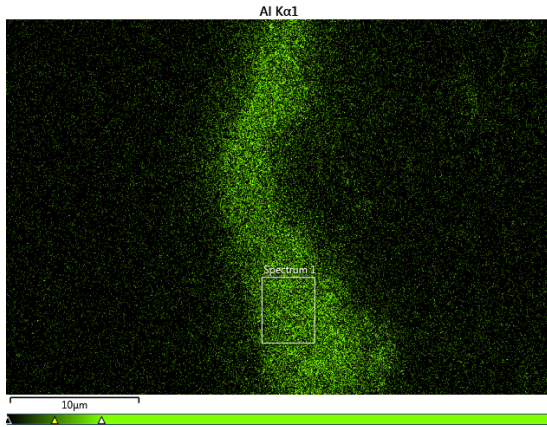
In particular, it is claimed that silica cementation as syntaxial quartz overgrowths occurred at a burial of 2 to 3 km. The fact that grain fragments were covered asymmetrically by silica layers means that deformation bands developed at great depth before the sand deposit reached the actual surface location and that the process of silica cementation occurred during or after the deformation band development (which produced grain breakage and rearrangement).



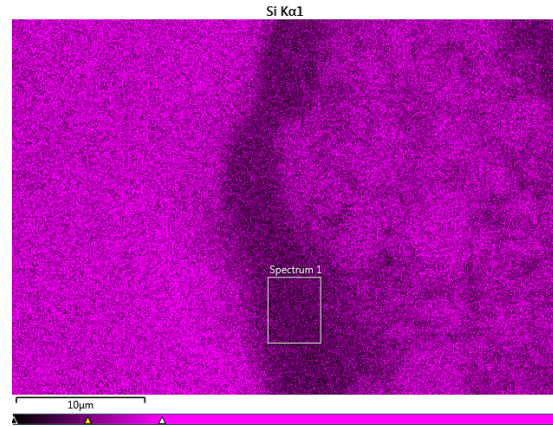
(a) CCI microscopy image



(b) EDX spectrum

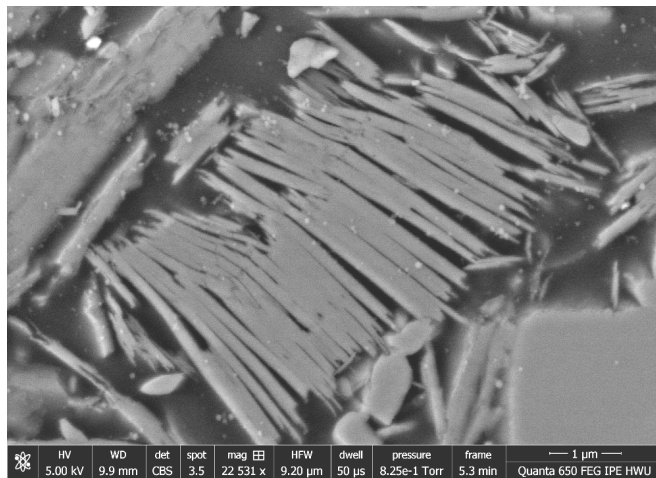


(c) clay fraction (Al)

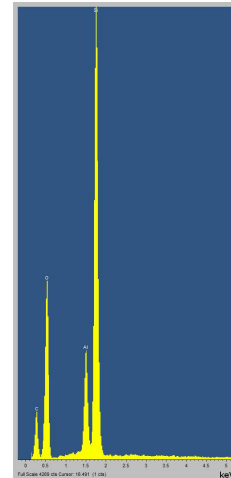


(d) silica fraction (Si)

**Figure 5.8:** Clay particles next to quartz micro-fragments in a multi-strand band from Bédoin 4.5: (a) Charged Contrast Imaging (CCI) figure of the sample, (b) Energy-Dispersive X-ray Diffraction (EDX) spectrum of the clay contained in the square reported in (c) and (d); (c) and (d) are EDX colour maps representing the clay and silica fractions, respectively, of the sample in (a).



(a) booklet of illitised kaolinite



(b) EDX

**Figure 5.9:** (a) SEM image of a kaolinite booklet from a multi-strand band in Bédoin 4.5; (b) EDX spectrum of the illitized kaolinite shown in (a).

Furthermore, the presence of clay within multi-strand bands and cluster and the transformation of clay from kaolinite to illite in these highly deformed zones, which is supposed to have occurred at an estimated temperature higher than 70°C, are in agreement with the hypothesis of deep burial.

**Table 5.1:** Summary of grain and cement characteristics observed in the three zones of distinct deformation band types: G = grains, C = clay cement, Q = syntaxial quartz overgrowths; \*interband, in the case of deformation band cluster (for them, damage zone was not inspected).

deformation band				undisturbed sand
zone	dilation	multi-strand	cluster	
core	G: intact or lightly fractured C: menisci, low content Q: few layers	G: survivor, surrounded by fine matrix C: low content, no menisci Q: many layers	G: survivor, surrounded by fine matrix, grain dissolution and re-cementation, micro-quartz C: low content, no menisci Q: many layers	G: intact or lightly fractured C: menisci, medium content Q: few layers
contour	G: intact or lightly fractured C: menisci, high content Q: few layers			
damage*	G: intact or lightly fractured C: menisci, medium content Q: few layers	G: intact and fractured C: low content	G: intact and fractured C: medium content, no menisci Q: many layers	

# Chapter 6

## Mechanical behaviour of natural and artificial samples

### 6.1 Introduction

This Chapter discusses laboratory-induced localised deformation in natural and artificially cemented and uncemented sands from Bédoin 3. For this purpose, a number of mechanical loading experiments, coupled with syn-deformation X-ray Tomography, were performed on samples. These tests aimed at a better understanding of the mechanical behaviour of this material and at the identification of the role of imperfections on the development of localised deformation at the laboratory scale. The following experiments were carried out:

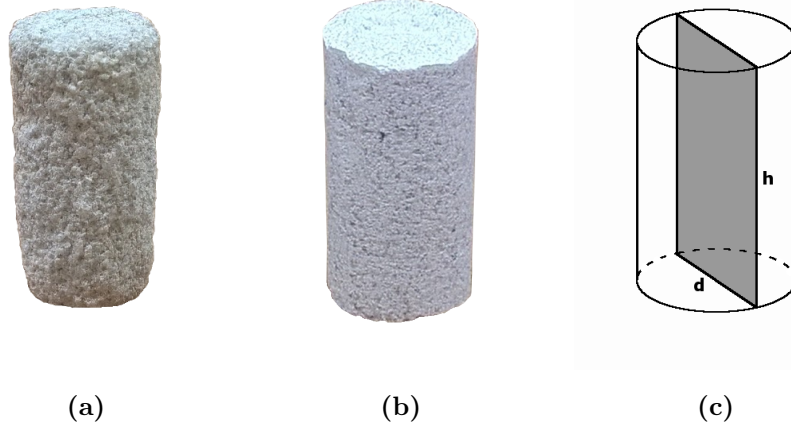
- one isotropic compression (up to 7 MPa) and three triaxial compression tests (at 1 MPa) on naturally cemented samples;
- two triaxial compression tests (at 1 MPa) on artificially cemented samples;
- one triaxial compression test (at 1 MPa) on uncemented Bédoin sand.

Figure 6.1 shows two of the six cemented samples: (a) a natural one and (b) an artificially cemented one. Some of the natural samples tested contained inclined depositional layering, which was not visible by naked eyes; other ones contained regions of enhanced porosity or an inclined dilation band.

Apparatus and tests setup are described in Section 4.1, including the device used to perform syn-deformation X-ray Computed Tomography, which enabled Digital Volume Correlation (DVC) by using the Tomowarp2 software (Sect. 4.3.1).

DVC results were produced by performing incremental correlation, i.e., correlation between each couple of consecutive scans acquired during the test (e.g., from scans 00, 01, and 02, DVC 00-01 and DVC 01-02 were performed). The results were obtained in the form of 3D maps representing the incremental evolution of strain





**Figure 6.1:** (a) Naturally and (b) artificially cemented samples used in the mechanical tests, and (c) schematic representation of a 2D vertical slice ( $h \cong 22$  mm,  $d \cong 11$  mm) extracted from 3D X-ray scans and DVC data of each sample.

fields, but they are shown here as 2D vertical slices (Fig. 6.1c). Maximum shear and volumetric strain field maps are shown in the same range of values for each map type in order to facilitate the comparison of strain fields between different steps of the tests and between distinct tests. Additionally, an overlap of both strain fields is shown to highlight the occurring processes. The overlap is carried out after transforming the maximum shear strain field map into a greyscale image and overlapping it with the volumetric strain field in transparency.

## 6.2 Isotropic compression test

### 6.2.1 Naturally cemented Bédoin sand

The cylindrical sample tested under isotropic compression was hand-carved from a block of undisturbed cemented sand from Bédoin 3 (further details in Chapter 3). The sample had a weight of 3.78 g and dimensions of  $h = 22.24$  mm and of  $d = 11.00$  mm.

The isotropic compression was performed by increasing confining pressure in steps of 1 MPa going from 0 MPa to 7 MPa, which is the maximum pressure supported by the cell, at a flow rate of 0.01 mL/min. Figure 6.2 shows the steps of pressure increase applied to the sample. The numbers 00 to 07 along the curve in Figure 6.2 indicate the sequence of *in situ* (i.e., during the test) X-ray scans performed at the beginning of the test and at the end of each 1 MPa confining pressure increase. The small peak between steps 02 and 03 is an anomaly due to the sample setup, which was fixed afterwards. Figures 6.3 (a) and (b) show two representative vertical slices extracted from the X-ray scans performed at the beginning (0 MPa)

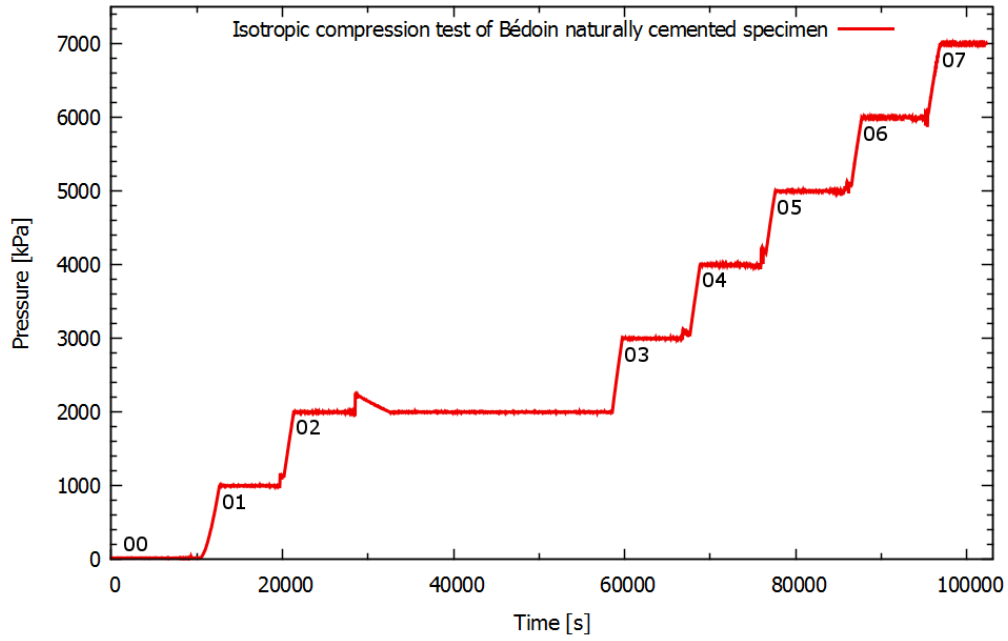


**Figure 6.2:** Curve representing the evolution with the time of the confining pressure applied to the sample. Numbers 00 to 07 along the curve refer to X-ray scans acquired during the test. Step 02 - 03 is longer than the other steps because of the night break during the test, whereas the small peak after scan 02 is an anomaly due to the sample setup.

and at the end of the test (7 MPa), respectively. A double membrane (Fig. 6.3) was used to prevent membrane perforation, which can be provoked by reaching high pressures during this test.

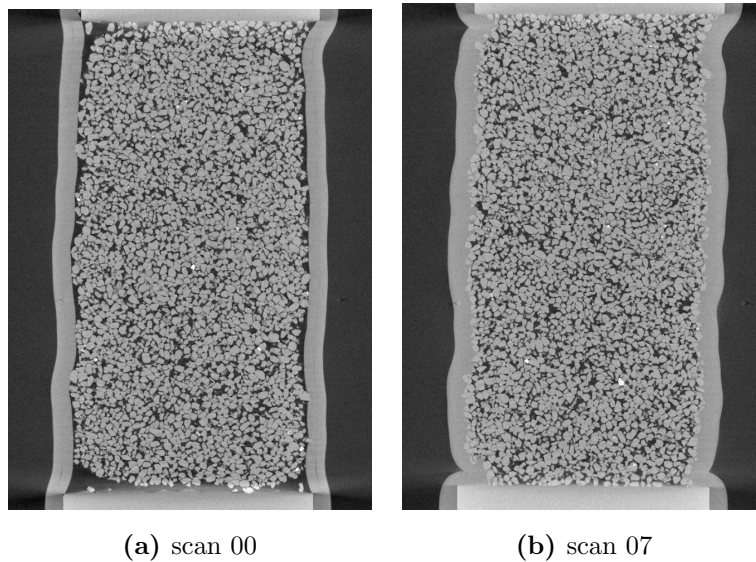


**Figure 6.3:** Vertical 2D sections of the sample X-ray scans (a) before isotropic compression and (b) after applying 7 MPa.

The maximum shear strain map shown in Figure 6.4 shows slightly inclined layers

of higher shear strain, which should correspond to the presence of inclined depositional layers. These layers could not be identified by naked eye and are not even visible in the X-ray images (Fig. 6.3a). The volumetric strain map shows dilation in one of the resolved inclined features at the top of the tested sample. Inclined layers with shear and volumetric strains were resolved only up to very small confining pressures (DVC 00-01, from 0 to 1 MPa), which implies that the potential depositional layers were characterised by very small rotation and sliding up to 1 MPa confining pressure whereas afterwards the whole system started compacting. For higher confining pressures, the sample did not develop any other localised deformation. The full description of the DVC results for this test is reported the Appendix B.1.

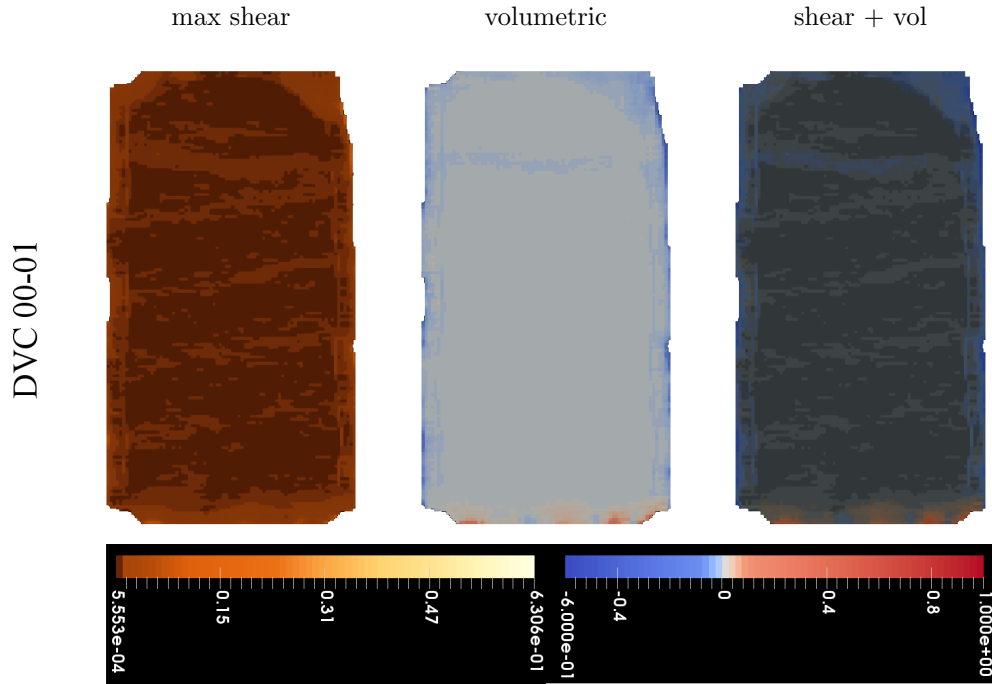


**Figure 6.4:** DVC step 00-01 of the isotropic compression test: after applying 1 MPa confining pressure, the sample developed inclined layers of shear and volumetric strain.

## 6.3 Triaxial compression tests

### 6.3.1 Naturally cemented Bédoin sand containing a region of enhanced porosity

A triaxial compression test was performed on a hand-carved cylindrical naturally cemented sand sample from Bédoin 3, with a length of 22.53 mm, a diameter of 11.03 mm, and a mass of 3.73 g. The sample contained a region with enhanced porosity at its lower part (Fig. 6.5a).

The sample was initially subjected to isotropic compression (confining pressure up to 1 MPa, with flow rate of 0.05 mL/min up to 0.5 MPa, then of 0.01 mL/min)



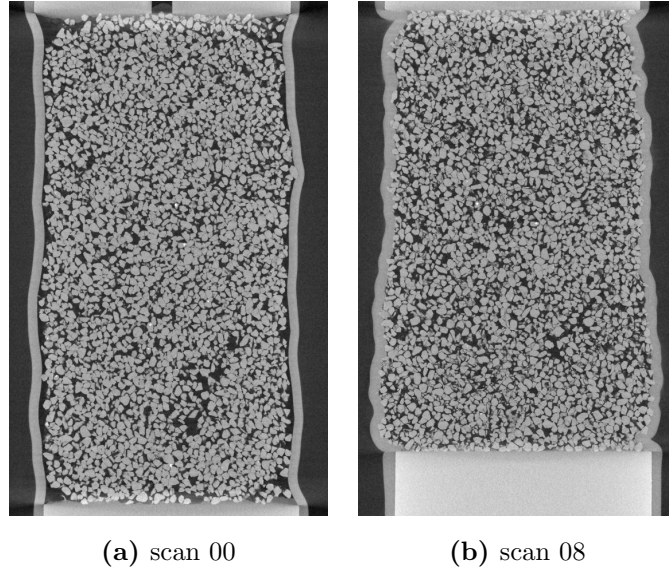


**Figure 6.5:** Vertical 2D slices extracted from X-ray scans acquired (a) before the isotropic compression and (b) after the deviatoric loading.

followed by deviatoric compression (rate of  $20 \mu\text{m}/\text{min}$ ). The test ended at 11% of axial strain and the sample was fully unloaded, with flow rate of  $0.1 \text{ mL}/\text{min}$  and moving down the piston at  $20 \mu\text{m}/\text{min}$  (Fig. 6.6). The sample failed at  $3.8 \text{ MPa}$  deviatoric stress at about 3% of axial strain. A very small decrease in deviatoric stress was observed after the peak stress. The stress drops in Figure 6.6 are due to relaxation; during the X-ray acquisition the displacement of the piston was temporarily halted for about 2 hours. X-ray pre- and post-deformation images (Fig. 6.5) revealed the internal structure of the sample. The post-deformation image shows a redistribution of the porosity, with partial shrinking of the pores in the region of enhanced porosity (further discussion in Sect. 6.5.1).

The shear strain map shows inclined layers (Fig. 6.7), which could be related to the depositional layers similarly to the observation in the sample tested under isotropic compression (Fig. 6.4).

A shear band developed near the region of enhanced porosity identified by the X-rays (Fig. 6.5a), but this does not seem correlated with the shearing along the depositional layers. This possibly implies that the region of increased porosity triggered the formation of a deformation band, while the depositional layers did not. The shear band, which started developing before the peak stress (DVC step 04-05, see in Appendix B.2.1 for the development of the shear bands corresponding to failure time interval), evolved into a network of shear bands. In particular, a dominant zigzag shear band (with dipping angle of  $42^\circ$ ) emerged from the network of bands at the lower part of the sample near the region of enhanced porosity (that is dilating at this stage) at axial strain lower than 6% (DVC 05-06, Fig. 6.8).

Another shear band with inclination of  $55^\circ$  to the horizontal developed along

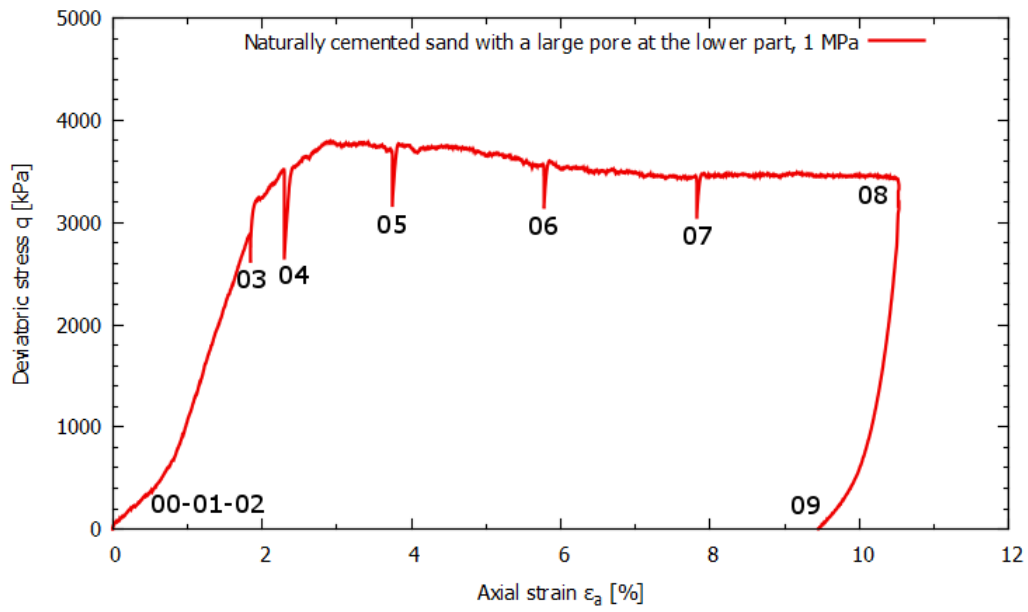


**Figure 6.6:** Stress-strain curve. Numbers 00-09 along the curve refer to X-ray scans acquired during the test and stress drops next to each number represent a relaxation of the loading system when the piston is paused to acquire the X-ray scan.

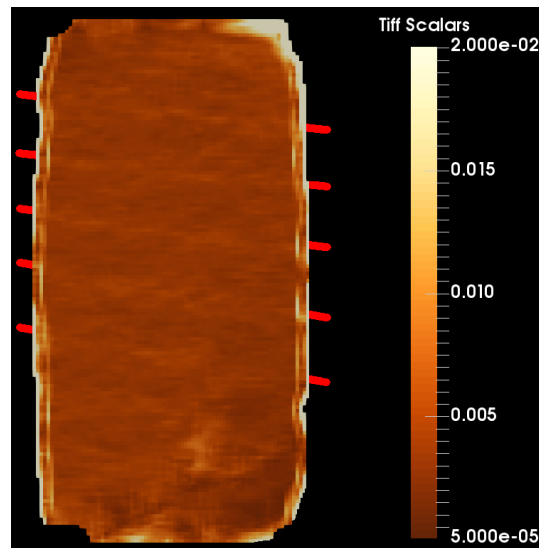


**Figure 6.7:** 2D vertical slice of the max shear strain field (DVC 00-01, confining pressure from 0 to 0.5 MPa) showing inclined layers characterised by higher shear, which can be related to depositional layering.

the sample by the end of the test (DVC 07-08). The band led to a network of bands in the upper part of the sample (3D view at: <https://doi.org/10.6084/m9.figshare.10079156.v2>). All shear bands are characterised primarily by compressive strains; dilation is more pronounced at the lower part of the sample, near the region of enhanced porosity where the first localised deformation occurred. During the unloading, the developed bands accommodated less shear and had a dilatant character, which indicates that although the stress release there were still ongoing processes in the bands (e.g., rotation, sliding, etc). The full description of the DVC results for this test is reported the Appendix B.2.1.

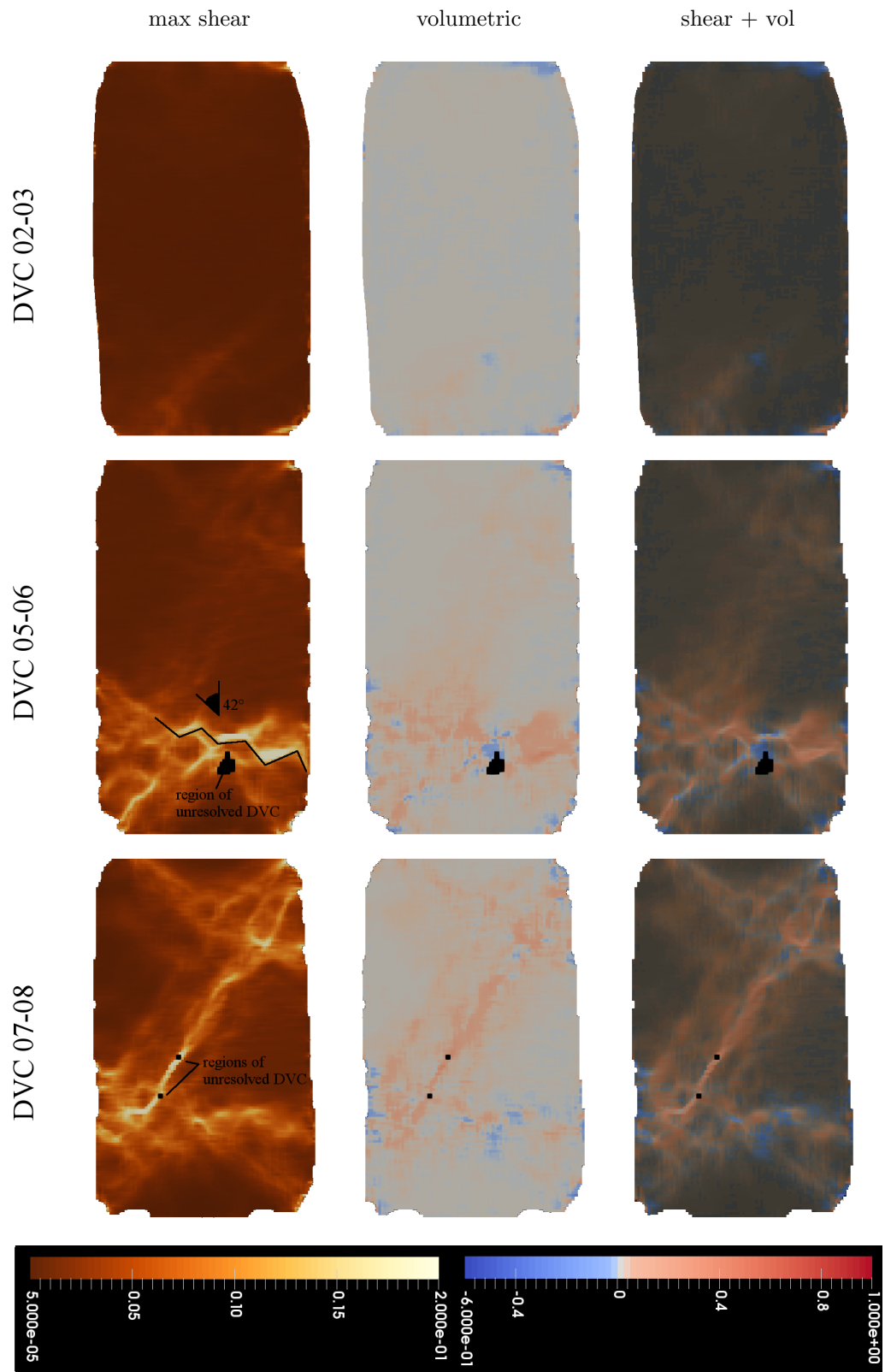


**Figure 6.8:** DVC results of the triaxial compression test on a naturally cemented sample containing a region of enhanced porosity at its lower part.

### 6.3.2 Naturally cemented Bédoin sand containing an elongated pore

A triaxial compression test was performed on a hand-carved cylindrical naturally cemented sand sample from Bédoin 3 with a length of 22.57 mm, a diameter of 11.01 mm, and a mass of 3.81 g. The sample contained an elongated pore ( $l = 5$  mm) in its mid-lower part and the pore was surrounded by clay cement (Fig. 6.9).

The sample was subjected to isotropic compression (confining pressure up to 1 MPa, with flow rate of 0.05 mL/min up to 0.5 MPa, then of 0.01 mL/min) followed by deviatoric compression (rate of  $20 \mu\text{m}/\text{min}$ ). The test ended at 11% of axial strain and the sample was fully unloaded, with flow rate of 0.1 mL/min and moving down the piston at  $20 \mu\text{m}/\text{min}$  (Fig. 6.10). The sample failed at 3.4 MPa of deviatoric stress at about 3% of axial strain (similarly to the previous sample). A very small decrease in deviatoric stress was observed after the peak. The stress drops in Figure 6.10 are due to relaxation, except for the stress drop of 0.4 MPa at  $\epsilon_a = 2.7\%$ . X-ray pre-and post-deformation images in Figure 6.9 show barreling at the upper part of the sample and a redistribution of the pore space, with partial shrinking of the elongated pore in the mid-height of the sample (further discussion in Sect. 6.5.2).

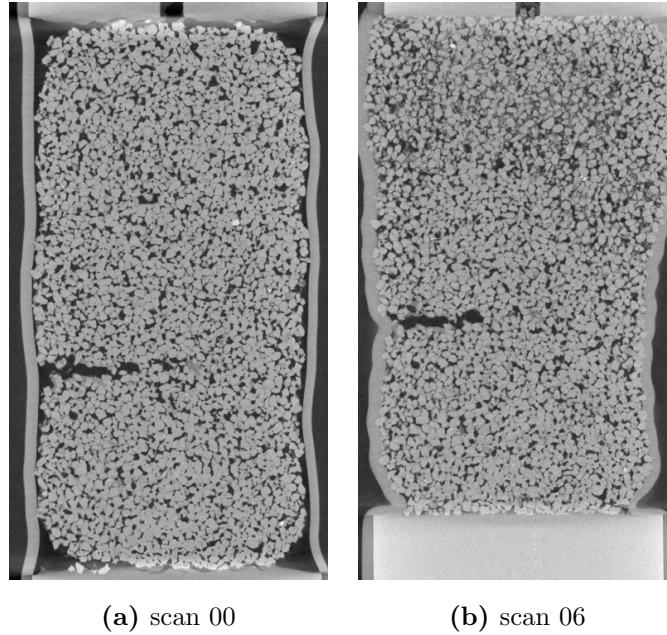


**Figure 6.9:** 2D vertical slices from the X-ray scans acquired (a) before the isotropic compression and (b) after the deviatoric loading, showing that the elongated pore did not collapse by the end of the test. Grain breakage and pore space rearrangement is also observable at the upper part of the sample in (b).

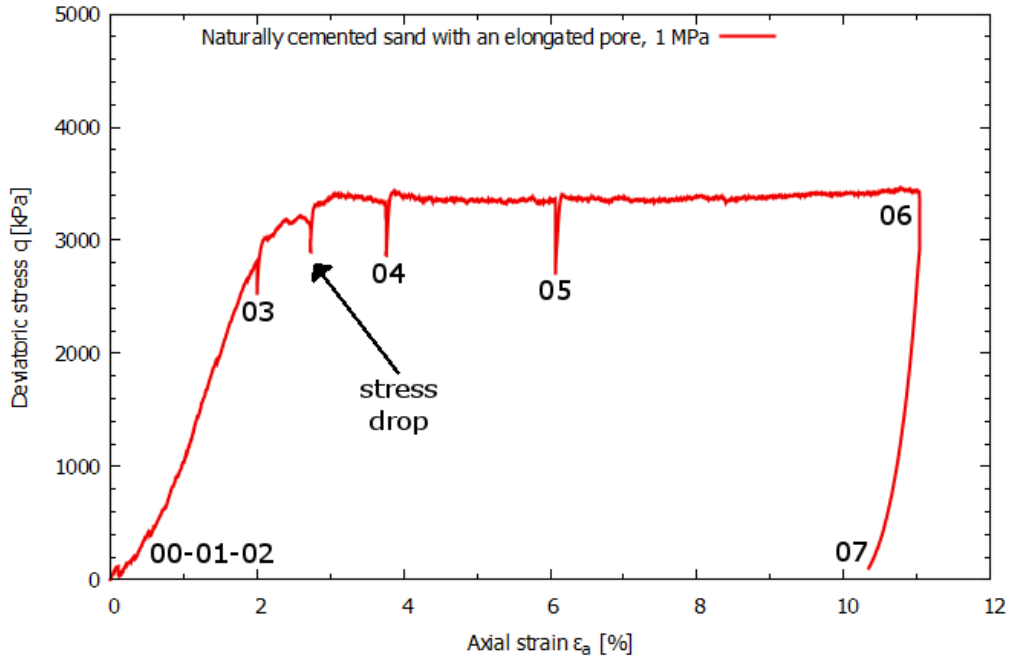


**Figure 6.10:** Stress-strain curve

The sample developed localised deformation with one shear band at the lower and one at the upper parts at  $-56^\circ$  and  $48^\circ$  to the horizontal (negative is clockwise), respectively (Fig. 6.11). The elongated pore showed a minor shear component.

With progressive loading, only the deformation at the upper part of the sample evolved into a dominant shear band composed by parallel shear planes inclined of about  $-48^\circ$  to the horizontal (see a 3D view at <https://doi.org/10.6084/m9.figshare.10081268.v1>). In addition, another shear band transversal ( $56^\circ$  to the horizontal) to the dominant one appeared at the top of the sample. Post deformation X-ray images show grain breakage occurring in the part of the sample where shear bands developed (Fig. 6.9b). All shear bands are characterised primarily by compressive strains; dilation is more pronounced at the lower part of the sample, near the elongated pore. The dominant and following shear bands developed a small shear component with dilatant character during unloading. The elongated pore at this stage showed a great shear component during unloading, yet characterised by dilation (similarly to the region of enhanced porosity in the previous sample during deviatoric loading, Section 6.3.1). The full description of the DVC results for this test is reported the Appendix B.2.2.

The elongated pore seems to not have triggered the localised deformation, differently from the region of enhanced porosity in the previous sample. The clay cement surrounding the elongated pore seems to have acted as reinforcement of the pore, which reported the highest shear strain value during unloading. Furthermore, part of the cement remained unbroken by the end of the test, as evidence of its resistance

under compression at this particular stress state (applied during the experiment).

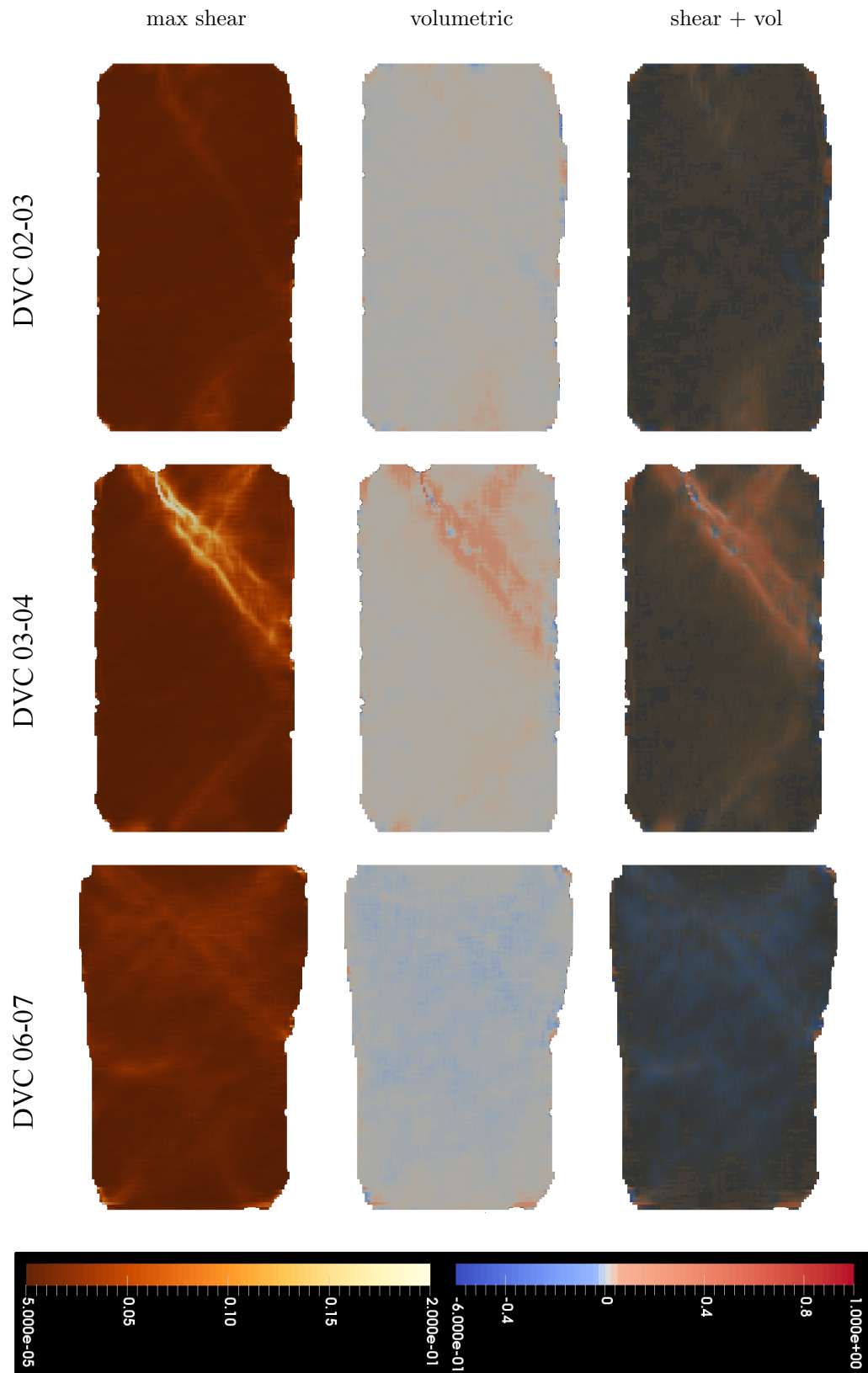


**Figure 6.11:** DVC results of the triaxial compression test on a naturally cemented sample containing an elongated pore

### 6.3.3 Naturally cemented Bédoin sand containing a pre-existing dilation band

Another triaxial compression test was performed on a hand-carved cylindrical naturally cemented sand sample from Bédoin 3 (length of 22.78 mm, a diameter of 11.86 mm, and a mass of 4.61 g) containing a pre-existing dilation band. The dilation band was identified through X-ray radiography and tomography of the sample (Fig. 6.12). The dilation band was inclined of  $32.5^\circ$  to the direction of  $\sigma_3$  (i.e., horizontal) at the beginning of the test (Fig. 6.12b) and it had a thickness of about 0.74 mm corresponding to 2 times the average grain size of Bédoin 3 sand. At the end of the test, the angle is reduced to  $31.5^\circ$  (Fig. 6.12c).

The sample was subjected first to isotropic compression (confining pressure up to 1 MPa, with flow rate of 0.05 mL/min up to 0.5 MPa, then of 0.01 mL/min), then to deviatoric compression (rate of  $20 \mu\text{m}/\text{min}$ ) up to 13% of axial strain rate, followed by unloading with flow rate of 0.1 mL/min and moving down the piston at  $20 \mu\text{m}/\text{min}$  (Fig. 6.13). The sample failed at 4.2 MPa of deviatoric stress at about 3% of axial strain. The deviatoric stress gradually dropped to 3.6 MPa after the peak. The stress drops in Figure 6.13 are due to relaxation. The post-deformation image shows barelling of the sample and a redistribution of the pore space (Fig. 6.12c). However, the dilation band is still visible as it did not collapse under deviatoric compression (further discussion in Sect. 6.5.3), as well as a region of enhanced porosity at the upper-right of the sample.

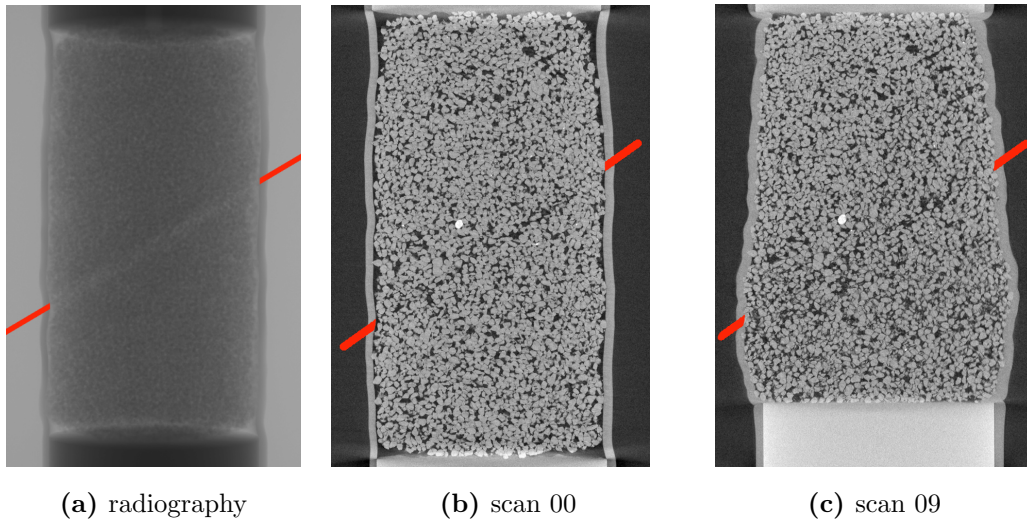


**Figure 6.12:** (a) X-ray radiography of the sample before the isotropic compression, revealing the presence of a dilation band (indicated by red lines). (b) and (c) are 2D vertical slices from the X-ray scans before the confining pressure and at the end of the deviatoric loading, respectively, showing the persistence of the dilation band, despite the deviatoric compression. The band is inclined of  $32.5^\circ$  to the horizontal in (b) and of  $31.5^\circ$  in (c). Note a region of enhanced porosity at the top-right of (b) and (c).



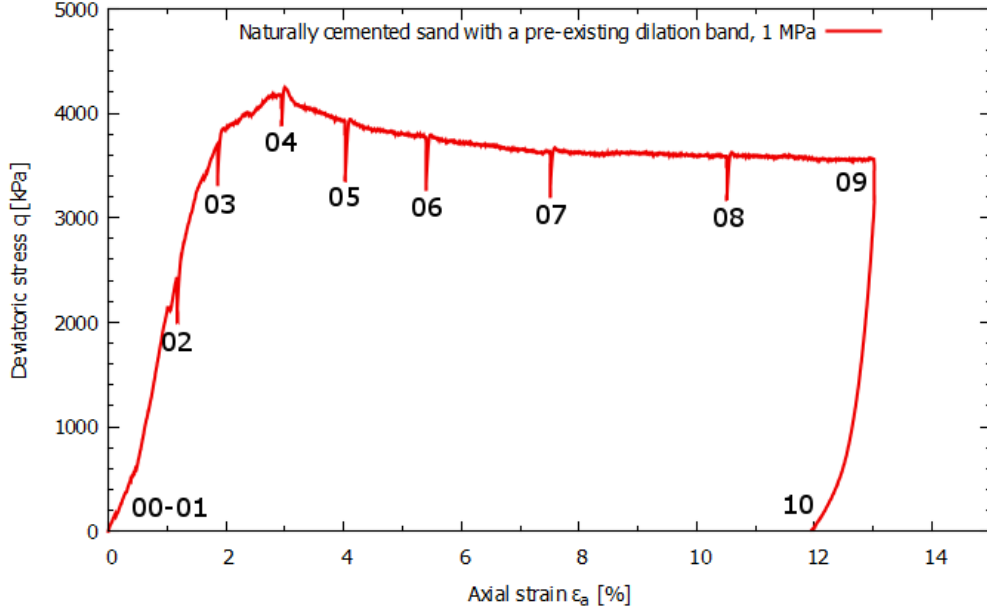


**Figure 6.13:** Stress-strain curve

The dilation band sheared and dilated at the beginning of the deviatoric compression (DVC 01-02, Fig. 6.14), while grain rearrangement was occurring in the rest of the sample, represented by distributed compression and dilation. The dilation band did not react to loading afterwards. The sample developed localised deformation at 3% (DVC 03-04) of axial strain with a zigzag shear band inclined at  $\pm 40^\circ$  to the horizontal at the lower part of the sample.

The shear band evolved into a network of bands at the lower part of the sample, below the location of the dilation band, which did not show further deformation. Shear bands in the network had inclinations of  $-48^\circ$  and  $42^\circ$  to the horizontal and they were characterised by compressive strain, whereas dilation developed near the intersection of shear bands in the region where shear occurred first (DVC 03-04). A single shear band from the network of bands cross-cut the pre-existing dilation band to reach the upper part of the sample, with an inclination of  $64^\circ$  to the horizontal (DVC 07-08, Fig. 6.14). It needs to be underlined that the latter band started to develop since DVC 03-04, where minor shear could be identified diagonally through the sample. Post deformation X-ray images show grain crushing occurring in the lower part of the sample where shear band network developed (Fig. 6.12c). The final shear strain configuration of the sample before performing unloading can be visualised in 3D at the following link: <https://doi.org/10.6084/m9.figshare.10084706.v1>. During unloading, a shear and dilation band developed along the band that connected the network of bands with the upper part of the sample, while no strain is observed along the pre-existing dilation band. The full description of the DVC results for this test is reported the Appendix B.2.3.

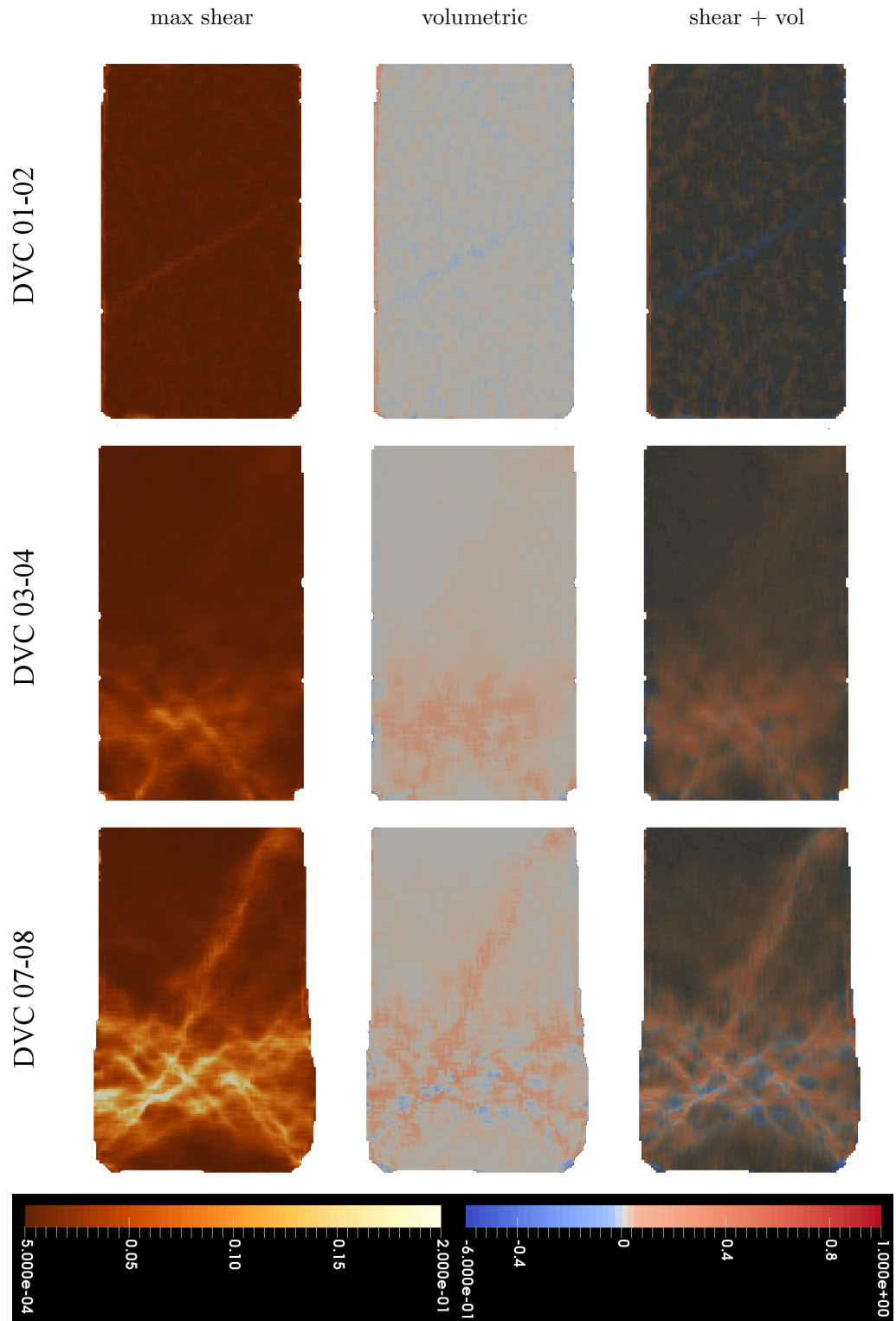


**Figure 6.14:** DVC results of the triaxial compression test on a naturally cemented sample containing a pre-existing dilation band.

The pre-existing band acted as a barrier that confined the network of shear band to the lower part of the sample, similarly to the behaviour of the elongated pore in Section 6.3.2 that divided the sample in two parts and influenced the shear band to localise mainly in one of the two.

The top part was reached by a further shear band arisen from the network of

shear bands and directed to the top of the sample. Interestingly, this shear band seems to have intercepted another region of enhanced porosity located at the top-right side of the sample observed in Figure 6.12. The region of enhanced porosity seems to have attracted the shear band, in a similar way to the region of enhanced porosity in the sample described in Section 6.3.1, which triggered the onset of the shear band.

#### 6.3.4 Artificially cemented Bédoin sand with 20% clay

This triaxial compression test was performed on a cylindrical sample artificially prepared with Bédoin 3 sand and 20% of kaolin clay cement, following the procedure described in Chapter 3. The sample was 21.08 mm long, with a diameter of 10.79 mm and a mass of 3.60 gr. The sample looked slightly denser in the upper part (Fig. 6.15a), due to either cement concentration or to grain packing.

Initially, the sample was subjected to 1 MPa isotropic compression, with flow rate of 0.05 mL/min up to 0.5 MPa, then of 0.01 mL/min. Then, a deviatoric loading was applied with a piston displacement rate of 20  $\mu\text{m}/\text{min}$  until 18% of axial strain. The specimen failed at 4 MPa deviatoric stress at about 9% of axial strain. The overall mechanical behaviour of the sample represented by the stress-strain curve of Figure 6.16 describes a material that is not as densely packed as the natural ones, which have displayed a clear peak stress.

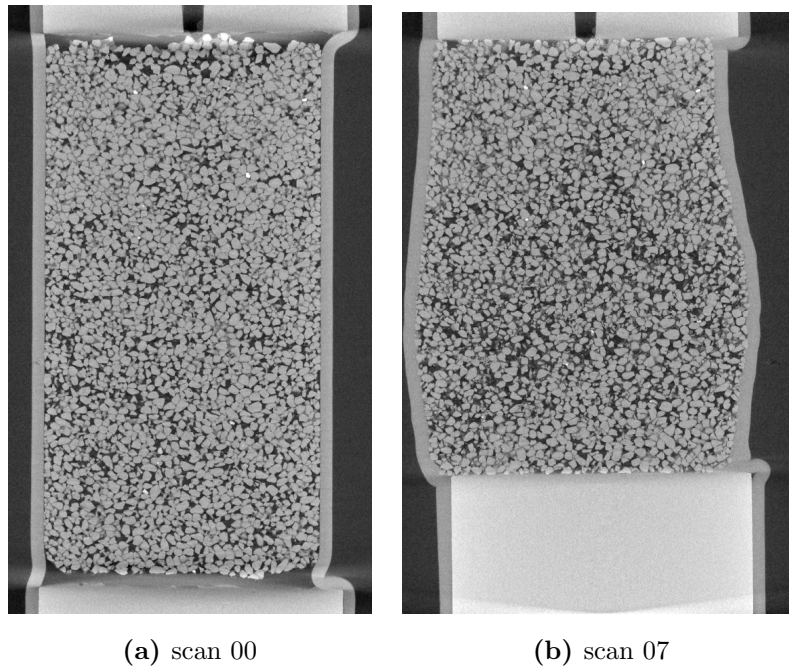


**Figure 6.15:** 2D vertical slices from the X-ray scan of the sample (a) before the isotropic compression and (b) after the deviatoric loading, showing details of the deformation: grain breakage, pore redistribution, and barrelling final configuration.

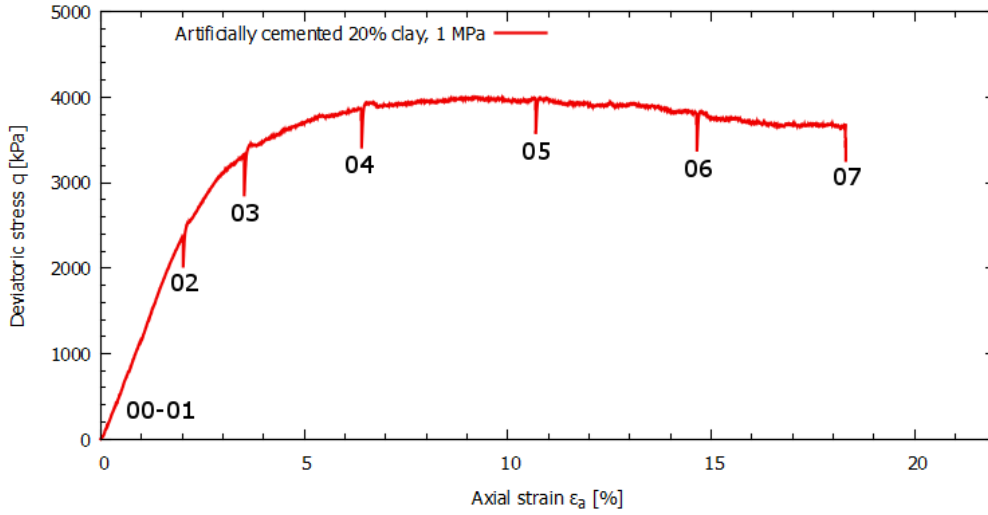


**Figure 6.16:** Stress-strain curve

Thin layers characterised by shear strain emerged during isotropic compression (DVC 00-01, Fig. 6.17), which could be connected with the dry sand pluviation during the artificial cementation procedure. This resembles to the inclined layers that were resolved during the isotropic compression in two of the natural samples, and were related to the existence of depositional layers. Differently from the sharper imperfections in the naturally cemented samples (i.e., small regions of enhanced porosity, elongated pore, dilation band), the more homogeneous artificial sample developed a network of shear bands distributed in the entire volume with inclination of  $-50^\circ$  and  $54^\circ$  to the horizontal (DVC 03-04 in Fig. 6.17 and 3D view available here: <https://doi.org/10.6084/m9.figshare.10084748.v2>). Shear strain (and bands) were more concentrated in the lower part, where a lower density of the sample was observed (Fig. 6.15a), but also where the piston was pushing the sample. The resolved shear bands are mainly characterised by compaction, and dilation is observed very locally only in some regions. The full description of the DVC results is reported in Appendix B.2.4.

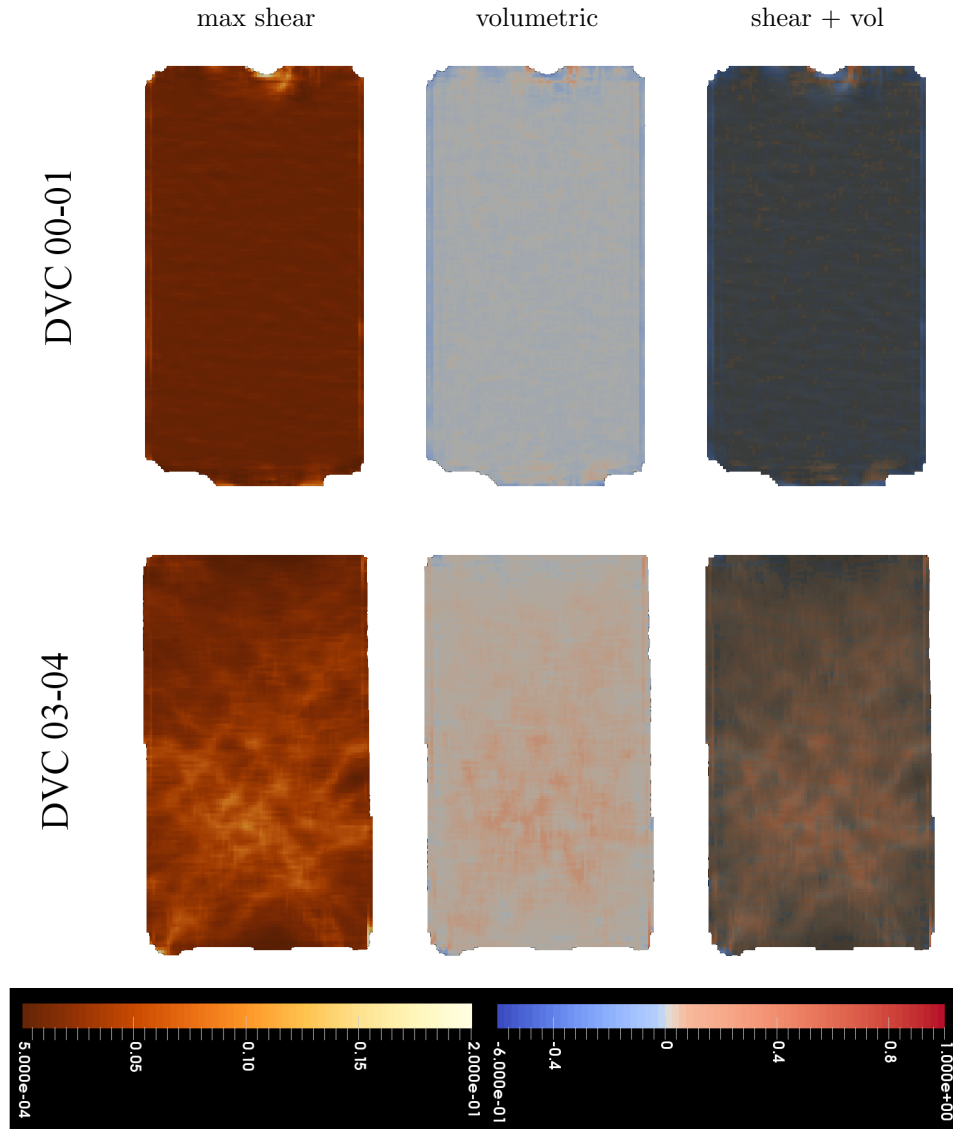


**Figure 6.17:** DVC results of the triaxial compression test on an artificially cemented sample with 20% of clay.

### 6.3.5 Artificially cemented Bédoin sand with 15% clay

Another triaxial compression test was performed on an artificially cemented sample composed by Bédoin 3 sand cemented with 15% of kaolin clay (length of 21.95 mm, a diameter of 10.85 mm, and a mass of 3.81 g). The X-ray image of the sample shows cement homogeneously distributed around the sand grains (Fig. 6.18a).

The sample was subjected first to isotropic compression (confining pressure up to 1 MPa, with flow rate of 0.05 mL/min up to 0.5 MPa, then of 0.01 mL/min), then to deviatoric compression with a piston displacement rate of 20  $\mu\text{m}/\text{min}$  up to 20% of axial strain. No unloading was performed in this test. The sample failed at a deviatoric stress of 3.6 MPa at about 8% of axial strain (Fig. 6.19). The sample did not show a peak, as seen in the naturally cemented samples, hence the deviatoric peak stress becomes the residual stress value. The post-deformation image shows

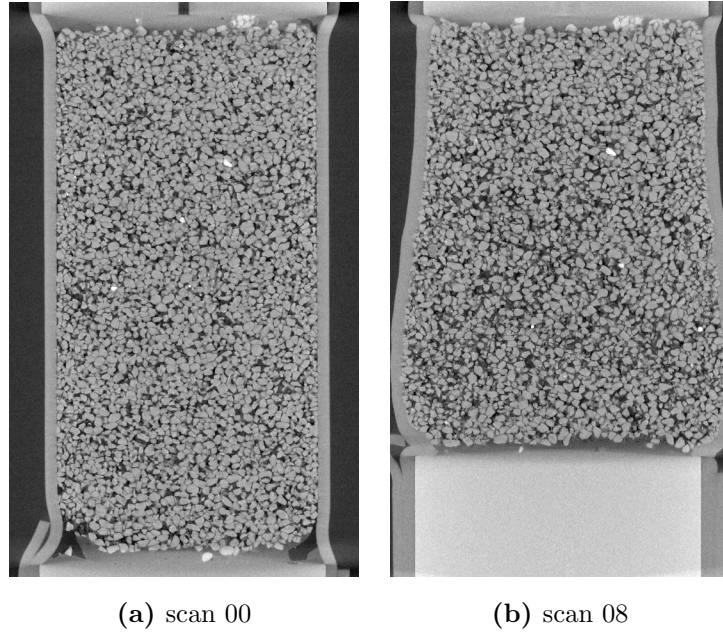


**Figure 6.18:** 2D vertical slices extracted from the X-ray scans acquired (a) before the isotropic compression and (b) after the deviatoric loading, showing the initial homogeneous cement distribution and the final deformation of the sample: grain breakage, new pore distribution, and barrelling configuration.

barrelling of the sample and a redistribution of the pore space (Fig. 6.18b).

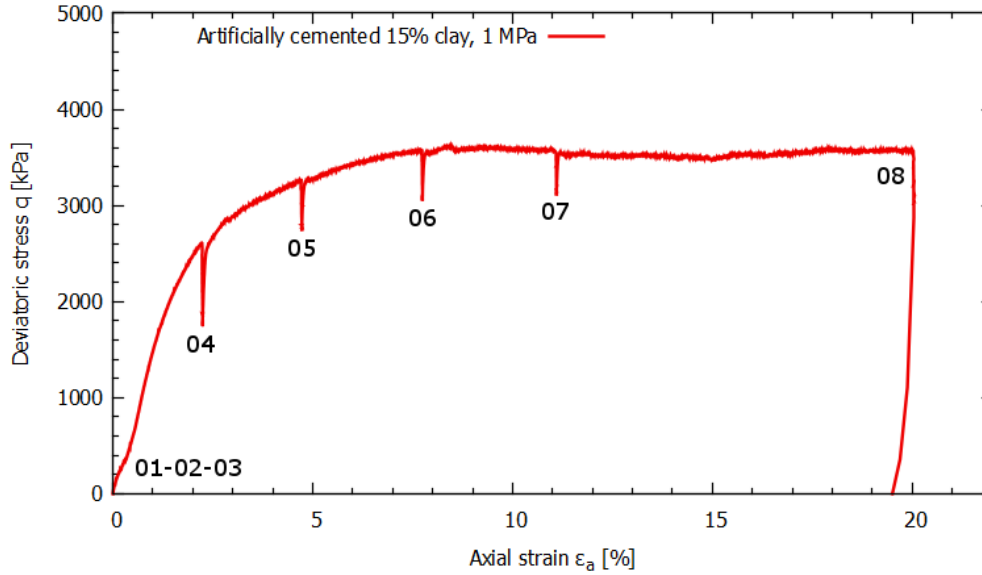


**Figure 6.19:** Stress-strain curve

Thin shearing layers emerged during isotropic compression (DVC 01-02, Fig. 6.20), similarly to the artificially cemented sample with 20% of clay content described in Section 6.3.4. The artificially cemented sample was affected by shear in the entire volume (DVC 04-05) and a network of shear bands developed at the lower part with inclination about  $\pm 50^\circ$  to the horizontal and characterised by compressive strain,

whereas dilation developed in the region that first developed shear (DVC 04-05), nearby the intersections between the shear bands (DVC 06-07, 3D view available here: <https://doi.org/10.6084/m9.figshare.10084742.v1>). The DVC results for this test are described in detail in Appendix B.2.5.

One of the shear bands started to extend towards the upper-right side of the sample, which reminds the shear band that reached the sample top end in the natural sample containing a pre-existing dilation band (DVC 07-08 in Fig. 6.14). Shear was reported slightly more concentrated in the lower part, as it occurred to the sample with 20% of clay.

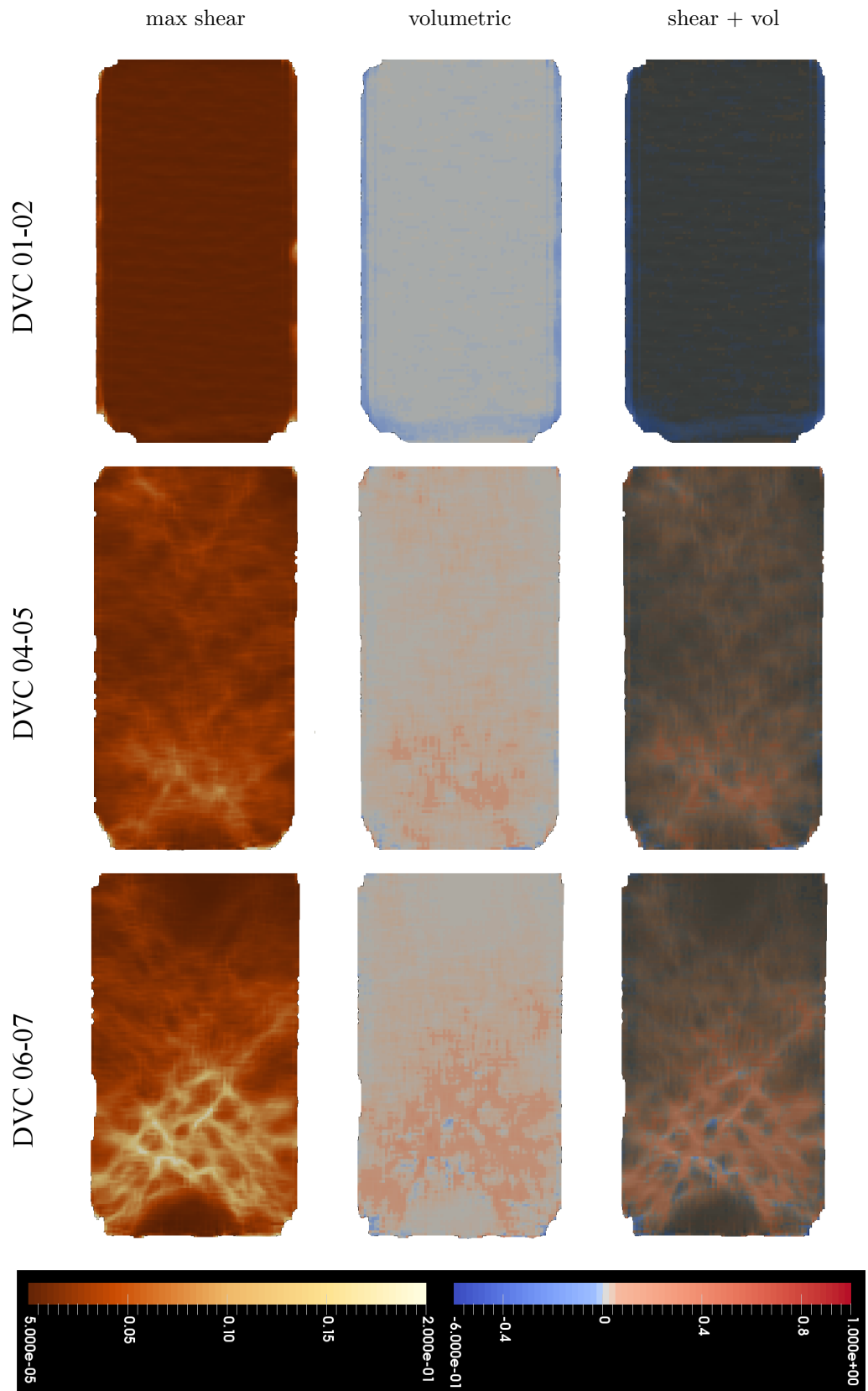


**Figure 6.20:** DVC results of the triaxial compression test on an artificially cemented sample with 15% clay.



### 6.3.6 Uncemented Bédoin sand

A last triaxial test was performed on uncemented Bédoin 3 sand. Sand grains were cleaned with the procedure described in Section 3.2.3 and poured through a funnel (the same as in Fig. 3.9) into a neoprene membrane sealed around ceramic platens at the two ends and stretched to create a cylindrical sample (see membrane stretcher in Fig. 3.6 in Andò (2013)). The sample had a weight of 2.96 g and reported the following dimensions:  $h = 23.39$  mm and  $d = 9.88$  mm. The X-ray image of the sample in Figure 6.21a shows a rather homogeneous sand grain packing within the sample.

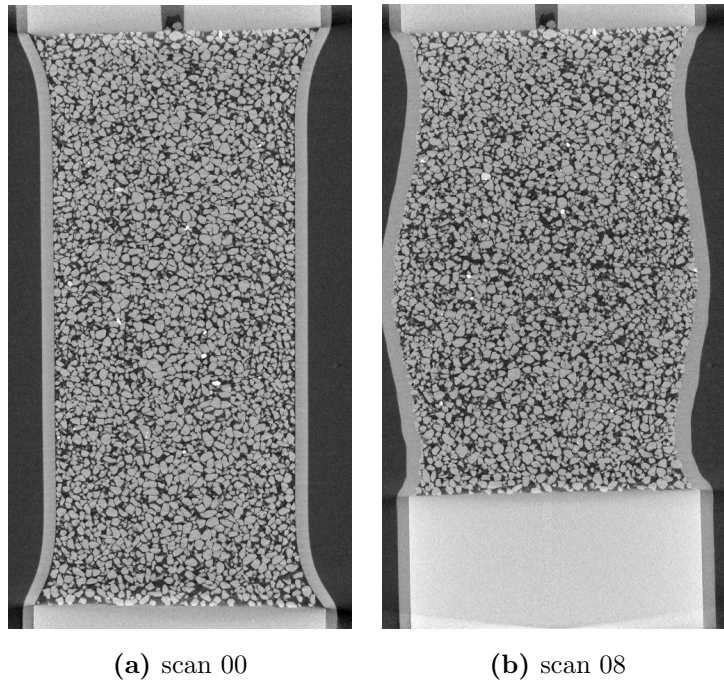


**Figure 6.21:** 2D vertical slices extracted from the X-ray (a) before isotropic compression and (b) after deviatoric loading, showing the maximum shortening of the sample reached during the test, which provoked grain fragmentation, porosity variation, and a barrelling shape of the sample.

The sample was subjected initially to isotropic compression (confining pressure up to 1 MPa, with flow rate of 0.05 mL/min up to 0.5 MPa, then of 0.01 mL/min). Then, deviatoric compression was applied with a piston displacement rate of 20  $\mu\text{m}/\text{min}$  up to 19% of axial strain, followed by full unloading (flow rate of 0.1 mL/min and piston speed of 20  $\mu\text{m}/\text{min}$ ). The sample failed at a deviatoric stress of 3 MPa at about 13% of axial strain (Fig. 6.22). A stress drop of about 0.3 MPa was observed at  $\epsilon_a = 11\%$ . A similar instability occurred to the natural sample with elongated pore (Fig. 6.10) and less evidently in the natural sample with pre-existing dilation band (Fig. 6.13) at the same phase of the test, i.e., right before reaching the highest deviatoric stress value. The sample did not show a peak, but it deformed

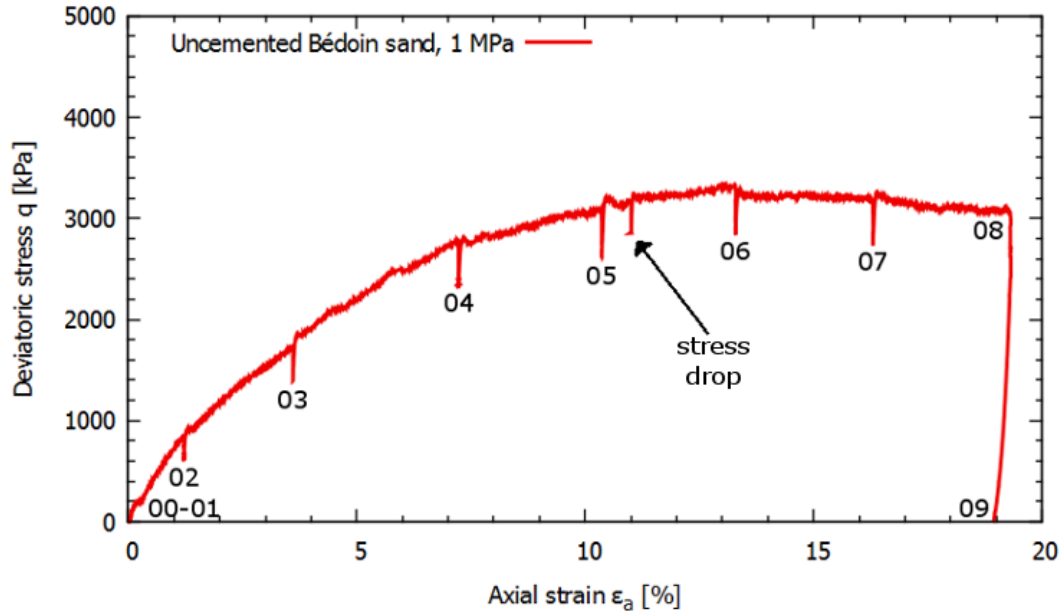


**Figure 6.22:** Stress-strain curve

under strain hardening, which is a typical behaviour of a low-dense material (Nova, 2012). The post-deformation image shows barrelling of the sample, grain breakage, and a redistribution of the pore space (Fig. 6.21b).

During the isotropic compression, the sample did not develop thin shear layers as occurred in the artificially cemented samples or inclined shear features as observed in the naturally cemented samples. The sample sheared in a region at the mid-top part (DVC 00-01, Fig. 6.23). With the deviatoric loading, small bands sheared initially in all the sample far from the sample ends (DVC 02-03); then, shear and compression localised at the centre, where a dominant shear band emerged from a network of bands, with an average inclination of  $35^\circ$  to the horizontal (DVC 05-06). Dilation occurred at the intersection between the dominant shear band and other bands. The network of bands evolved into conjugate shear bands by the end of the deviatoric loading (DVC 07-08), where compression developed along the bands and dilation in parts of bands or around them (DVC 07-08 in Fig. 6.23 and 3D view available here: <https://doi.org/10.6084/m9.figshare.10084796.v1>). In fact, the two bands seemed composed by many sub-parallel shear bands with an average inclination of  $\pm 35^\circ$ . Unloading is dominated by dilation, as for all the other samples, with grain rearrangement that created two shear bands (DVC 08-09). A complete description of the DVC results for this test is reported in Appendix B.2.6.

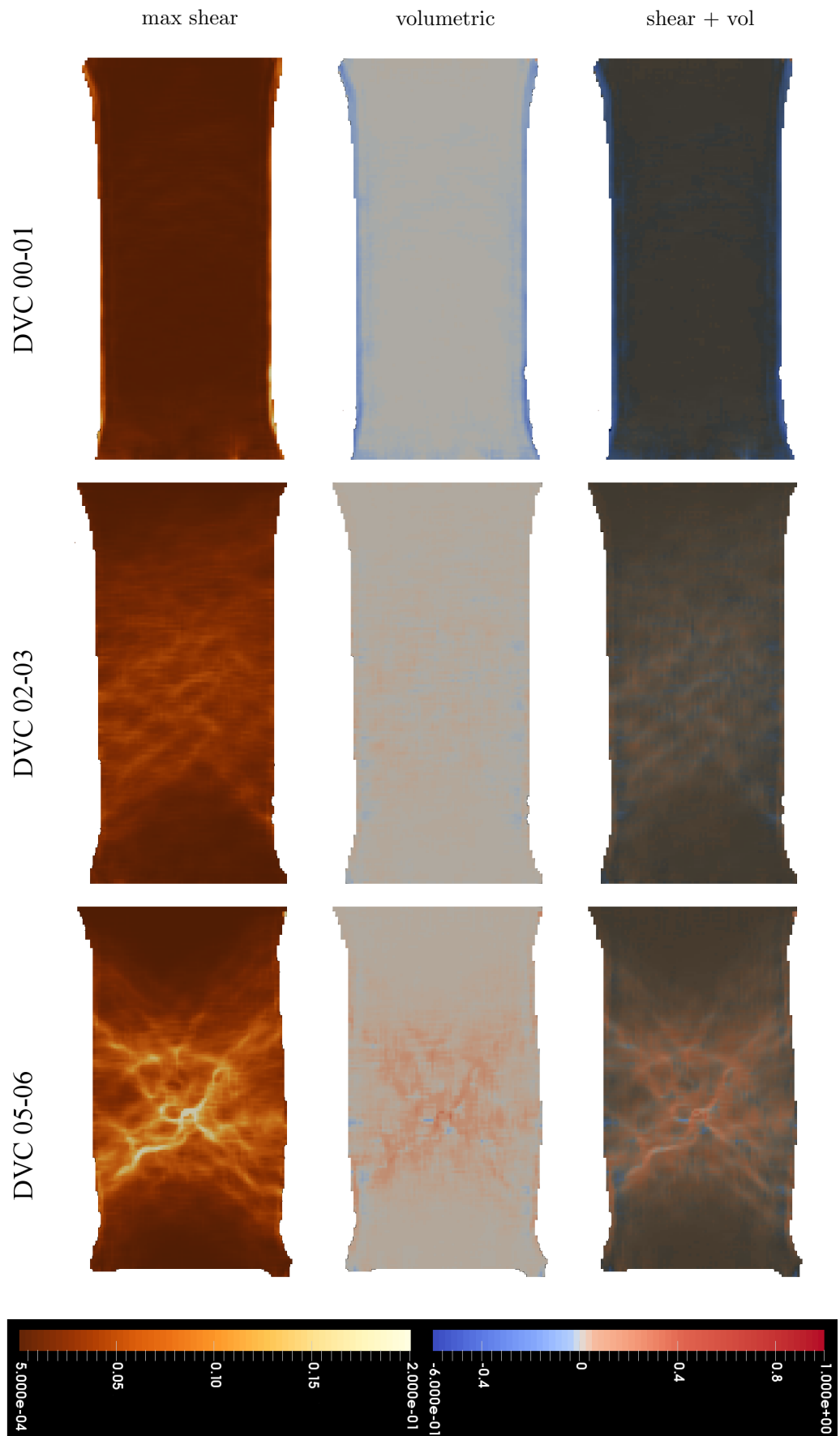


**Figure 6.23a:** DVC results of the triaxial compression test on an uncemented Bédoine sand sample.

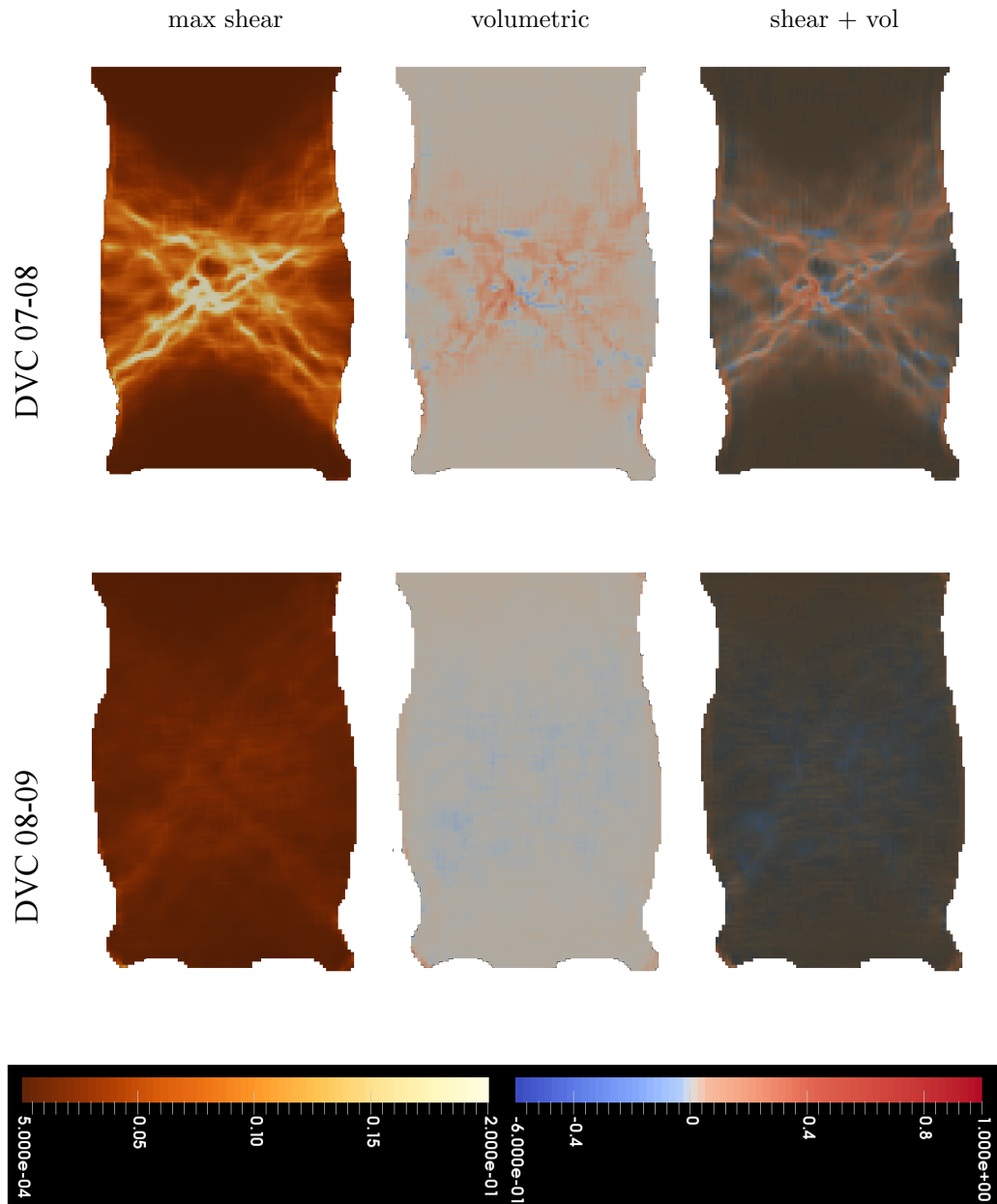


Figure 6.23b

## 6.4 Discussion

### 6.4.1 Introduction

A preliminary overview of the mechanical tests (Fig. 6.24) shows that in all samples the onset of strain localisation and the development of the first dominant shear band occurred before or at the peak stress. This is in agreement with several experimental findings on sands under triaxial compression (Desrues and Viggiani, 2004; Hall et al., 2010; Andò et al., 2012; Takano et al., 2015). However, Figure 6.24 points out the different timing of localised deformation in naturally and in artificially prepared samples: naturally cemented samples reached the peak stress faster than the arti-

ficially cemented and uncemented ones. The behaviour of the three sample types - naturally cemented, artificially cemented and uncemented - is discussed and compared in the following sections, supported by Tables 6.1, 6.2, and 6.3 that describe the samples and their deformation. In particular, the samples share similar values of bulk density, they reached a maximum deviatoric stress in the range 3.3 - 4.2 MPa, reporting shear bands inclined between 35° and 64° to the horizontal.

**Table 6.1:** Sample names and descriptions of the tests run in this doctoral work

sample name	test description
NatIso	isotropic compression of naturally cemented sample (Sect. 6.2.1)
Nat	triaxial compression of naturally cemented sample containing a region of enhanced porosity (Sect.6.3.1)
NatPore	triaxial compression of naturally cemented sample containing an elongated pore (Sect. 6.3.2)
NatDB	triaxial compression of naturally cemented sample containing a pre-existing dilation band (Sect. 6.3.3)
Artif20	triaxial compression of an artificially cemented sample with 20% clay (Sect. 6.3.4)
Artif15	triaxial compression of an artificially cemented sample with 15% clay (Sect. 6.3.5)
Uncement	triaxial compression of an uncemented Bédoin 3 sand sample (Sect. 6.3.6)

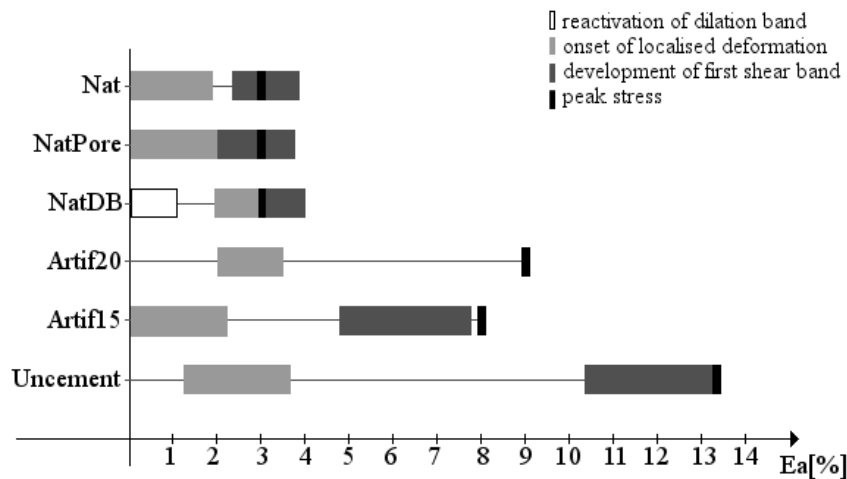


**Figure 6.24:** Overview of triaxial test results by combining DVC observations with peak stress values from the stress-strain curves: the range of values reported in the plot corresponds to the DVC step where each of the processes was identified.

**Table 6.2:** Summary of the triaxial compression tests. Band angle is measured to the direction of the minor principal stress  $\sigma_3$  (i.e., horizontal). Band distribution is referred to the final configuration. Signs of the angles are reported to simplify the angles identification in the 2D slices from the strain field maps, and a positive angle orientation is measured anticlockwise to the horizontal. For samples details, refer to Table 6.1.

sample name	$q_{peak}$ [MPa]	band distribution and loca- tion in the sample	band angle [°]
Nat	3.8	two sub-parallel bands at lower and upper parts, third band from lower to upper sample ends $\perp$ the other two bands	$42, -35^\circ, 55^\circ$
NatPore	3.4	dominant band at the top of sample, other two band subp-arallel, one at top end, the other at lower end	$-48^\circ, 56^\circ, 48^\circ$
NatDB	4.2	network of bands at lower part with two sub-conjugate inclinations, third band from lower to upper part	$-48^\circ, 42^\circ, 64^\circ$
Artif20	4	network of bands at lower part with two sub-conjugate inclinations	$-50^\circ, 54^\circ$
Artif15	3.6	network of bands at lower part with conjugate inclinations	$\pm 50^\circ$
Uncement	3.3	two conjugate bands at centre	$35^\circ, -37^\circ$

**Table 6.3:** Samples dimensions and bulk density (sample details in Table 6.1). Note that the bulk density values were calculated on perfect cylinders generated with the samples average measures of h and d (the real samples are irregular cylinders).

sample name	weight w [g]	height h [mm]	diameter d [mm]	bulk density $\gamma$ [g/mm <sup>3</sup> ]
NatIso	3.78	22.24	11.00	$1.79 \cdot 10^{-3}$
Nat	3.73	22.53	11.03	$1.73 \cdot 10^{-3}$
NatPore	3.81	22.57	11.01	$1.77 \cdot 10^{-3}$
NatDB	4.61	22.78	11.86	$1.83 \cdot 10^{-3}$
Artif20	3.60	21.08	10.79	$1.87 \cdot 10^{-3}$
Artif15	3.81	21.95	10.85	$1.88 \cdot 10^{-3}$
Uncement	2.96	23.39	9.88	$1.65 \cdot 10^{-3}$

#### 6.4.2 Assessing the mechanical response of the naturally cemented samples

The results of mechanical tests performed on naturally cemented samples from Bédoin 3 indicate that some of the imperfections, which occurred in the natural material either due to deposition or due to deformation processes, have affected the occurrence of laboratory-induced localised deformation. This was assessed based on the shear and volumetric strain maps that visualised the laboratory-induced deformation bands developed in the samples. Note that the observations are restricted by what takes place between two consecutive scans, i.e., the processes were not monitored continuously but rather in consecutive time steps. In particular, inclined depositional layers within the natural weakly cemented samples (Fig. 6.4 and 6.7), which accommodated mainly shear strain during the isotropic compression (up to 1 MPa), have not affected the onset of localised deformation during the deviatoric loading. The region of enhanced porosity in Figure 6.5a seems to have affected the onset of localised deformation, since the latter developed in the region around it (DVC 02-03 in Fig. 6.8). Conversely, the elongated pore (Fig. 6.9) did not appear to trigger the onset and evolution of localised deformation near by, since the latter developed in the top part of the sample. However, note that the elongated pore was surrounded by clay cement that seems to have supported the pore. The pre-existing dilation band (Fig. 6.12) acted in a similar way to the elongated pore, i.e., it did not further affect the onset and evolution of laboratory induced deformation; the dilation band itself accommodated some shear and dilation up to less than 2% of axial strain, then the band remained inactive. The dilation band split the sample in two parts and it seems to have confined the onset of localised deformation only

in the lower part, with a single shear band reaching the upper part of the sample at a later stage of the deformation.

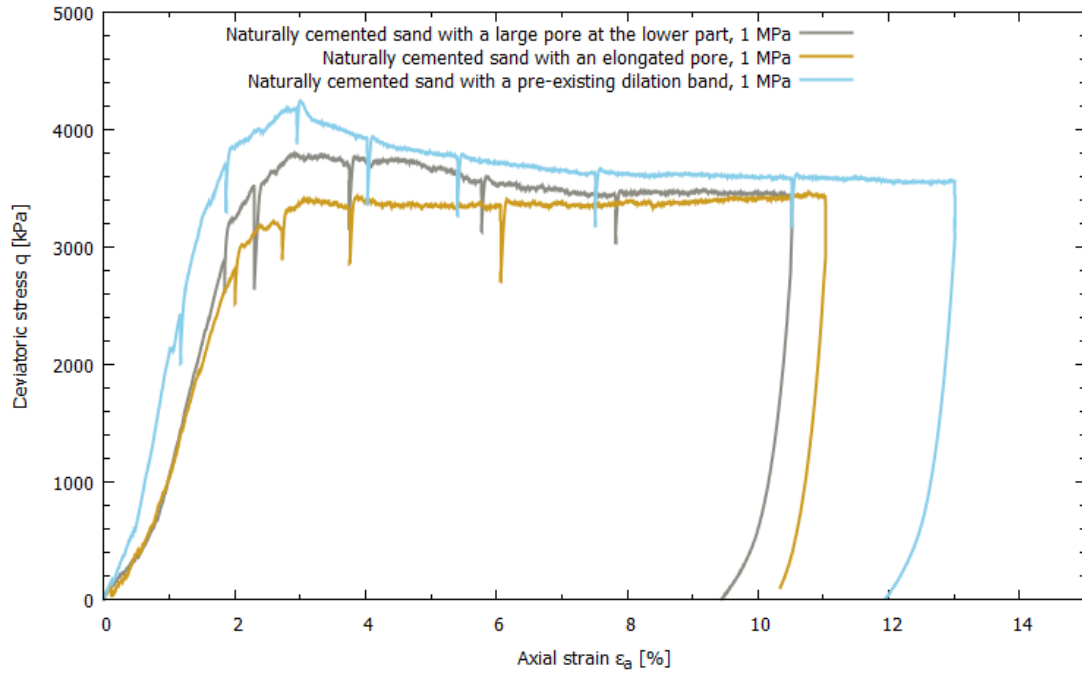


**Figure 6.25:** Stress-strain curves of the natural samples

In terms of mechanical resistance, the stress-strain curves of the three natural samples (Fig. 6.25) show differences in the initial conditions, followed by a similar value at residual state. In particular, the sample containing a pre-existing dilation band showed a strain softening behaviour, whereas the other two samples showed less or no softening. In detail, the sample with pre-existing dilation band reported the highest stiffness (stiffness or Young's modulus  $E$  is represented by the inclination of the stress-strain curve, since  $E = \Delta\sigma_{ax}/\Delta\epsilon_{ax}$ ). The high stiffness suggests that the pre-existing dilation band in the sample's volume may have strengthened the material. The peak stress value is reached at  $\epsilon_a = 3\%$  for the three samples (Fig. 6.25), thus showing the consistency of the material properties despite the presence of local imperfections (i.e., depositional layers, region of enhanced porosity, elongated pore, pre-existing dilation band). Figure 6.25 shows that the sample with the pre-existing dilation band reached the highest deviatoric stress (see values in Table 6.2). The sample containing an elongated pore failed with the lowest peak stress value, despite its bulk density is not the lowest one among the three samples (Table 6.3). The role of the imperfections in the strain localisation is further discussed in Section 6.5. The three samples reach a similar value of the residual stress at the end of the test (Fig. 6.25), being this value slightly higher for the sample with the pre-existing dilation band (3.6 MPa) than for the other two samples (3.4 MPa).

The DVC results in Figure 6.26 show that localised deformation in the three



naturally cemented samples occurred as a narrow shear plane, which developed mainly compressive volumetric strains. As the deformation evolved, these shear bands became part of a network of bands, with exception for the sample with the elongated pore, where a set of primary shear bands in conjugate directions developed. The three samples share similar band patterns within the tested strain range (tests stopped from 10% to 13% axial strain) and they are summarised in Table 6.2: dominant shear bands at upper and/or lower part of the samples and a later shear band that connects lower with upper part. The sample with the elongated pore did not develop a band from lower to upper part; however, when the dominant band at the top reached the top-right side of the sample, another shear band developed at the sample lower end. During the unloading of the three samples, smaller shear components and higher dilatant volumetric strains were resolved along the laboratory-induced deformation bands. This indicates that local stress distribution during unloading led to potential grain rotation and sliding. However, shearing accompanied by grain crushing (compaction) was documented in Charalampidou et al. (2014a) during the unloading of sandstone samples that developed shear-enhanced compaction bands.

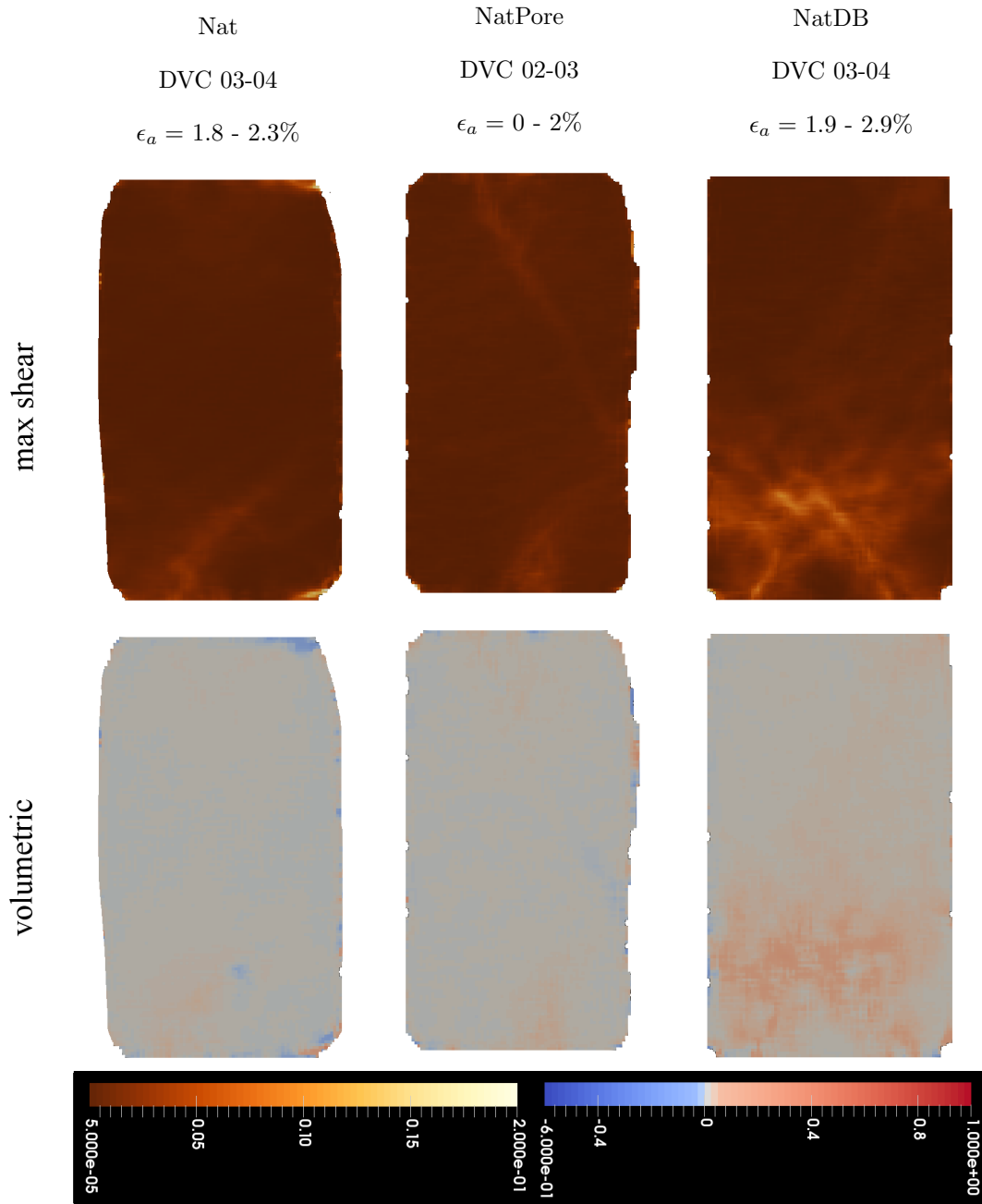


**Figure 6.26:** Comparison of naturally cemented samples at the onset of localised deformation (sample details in Table 6.1)

### 6.4.3 Assessing the mechanical response of the artificially cemented and uncemented samples

A comparison between the mechanical response of the uncemented and artificially cemented samples shows that the uncemented sample had a much smaller stiffness than the artificially cemented ones since the beginning of the deviatoric loading (Fig. 6.27). This behaviour is typical of low-dense sands (Nova, 2012), as it is the case for this uncemented sand sample, which reported the lowest bulk density (Table 6.3). The peak stress is reached much later in the uncemented sample with respect to

the artificially cemented ones. The artificially cemented sample with 20% of clay cement reached the highest peak stress value among the three samples (Fig. 6.27), thus showing that the higher clay content increased its resistance. At the end of the tests, the two cemented samples reached a similar value of 3.6 MPa. This suggests that the two samples had a similar resistance once they overcame the resistance provided by the cement, as expected. The residual stress for the uncemented sand sample is lower than the other two samples (Fig. 6.27), proportionally to its bulk density.

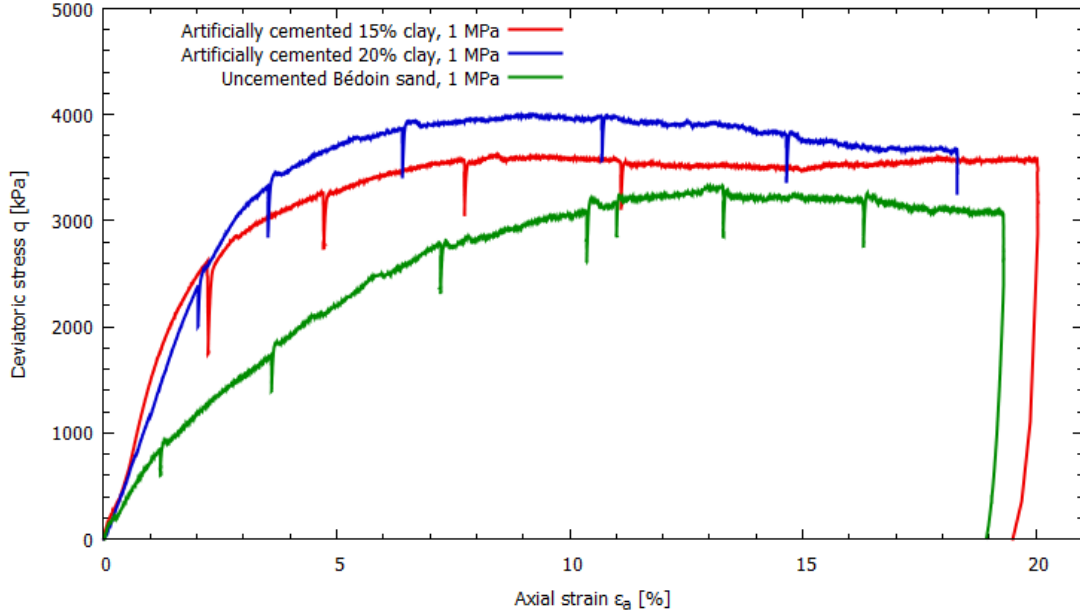
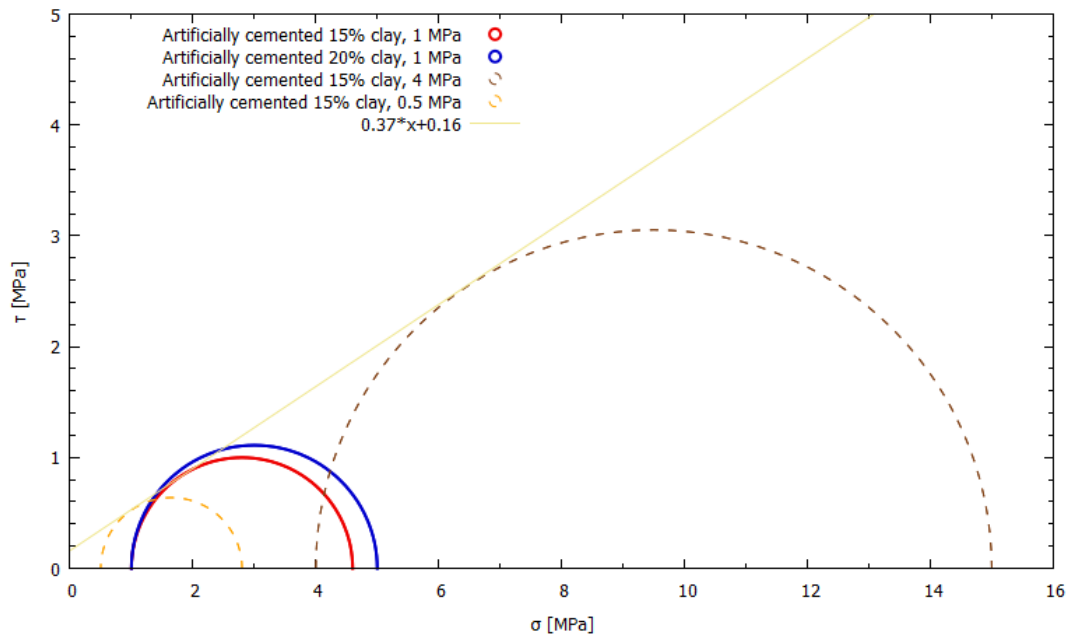


**Figure 6.27:** Stress-strain curves of uncemented and artificially cemented samples

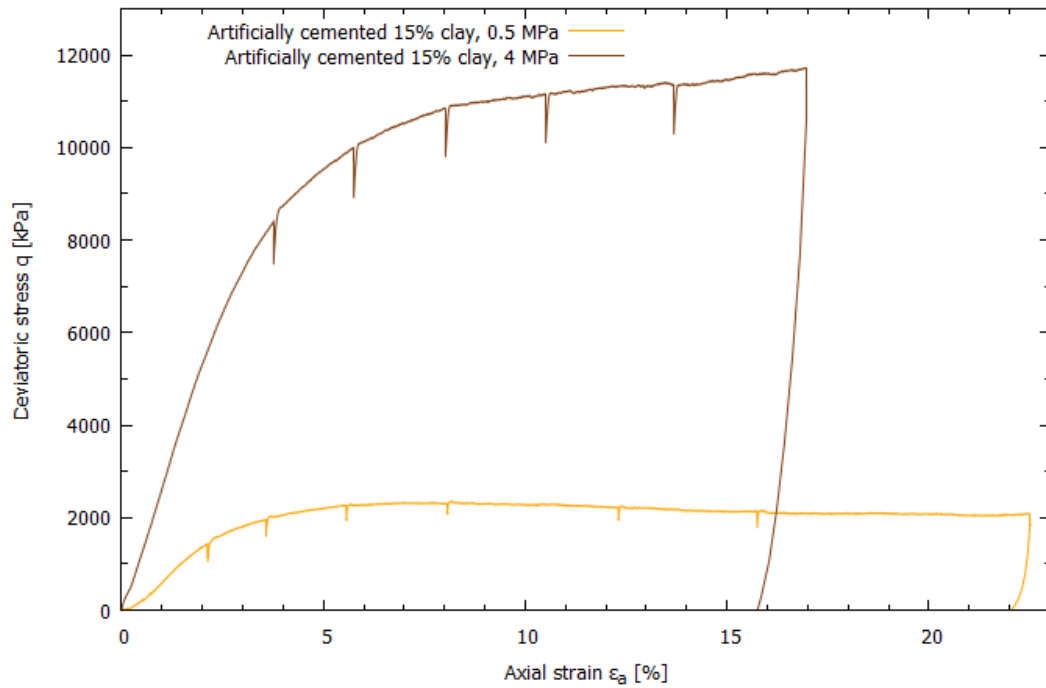
The Mohr-Coulomb failure envelope was obtained from three circles that describe mechanical behaviour of three artificially cemented samples containing 15% of clay cement and tested with triaxial compression at a confining pressure of 0.5 MPa, 1 MPa, and 4 MPa (Fig. 6.28a). The test on the sample with confining pressure of 1 MPa was analysed with DVC in this doctoral work (Sect. 6.3.5), whereas for the other two tests only the stress-strain curves are shown in Figure 6.28b. The failure envelope in Mohr's plane is tangent to the three circles, which suggests that the material constituting the three artificial samples is similar, thus confirming the repeatability of the cementation procedure.

The resultant inclination  $\phi_p$  of the Mohr-Coulomb failure envelope at the peak stress ( $p$ ) is  $\phi_p = 33.7^\circ$  (obtained from Fig. 6.28a) and Coulomb's solution that describes the theoretical inclination  $\theta_C$  of the shear band to the minor principal axis (Nova, 2012):

$$\theta_C = 45^\circ + \frac{\phi_p}{2} \quad (6.1)$$



(a) Mohr's circles



(b) stress-strain curves

**Figure 6.28:** (a) Mohr's circles of tests on artificially cemented samples shown in Fig. 6.27 and in (b), with failure envelope inclined of  $33.7^\circ$  tangent to three circles (red, brown, and orange) that represent three triaxial tests run on the three samples containing 15% of clay and confined at pressures of 0.5, 1, and 4 MPa; (b) stress-strain curves of the artificially cemented samples containing 15% of clay cement and confined with 0.5 MPa and 4 MPa (not analysed in this work).

provided a value of  $\theta_C = 61.85^\circ$ .  $\theta_C$  was used in the following equations from Mohr's circle to determine the cohesion  $c$  of the sample, knowing the relation 6.4:

$$\sigma_p = \frac{\sigma_1 + \sigma_3}{2} + \frac{\sigma_1 - \sigma_3}{2} \cos 2\theta_C \quad (6.2)$$

$$\tau_p = \frac{\sigma_1 - \sigma_3}{2} \sin 2\theta_C \quad (6.3)$$

$$\tau_p = \sigma_p \tan \phi_p + c \quad (6.4)$$

where  $\sigma_1 = 4.6$  MPa and  $\sigma_3 = 1$  MPa. The cohesion was equal to 0.29 MPa. Due to the significant difference between  $\theta_C$  and the empirical value  $\theta_{DVC} = 50^\circ$  measured from the DVC results (step 05-06, Fig. 6.20), alternative solutions to that of Coulomb (Eq. 6.1) were also explored. In fact, since 1972 Oda (1972) underlined that the theoretical (Coulomb's) and empirical angles are generally not equal. An alternative solution to Coulomb's one was proposed by Roscoe (Nova, 2012), it is shown in Eq. 6.5 and it consists of substituting the friction angle  $\phi$  with the dilatancy angle at peak  $\psi_p$ , which is defined by Bolton (1986):

$$\theta_R = 45^\circ + \frac{\psi_p}{2} \quad (6.5)$$

$$\sin \psi_p = -\frac{\left(\frac{d\epsilon_1}{d\epsilon_3}\right)_p + 1}{\left(\frac{d\epsilon_1}{d\epsilon_3}\right)_p - 1} \quad (6.6)$$

$\psi_p$  for the artificially cemented sample with 15% of clay content was calculated by measuring the variation of the major and minor principal strains  $d\epsilon_1$  and  $d\epsilon_3$  from the X-ray scans of the sample at the beginning of the test (scan 00) and at peak (scan 06). The computation provided a value of  $\psi_p = -22^\circ$ , thus the failure angle defined by Roscoe's solution was equal to  $\theta_R = 34^\circ$ , meaning that the results do not fit Roscoe's solution either. A further solution proposed by Arthur considers an average angle between the two ones used in Coulomb' and Roscoe' solutions:

$$\theta_A = 45^\circ + \frac{\psi_p + \phi_p}{4} \quad (6.7)$$

and this returned a value of  $\theta_A = 48^\circ$ , which describes the experimental results better than the other two solutions.

The DVC outcomes of the tests showed that the three artificially prepared samples (Fig. 6.29) started to develop localised deformation at values of axial strain (0 - 3.6%) similar or slightly higher than those for the naturally cemented samples (0 - 2.9%, Fig. 6.26) although the macroscopic failure took place at much higher axial strains ( $\sim 8$  - 13.3%). The artificial samples did not develop clear failure planes, as

seen in the natural samples, but rather regions where deformation localised. The regions of localised deformation are located towards the sample ends in the artificially cemented samples and at the centre in the uncemented sand sample.

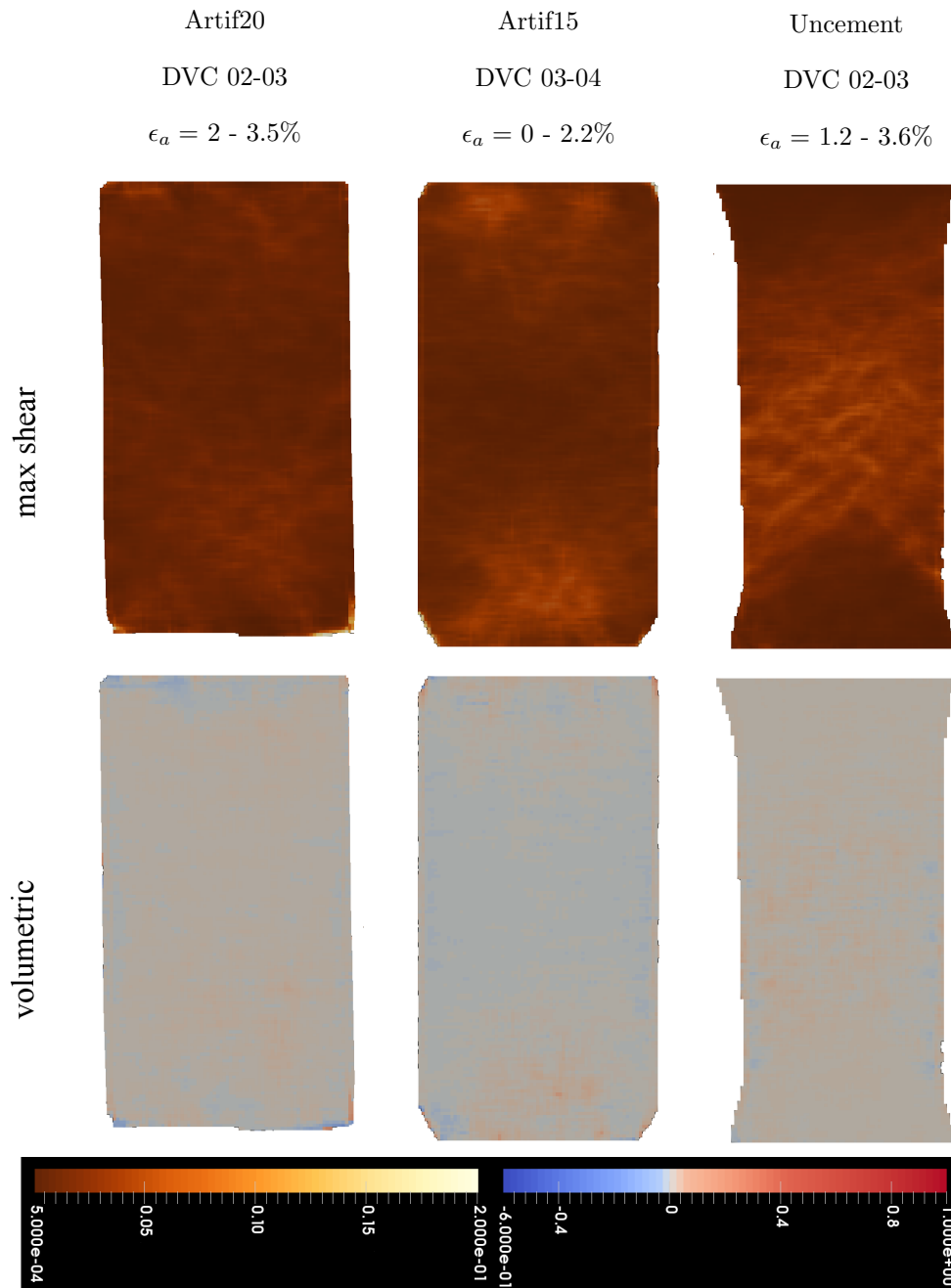


**Figure 6.29:** Comparison of artificially cemented samples at the onset of localised deformation (sample details in Table 6.1)

The DVC results at peak stress for the artificially cemented sample with 20% of clay are not available, thus the sample with 15% of clay and the uncemented one are discussed directly in comparison with the natural sample in the following Section.

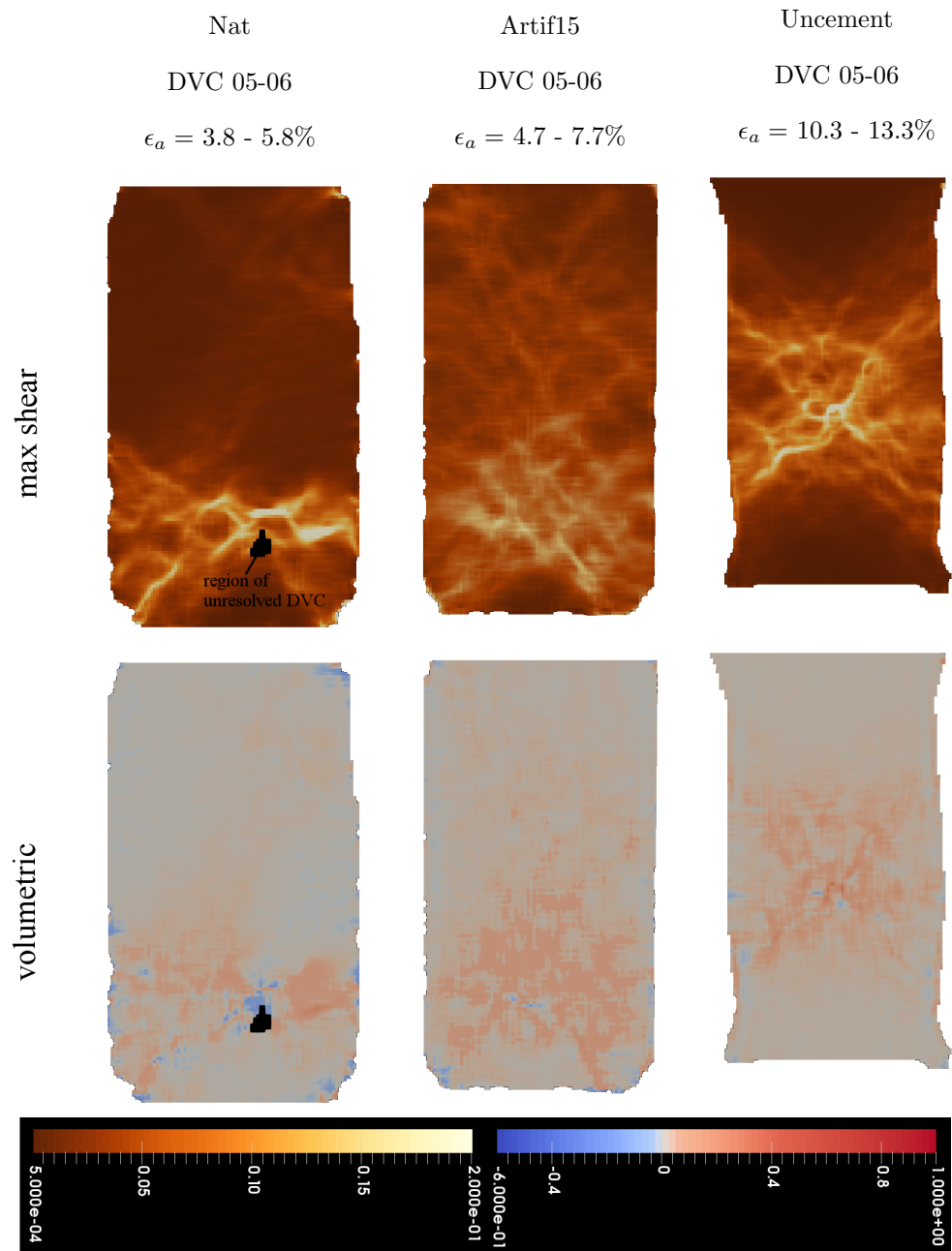
#### 6.4.4 The effect of imperfections on natural samples in comparison with artificially cemented and uncemented samples

Natural imperfections coming either from diagenetic processes or due to deformation appear to have affected the onset and evolution of localised deformation spatially but also potentially from a mechanical point of view.

Natural samples contained the above-mentioned imperfections, while these were absent in artificially cemented and uncemented samples. In particular, during the onset of localised deformation (as this is defined by the DVC strain intervals), shear bands are better defined in natural samples (Fig. 6.26) than in artificially cemented and uncemented ones (Fig. 6.29). Note that the macroscopic failure took place earlier in the natural samples than in the artificial ones. Thus, the grain scale processes leading to the band formation took place at bigger strains in the artificial samples and for this reason the bands were not well-defined.

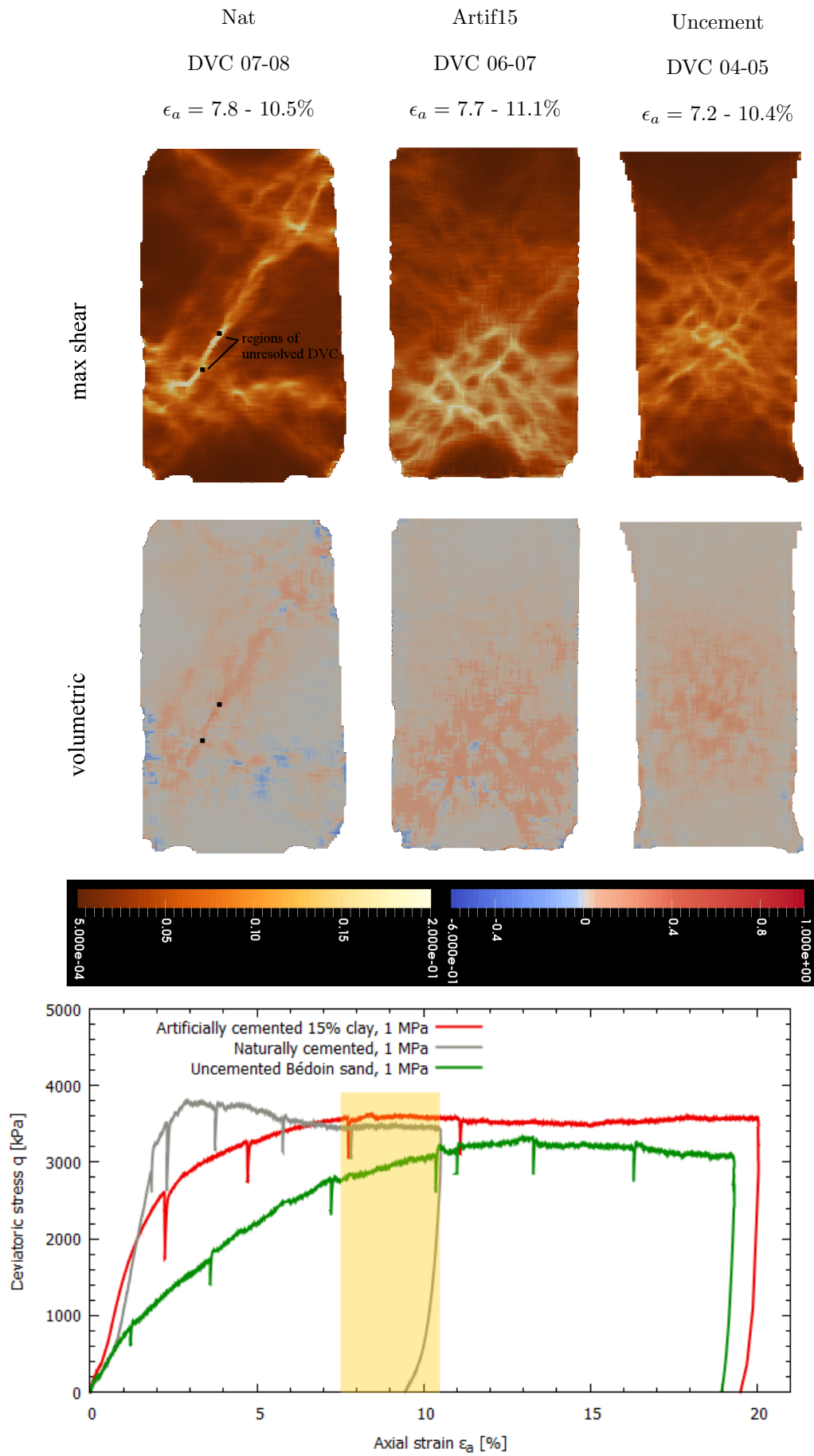
The three sample types reached the peak stress at different axial strain values (Fig. 6.30 and stress-strain curve in Fig. 6.31), as also indicated in Table 6.1. In particular, natural samples failed at lower axial strains than the artificially prepared ones. Figure 6.30 shows that the naturally cemented sample (Nat) developed fewer shear bands instead of a wide network of bands that occupies a considerable volume of the sample, as it is visible in the other two sample types (Artif15 and Uncement). The number of bands that developed within the samples could be related to the presence of the imperfection in the sense that the latter seems to control the spatial distribution of the bands. In particular, with the exception of the natural sample with the a region of enhanced porosity (Nat), localised deformation did not develop with correspondence to the natural imperfections (depositional layers, inclined dilation band, and elongated pore).

Figure 6.31 shows that macroscopic failure occurred earlier in the natural sample than it the artificially cemented and uncemented ones. For example, by selecting a range of axial strain (e.g.,  $\epsilon_a = 7.5 - 10.5\%$ ) and comparing the DVC strain maps in that range (Fig. 6.31), it can be seen that the natural sample developed other shear bands after the dominant one (Fig. 6.30) and expanded the localised deformation towards the top of the sample, whereas the artificially cemented sample developed its dominant shear band surrounded by a network of band and the uncemented sample developed the network of bands but not yet the dominant shear band within it.



**Figure 6.30:** Comparison of naturally, artificially cemented and uncemented samples at the onset of a dominant shear band/s (sample details in Table 6.1)





**Figure 6.31:** DVC of naturally, artificially cemented and uncemented samples at an axial strain range highlighted in yellow in the stress-strain curve (sample details in Table 6.1)

### 6.4.5 The effect of clay content on natural, artificially cemented, and uncemented samples

This work explored how different imperfections due to deposition or to natural deformation processes could affect localised deformation at the laboratory-scale. However, other parameters, such as the clay content were also investigated.

For example, the greater clay content in the artificially cemented sample with respect the natural and uncemented ones was questioned for having determined a wider shear distribution in the artificially cemented samples, where wider networks of shear bands developed. Because shear is distributed in a greater number of bands in Artif15 (Fig. 6.30), the shear intensity along each band of the network is lower than the intensity along the fewer bands of the other two samples. This is in agreement with den Brok et al. (1997), who observed that a higher cement content predisposed a lower stress concentration. In addition, Wang and Leung (2008) explained this process through a numerical simulation by showing the difference of force distribution in uncemented and cemented (2% of cement) grains. The results of the triaxial compression test showed that the cemented grains developed less stress concentration than the uncemented ones (Fig. 6.32).

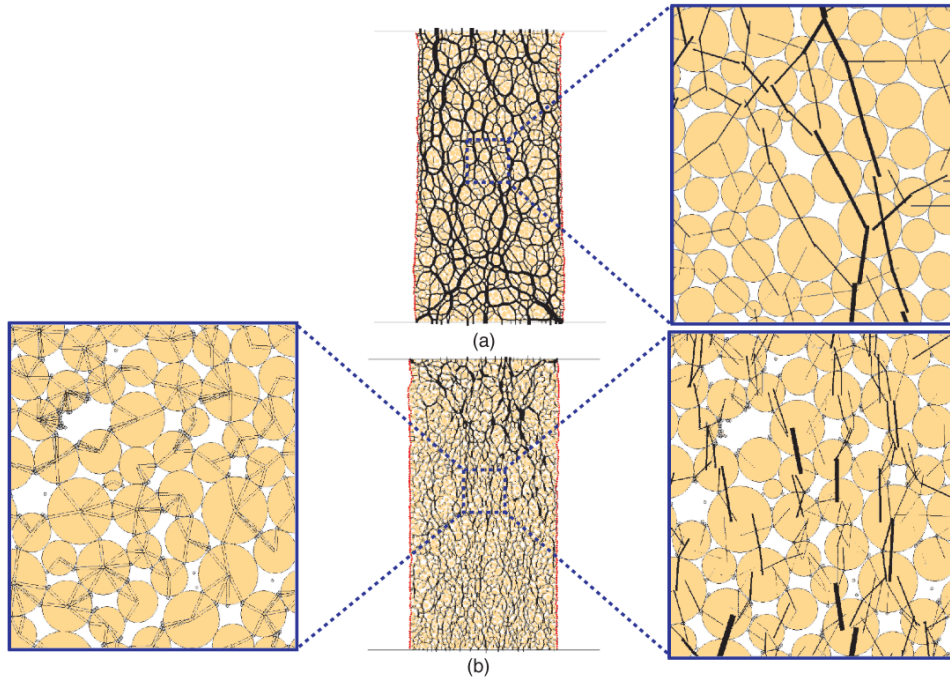


**Figure 6.32:** Force-chain distributions in (a) uncemented and (b) 2% (Portland) cemented samples in a simulation of triaxial compression test at confining pressure of 50 kPa and axial strain of 1.76%: in the uncemented sample the force chains are fewer and thicker, where thickness represents the magnitude of contact normal forces (Wang and Leung, 2008).

The role of cement content was also studied in Tagliaferri et al. (2011). In

this study, a bio-cemented sample exhibited a higher stiffness than the uncemented sand sample, thus attributing to the presence of cement (i.e., calcite) the different behaviour of the samples under triaxial compression (Fig. 6.33). In this doctoral work, indeed, the naturally cemented samples showed a higher stiffness (Fig. 6.31) in accordance with previous observations (Tagliaferri et al., 2011). Moreover, the sample containing the dilation band was stiffer than the other two (Fig. 6.25); thus, it is argued that some of the observed natural imperfections could contribute to the stiffness of the material. In addition, the quartz overgrowths (see Chapter 5), which are distributed inside and outside deformation bands in Bédoin 3, could have also contributed to the higher resistance of the naturally cemented material.

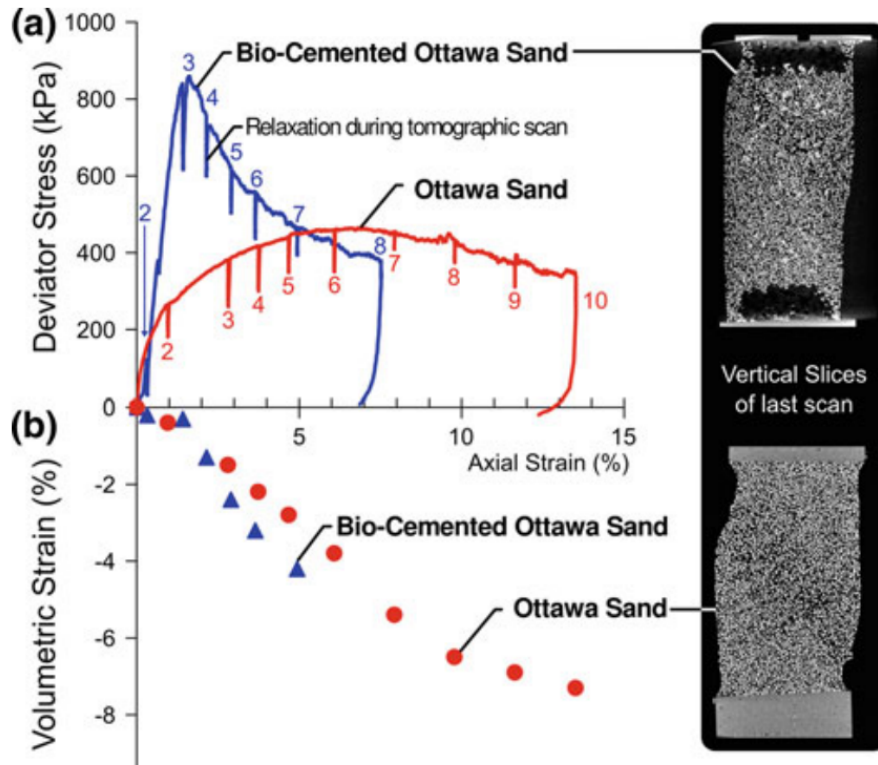


**Figure 6.33:** Stress-strain curves of artificially bio-cemented and uncemented sand samples tested with triaxial compression at a confining pressure of 100 kPa: (a) deviatoric stress-strain and (b) volumetric stress-strain responses. The cemented sample showed a dilative response and a high deviatoric peak stress, differently from the contractive response of the uncemented one (Tagliaferri et al., 2011).

#### 6.4.6 Properties and patterns of shear bands

All tested sample (naturally cemented, artificially cemented, and uncemented) developed single or networks of shear bands, which were characterised mainly by compressive volumetric strains (e.g., DVC 07-08 in Figure 6.23), despite the differences between the samples discussed above.

During the triaxial compression tests, the sample platens were kept co-axial to force deformation to develop in the form of multiple bands, similar to the deformation patterns observed in the Bédoin outcrops. A similar choice was made for the triaxial test performed by Desrues et al. (2018). In order to guarantee coaxiality of the platens, a flat piston edge was chosen (see scheme of the sample setup in Fig. 4.1), whereas a curved (i.e., semi-spherical) edge of the piston would enable the platen in contact with the piston to rotate. When one of the two platens is free to rotate, the sample develops a single narrow shear plane within the wider shear zone (e.g., Fig. 6.34).

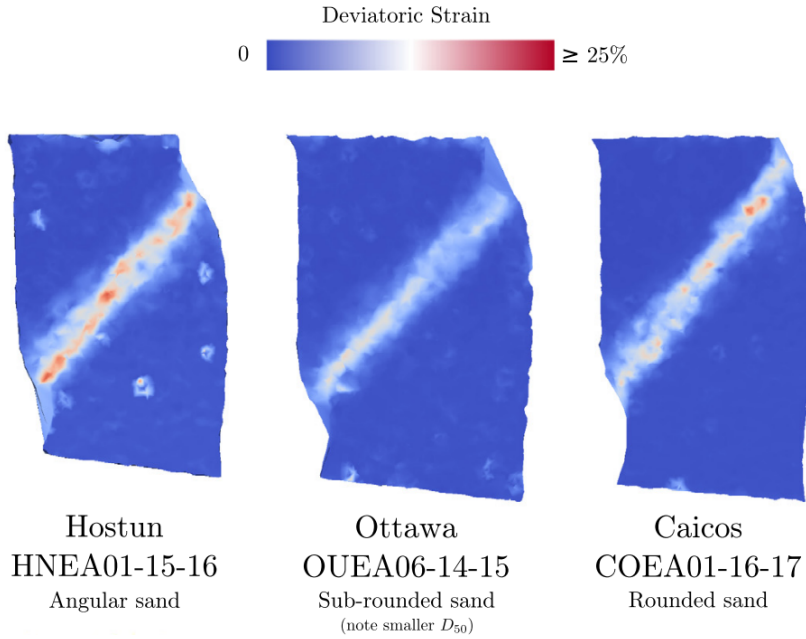


**Figure 6.34:** 2D vertical slices of the strain field maps of uncemented sand (Hostun, Ottawa, and Caicos) samples tested under triaxial compression: the samples exhibit a single shear band because the ceramic platen at the lower part of the sample is free to rotate during the deviatoric compression (i.e., curve-edged piston) (Desrues and Andò, 2015). Details of the sands can be found in Table 6.4 with respect to the works in Alikarami and Torabi (2015) and Desrues and Andò (2015).

The choice of the type of piston edge does not affect the inclination of the shear band/s at failure, i.e., whether it is a single shear band or a shear band network the angle is nearly the same. As a demonstration, the samples tested in this doctoral work with flat-edged piston failed at angles  $\theta_{peak}$  in the range 40 - 50° to the horizontal. The failure angles measured in tests where a curved-edged piston was used belong to the same range of values (Table 6.4), even the angles obtained from different sands and at different confining pressures. The only exceptions are two uncemented sand samples that reported two opposite extreme values, the lowest one (35°) for the uncemented sample tested in this doctoral work and the highest value (54°) for an uncemented sand sample tested in a similar setup (i.e, flat-edged piston)

in Desrues et al. (2018). Therefore, it is argued that imperfections in the natural samples tested in this doctoral work did not affect the shear band inclination, since this is similar in naturally cemented and in artificially cemented and uncemented samples.

A final remark about the values of  $\theta_{peak}$  reported in Table 6.4 is that a single angle was measured for simplicity from the DVC maps, despite the fact that the failure plane is not necessarily planar. This means that the failure angle would be better defined with more than one angle, as for example was done by Alabdullah (2010) who measured two values of  $\theta$  to capture the complex geometry of the bands. The DVC results in Figure 6.30 showed that the bands in the three compared sample types are not planar. The artificially cemented sample with 15% of clay (Artif15) developed a dominant *zigzag*-shaped shear band within a network of bands. This is similar to the shear band observed in one of the natural samples (Nat). The *zigzag* shape suggests that the shear bands derived from the intersection of cross-cutting shear bands within the sample. In the uncemented sand sample (Uncement), the shear band did not develop a *zigzag* shape, but also in this case the band was not planar.

**Table 6.4:** Details of samples tested (in this doctoral work and in previous works) with triaxial compression and analysed with Digital Volume Correlation (DVC) that enabled the measurement of  $\theta_{peak}$ .  $\theta_{peak}$  is measured to the direction of the minor principal stress  $\sigma_3$  (i.e., horizontal) and from the DVC results published in each respective work. Note that the spatial resolution of the X-ray scans that provided DVC strain field maps is of about 15  $\mu\text{m}/\text{px}$  for all samples, except for Desrues et al. (2018), where it is 100  $\mu\text{m}/\text{px}$ .

<b>work</b>	<b>sample description</b>	<b><math>D_{50}</math> [<math>\mu\text{m}</math>]</b>	<b>piston edge</b>	<b><math>\sigma_3</math> [MPa]</b>	<b><math>\epsilon_a</math> [%]</b>	<b><math>\theta_{peak}</math> [°]</b>
This work	Nat	312	flat	1	2.3-3.8	42
	NatPore	312	flat	1	2-3.7	48
	NatDB	312	flat	1	2.9-4.0	40
	Artif15	312	flat	1	4.7-7.7	50
	Uncement	312	flat	1	10.3-13.3	35
Tagliaferri et al. (2011)	Ottawa sand, bio-cemented	250	curved	0.1	2.2-2.9	50
	uncemented	250	curved	0.1	8.0-9.7	46
Alikarami and Torabi (2015)	Ottawa sand, uncemented	310	curved	0.1	4.8-5.7	50
			curved	4	3.8-5.8	41.5
			curved	7	4.3-5.8	50
	Hostun sand, uncemented	338	curved	0.1	3.9-5.1	47
			curved	1	3.8-7.6	49
			curved	2	5.9-7.9	47
			curved	3	5.8-8.6	48.5
			curved	4	9.0-9.9	45
			curved	7	13.6-15.1	45
Desrues and Andò (2015)	Caicos sand, uncemented	420	curved	0.1	2.7-3.7	50
Desrues et al. (2018)	Hostun sand, uncemented	338	flat	0.1	6.3-6.7	54.5

## 6.5 Further comments regarding the observed imperfections

### 6.5.1 Behaviour of the enhanced pore

The naturally cemented sample containing a region of enhanced porosity showed that a weak imperfection attracted the localised deformation, in agreement with Desrues et al. (1996) and Desrues and Viggiani (2004). The region showed shearing (Fig. 6.7) and dilation during the isotropic compression phase (DVC 00-01 in Fig. 6.8), then it triggered the onset of a shear band next to it. The region of enhanced porosity kept dilating during all the steps of deviatoric loading.

The prevented collapse of high-porosity regions was explained through a numerical simulation of a triaxial compression test in uncemented sands (Wang and Leung, 2008). Wang and Leung (2008) identified an arch structure around an enhanced pore, where the arch contained a *webbed* force distribution. The webbed pattern of forces reduced the force concentration in the arch, thus minimising the risk of the pore collapse and enabling also a further dilation. Therefore, dilation could develop until the webbed force distribution existed. The analysis of force distribution in the Bédoin samples tested under triaxial compression goes beyond the scopes of this doctoral work, but it is envisaged in future works, especially because X-ray tomographic data of a real example are available.

### 6.5.2 Properties and behaviour of the elongated pore

The elongated pore inside the sample, which was tested under triaxial compression (Sect. 6.3.2), affected the localised deformation in a different way, i.e., by not triggering the formation of the shear band in the region around it (Fig. 6.35). The elongated pore is oriented orthogonal to the long axis of the sample and it is longer than the sample radius. It was characterised by high resistance as it did not collapse during the triaxial compression (Fig. 6.35b). A contribution to this resistance is attributed to the cement that surrounded the pore. The cement had a variable thickness (Fig. 6.35d), which in some parts reached a value comparable to the average grain size of about  $300\text{ }\mu\text{m}$ . Globally, the pore reported a volume shrinkage from  $0.81\text{ mm}^3$  to  $0.56\text{ mm}^3$  (equivalent to a change in volume from about 21 to 15 grains). Since the cement was not fully crushed during the triaxial test, it was collected at the end of the test to analyse its composition, which was shown to be kaolin clay (Fig. 6.36).

In previous experiments made by Desrues et al. (1996) and Desrues and Viggiani (2004), hard inclusions asymmetrically placed in samples induced strain localisation



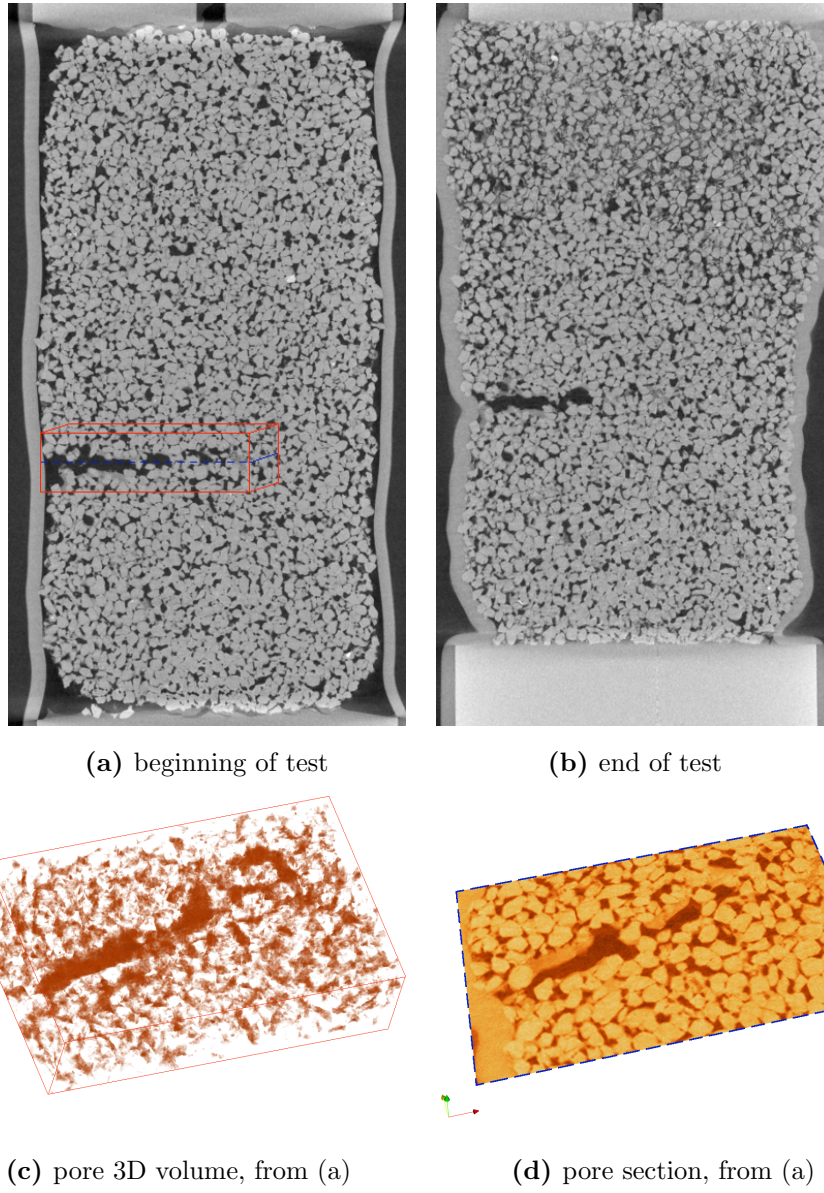


**Figure 6.35:** (a) and (b) are vertical slices of X-ray scan of the sample NatPore before isotropic compression and at the end of the deviatoric loading, respectively, showing that the elongated pore did not collapse under compression and that localised deformation occurred far from the elongated pore, at the top of the sample; (c) 3D volume of the elongated pore (in dark) extracted from (a) (3D view available at <https://doi.org/10.6084/m9.figshare.10125878.v1>), and (d) horizontal section of it (see dashed blue line in (a) for orientation) that shows the variable thickness of the cement (orange) around the pore.



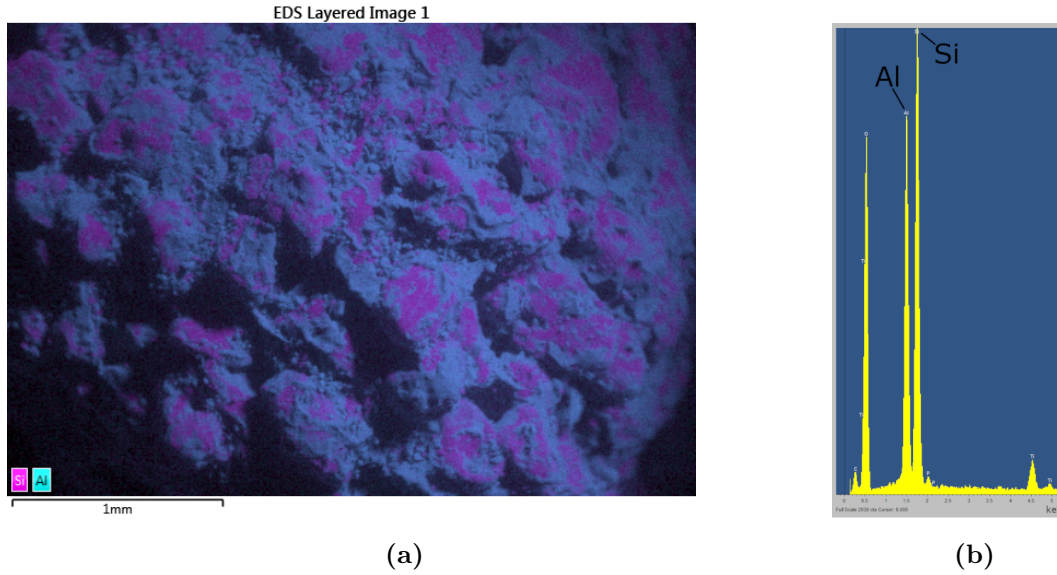


**Figure 6.36:** Energy-Dispersive X-ray Spectroscopy (EDS) of a piece of the cement surrounding the elongated pore: (a) map and (b) spectrum. The map shows the clay fraction (Al = aluminium) covering the sand grains (Si = silicium) and the spectrum provides the specific composition of (a), corresponding to clay (Al - Si).

along them. Conversely, symmetric conditions of the sample - e.g., parallel platens and symmetric imperfections - stabilised the sample and provoked multiple localisation modes (Desrues et al., 1996). In this doctoral work, the elongated pore was asymmetric with respect to the sample axis, but localised deformation did not intercept it. This contradicts the predicted behaviour (Desrues et al., 1996; Desrues and Viggiani, 2004), but it is in agreement with Charalampidou et al. (2014b), who observed that high density inclusions in a sandstone sample shifted the localised deformation to develop far from them. Note that the samples tested in Desrues et al. (1996) and in Desrues and Viggiani (2004) were prismatic and cylindrical, composed by uncemented sand and with regularly-shaped inclusions (cylindrical and spherical) made of cotton and of wood, whereas the sample containing the elongated pore was an irregular cylinder composed by cemented sand. Therefore, it is argued that these differences - i.e., the presence of cement in the grain assembly and the properties of the imperfection - can induce strain localisation far from the imperfection.

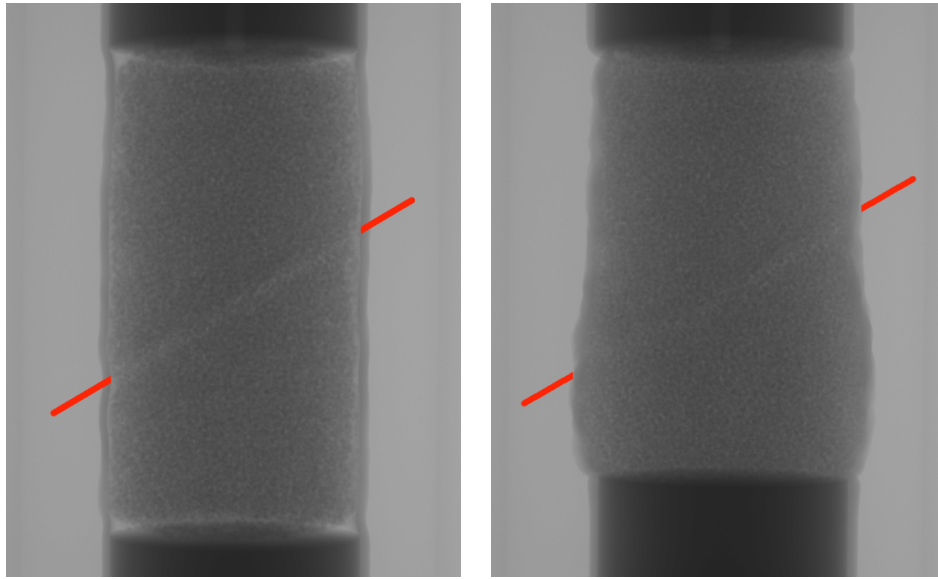
### 6.5.3 The non-reactivation of the pre-existing dilation band

The results of the triaxial compression test performed on the natural sample with pre-existing dilation band showed that the dilation band did not collapse with the deviatoric compression. During the triaxial test, the dilation band reactivated at the very beginning of the deviatoric loading, showing both shear and dilatant strains. However, soon after 2% of axial strain, the dilation band remained inactive (Fig.

6.14), while deformation localised below the band in a network of shear bands inclined in conjugate directions  $\pm 45^\circ$  to the horizontal (i.e.,  $\sigma_3$ ). Then, an individual shear band developed from the network of bands to the top end of the sample, with an inclination of  $64^\circ$  to the horizontal (Table 6.2) cross-cutting the dilation band, which remained still inactive. At the end of the test, the dilation band reported less porosity but still identifiable within the sample, as shown by the X-ray tomography (Fig. 6.12c) and radiography (Fig. 6.37b).

The interrupted reactivation of the dilation band can be explained by referring to Sibson's theory introduced in 1990 about the relationship between the directions of principal stresses and of failure planes (Sibson, 1990). Sibson (1990) defined the *reactivation angle*  $\theta_r$  as the angle between the direction of the major principal stress  $\sigma_1$  and the fault plane (herein deformation band). According to Sibson, the deformation band is favourably oriented if  $12^\circ < \theta_r < 42^\circ$ , whereas is unfavourably oriented if  $\theta_r < 12^\circ$  or  $42^\circ < \theta_r < 54^\circ$  and severely misoriented when  $\theta_r > 54^\circ$ . In the sample tested under triaxial compression, the angle of the pre-existing dilation band with respect to  $\sigma_1$  (where  $\sigma_1 = \sigma_a$  in a triaxial compression test (Atkinson and Bransby, 1978)) is  $57.5^\circ$  (and  $58.5^\circ$  by the end of the test), which would correspond to a severely misoriented band. It is suggested for future work to verify this theory by performing a triaxial test on a sample with a pre-existing dilation band inclined with a favourably oriented angle.

Another contribution to the preservation of dilation bands in Bédoin could have derived from the precipitation of cements along the bands, which contributed to the increase of the material resistance (Sect. 6.4). This interpretation is a consequence of observed thick clay layers in the contours of another dilation band sample from Bédoin 3 (Fig. 5.1c in Chapter 5). In addition to this, deformation bands in Bédoin 3 were interpreted by Philit et al. (2015) as fluid conduits that contributed to the drainage system developed in the deposit. In fact, cement along the dilation band in the sample tested under triaxial compression could not be identified because the band was too thin (average thickness of about  $743 \mu\text{m}$ , corresponding to 2 times the grain diameter) to capture details with a X-ray scan resolution of  $15 \mu\text{m}/\text{px}$ . Further analysis at high resolution of structural properties of dilation bands from Bédoin field is envisaged in order to understand their properties.



(a) beginning of test

(b) end of test

**Figure 6.37:** X-ray radiographies of the naturally cemented sample with pre-existing dilation band before isotropic compression (a) and at the end of deviatoric loading (b): the dilation band did not collapse under compression. Red markers outside the sample identify the dilation band plane.

# Chapter 7

## Porosity and permeability calculations

### 7.1 Introduction

This Chapter presents porosity and permeability calculations, based on X-ray images of undisturbed natural samples, of natural samples that contain deformation bands, and of natural and artificially cemented samples tested under triaxial compression. The aim is to characterise porosity and permeability in different zones of deformation bands and to compare particular volumes of interest in natural and artificial samples.

Porosity was calculated on binarised images using two different methods: Fiji (ImageJ) and PAT software (Chapter 4). The binarisation procedure is the same in both methods. The difference between the two is that Fiji provides freedom of selecting irregular-shaped sub-volumes from a sample, thus enabling the porosity calculation on distinct zones that can be curved, as for example a band core. These zones were identified in the samples containing deformation bands and they were used to create a graphical representation of deformation band structure. PAT software was used to run porosity on samples before and after being tested with triaxial compression. Similarly, permeability calculations (using the PAT software) were performed on the samples tested with triaxial compression experiments.

### 7.2 Porosity and permeability of Bédoin sands in the literature

Porosity and permeability of natural undisturbed and deformed sand samples from Bédoin were measured in previous works and documented in the literature (Saillet and Wibberley, 2013; Philit et al., 2015, 2018). The data from those works is summarised in Table 7.1. The porosity values reported in the table were calculated from

**Table 7.1:** Porosity  $\phi$  and permeability  $\kappa$  values of samples collected from Bédoin, in literature. Permeability was measured normal ( $\perp$ ) and parallel ( $//$ ) to the band.

reference	sample type	$\phi$ [%]	$\kappa$ [mD] (confin. 20 MPa)
Saillet and Wibberley (2013)	fault	9 - 17	-
	cluster	21 - 31	$\perp (0.51 - 0.75) \cdot 10^{+1}$ $// 2.95 \cdot 10^{+1}$
	multi-strand band	3 - 16	$\perp (0.07 - 2.55) \cdot 10^{+2}$
	single-strand band	24 - 34	$\perp (1.47 - 2.42) \cdot 10^{+2}$
	undisturbed sand	$30 \pm 2$	$(1.73 - 3.82) \cdot 10^{+2}$
Philit et al. (2015)	shear band	0 - 5	-
	undisturbed sand	29 - 34	-
Philit et al. (2018)	band	5 - 12	-
	interband (20%)	14 - 18	-
	undisturbed sand	27 - 37	-

2D image analysis of thin sections (Scanning Electron Microscopy and Cathodoluminescence). Each study proposed a different way to classify sample types. Saillet and Wibberley (2013) classified samples as: undisturbed sand, single-strand band, multi-strand band, cluster, and fault. The porosity value of the undisturbed sand was in the range  $30 \pm 2\%$ . Calculations from single-strand bands and clusters reported values close to those of the undisturbed sand of about 30% (Saillet and Wibberley, 2013), whereas porosity in multi-strand bands and in faults was lower or close to zero. Philit et al. (2015, 2018) proposed a simpler distinction between sample types belonging to undisturbed sand, interband, and (shear) band. The porosity range of the undisturbed sand was wider (27 - 37 %) than in Saillet and Wibberley (2013), yet it comprised the value of 30%. Porosity in the deformation bands varied from 0 to 12%, and the values between those for band and for undisturbed sand corresponded to the interband, which was defined in Philit et al. (2018) as the material between strands within a deformation band cluster.

Permeability was measured by Saillet and Wibberley (2013) by employing a special laboratory apparatus designed by Wibberley. The apparatus enabled permeability measurement with the condition that samples need to be confined with a minimum pressure of 10 MPa (and a maximum one of 100 MPa), which could have affected the weakly cemented Bédoin sand samples. The minimum values available in Saillet and Wibberley (2013) and reported in Table 7.1 are for a confining pressure of 20 MPa.

The values in Table 7.1 show an overall difference of 1 - 2 orders of magnitude

between undisturbed sand/single strand bands and the more intense deformation band types. In the samples with deformation band cluster, permeability was calculated orthogonal ( $\perp$ ) and parallel ( $\parallel$ ) to the band by coring the sample in the two orientations with respect to the band plane. The resultant difference in permeability was of about one order of magnitude.

## 7.3 Selected samples for the calculations

Natural and artificially cemented samples, and uncemented sand from Bédoin described in Chapter 6 were used for porosity and permeability calculations. A representative horizontal slice, extracted from the 3D X-ray scan of a naturally (Nat, from Bédoin 3) and an artificially cemented (Artif15) samples, is shown in Figure 7.1 with the correspondent binarised slice, which is the one used in the calculations. The membrane, surrounding the sample during the mechanical loading, was removed with image processing. In Artif15 it is possible to distinguish the cement between grains (in grey). The thresholding algorithm used to binarise the X-ray scans is described in Section 4.3.2.

Figure 7.2 shows X-ray and correspondent binarised slices of two samples of multi-strand bands, which belonged to Bédoin 4.5. In ISBS4503 one of the strands is visible with the surrounding interband, whereas no distinction between strand and interband was identified in ISBS4501.

Finally, a single-strand band and a dilation band from Bédoin 3 are shown in Figure 7.3. The former has an average thickness of 1.5 mm whereas the latter 1.3 mm and can be identified in the figures because of the red staining particles contained within the bands.

## 7.4 Porosity analysis

### 7.4.1 Porosity calculations with Fiji

Porosity ( $\phi$ ) was calculated with Fiji (see Sect. 4.3.2) on the binarised images of the naturally and artificially prepared samples presented above. Porosity calculations were performed in the whole sample and in sample sub-volumes to distinguish different band zones (i.e., core, contour, damage, and interband) (see sub-volumes in Fig. 7.4 and 7.5).

The analysed samples are listed in Table 7.2 with indication of their volume and of the equivalent average number of grains, to give a practical quantification of the volume. The average number of grains was calculated by assuming the grains to be perfect spheres of diameter equal to the sand  $d_{50}$  (i.e., 310  $\mu\text{m}$ ). Values no. 11 - 13

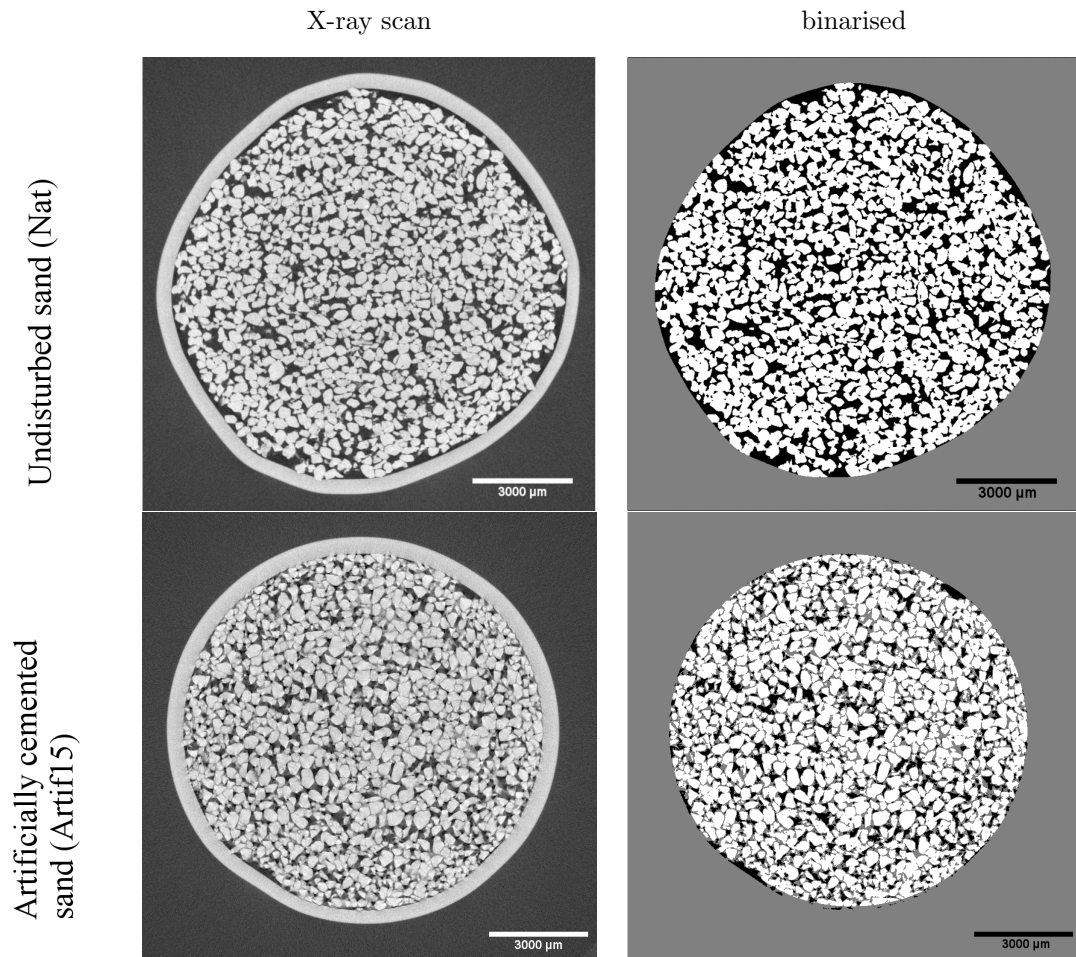


**Figure 7.1:** X-ray slices (tomography (left) and correspondent binarised image (right)) of two cylindrical samples: undisturbed (cemented) sand from Bédoin (Nat, Fig. 6.5a) and artificially cemented Bédoin sand (Artif15, Fig. 6.18a) (black = pore, white = solid). Image resolution for the two X-ray scans is 15  $\mu\text{m}/\text{px}$ .



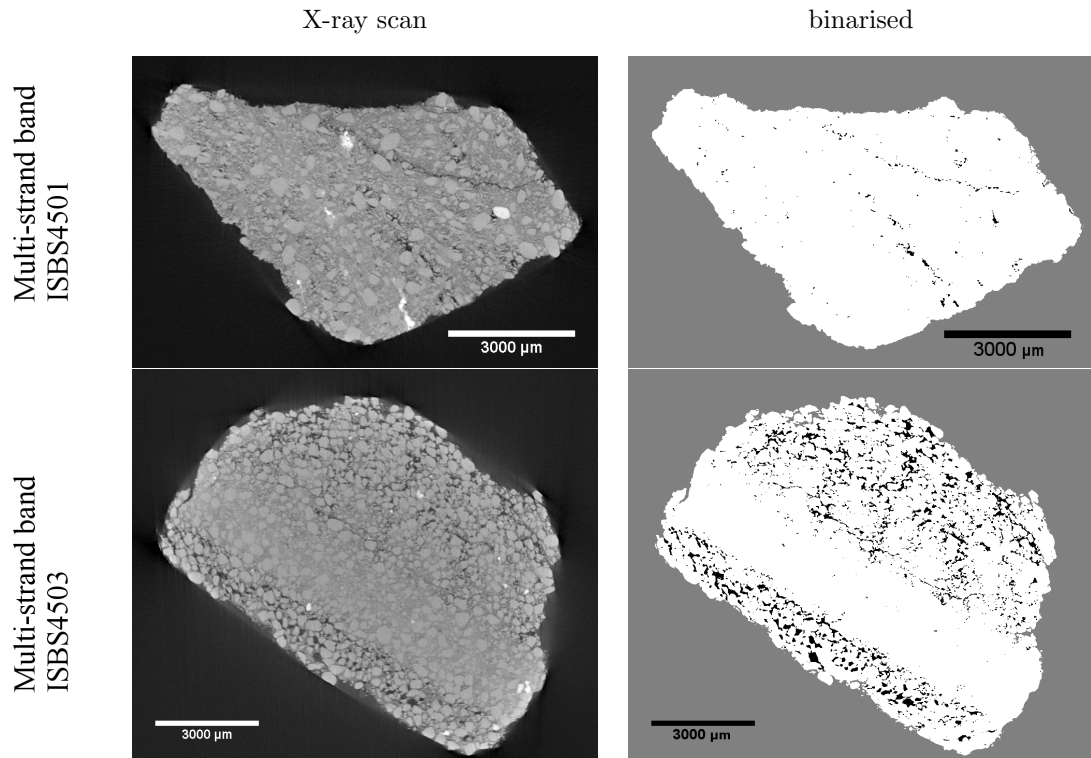


**Figure 7.2:** X-ray slices (tomography (left) and correspondent binarised image (right)) of two deformation band samples, multi-strand bands ISBS4501 and ISBS4503, from Bédoin 4.5 (black = pore, white = solid). Image resolution for the two X-ray scans is 15  $\mu\text{m}/\text{px}$ .

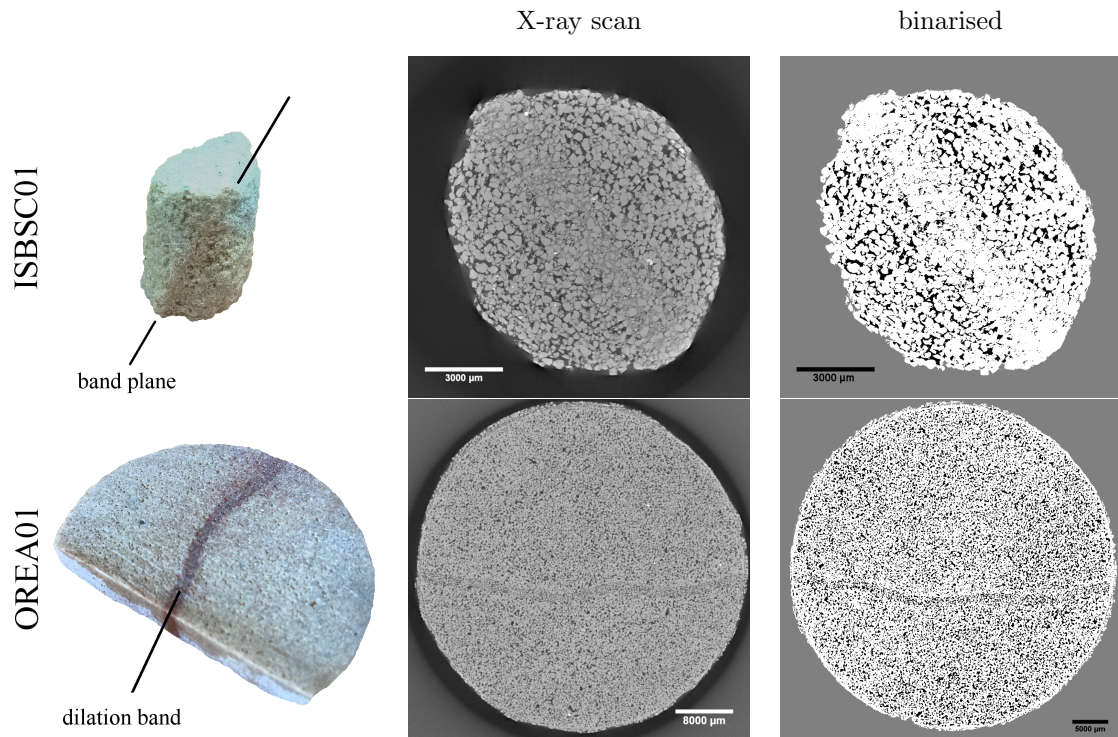


**Figure 7.3:** (from left to right) Sample, X-ray tomography, and correspondent binarised slice of two deformation band samples, single-strand band ISBSC01 and dilation band OREA01 (black = pore, white = solid). Image resolution for ISBSC01 is 10.5  $\mu\text{m}/\text{px}$ , for OREA01 is 27  $\mu\text{m}/\text{px}$ .



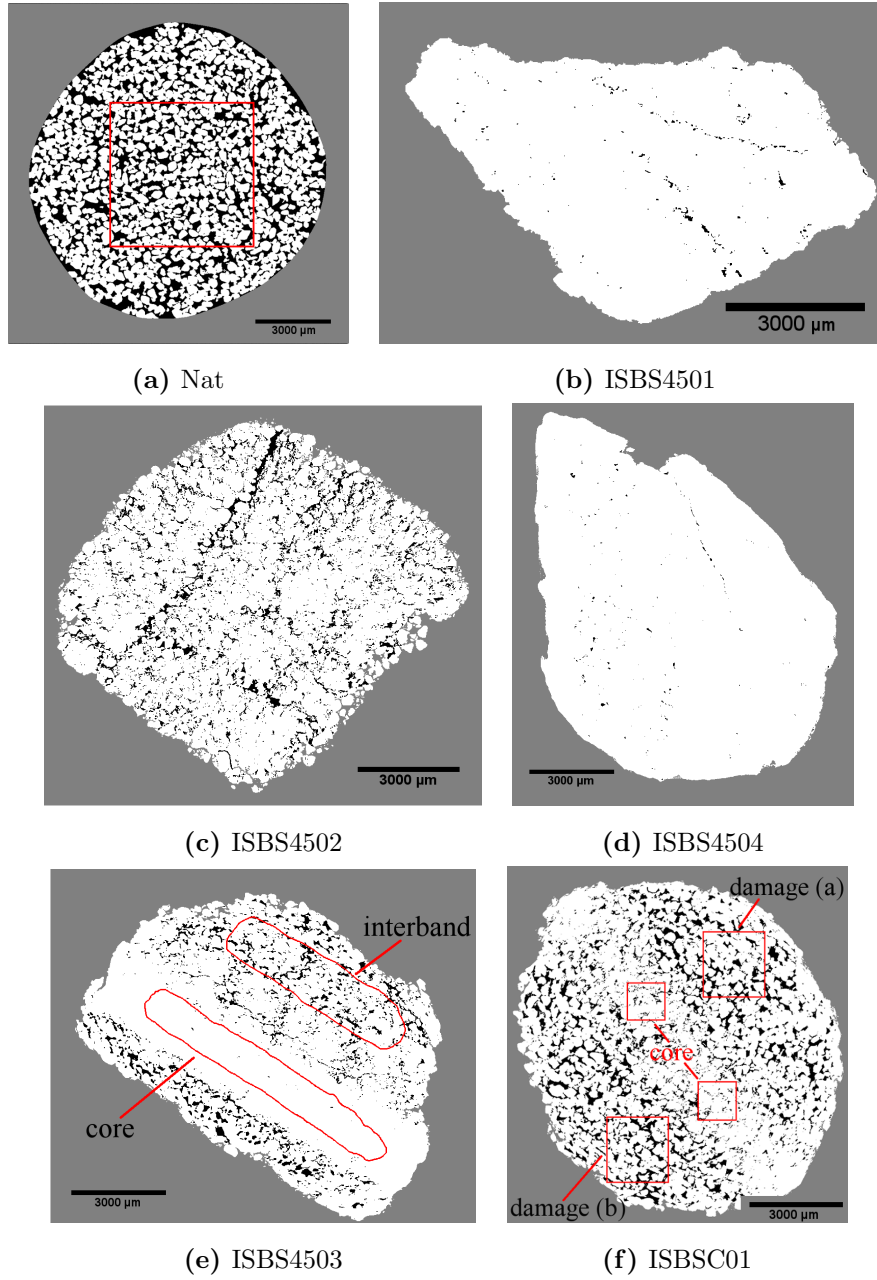


**Figure 7.4:** X-ray binarised slices extracted from the natural samples, showing volumes and sub-volumes (contours in red and with name of the respective zone) selected for porosity calculation with Fiji: (a) undisturbed sand, (b, c, d, e) multi-strand bands, and (f) single-strand band. Image resolution is  $15 \mu\text{m}/\text{px}$  for all samples except (f), which has a resolution of  $10.5 \mu\text{m}/\text{px}$ .

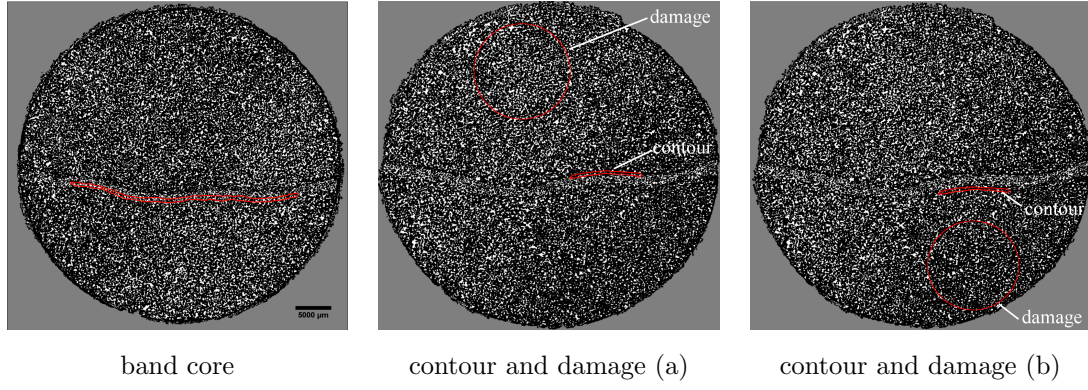


**Figure 7.5:** X-ray binarised slices extracted from the dilation band OREA01 showing the sub-volumes (contours in red) selected for porosity calculation with Fiji, with indication of distinct zones: band core, contour, and damage zones, where a and b are the two sides of the dilation band (black = solid, white = pore). [Res.  $27 \mu\text{m}/\text{px}$ ].

**Table 7.2:** Porosity calculations performed with Fiji on undisturbed sand and on deformation band samples (multi-strand, single-strand, and dilation bands) from Bédoin 3 and 4.5 (ref. to Fig. 3.1). Band zones refer to Fig. 7.4 and 7.5.

value no.	sample type and band zone	sample name	sample vol [vx]	average no. grains	$\phi$ [%]
01	undisturbed sand	Nat	$1.80 \cdot 10^{+8}$	25984	33.33
Multi-strand bands					
02	core	ISBS4501	$2.36 \cdot 10^{+8}$	50828	0.49
03	core	ISBS4504	$6.03 \cdot 10^{+8}$	130312	0.21
04	core	ISBS4502	$2.84 \cdot 10^{+8}$	58472	4.90
05	core	ISBS4503	$4.53 \cdot 10^{+7}$	9802	0.04
06	interband	ISBS4503	$1.51 \cdot 10^{+7}$	3056	6.32
Single-strand band					
07	core	ISBSC01	$8.32 \cdot 10^{+5}$	56	8.47
08	core	ISBSC01	$8.32 \cdot 10^{+5}$	58	6.12
09	damage (a)	ISBSC01	$8.48 \cdot 10^{+6}$	502	20.22
10	damage (b)	ISBSC01	$8.48 \cdot 10^{+6}$	501	20.52
Dilation band					
11	core	OREA01	(from Tab.7.3 : avg. 01 - 11)		30.46
12	contour (a)	OREA01	(from Tab.7.3 : avg. 12 - 16)		12.81
13	contour (b)	OREA01	(from Tab.7.3 : avg. 17 - 21)		18.74
14	damage (a)	OREA01	$1.34 \cdot 10^{+8}$	130488	22.74
15	damage (b)	OREA01	$1.34 \cdot 10^{+8}$	131816	21.94

reported in Table 7.2 are an average of porosity calculated on several sub-volumes belonging to the same band zone of OREA01, e.g., value no. 11 in Table 7.2 is an average of values no. 01 - 11 reported in Table 7.3.

**Table 7.3:** Porosity calculations of the dilation band OREA01 in distinct band zones identified within the sample, as shown in Figure 7.5.

value no.	sample zone	sample vol [vx]	avg no. grains	$\phi$ [%]
01	core	$1.63 \cdot 10^{+5}$	143	30.62
02	core	$4.37 \cdot 10^{+5}$	379	31.18
03	core	$1.36 \cdot 10^{+6}$	1161	32.67
04	core	$1.36 \cdot 10^{+6}$	1210	29.85
05	core	$1.36 \cdot 10^{+6}$	1197	30.58
06	core	$1.36 \cdot 10^{+6}$	1200	30.34
07	core	$1.36 \cdot 10^{+6}$	1206	30.05
08	core	$1.30 \cdot 10^{+6}$	1135	31.01
09	core	$1.30 \cdot 10^{+6}$	1155	29.76
10	core	$1.05 \cdot 10^{+6}$	935	29.53
11	core	$2.94 \cdot 10^{+5}$	270	27.11
12	contour (a)	$1.02 \cdot 10^{+5}$	111	13.63
13	contour (a)	$1.02 \cdot 10^{+5}$	113	12.13
14	contour (a)	$1.02 \cdot 10^{+5}$	113	11.79
15	contour (a)	$1.02 \cdot 10^{+5}$	112	12.39
16	contour (a)	$1.02 \cdot 10^{+5}$	110	14.11
17	contour (b)	$1.02 \cdot 10^{+5}$	109	15.38
18	contour (b)	$1.02 \cdot 10^{+5}$	103	19.60
19	contour (b)	$1.02 \cdot 10^{+5}$	101	21.11
20	contour (b)	$1.02 \cdot 10^{+5}$	104	18.59
21	contour (b)	$1.02 \cdot 10^{+5}$	104	19.01
22	damage (a)	$1.34 \cdot 10^{+8}$	130488	22.74
23	damage (b)	$1.34 \cdot 10^{+8}$	131816	21.94

The lowest porosity values ( $\sim 0\%$ ) were measured in the core zone of the multi-strand deformation bands, whereas the values for the single-strand band were higher ( $\sim 7\%$ ) and similar to the interband of the multi-strand bands (6.32%). The damage zones of the single-strand band had similar values at the two sides ( $\sim 20\%$ ) of the deformation band and these values were also similar to the damage zone ( $\sim 22\%$ ) around the dilation band. The dilation band core reported porosity (30.46%) close to the undisturbed sand (33.33%). Its contours had much lower porosity than the

dilation band core and with distinct values for the two sides (about 13% and 19%).

## 7.4.2 Porosity calculations with PAT

Porosity in the natural, artificially cemented, and uncemented samples were also calculated with the PAT software introduced in Section 4.3.2. Porosity was calculated on the same deformation band samples employed in the calculations with Fiji (Table 7.2) but not on the same sub-volumes because PAT calculates porosity only on prismatic volumes and not on volumes with irregular shapes; therefore, prismatic sub-volumes were extracted from the different band zones (Fig. 7.6).

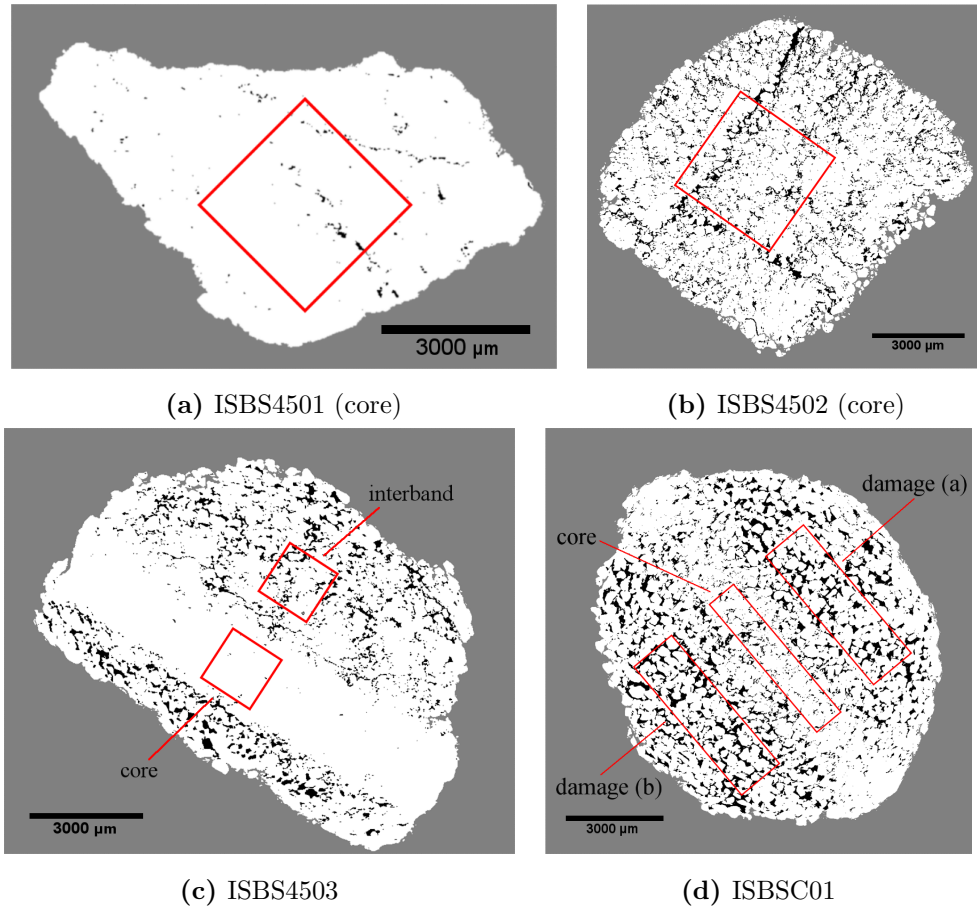


**Figure 7.6:** X-ray binarised slices of the deformation band samples showing the sub-volumes (contours in red) selected for porosity calculation with PAT: (a, b, c) multi-strand bands, and (d) single-strand band.

In addition, porosity calculations were performed on the samples tested with triaxial compression. From these samples, a prismatic sub-volume was extracted far from the boundaries that are prone to alteration, in order to perform the calculations (Fig. 7.8). Furthermore, porosity was calculated at the beginning and at the end of the test, with the aim of understanding the porosity variation within the samples due to deformation processes.



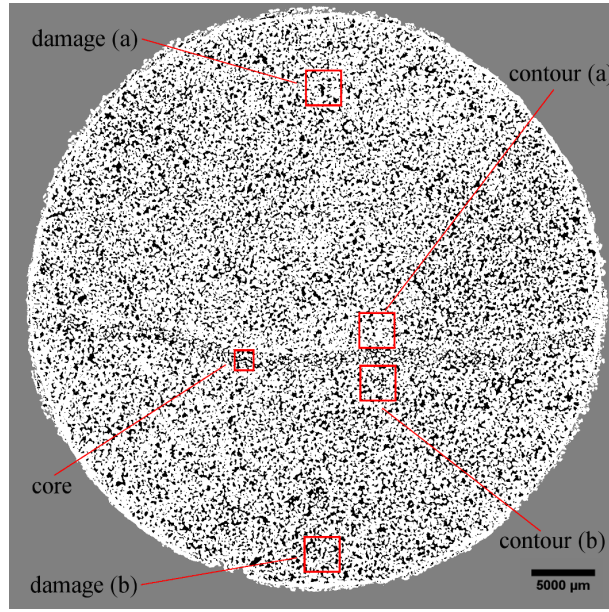


**Figure 7.7:** X-ray binarised slice of the dilation band sample OREA01, showing the sub-volumes selected for porosity calculation with PAT.

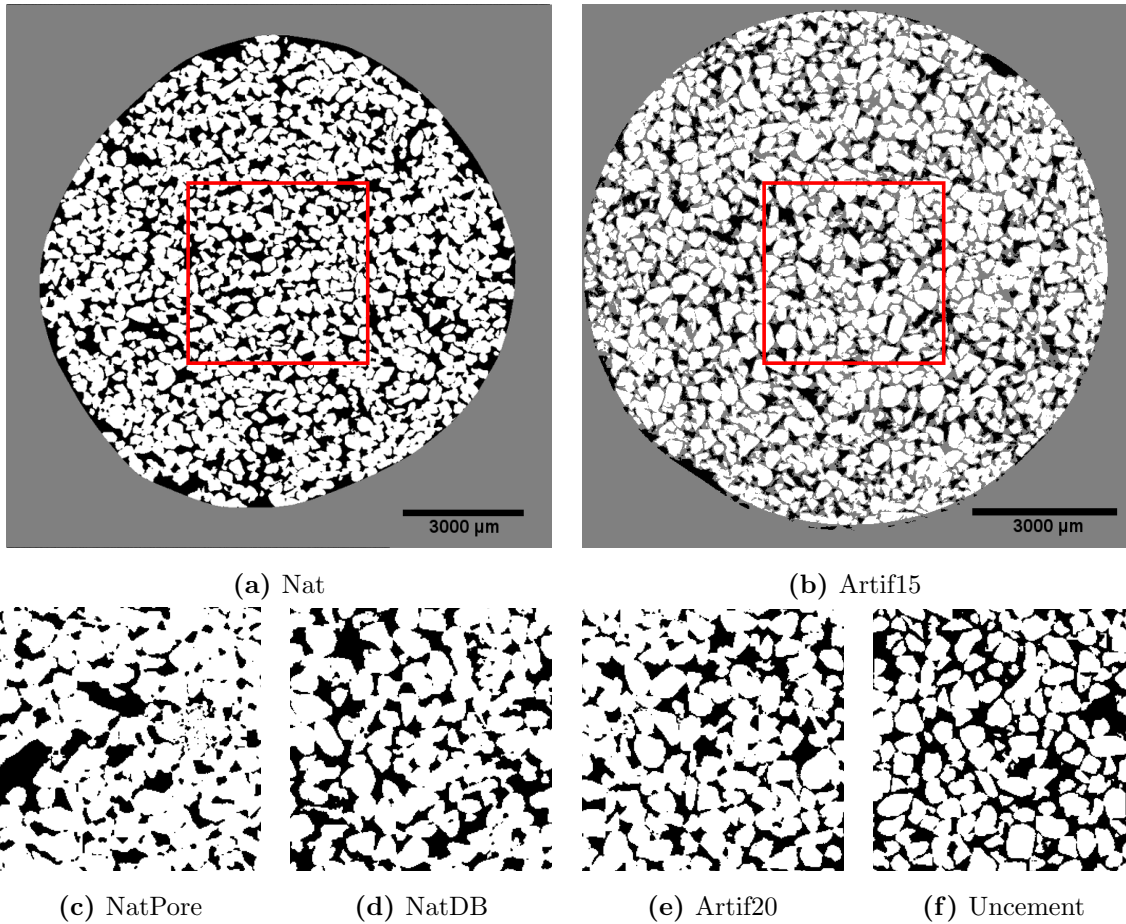


**Figure 7.8:** X-ray binarised slices of the tested samples (sample name and test described in Table 6.1) used for porosity calculation with PAT: (a - b) slices of the sample with sub-volume (contours in red), showing the central location of it within the sample, and (c - f) slices from the sub-volumes (selected with similar location) of the other tested samples. Note that only NatPore (c) contained part of the imperfection (i.e., elongated pore).

**Table 7.4:** Porosity calculation with PAT of the natural samples containing deformation bands (multi-/single-strand and dilation bands, Fig. 7.6) and 7.7 from Bédoin 3 and 4.5.

value no.	sample type, name, and band zone	sample vol [vx]	avg no. grains	$\phi$ [%]
Multi-strand bands:				
01	ISBS4501, core	$8.00 \cdot 10^{+6}$	1717	0.06
02	ISBS4502, core	$1.56 \cdot 10^{+7}$	3204	0.62
03	ISBS4503, core	$2.00 \cdot 10^{+6}$	430	0.06
04	ISBS4503, interband	$8.00 \cdot 10^{+6}$	252	2.03
Single-strand band ISBSC01:				
05	core	$4.00 \cdot 10^{+6}$	257	3.31
06	damage (a)	$7.50 \cdot 10^{+6}$	411	14.40
07	damage (b)	$7.50 \cdot 10^{+6}$	401	15.50
Dilation band OREA01:				
08	core	$1.25 \cdot 10^{+5}$	118	25.00
09	contour (a)	$5.00 \cdot 10^{+5}$	480	23.70
10	contour (b)	$5.00 \cdot 10^{+5}$	500	20.60
11	damage (a)	$1.00 \cdot 10^{+6}$	939	25.50
12	damage (b)	$1.00 \cdot 10^{+6}$	1000	20.80

From the deformation band samples, the multi-strand bands reported the lowest porosity values ( $\sim 0\%$ ), with a slightly higher value in the interband ( $\sim 2\%$ ) (Table 7.4). The single-strand band reported a higher porosity ( $\sim 3\%$ ) than the multi-strand ones and the damage zone around it had a nearly homogeneous porosity of 15% at the two sides. The dilation band reported values that differentiate in the three zones of max. 5% from the core (25%). Contour and damage zone were found asymmetric with respect to the core zone, with one side of the band (a) more porous than the other one (b).

From the tested samples and at the beginning of the test, the undisturbed sand Nat reported a higher porosity (32%) than all the other cemented samples and the highest porosity value was attributed to the uncemented sand sample (34.3%), as expected (Table 7.5). The other two naturally cemented samples NatPore and NatDB reported a lower porosity ( $\sim 22\%$  and  $27\%$ ) than Nat, which is consistent with the bulk density values discussed in Chapter 6 (see Table 6.3). Porosity in the two artificially cemented samples Artif20 and Artif15 was found similar ( $\sim 28\%$  and  $25.5\%$ ) to the values of the natural ones.

Porosity at the end of the test was found higher than that at the beginning of the test, in all the samples (Table 7.5). Considering that the samples have been

**Table 7.5:** Porosity calculation with PAT of naturally and artificially cemented samples tested with triaxial compression (for test names, refer to Table 6.1). Sub-volumes are shown in Fig. 7.8.

value no.	sample name and test phase	sample vol [vx]	avg no. grains	$\phi$ [%]
	Nat (undisturbed sand):			
01	beginning test	$1.57 \cdot 10^{+7}$	2277	32.00
02	end test	$1.56 \cdot 10^{+7}$	-	37.00
	NatPore:			
03	beginning test	$1.56 \cdot 10^{+7}$	2638	21.80
04	end test	$1.56 \cdot 10^{+7}$	-	21.90
	NatDB:			
05	beginning test	$1.56 \cdot 10^{+7}$	2468	26.90
06	end test	$1.56 \cdot 10^{+7}$	-	36.40
	Artif20:			
07	beginning test	$1.56 \cdot 10^{+7}$	2441	27.80
08	end test	$1.56 \cdot 10^{+7}$	-	36.30
	Artif15:			
09	beginning test	$1.56 \cdot 10^{+7}$	2276	25.40
10	end test	$1.56 \cdot 10^{+7}$	-	35.40
	Uncement:			
11	beginning test	$1.56 \cdot 10^{+7}$	2220	34.30
12	end test	$1.56 \cdot 10^{+7}$	-	35.80

compressed at high pressures, one would expect a porosity reduction. However, a porosity increase up to 10% was calculated, which is physically not realistic. An explanation for this is attributed to the binarisation procedure at the resolution of  $15\mu\text{m}/\text{px}$ , which was not able to identify the small grain fragments produced during the triaxial compression. In fact, the thresholding algorithm Intermodos selected univocally for all the samples analysed in this work, is generally suitable for images with bimodal histogram, and at the end of the test the histograms of the sample images became less bimodal (Fig. 7.9). Due to time limitations, a single thresholding algorithm was employed, which provided good results for deformation band samples and for the samples before undergoing triaxial compression but a less good result for the samples after being deformed.

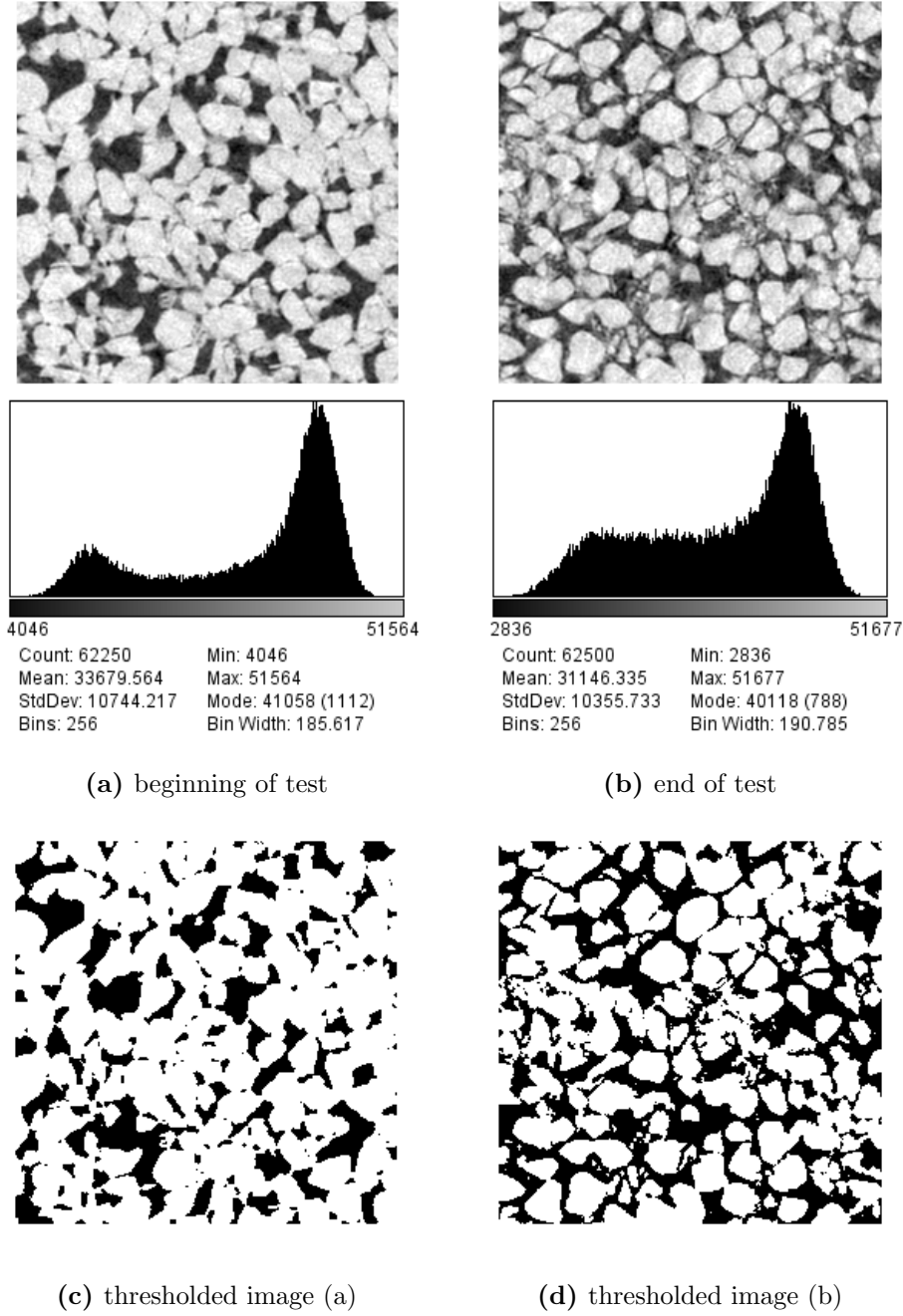


**Figure 7.9:** Image histograms of X-ray scans of the sample NatDB (a) at the beginning and (b) at the end of the test and correspondent thresholded images (c) and (d): in (a) the histogram is bimodal, and the two peaks identify the pore space (greyscale value: 13500) and the grains (greyscale value: 41500); in (b) the values between the two peak grow in frequency, therefore the peak that identifies the pores is more vague.

### 7.4.3 Discussion

The porosity calculations obtained with Fiji provided values slightly higher than the values calculated with PAT for multi-strand and single-strand bands, with a porosity difference of about 5%. The values for the dilation band sample OREA01 reported a much higher difference, reaching 10% of difference for the porosity at the



band contour (a). Despite the high difference for the dilation band, the software PAT identified the porosity asymmetry of the band sides (contours (a) and (b)) with respect to the core, consistently with the values obtained with Fiji. Such asymmetry could be caused by gravity effect on the solid particles transported within the dilation band, according to the hypothesis of flow conduit for the observed dilation band (see Sect. 6.5.3). Finally, symmetry in the damage zone at the two sides of the single-strand band core is also consistently detected with the two calculation methods. Due to the limits of the PAT software in analysing curved and irregular sub-volumes, especially for the dilation band sample, the porosity calculations obtained with Fiji are considered more representative of the material properties.

On the basis of the porosity values obtained with Fiji, a schematic representation of the three deformation band types observed (i.e., multi-strand, single-strand, and dilation bands) was produced and this is shown in Figure 7.10.

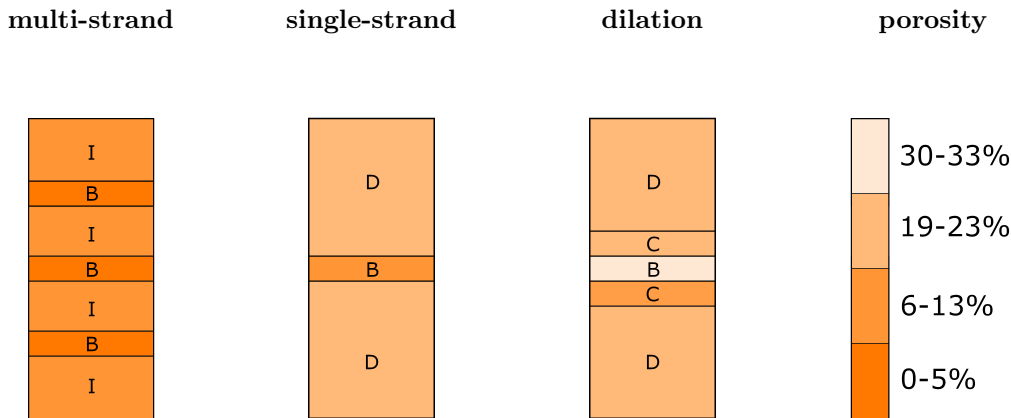


**Figure 7.10:** Schematic representation of porosity in the three deformation band types analysed: multi-strand, single-strand, and dilation bands. The representation reports the zonation for the three band types, according to observations: B = band core, C = contour, D = damage zone, I = interband.

The schematic representation (Fig. 7.10) summarises the porosity characteristics of the deformation band samples analysed in this work in a simple way, expressing in lighter colours a higher porosity. The distance between strands as well as the band thickness are not in scale; however, the deformation band cores (B, Fig. 7.10) for the three sample types here analysed had similar thickness (1.3 - 2.5 mm). Porosity values for each zone are reported in the legend, according to the calculations obtained. Considering the analysis performed by Philit et al. (2015), higher porosity corresponded to lower degree of cataclasis. This is in agreement with the observations reported for the three sample types at Scanning Electron Microscopy shown in Chapter 5, where grain fragments and microfragments surrounding few survivor

grains were observed in the multi-strand bands (Fig. 5.2) and semi-intact grains in the dilation band core (Fig. 5.1b).

Finally, porosity values in the literature are considered to overestimate the porosity in the single-strand band type, since this band type was reported to have porosity close to that of the undisturbed sand (24 - 34%, Table 7.1), while in the current calculations the band reported a porosity value of about 7% in the core and 20% in the damage zone. However, a direct comparison of values should not be performed, because porosity was calculated with different methods and sample sizes (values from literature were measured on 2D SEM photomicrographs (Saillet and Wibberley, 2013)).

## 7.5 Permeability analysis

### 7.5.1 Permeability calculations with PAT

Permeability was measured with the software PAT on the same prismatic sub-volumes used for porosity calculation with PAT from deformation band samples (Fig. 7.6 and 7.7) and from naturally and artificially prepared samples tested with triaxial compression (Fig. 7.8). The software computed the permeability along three orthogonal directions (x, y, and z), which enabled the characterisation of permeability in the three directions (Fig. 7.11). In particular, the samples containing deformation bands were oriented so that the direction of the deformation band was parallel to the x direction. Therefore,  $\kappa_x$  and  $\kappa_z$  provided the permeability values along the two directions that define the deformation band plane, with  $\kappa_y$  orthogonal to it.

The samples used for the mechanical tests reported permeability values (Table 7.6) in the orders of  $10^{+3}$  -  $10^{+4}$  mD for the artificially cemented samples and also for the natural ones, despite their natural imperfections. The samples with the lowest values ( $10^{+3}$  mD) among this group are NatPore and Artif15. One would imagine the uncemented sand sample Uncement to be the most permeable one, but in fact its permeability is similar to that of the cemented samples, both naturally and artificially. All the tested samples had similar values in the three directions, which is due to the fact that imperfections were partially included or not at all present in the analysed sub-volumes. Figure 7.8 shows a representative slice from each volume analysed, showing that only NatPore included part of the elongated pore, whereas all the other sub-volumes did not present natural imperfections. Note that permeability was not calculated for the post-deformation samples, since the porosity values for the same subvolumes were considered not representative, as discussed in Section 7.4.2.

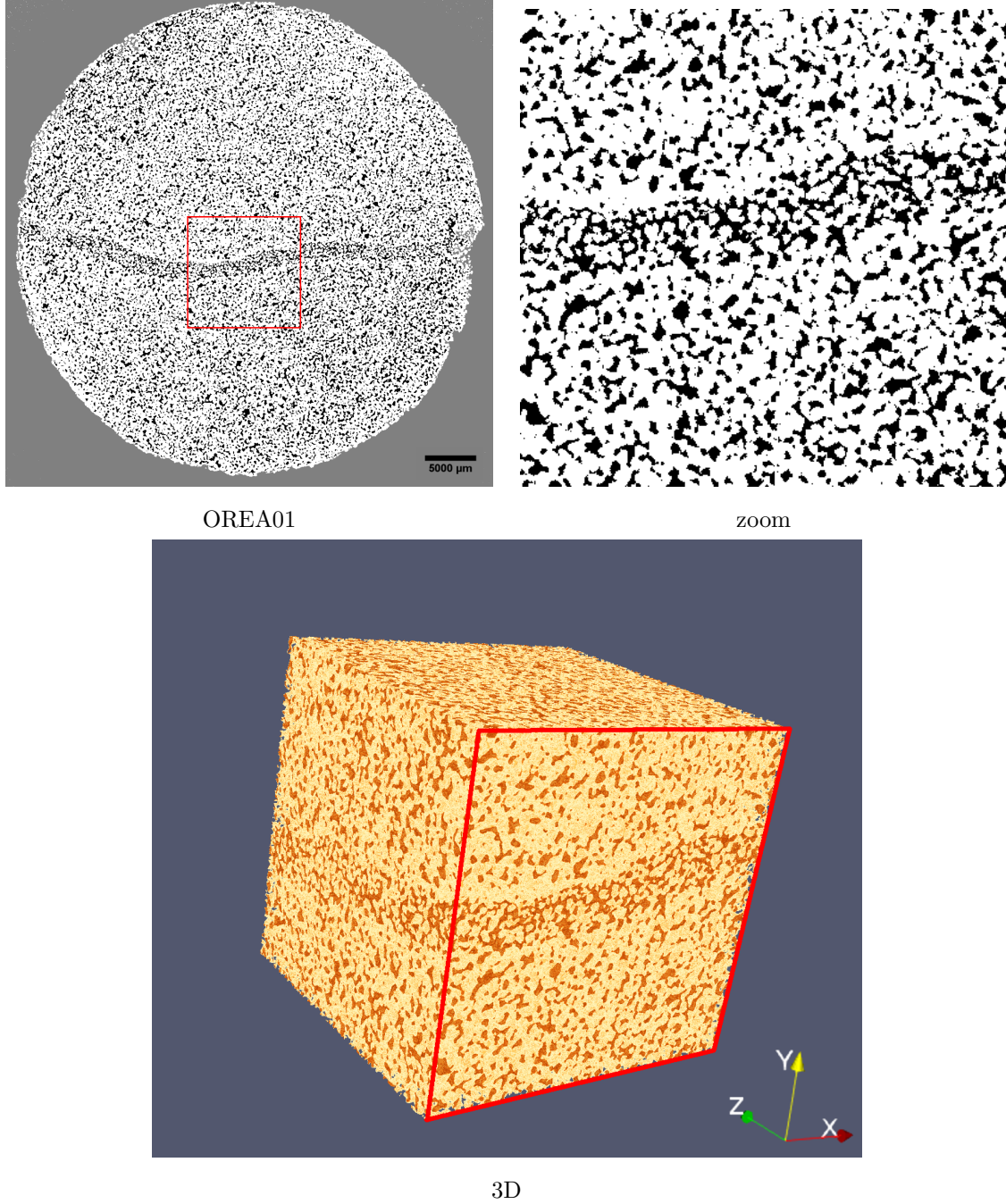


**Figure 7.11:** Orientation of the reference system  $(x, y, z)$  for the dilation band sample OREA01.

With respect to the samples containing natural deformation bands, permeability in the multi-strand bands is near to zero in all directions, with exception for the interband, which presented a permeability contrast of 4 orders of magnitude between the direction parallel to the deformation band (1.62 mD) and the other two directions ( $10^{-4}$  mD). The single-strand band ISBSC01 reported zero permeability in the core, similarly to the multi-strand bands, and a damage zone with 1 order of magnitude lower permeability ( $10^{+3}$  mD) than that of the undisturbed sand. The band reported a permeability along the direction y (orthogonal to the deformation band plane) 0.5 - 1 order of magnitude higher than that in the other two directions. The permeability values at the two sides of the single-strand band ISBSC01 (damage (a) and (b), Fig. 7.6) are similar. The dilation band OREA01 reported similar values in the three directions for core, contour, and damage zones. Core and contours had permeability of the same order of magnitude ( $10^{+3}$  mD), whereas the damage zone reported higher values on one side (a) with respect to the other one (b) that has permeability values close to those of core and contours.

## 7.5.2 Discussion

The permeability values in the analysed samples are proportional to the porosity calculations: high permeability occurs in highly porous samples and vice versa. The artificially cemented samples have similar values to those of the natural ones, which is due to the fact that imperfections are only partially included in the sub-volumes.

In the deformation band samples, multi-strand bands were highly compacted, thus the flow was halted in a similar way in all directions (zero permeability). The single-strand band core reported a permeability similar to the multi-strand bands, whereas the damage zone had a value 1 - 2 orders of magnitude smaller than that of the undisturbed sand. The permeability data for the dilation band did not clearly assess the flow properties of the sample, which was characterised by similar values in all the band zones with a maximum oscillation of 0.5 order of magnitude. Core and contours reported a permeability of 0.5 - 1 orders of magnitude smaller than the undisturbed sand, whereas the damage zone had a permeability comparable to that of the undisturbed sand, with a small difference in the two sides of the band.

The permeability calculations for multi-strand, single-strand bands, and undisturbed sand presented in this Chapter are 1 - 2 orders of magnitude higher than the ones reported in the literature (Table 7.1). The difference could be interpreted taking into account the distinct procedures for data acquisition, i.e., laboratory measurement with permeameter in Sallet and Wibberley (2013) and image analysis in this doctoral work. In addition, the permeameter used in Sallet and Wibberley (2013) required a confining pressure on the sample, which was of about 20 MPa for

**Table 7.6:** Permeability calculations with PAT of naturally and artificially cemented samples tested in Chapter 6 and of deformation band (multi-strand, single-strand, and dilation bands) samples from Bédoin 3 and 4.5. For sample names and for sub-volumes, refer to Table 6.1 and to Fig. 7.6, Fig. 7.7, and 7.8.

value no.	sample type, name, and test phase	$\kappa_x$ [mD]	$\kappa_y$ [mD]	$\kappa_z$ [mD]
Tested samples (see Ch. 6):				
01	Nat (undisturbed sand)	$2.66 \cdot 10^4$	$2.50 \cdot 10^4$	$2.70 \cdot 10^4$
02	NatPore	$4.68 \cdot 10^3$	$4.34 \cdot 10^3$	$5.28 \cdot 10^3$
03	NatDB	$1.29 \cdot 10^4$	$1.43 \cdot 10^4$	$1.41 \cdot 10^4$
04	Artif20	$1.55 \cdot 10^4$	$1.57 \cdot 10^4$	$1.41 \cdot 10^4$
05	Artif15	$4.53 \cdot 10^3$	$3.46 \cdot 10^3$	$2.04 \cdot 10^3$
06	Uncement	$2.45 \cdot 10^4$	$2.28 \cdot 10^4$	$2.33 \cdot 10^4$
Multi-strand bands:				
07	ISBS4501, core	0	0	0
08	ISBS4502, core	$3.01 \cdot 10^{-4}$	0	$4.37 \cdot 10^{-5}$
09	ISBS4503, core	0	0	0
10	ISBS4503, interband	1.62	$1.62 \cdot 10^{-4}$	$8.89 \cdot 10^{-4}$
Single-strand band ISBSC01:				
11	core	0	7.63	0
12	damage (a)	$7.29 \cdot 10^2$	$1.05 \cdot 10^3$	$9.91 \cdot 10^2$
13	damage (b)	$1.16 \cdot 10^3$	$1.08 \cdot 10^3$	$1.19 \cdot 10^3$
Dilation band, OREA01:				
14	core	$6.96 \cdot 10^3$	$7.73 \cdot 10^3$	$7.16 \cdot 10^3$
15	contour (a)	$6.92 \cdot 10^3$	$3.86 \cdot 10^3$	$6.64 \cdot 10^3$
16	contour (b)	$4.22 \cdot 10^3$	$3.51 \cdot 10^3$	$3.86 \cdot 10^3$
17	damage (a)	$1.02 \cdot 10^4$	$1.02 \cdot 10^4$	$8.68 \cdot 10^4$
18	damage (b)	$6.13 \cdot 10^3$	$7.99 \cdot 10^3$	$1.95 \cdot 10^3$

the values reported in Table 7.1, while the samples measured with image analysis were not under pressure. The sample dimension was also slightly different, since the permeameter required cores of 20 - 25 mm of diameter and the sub-volumes measured in this work are about 5 mm wide and the size became smaller when specific zones of the band were extracted. This implies also that individual zones within the bands could be isolated for permeability calculation with image analysis, whereas this could not be executed with the permeameter, which provided permeability of the entire sample.

# Chapter 8

## Conclusions and Perspectives

### 8.1 Summary of the work and conclusions

This work has been focused on the micro-mechanics of weakly cemented sands. The motivation to study such materials stemmed from observations of deformation bands in weakly cemented sand outcrops at Bédoin, France. Deformation bands have been identified in many sandstones and sand deposits (as well as in other rock types), which were studied for construction purposes and as potential fluid reservoirs. Therefore, understanding the origin and evolution of this type of localised deformation in an analogue sand deposit, i.e., Bédoin, can contribute to advances in the management of the subsurface and its resources. A number of previous studies focused on the characterisation and the conditions for the occurrence of natural deformation bands in sand or sandstone deposits at the outcrop scale. The scope of this work has been to study the weakly cemented Bédoin sand at the laboratory scale. This included both characterising the natural material (undisturbed sand samples and samples containing natural deformation bands) and assessing the localised deformation patterns that developed when the material was mechanically loaded in the laboratory.

The weakly cemented sands have been collected through careful sampling with an innovative tool and procedure, which preserved their natural imperfections. The material has been inspected through polished thin sections at the Scanning Electron Microscopy, showing increasing grain fragmentation and decreasing porosity going from undisturbed sand and dilation band to single-strand bands, multi-strand bands, and cluster. Silica and clay cements have been also observed at nano-scale. In particular, syntaxial quartz overgrowths have been identified in all sample types, not only in deformation bands but also in undisturbed sand; however, quartz overgrowths have reported higher content in multi-strand bands and cluster. Conversely, clay cement reported higher content in undisturbed sand and dilation band rather than in multi-strand bands and cluster. The advanced image analysis (Charging

Contrast Imaging and Energy Dispersive X-ray Diffraction) of the silica and clay cements revealed processes - i.e., syntaxial quartz overgrowths and illitization of kaolinite - that must have required temperatures higher than 70° in order to occur.

The observations of samples through non-destructive X-ray Computed Tomography enabled the identification of natural imperfections: depositional layers, region of enhanced porosity, elongated pore surrounded by cement, and pre-existing dilation band. One of these imperfections, i.e., the depositional layers, was only visible through Digital Volume Correlation, performed on syn-deformation X-ray Tomography scans. Triaxial and isotropic compression tests and processing of syn-deformation images of the Bédoin sand samples containing these imperfections have shown that shear bands were triggered by regions of enhanced porosity, but not by the elongated pore surrounded by cement. In addition, depositional layers in the samples did not influence the development of shear bands and the pre-existing dilation band started to reactivate but then it soon stopped without showing any further evolution. In particular, it is argued that the cement surrounding the elongated pore reinforced locally the material, thus making the sample more resistant, and that the pre-existing dilation band was not favourably oriented for the reactivation.

The artificially cemented samples, prepared with an original cementation procedure that reproduced similar structure and composition of the natural Bédoin sediment but without reproducing the observed imperfections, have shown that localised deformation developed with a network of shear bands that occupied a larger volume of the sample than the volume affected by the laboratory-induced shear bands in the natural samples. In addition, the analysis of the mechanical behaviour has shown a delay in the peak stress exhibition and lower values of the peak stress with respect to the natural samples.

Non-destructive image acquisition has also enabled porosity and permeability calculations on 3D volumes of weakly cemented sands through the software Fiji (ImageJ) and an in-house software Pore Analysis Tool. The porosity values have reported a great reduction and have characterised distinct zones in deformation bands, such as core, contours, and damage zone. Porosity reduced from about 30% in undisturbed sand to values lower than 10% in the core of single- and multi-strand bands, with the latter closer to zero. The two band types did not show contours, but in the multi-strand bands an interband zone has been identified, with porosity similar to that of single-strand bands. A dilation band has shown porosity in the core of about 30%, similar to that in the undisturbed sand, while its contours have reported half of that value. Permeability analysis has shown a reduction of 3 - 4 orders of magnitude from undisturbed sand to single- and multi-strand bands, whereas the dilation band has reported a reduction of about one order of magnitude.

Considering the objectives initially defined in Chapter 1, the following conclu-



sions are drawn for the natural material:

- grain fragmentation observed in the Bédoin outcrops could be considered the principal local source of silica for re-precipitation as syntaxial quartz overgrowths in the Bédoin sands;
- a great amount of clay is assumed to have infiltrated the Bédoin sediments at a later stage, after the occurrence of localised deformation;
- considering a gradient of about 30°C per km, it is argued that the Bédoin sands reached a great depth of about 2 - 3 km, which would have enabled the occurrence of the observed processes - i.e., illitization of kaolinite and syntaxial quartz overgrowths - thus extending the burial depth estimations reported in the literature (depth of 0.5 - 1.3 km);
- all the analysed deformation bands of Bédoin showed proportional relationship between porosity and permeability. Porosity enabled the distinction of zones in each band type; permeability in single- and multi-strand bands reported a value equal to zero (according to an image resolution of 10.5 - 27  $\mu\text{m}/\text{px}$ ); in a dilation band permeability was 0.5 - 1 order of magnitude lower than that of the undisturbed sand ( $10^{+4}$ ).

Moreover, with regards to the assessment of the mechanical behaviour of the Bédoin material, it can be concluded that:

- the artificially cemented and uncemented sand samples seemed to exhibit a delayed peak stress compared to the natural samples;
- although bands of localised deformation developed, the stress-strain curves did not show clear stress drops (only few exceptions); therefore, the weakly cemented sands exhibited a mechanical behaviour more similar to sands rather than to cemented sands;
- the onset of localised deformation occurred in a narrower volume within the natural samples, whereas in the artificially cemented and uncemented samples it occurs in a wider volume;
- some of the natural imperfections in the Bédoin weakly cemented sands may have influenced the occurrence of laboratory-induced shear bands (i.e., regions of enhanced porosity), some other imperfections have not (i.e., depositional layers, pore surrounded by cement, pre-existing dilation band), while the absence of these imperfections (i.e., artificially cemented samples) may have promoted a strain localisation within a wider volume, expressed through the appearance of a wider network of bands;

- some of the imperfections (i.e., elongated pore surrounded by cement and the pre-existing dilation band) seem to have strengthened the samples;
- the imperfections seem to not have played a role in the inclination of the laboratory-induced shear bands.

A significant part of this doctoral work has been produced by performing image analysis. The results obtained and the related conclusions show the advantages of combining a destructive 2D image acquisition technique at very high resolution (Scanning Electron Microscopy) with a non-destructive one at a lower resolution (X-ray Computed Tomography) but with 4D (3D + time) characterisation of laboratory-induced deformation, thus enabling to target different aspects of the processes occurring in the weakly cemented sands from Bédoin.

## 8.2 Perspectives for future work

This doctoral work has been focused on the mechanical behaviour of weakly cemented sands in their natural depositional condition and characterised by natural imperfections, derived from diagenetic and later deformation processes. Other important factors, such as packing density or cement composition, have just been mentioned. The quality of the sample ends also plays a role in the mechanical behaviour of the samples, as much as their imperfections; however, such effect has not been measured in this study. The mechanical tests have been performed on relatively small samples ( $d = 11$  mm,  $h = 22$  mm) in order to improve image resolution, thus the size effect should be also considered when interpreting the results. More experiments could be performed on larger samples to explore the size effect and to study the role of other factors in the mechanical behaviour of the material. Further tests at higher confining pressure that reproduce the burial conditions, inferred from the microscopic observations, are also recommended.

The experimental work has mainly concentrated on the mechanical behaviour of 4 naturally weakly cemented samples compared to that in artificially cemented and uncemented Bédoin sand samples. Non-destructive methods, such as X-ray Computed Tomography and Digital Volume Correlation, have been used to assess the mechanical behaviour of the samples and to understand the influence of particular natural imperfections on the deformation band occurrence. Further experiments are required to broaden the current understanding of the role of imperfections in naturally weakly cemented samples on the deformation band occurrence.

The reactivation of a pre-existing bands of localised deformation is particularly interesting, especially during field (usually faults) applications that involve the injection of fluids. In this work, the effects of a natural dilation band inclined at  $32.5^\circ$

to the horizontal has been investigated when the sample was subjected to laboratory loading. More samples containing natural deformation bands in different orientations could be tested to further comment on the deformation band reactivation within weakly cemented sands.

In this work, porosity and permeability have been calculated within the tested samples via image processing. To better understand the fluid transport properties in the Bédoin material, Neutron-beam time at 2 European Neutron facilities has been awarded to monitor in 3D the oil front within the Bédoin samples. The advantage of using oil against water is that the weakly cemented samples keep their structural integrity during the oil injection, while with water injection they do not.

# Appendix A

## Sampling blocks of weakly cemented sand

The sampler was built to extract material from vertical outcrops. The tool produced prismatic blocks of weakly cemented material with a triangular base, which was chosen for the advantage of cutting the vertical surface without the need to cut also the material that surrounds the block of interest. The following procedure was adopted to assembly the sampler pieces:

1. A step in the outcrop is excavated, by removing the top part of the outcrop right above the sample to extract;
2. the metallic triangular plate with handle (Fig. 3.4a) is slowly and progressively inserted in horizontal way below the sample to extract, while hand pressure is exerted on the wooden handle and sand is simultaneously excavated under the metallic plate;
3. with the help of a hand saw, two vertical cuts are slowly performed along the two sides of the triangular plate inserted in the outcrop; the cuts are performed until the metallic triangular plate is reached;
4. the two short wooden plates (Fig. 3.4a) are inserted where the saw cuts were performed; the two pieces can be jointed to the horizontal triangular plate (see the four big holes in the triangular plate, Fig. 3.4a) and they are temporarily blocked with clamps (Fig. 3.4b);
5. the third long wooden plate (Fig. 3.4a) is positioned vertical and parallel to the outcrop surface and it is screwed to the other two wooden plates still blocked with clamps;
6. the plate containing the sample is lifted and the three wooden plates are screwed to the triangular plate that is provided with holes for this purpose

(see the six small holes in the triangular plate, Fig. 3.4a), so that the clamps can be removed.

At the end of this procedure, the triangular block of naturally cemented sand is incorporated in the triangular-based prismatic box (Fig. 3.4c), which can be carried with the use of the provided handle.

# Appendix B

## Detailed analysis of the mechanical tests with in situ X-ray Computed Tomography

### B.1 Isotropic compression test of a natural sample from Bédoin

The complete set of DVC results shown in Figure B.1 is described below:

**DVC 00-01** During the first step of isotropic compression, the sample developed shear bands subparallel to the sample ends. The shear bands was interpreted to represent the contact between depositional layers that constituted the sample. These shear bands did not show a volumetric variation, except for the thicker band at the upper end of the sample, whose shear corresponded to dilation. Shear was generated also at the upper and lower ends, due to the contact between the sample and the ceramic platens, despite the lubrication (Fig. 4.1b). In particular, the upper end of the sample was affected by dilation, whereas the lower one by compression and less dilation.

**DVC 01-02 to 06-07** The DVC of the steps from 01-02 to 06-07 did not show any localised strain localisation (e.g. shear bands), neither in shear nor in volumetric strain fields. Shear was detected at the sample boundaries, representing the deformation at the contact between the neoprene membrane, the ceramic platens, and the sample. The volumetric strain field maps and the overlaps showed small regions of compression and of dilation distributed homogeneously in all the sample.

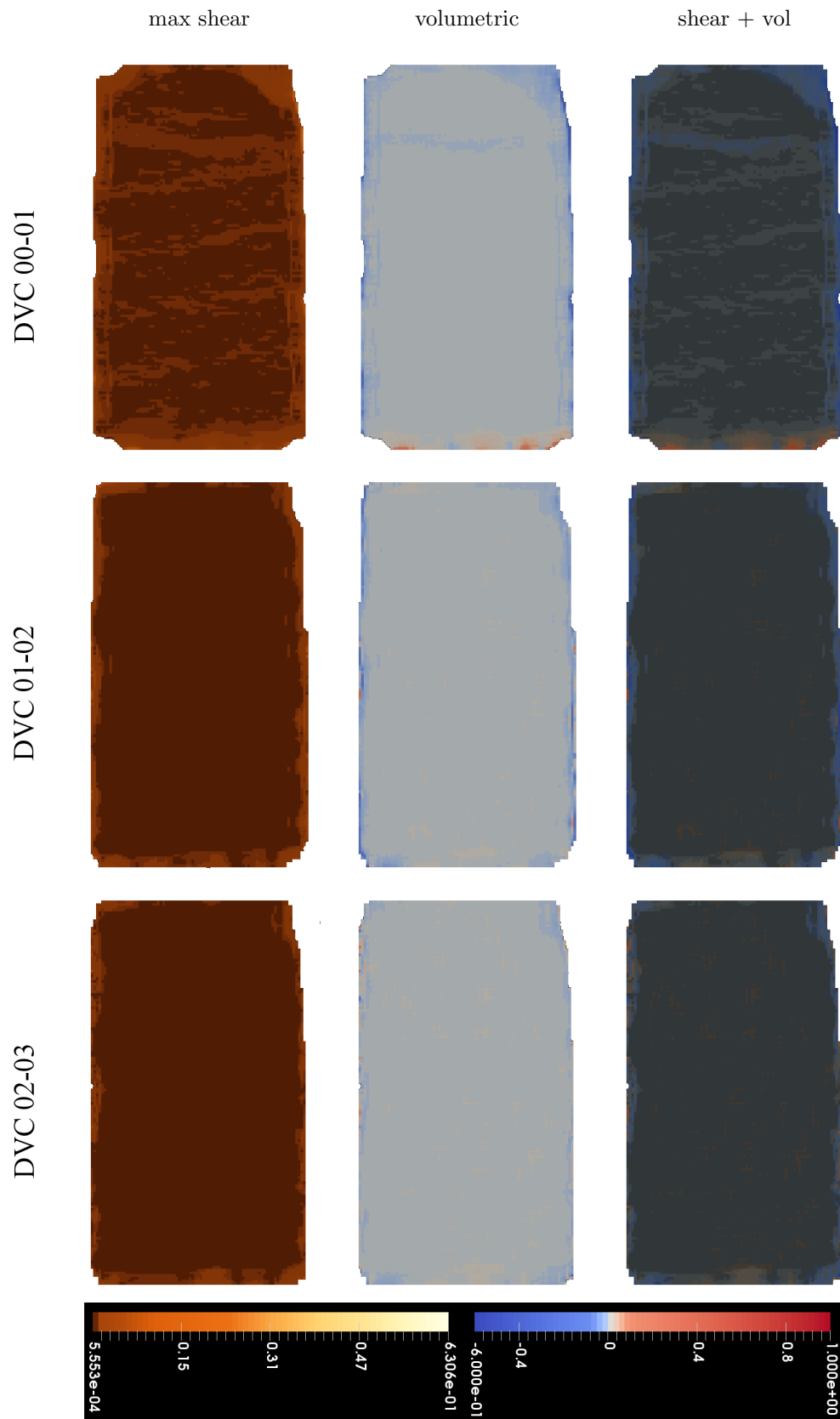


**Figure B.1a:** DVC results of the isotropic compression test

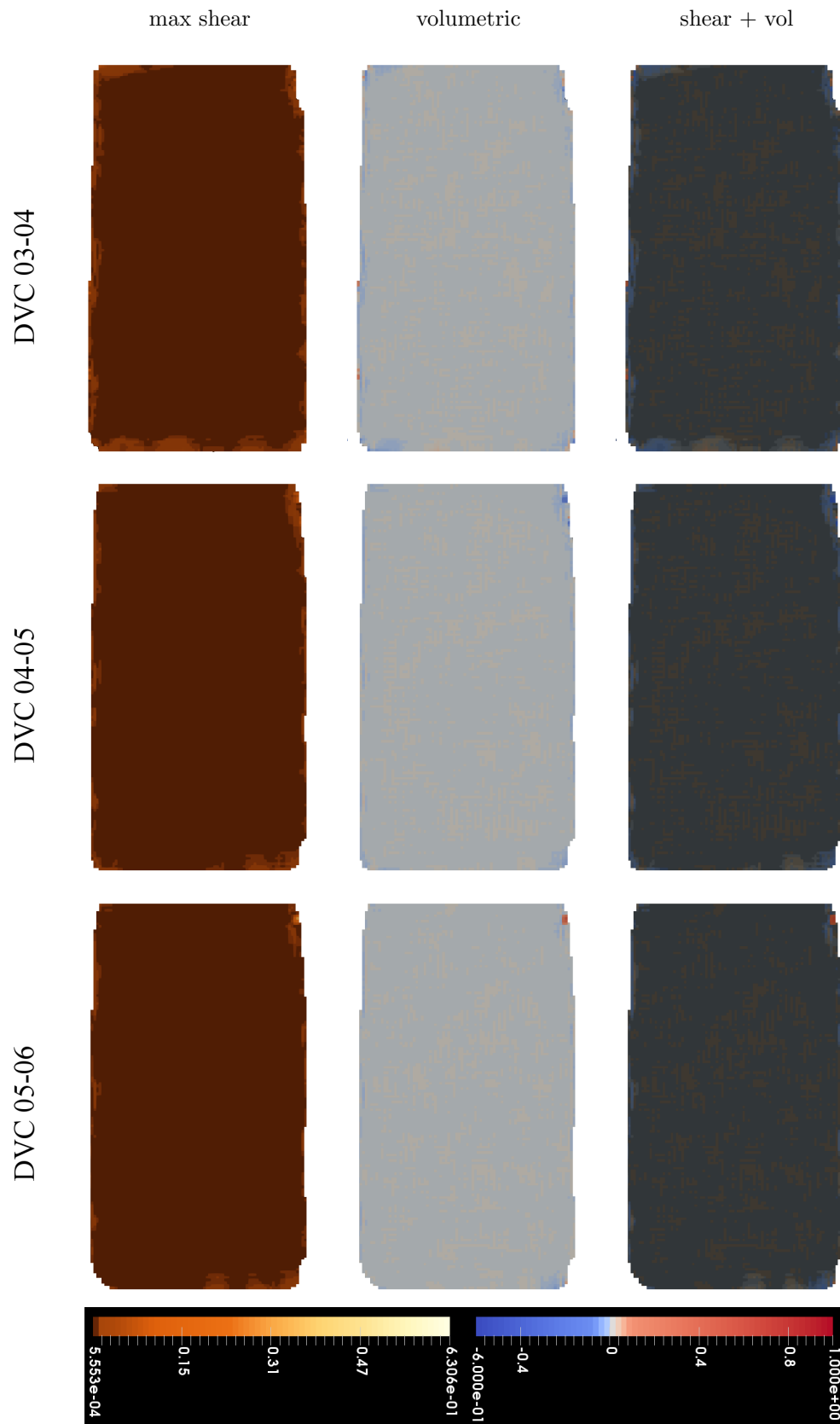


Figure B.1b



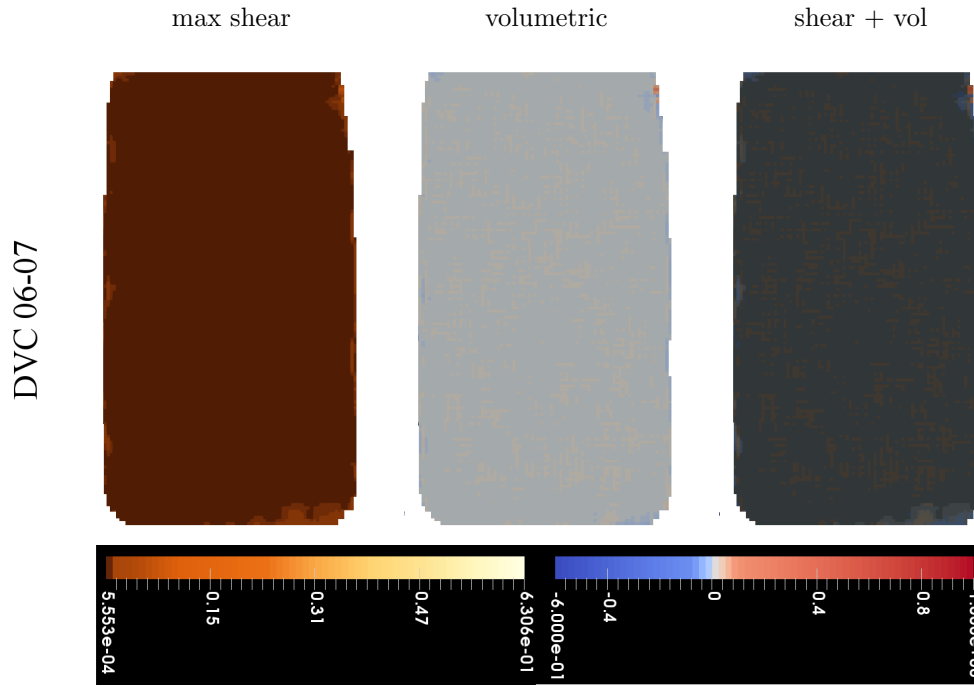


Figure B.1c

## B.2 Triaxial compression tests

### B.2.1 Naturally cemented Bédoin sand containing a region of enhanced porosity

The complete set of DVC results shown in Figure B.2 is described below:

**DVC 00-01 and 01-02** The confining pressure of 1 MPa was reached in two steps: 00-01 and 01-02. In the first step (DVC 00-01) that led to a confining pressure of 0.5 MPa, the sample showed in the volumetric strain field map a dilating region, which seems to correspond to the region of enhanced porosity. In the second step of the isotropic compression (DVC 01-02) that led to a confining pressure of 1 MPa, a small increment of dilation was reported in the same region.

**DVC 02-03** With the beginning of deviatoric loading, the onset of strain localisation occurred along a shear zone at the lower of the sample. Shear along the zone corresponded to compression, except for the small region of dilation that developed during the previous steps of isotropic compression (DVC 00-01 and 01-02) and that continued to dilate. The rest of the sample was affected by low degree of distributed dilation and compression.

**DVC 03-04** In this small DVC step, further development of shear occurred along the shear zone identified in the previous step. More compression grew around the shear zone in the lower part of the sample, while the small region of dilation developed further dilation.

**DVC 04-05** The shear zone developed high shear intensity, thus defining a clear shear band with inclination of  $42^\circ$  to the minor principal stress  $\sigma_3$  (i.e. horizontal). The peak stress is reached at  $\epsilon_a = 3\%$  and with a value of the deviatoric stress  $q = 3.8$  MPa (Fig. 6.6). Shear grew at the upper-right side of the sample. The dilated region at the lower part of the sample continued to dilate and the overlap of the two strain field maps revealed that this dilated region was located below the shear band, which is dominated by compression.

**DVC 05-06** The shear band evolves into a *zigzag* shear band with inclinations of  $-55^\circ$  and of  $35^\circ$  to the horizontal (negative angle is clockwise from horizontal). The shear band grew towards the sample sides, surrounded by other shear bands of less shear intensity, forming together a small network of bands. Compression and small regions of dilation developed in this region. Shear and compression develop also at the top and in the central part of the sample, where a shearing region seems to connect diagonally lower-left and upper-right sheared zones. The black region identifies an uncorrelated volume with DVC due to a high degree of deformation.

**DVC 06-07** Volumetric compression seems to decrease in this step with respect to the previous one, whereas dilation in the region of enhanced porosity grew in intensity and width. The dominant band at the lower part of the sample seems to lose its zigzag aspect. The diagonal zone from lower-left to upper-right developed further shear and compression.

**DVC 07-08** Another band of intense shear developed in the diagonal zone that connected lower-left with upper-right part of the sample, with inclination of  $55^\circ$  to the horizontal. A further band orthogonal to latter one develops at the upper part of the sample, inclined of  $-35^\circ$  to the horizontal and looking subparallel to the shear band at the lower part of the sample. Volumetric compression at the lower part of the sample was reduced to few small regions, as well as dilation. On the contrary, compression developed along the diagonal shear band, whereas dilation appeared at the intersection between the later two bands. A tridimensional view of the maximum shear strain field map at this DVC step is available at the following link: <https://doi.org/10.6084/m9.figshare.10079156.v2>.

**DVC 08-09** During the deviatoric unloading, shear correspondent to volumetric dilation developed along the shear bands risen during the deviatoric loading.

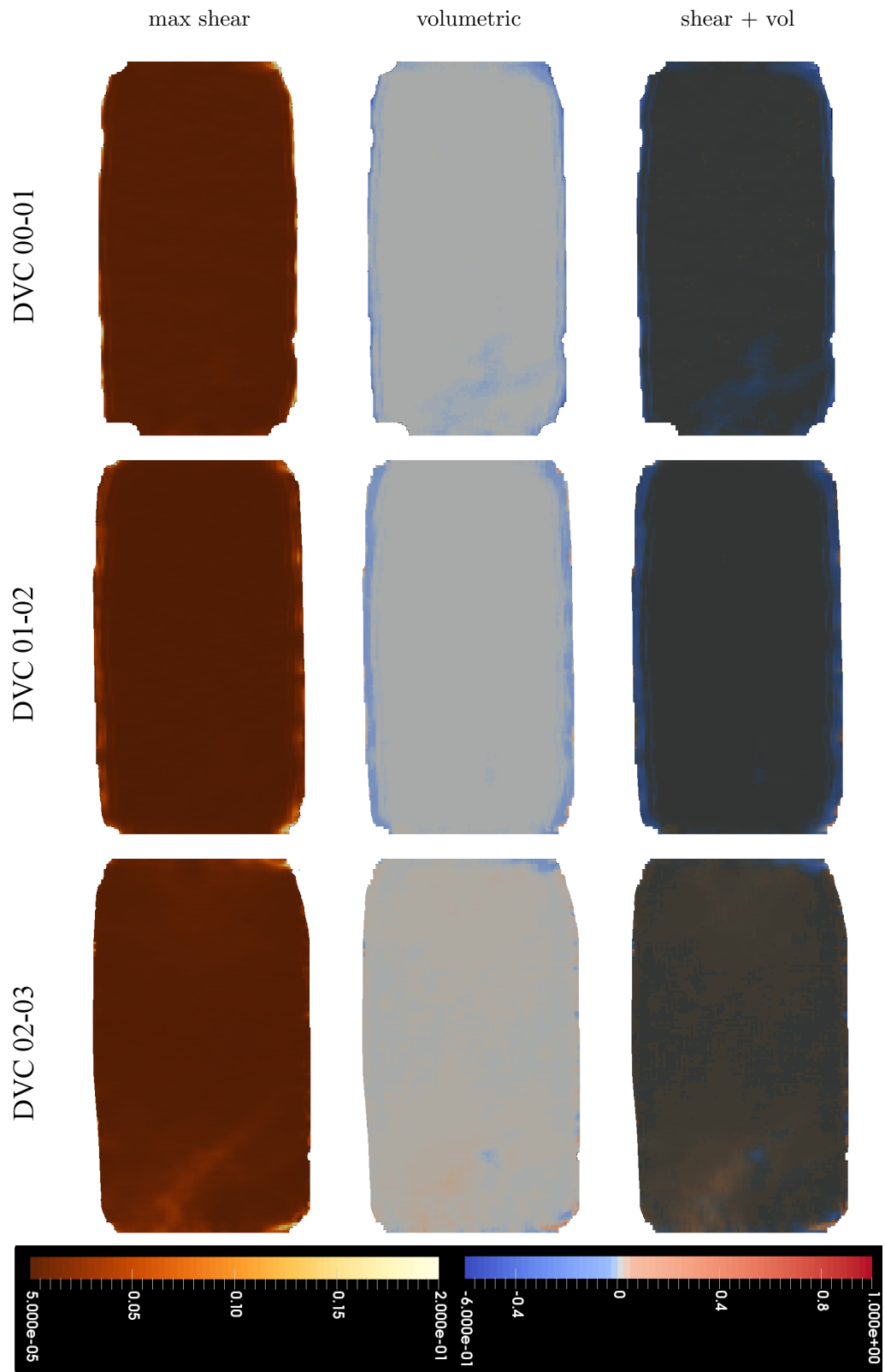


**Figure B.2a:** DVC results of the triaxial compression test on a naturally cemented sample containing a region of enhanced porosity

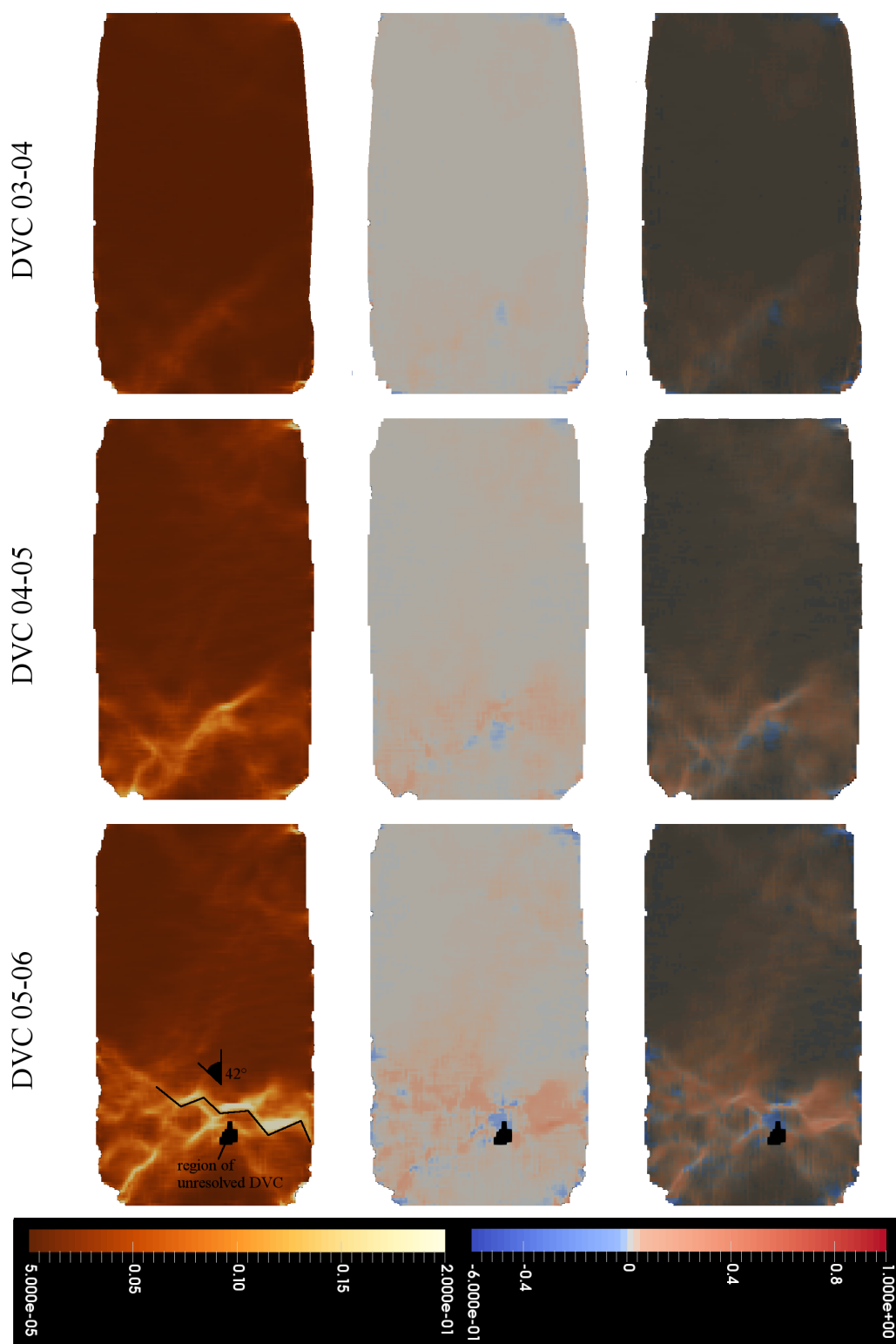


Figure B.2b

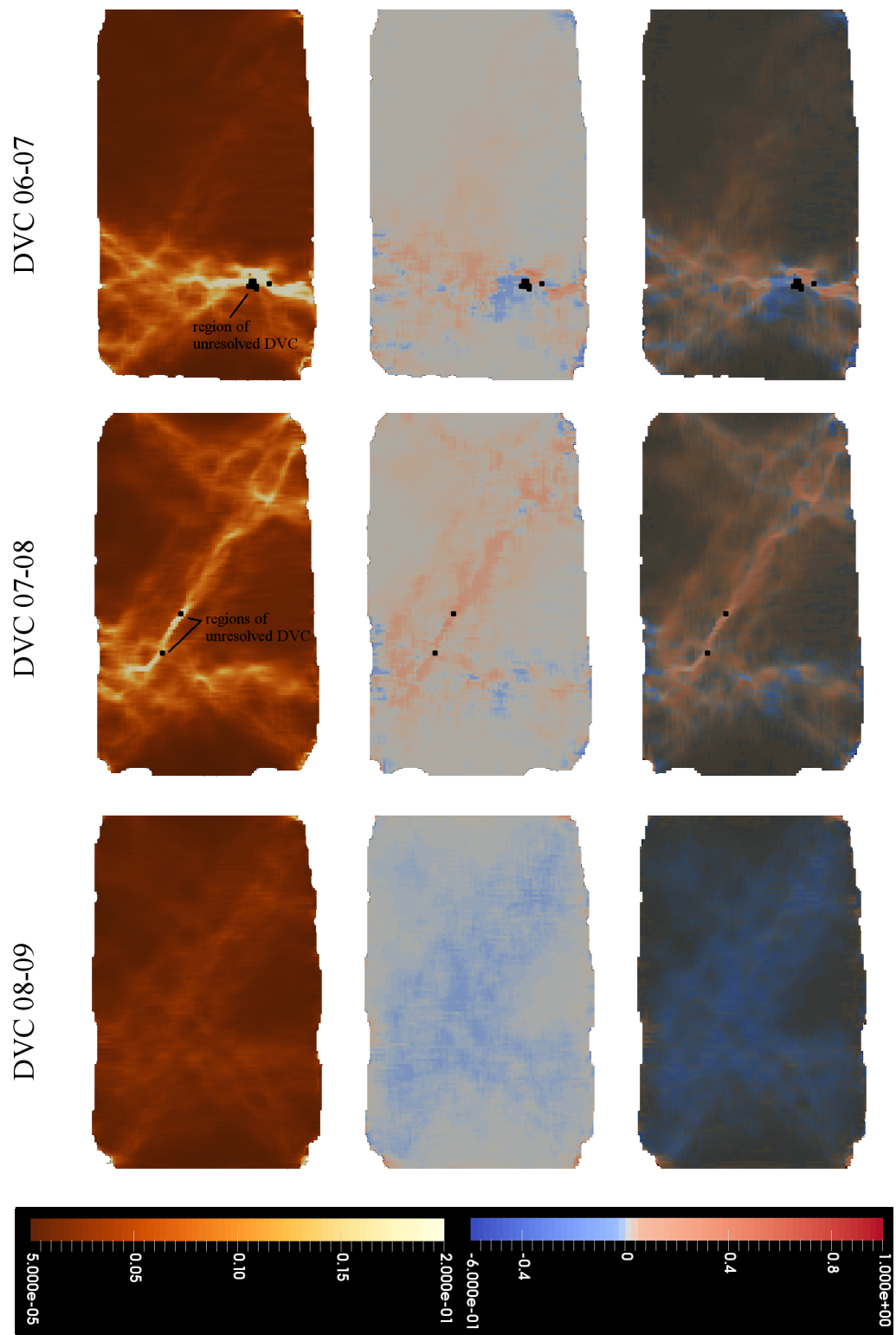


Figure B.2c

## B.2.2 Naturally cemented Bédoin sand containing an elongated pore

The complete set of DVC results shown in Figure B.3 is described below:

**DVC 00-01** Confining pressure was applied in two steps, 00-01 until 0.5 MPa

and 01-02 until 1 MPa, and only the DVC maps of the first step are available. With the first step of confining pressure there was a minor occurrence of shear and volumetric strains, distributed rather homogeneously in the sample with small regions of minor compression and dilation.

**DVC 02-03** When deviatoric loading was applied, deformation localised in two shear zones at the upper and lower ends of the sample at  $-56^\circ$  and  $48^\circ$  (negative is clockwise from horizontal), respectively, and meeting at the central and right side of the sample. The overlap of the two strain maps shows that the shear developed in this step corresponded to volumetric compression close to the sample ends and to volumetric dilation at the central and right side of sample, where the two shear zones meet. In the maximum shear strain field map, a small region at the central and left side of the sample that corresponds to the elongated pore showed a small component of shear, but the volumetric strain field map did not indicate any perceptible volumetric variation.

**DVC 03-04** The peak stress value of 3.4 MPa was reached at 3% of axial strain and, before reaching the peak, the sample was affected by a stress drop (Fig. 6.10). The DVC maps of this step show that a dominant shear bands composed by parallel shear planes developed close to the top end of the sample and with inclination of  $-48^\circ$  (negative angle is clockwise from horizontal) (see a 3D view at <https://doi.org/10.6084/m9.figshare.10081268.v1>). The high shear rate of the band corresponded to a great volumetric compression, whereas small regions of dilation developed between the sub-parallel shear planes and along the right side of the sample. In addition, another shear band transversal ( $56^\circ$ ) to the dominant ones appeared at the top of the sample, which showed volumetric compression. The shear plane at the lower end of the sample did not develop intense shear, differently from the top end; however it reported shear also during this DVC step, showing a conjugate direction ( $48^\circ$ ) to that of the dominant shear band at the top part of the sample.

**DVC 06-07** During deviatoric unloading, shear developed principally in the top part of the samples, especially along the dominant band (at  $-45.5^\circ$ , where negative is clockwise with respect to  $\sigma_3$ ) and along the later shear band at the top of the sample. Minor regions of shear was identified at the lower part of the sample, but less spatially organised. The elongated pore, which seemed to not react during the deviatoric loading, finally showed high shear with dilatant component during this step.

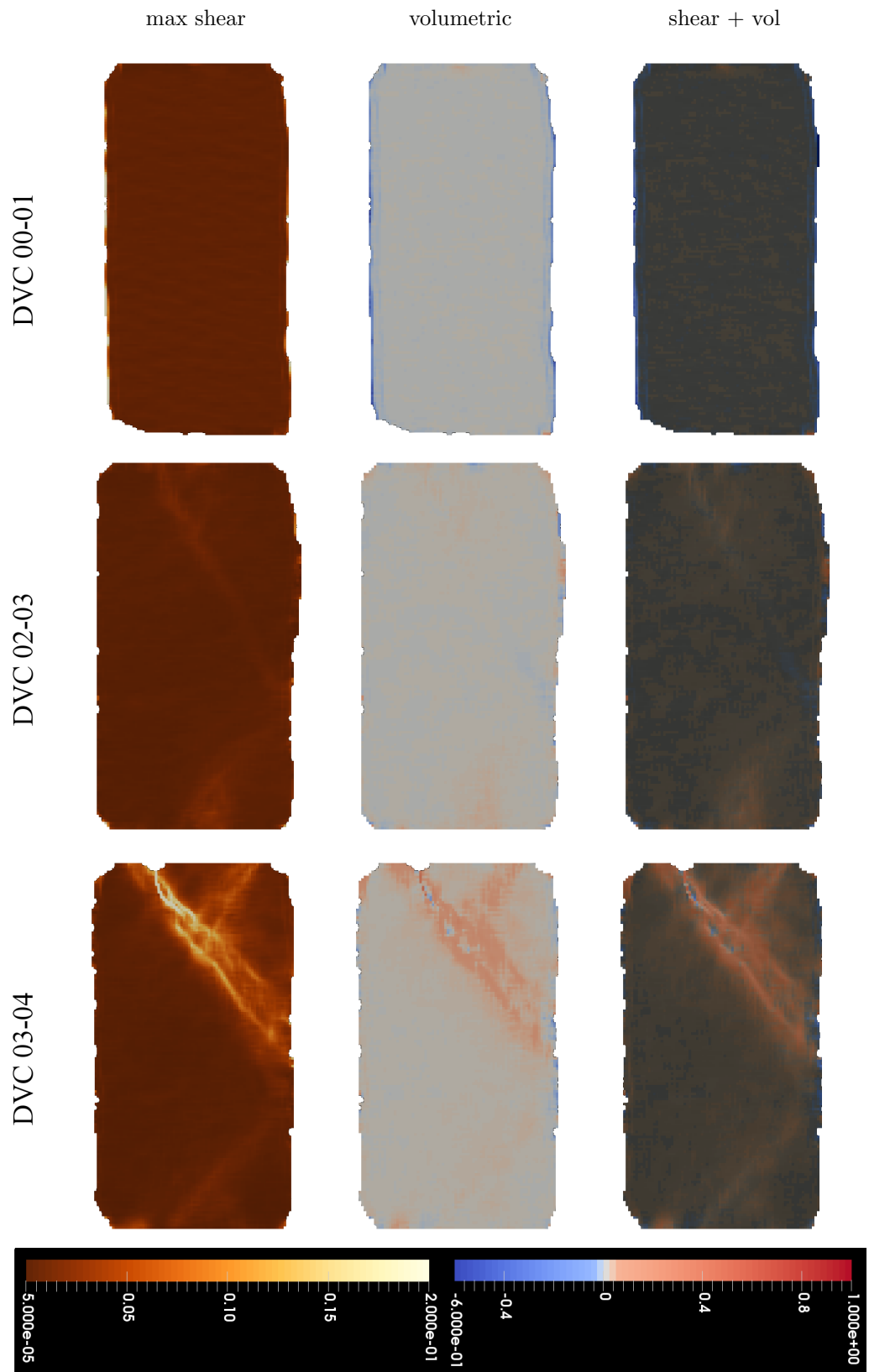


**Figure B.3a:** DVC results of the triaxial compression test on a naturally cemented sample containing an elongated pore

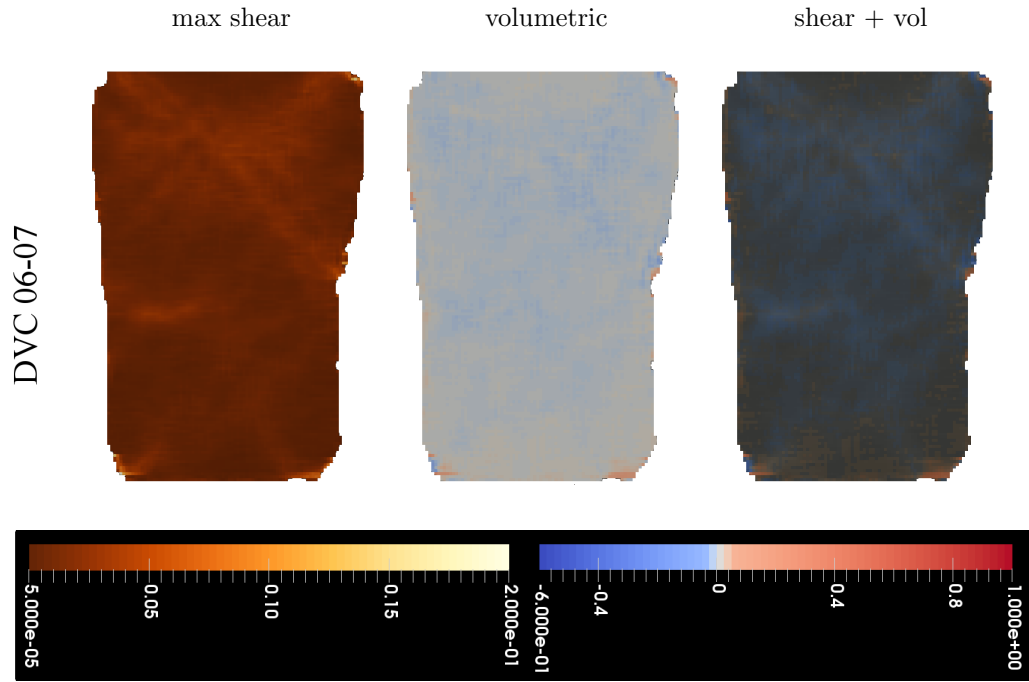


Figure B.3b

### B.2.3 Naturally cemented Bédoin sand containing a pre-existing dilation band

The complete set of DVC results shown in Figure B.4 is described below:

**DVC 00-01** The confining pressure of 1 MPa was reached during this step. Confining pressure generated a low degree of shear distributed rather homogeneously in the sample.

**DVC 01-02** When the deviatoric loading was applied, the pre-existing dilation band inclined of  $32.5^\circ$  started to shear. The volumetric strain field map and the overlap showed that this shear provided further dilation to the dilation band. The rest of the sample was affected by small distributed shear regions of dilation and compression, similarly to the previous step but with higher intensity.

**DVC 02-03** From about 1% of axial strain, the dilation band became hardly detected in the maximum shear strain field map of the sample, whereas is not visible at all in the volumetric one. The sample started to develop a sheared region close to the lower end and a lower shear component appeared on the upper-right end of the sample. Shear corresponded to volumetric compression at lower and upper parts of the sample.

**DVC 03-04** During this step, the stress-strain curve shows stress fluctuations (see Fig. 6.13). The sample reached a peak stress value of about 4.2 MPa at an axial strain of 3%. The onset of localised deformation was observed in the lower part of the sample, where a zigzag shear zone developed within a highly sheared



zone. Minor shear appeared at the upper-right side of the sample. All the shear developed in this step corresponds principally to volumetric compression.

**DVC 04-05** The zigzag shear band at the lower part of the sample grew in intensity, thus defining a dominant shear band (inclinations of  $\pm 40^\circ$  to the horizontal) extending towards the right side of the sample. A diagonal shear zone from lower-left to upper-right of the sample was identified, with an angle of  $65^\circ$  to the horizontal. The shear zone at the lower part of the sample was still dominated by volumetric compression, but small regions of dilation developed in the compressed region, at the intersection between the dominant zigzag shear band and the later diagonal shear zone.

**DVC 05-06** This step showed a further development of the processes observed in the previous step.

**DVC 06-07** A network of shear bands developed at the lower part of the sample, showing a high shear degree. The network of shear bands corresponded to small regions of intense compression and dilation in the volumetric strain map. Shear and volumetric compression grew along the diagonal shear zone that goes towards the top-right end of the sample. The rest of the sample develops small regions of compression and of dilation with small intensity, similarly to step 01-02.

**DVC 07-08** The shear bands in the network at the lower part of the sample showed preferential inclinations of  $-48^\circ$  and  $42^\circ$  to the horizontal. The diagonal shear band that connected lower-left with upper-right ends of the sample with an inclination of  $64^\circ$  reported a well-developed compression component.

**DVC 08-09** The shear band network showed less shear and compression intensities, while the diagonal shear band developed further intense shear with compression. Dilation was still reported in the region of the shear band network. The 3D shear strain field map (<https://doi.org/10.6084/m9.figshare.10084706.v1>) shows that the bands in the network follow the two main directions ( $-48^\circ$  and  $42^\circ$ ).

**DVC 09-10** During the deviatoric unloading, shear and dilation developed with higher intensity along the diagonal shear band with inclination of  $63^\circ$  to the horizontal and with high intensity at the centre of the sample. The network of shear bands at the lower part of the sample did not show unloading. The dilation band, active in step 01-02, did not reactivate during the unloading.

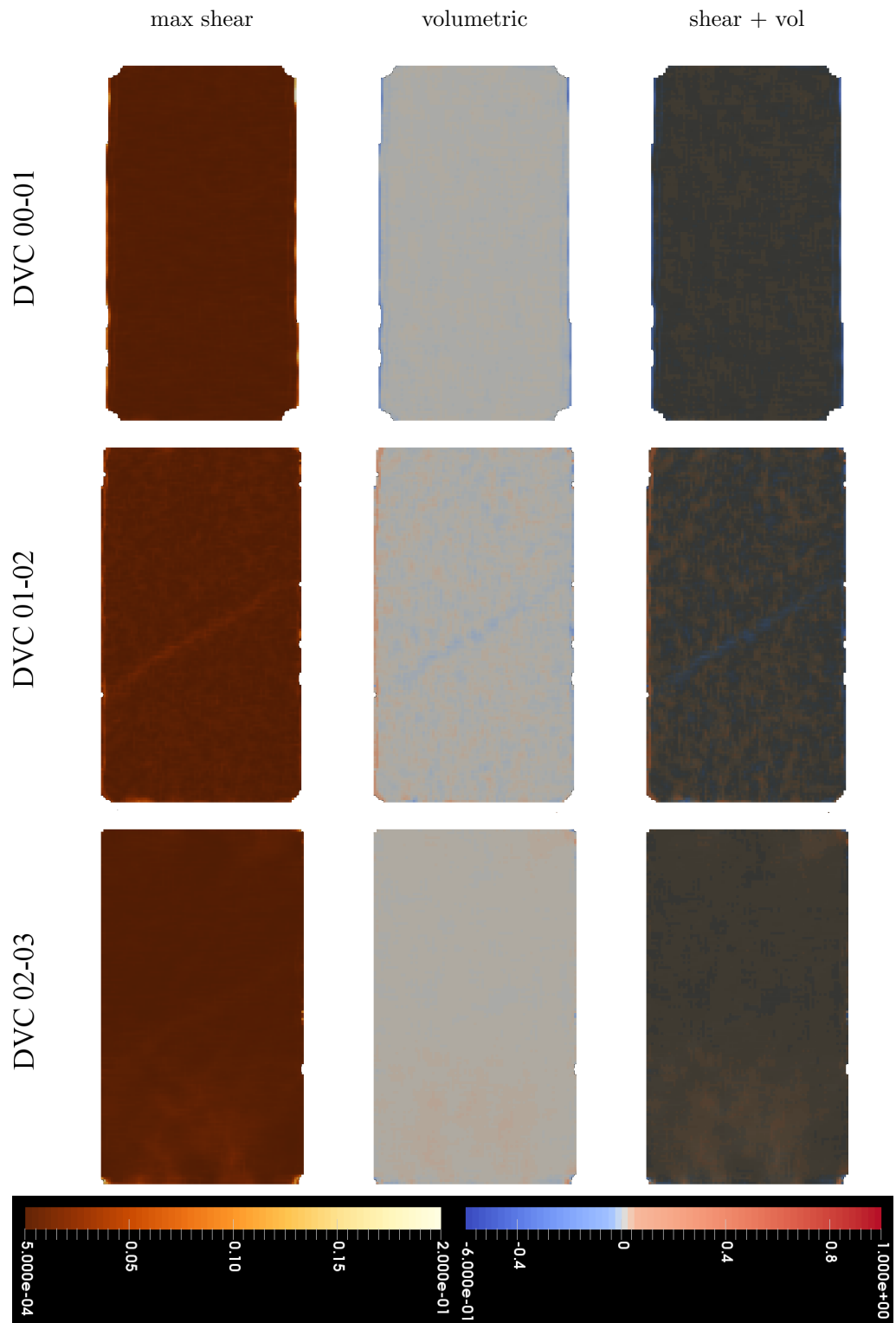


**Figure B.4a:** DVC results of the triaxial compression test on a naturally cemented sample containing a pre-existing dilation band

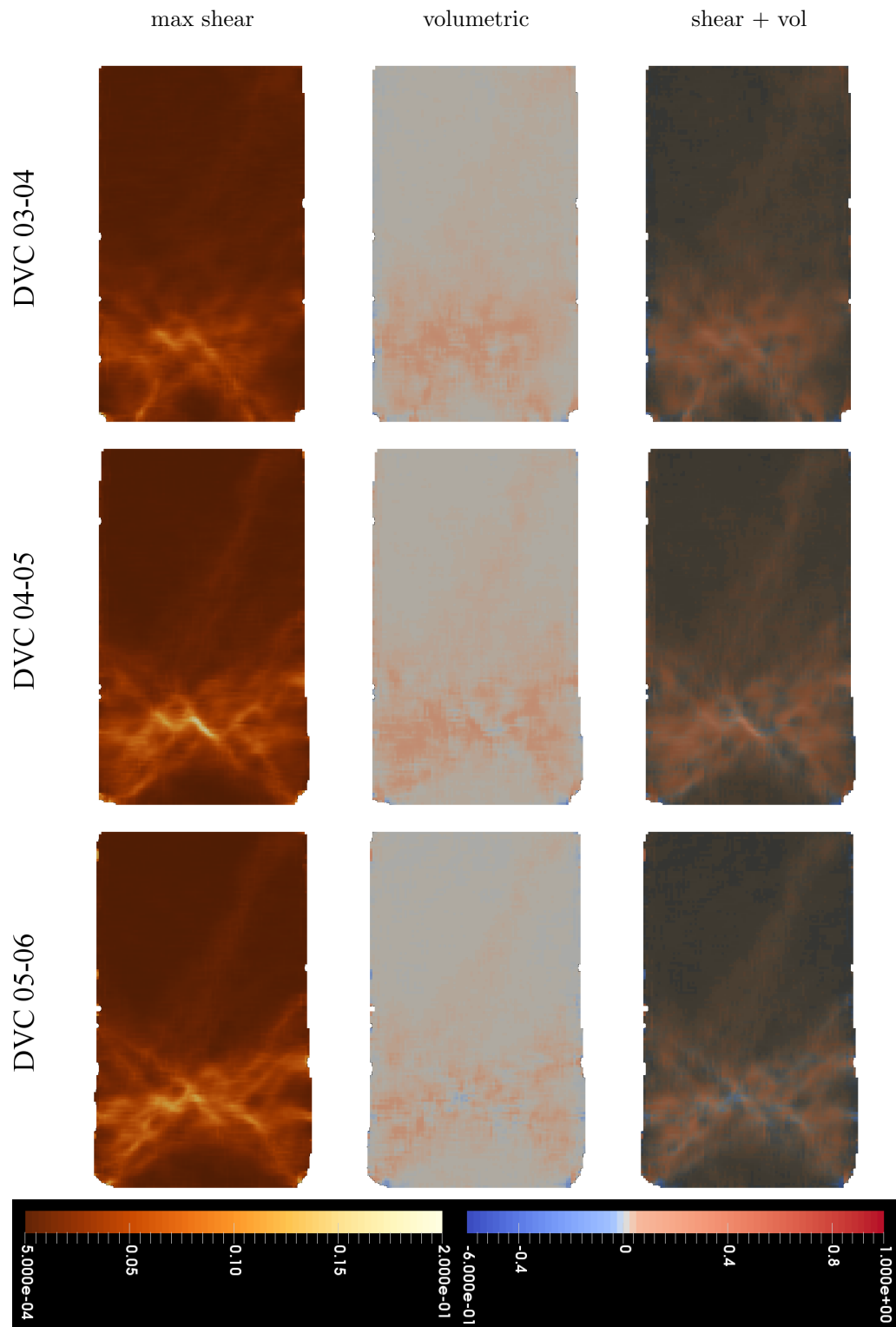


Figure B.4b

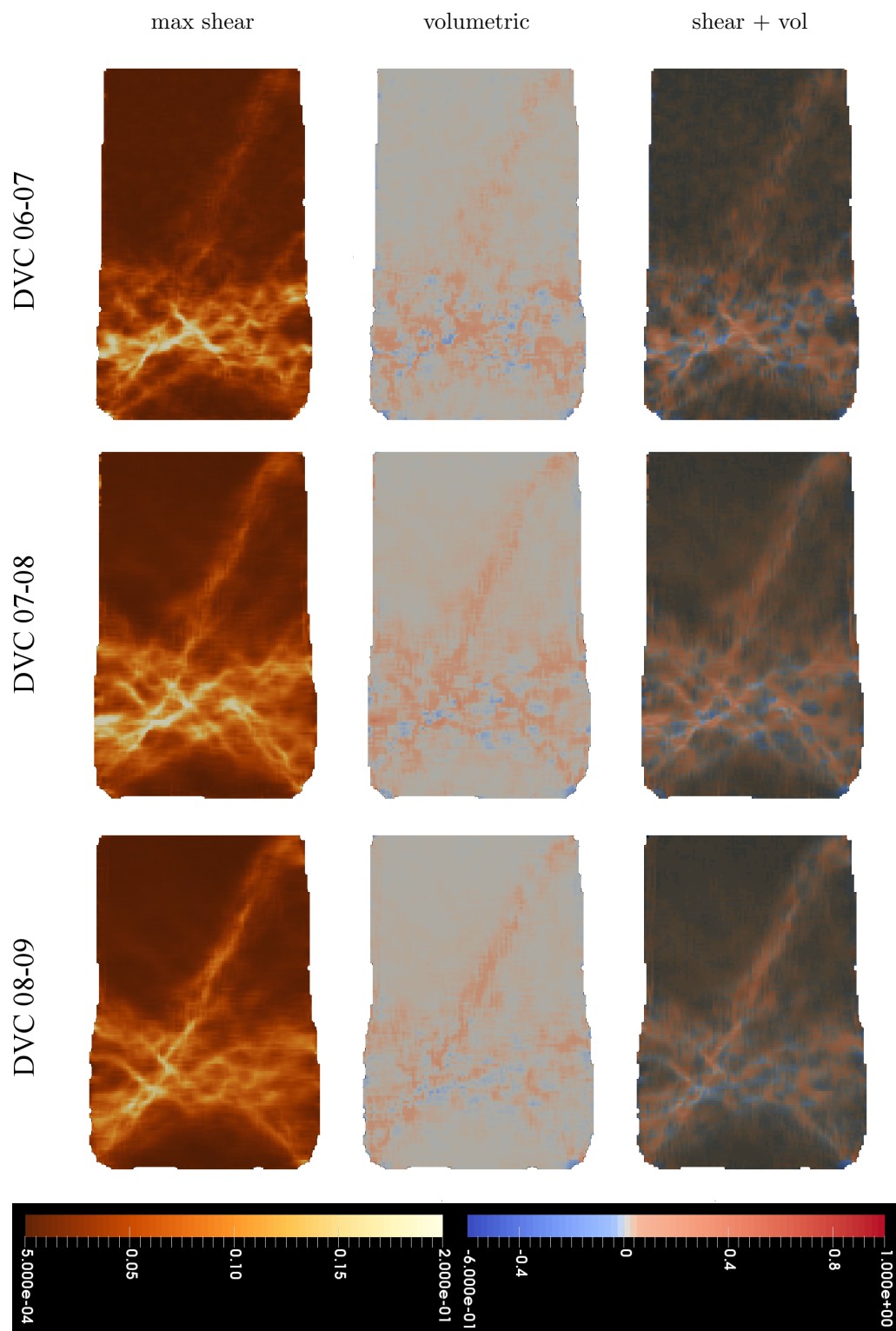


Figure B.4c

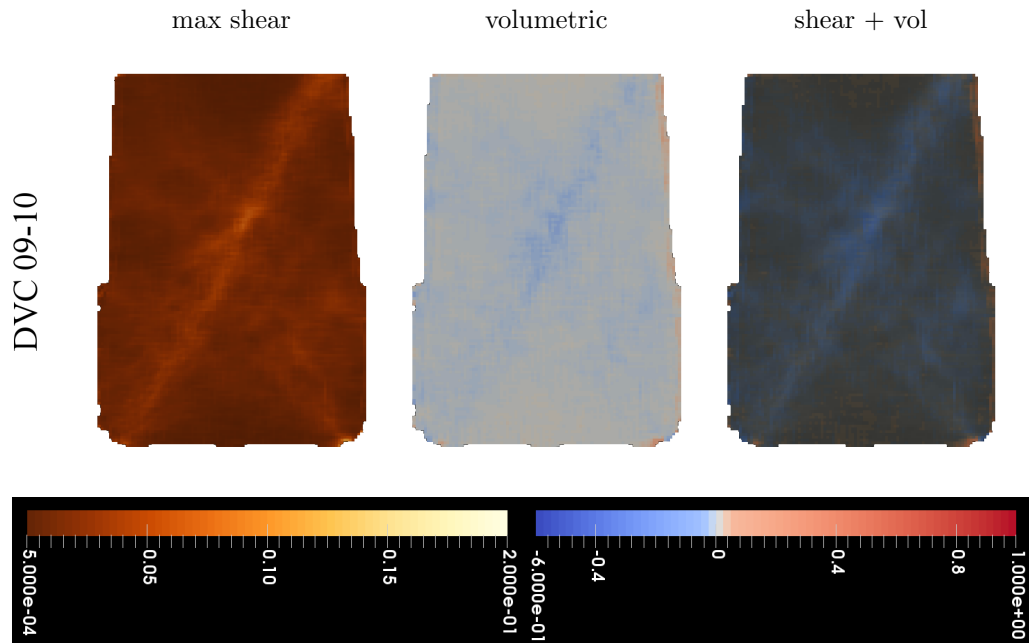


Figure B.4d

### B.2.4 Artificially cemented Bédoin sand with 20% clay

DVC results are described in detail below for each DVC step (Fig. B.5) of this triaxial compression test. DVC steps 04-05, 05-06, and 06-07 are not available due to unsolved issues arisen with the DVC computation.

**DVC 00-01** With the application of 1 MPa of confining pressure, shear developed at small degree in thin layers distributed along the sample. Compression and dilation corresponded to this shear component. More intense shear developed at the upper and lower ends of the sample with compression and dilation, due to the friction between sample and ceramic platens.

**DVC 02-03** Deformation localised primarily at the lower part of the sample than at the top, with compression dominating all along the sample, except for the upper and lower ends of the sample that developed dilation.

**DVC 03-04** Shear intensified in all the sample, corresponding to volumetric compression. It seems to have developed a network of shear bands, with preferential inclinations of  $-50^\circ$  and  $54^\circ$  to the horizontal. The maximum shear strain field map of this step can be observed in 3D at the following link: <https://doi.org/10.6084/m9.figshare.10084748.v2>.

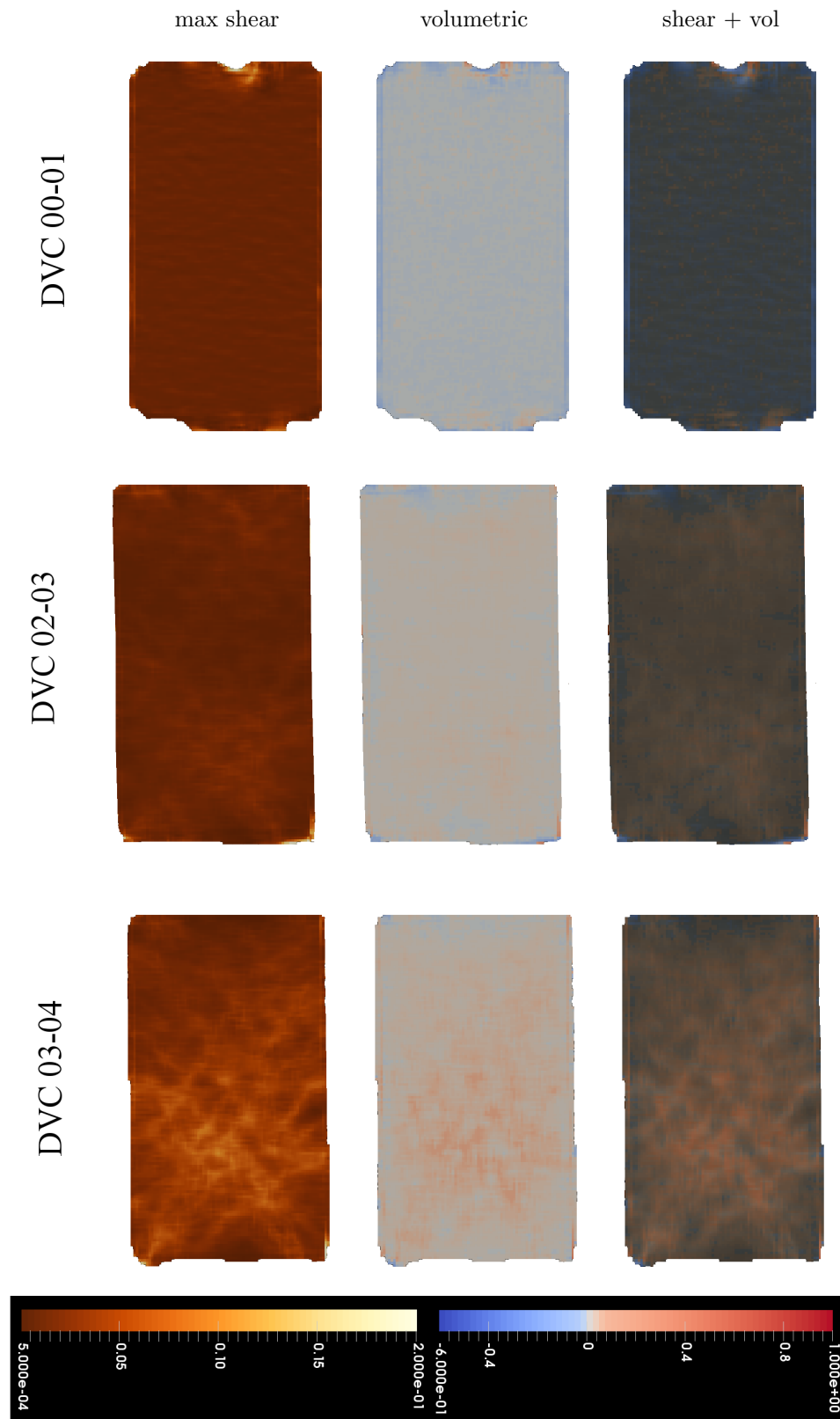


**Figure B.5:** DVC results of the triaxial compression test on an artificially cemented sample with 20% of clay

### B.2.5 Artificially cemented Bédoin sand with 15% clay

DVC results are described in detail below for each DVC step in Figure B.6. DVC of step 07-08 is not available because of an unsuccessful image correlation during the computation.

**DVC 01-02** Sheared zones looking like thin horizontal layers were distributed along the sample with the application of 0.5 MPa of confining pressure. In terms of volumetric variation, small regions of volumetric compression and dilation developed along these layers in the sample. More localised shear and dilation is detected at the lower end of the sample.

**DVC 02-03** The application of another 0.5 MPa of confining pressure did not show relevant effects on the sample, neither in terms of shear nor in terms of volumetric variation, except for the sample boundaries.

**DVC 03-04** Shear started to localise close to the lower and upper ends of the sample. High level of shear corresponded principally to volumetric compression, but small regions of dilation also developed in the highly compressed regions at the two ends of the sample.

**DVC 04-05** Shear increased in all the sample and a region of higher shear intensity developed in the lower part corresponding to volumetric compression and few regions of dilation in the highly compressed region.

**DVC 05-06** A dominant shear band emerged from the sheared zone now evolved into a network of bands at the lower part of the sample. The shear band had a characteristic zigzag shape, similar to what observed in the natural samples in Sections B.2.1 and B.2.3, which is interpreted to develop from the intersection between bands of conjugate directions, inclined of  $\pm 50^\circ$  to the horizontal. Two small regions of dilation developed above the major shear band, as shown by the overlap, but the sample was principally affected by compression.

**DVC 06-07** When the peak stress is reached at about  $\epsilon_a = 8\%$ , all the shear bands in the network developed high shear intensity (see the 3D view at the following link: <https://doi.org/10.6084/m9.figshare.10084742.v1>). The shear bands followed the conjugate directions with inclination of about  $\pm 50^\circ$  to the horizontal, with one of the shear bands that started to extend towards the upper-right side of the sample. All the bands in the network reported intense shear and this corresponded to volumetric compression. In the regions nearby the intersections between the shear bands of the network, new small regions of dilation developed.

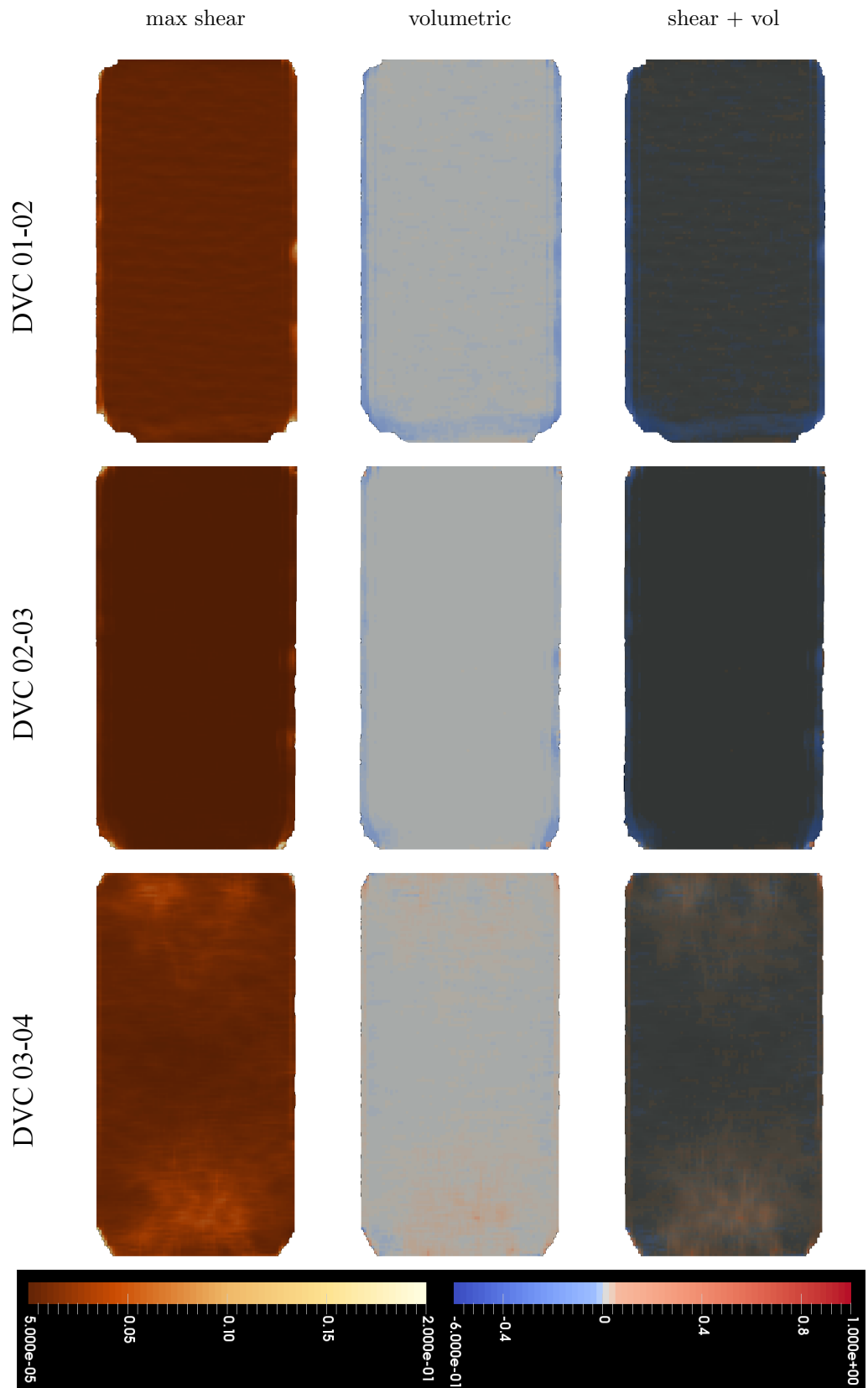


**Figure B.6a:** DVC results of the triaxial compression test on an artificially cemented sample with 15% clay



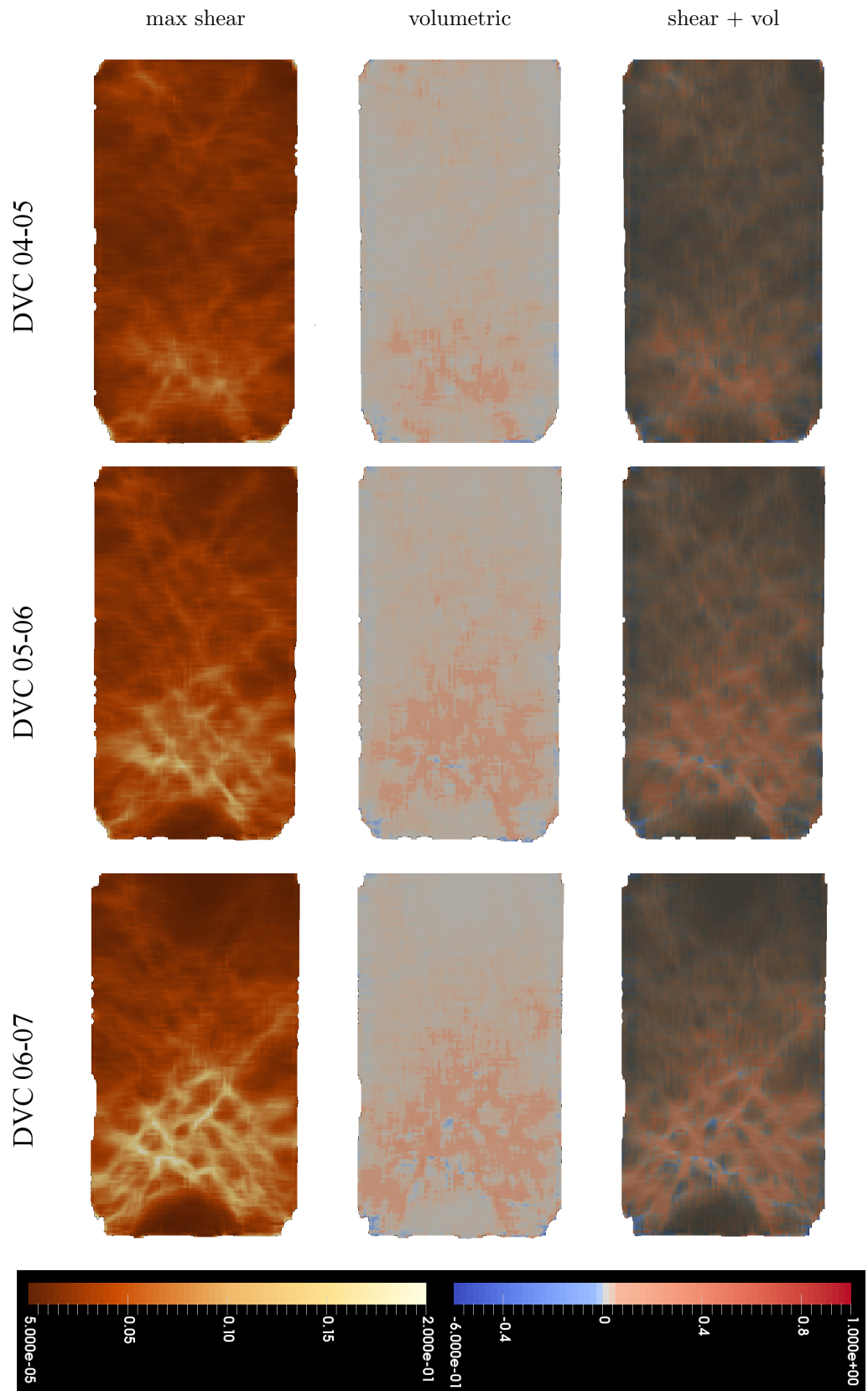


Figure B.6b

### B.2.6 Uncemented Bédoin sand

The DVC results are described below for each DVC step in Figure B.7:

**DVC 00-01** During the confining pressure, the maximum shear strain field showed an overall low shear degree, except for the lower part of the sample, which developed shear at the contact with the ceramic platen, and for a region in the central part of the sample. The sheared regions developed at the lower and at the centre of the sample were affected by dilation.

**DVC 01-02** An increase of shear and dilation in the central part of the sample was reported, but also a growth of compression at lower degree in all the sample.

**DVC 02-03** Localise deformation seemed to develop in the middle of the sample with the creation of shear zones. The volumetric strain field map showed small regions of compression and of dilation distributed along the shear zones.

**DVC 03-04** Shear grew in all the sample, especially in the central region with higher shear intensity along short shear zones that seem to form a network of narrow bands. A diffused volumetric compression emerged at the centre of the sample, and the regions with more intense shear reported compression. Volumetric dilation was less evident than compression.

**DVC 04-05** Shear intensity grew along the narrow bands in the network. The shear bands in the network showed nearly-conjugate directions of  $-35^\circ$  and  $41^\circ$  (negative angle is clockwise from horizontal) to the horizontal direction. Volumetric compression developed widely at the centre of the sample, with few small regions of dilation in it.

**DVC 05-06** The deviatoric peak stress was reached during this step (Fig. 6.22). A dominant shear band emerged from the network of bands, with an average inclination of  $35^\circ$  to the horizontal. The shear band was crossed transversally by a shorter shear band. From a volumetric point of view, the two shear bands reported high compression, but dilation emerged close to their intersection.

**DVC 06-07** The network of shear bands developed further shear intensity, where the bands have nearly-conjugate directions of  $35^\circ$  and  $-40^\circ$  (negative angle is clockwise from horizontal) to the horizontal. The bands of shear reported high compression, with dilation nearby the intersections between the bands.

**DVC 07-08** The sample took a barrel-like shape, with dilation and compression increasing at the centre where two major shear directions intersected ( $-37^\circ$  and  $35^\circ$ ) (see the 3D view at the following link: <https://doi.org/10.6084/m9.figshare.10084796.v1>).

**DVC 08-09** During the unloading, the sample showed a shear component in the central part of the sample. Two shear bands can be identified, one of which seems to not coincide with one the conjugate shear bands developed during the deviatoric loading, since the bands reported a higher inclination of  $60^\circ$  to the horizontal, from the previous inclination of  $35^\circ$ . Dilation was principally identified during the unloading.

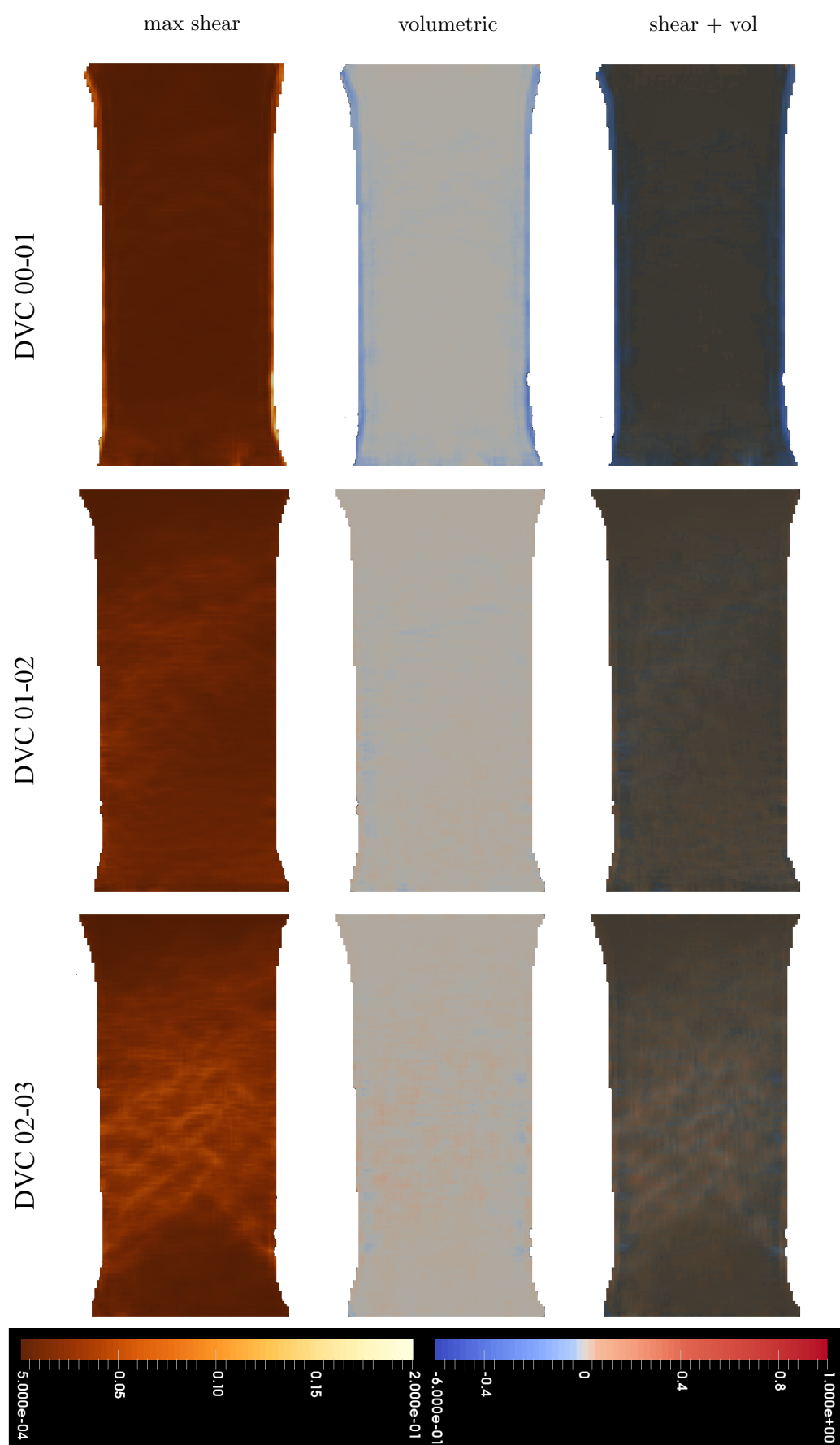


**Figure B.7a:** DVC results of the triaxial compression test on an uncemented Bédoine sand sample

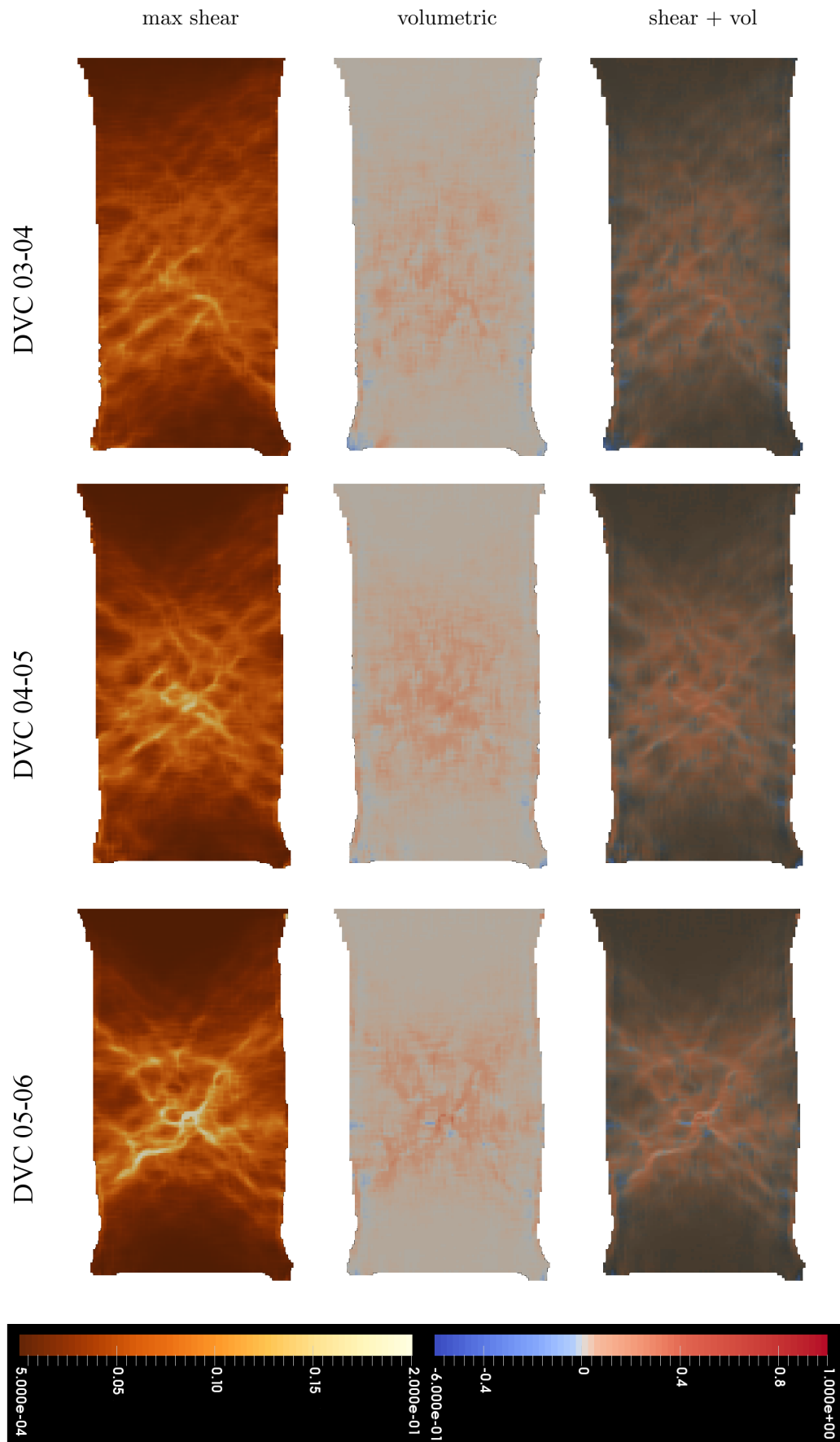


**Figure B.7b:** DVC results of the triaxial compression test on an uncemented Bédoine sand sample

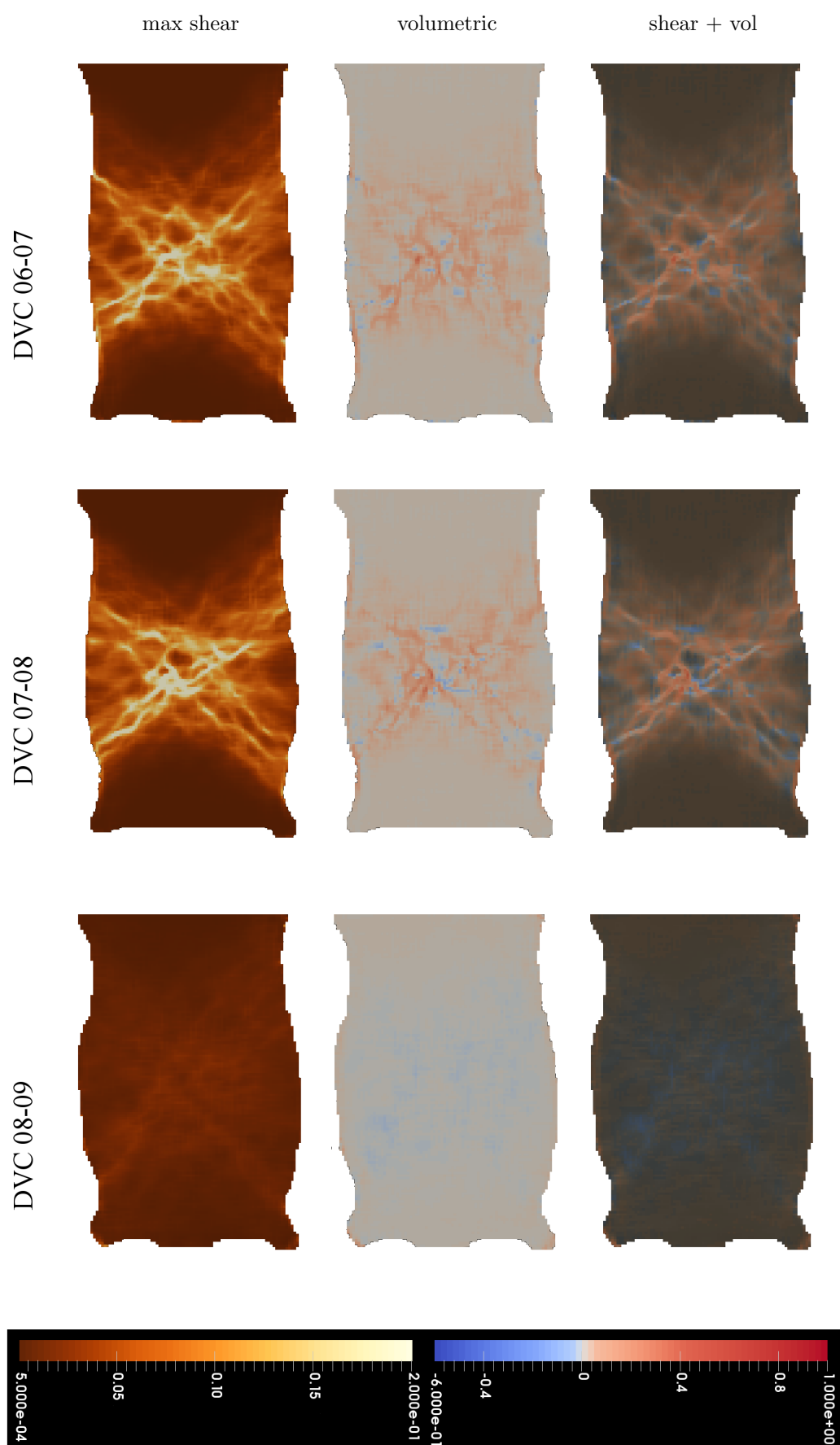


Figure B.7c

# Bibliography

- J. Alabdullah. Testing unsaturated soil for plane strain conditions: A new double-wall biaxial device. *PhD Thesis*, pages 1–208, 2010.
- R. Alikarami and A. Torabi. Micro-texture and petrophysical properties of dilation and compaction shear bands in sand. *Geomechanics for Energy and the Environment*, 3:1–10, Sep 2015.
- R. Alikarami, A. Torabi, D. Kolyukhin, and E. Skurtveit. Geostatistical relationships between mechanical and petrophysical properties of deformed sandstone. *International Journal of Rock Mechanics and Mining Sciences*, 63:27–38, 2013.
- E. Andò. Experimental investigation of microstructural changes in deforming granular media using x-ray tomography. *PhD Thesis*, pages 10–229, 2013.
- E. Andò, S. A. Hall, G. Viggiani, J. Desrues, and P. Bésuelle. Grain-scale experimental investigation of localised deformation in sand: A discrete particle tracking approach. *Acta Geotechnica*, 7(1):1–13, 2012.
- M. A. Antonellini, A. Aydin, and D. D. Pollard. Microstructure of deformation bands in porous sandstones at arches national park, utah. *Journal of Structural Geology*, 16(7):941–959, Jul 1994.
- J. H. Atkinson and P. L. Bransby. *The Mechanics of Soils: An Introduction to Critical State Soil Mechanics*. McGraw-Hill, 1978.
- A. Aydin. Small faults formed as deformation bands in sandstone. *Proceedings of conference II: Experimental studies of rock friction with application to earthquake prediction: Menl Park, U.S. Geological Survey*, pages 591–616, 1977.
- A. Aydin. Small faults formed as deformation bands in sandstone. *Pure and Applied Geophysics*, 116:913–930, 1978.
- A. Aydin and A. M. Johnson. Development of faults as zones of deformation bands and as slip surfaces in sandstone. *Pure and Applied Geophysics*, 116(4-5):931–942, 1978.

- A. Aydin and A. M. Johnson. Analysis of faulting in porous sandstones. *Journal of Structural Geology*, 5(1):19–31, 1983.
- A. Aydin, R. I. Borja, and P. Eichhubl. Geological and mathematical framework for failure modes in granular rock. *Journal of Structural Geology*, 28(1):83–98, 2006.
- G. Ballas, R. Soliva, J.-P. Sizun, A. Benedicto, T. Cavailhes, and S. Raynaud. The importance of the degree of cataclasis in shear bands for fluid flow in porous sandstone, provence, france. *AAPG Bulletin*, 96(11):2167–2186, Nov 2012.
- G. Ballas, R. Soliva, J. P. Sizun, H. Fossen, A. Benedicto, and E. Skurtveit. Shear-enhanced compaction bands formed at shallow burial conditions; implications for fluid flow (provence, france). *Journal of Structural Geology*, 47:3–15, 2013.
- G. Ballas, R. Soliva, A. Benedicto, and J.-P. Sizun. Control of tectonic setting and large-scale faults on the basin-scale distribution of deformation bands in porous sandstone (provence ,france). *Marine and Petroleum Geology*, 55:142–159, 2014.
- G. Ballas, H. Fossen, and R. Soliva. Factors controlling permeability of cataclastic deformation bands and faults in porous sandstone reservoirs. *Journal of Structural Geology*, 76:1–21, 2015.
- F. Balsamo and F. Storti. Size-dependent comminution, tectonic mixing, and sealing behavior of a. *Geological Society of America Bulletin*, (3-4):601–619, Mar .
- F. Balsamo, F. H. R. Bezerra, M. M. Vieira, and F. Storti. Structural control on the formation of iron-oxide concretions and liesegang bands in faulted, poorly lithified cenozoic sandstones of the paraiba basin, brazil. *Bulletin of the Geological Society of America*, 125(5-6):913–931, 2013.
- J. Baruchel, J.-Y. Buffière, E. Maire, P. Merle, and G. Peix. *X-Ray Tomography in Material Science*. Hermes Science Publications, 2000.
- P. Baud, V. Vajdova, and T. F. Wong. Shear-enhanced compaction and strain localization: Inelastic deformation and constitutive modeling of four porous sandstones. *Journal of Geophysical Research: Solid Earth*, 111(12):1–17, 2006.
- P. Bésuelle. Compacting and dilating shear bands in porous rock: Theoretical and experimental conditions. *Journal of Geophysical Research*, 106(B7):435–442, 2001.
- P. Bésuelle, J. Desrues, and S. Raynaud. Experimental characterisation of the localisation phenomenon inside a vosges sandstone in a triaxial cell. *International Journal of Rock Mechanics and Mining Sciences*, 37(8):1223–1237, Dec 2000.
- M. D. Bolton. The strength and dilatancy. *Géotechnique*, 36(I):65–78, 1986.

- R. I. Borja and A. Aydin. Computational modeling of deformation bands in granular media. i. geological and mathematical framework. *Computer Methods in Applied Mechanics and Engineering*, 193(27-29):2667–2698, 2004.
- R. I. Borja, X. Song, A. L. Rechenmacher, S. Abedi, and W. Wu. Shear band in sand with spatially varying density. *Journal of the Mechanics and Physics of Solids*, 61(1):219–234, 2013.
- P. Bésuelle and J. W. Rudnicki. Localization: Shear bands and compaction bands. *Mechanics of Fluid-Saturated Rocks.*, (Chapter 5):219–321, 2004.
- J. O. Buckman, P. W. M. Corbett, and L. Mitchell. Charge contrast imaging (cci): Revealing enhanced diagenetic features of a coquina limestone. *Journal of Sedimentary Research*, 86(Mar):1–15, 2016.
- J. Buckman. Use of automated image acquisition and stitching in scanning electron microscopy: Imaging of large scale areas of materials at high resolution: Sem image stitching. *Microscopy and Analysis*, Jan 2014:13–16, 1 2014. ISSN 0958-1952.
- S. D. Burley, J. Mullis, and A. Matter. Timing diagenesis in the tartan reservoir (uk north sea): constraints from combined cathodoluminescence microscopy and fluid inclusion studies. *Marine and Petroleum Geology*, 6(2):98–120, May 1989.
- S. Cashman and K. Cashman. Cataclasis and deformation-band formation in unconsolidated marine terrace sand, humboldt county, california. *Geology*, 28(2):111–114, 2000.
- S. M. Cashman, J. N. Baldwin, K. V. Cashman, K. Swanson, and R. Crawford. Microstructures developed by coseismic and aseismic faulting in near-surface sediments, san andreas fault, california. *Geology*, 35(7):611, 2007.
- M. E. Cates, J. P. Wittmer, J.-P. Bouchaud, and P. Claudin. Jamming, force chains, and fragile matter. *Physical Review Letters*, 81(9):1841–1844, 1998.
- T. Cavailhes, R. Soliva, A. Benedicto, D. Loggia, R. A. Schultz, and C. A. Wibberley. Are cataclastic shear bands fluid barriers or capillarity conduits ? insight from the analysis of redox fronts in porous sandstones from provence, france. *2nd International Conference on Fault and Top Seals – From Pore to Basin Scale*, pages 1–3, Sept 2009.
- I. Cavarretta. The influence of particle characteristics on the engineering behaviour of granular materials. *PhD Thesis*, 2010.



- E.-M. Charalampidou. Experimental study of localised deformation in porous sandstones. *PhD Thesis*, 2011.
- E.-M. Charalampidou, S. A. Hall, and S. Stanchits. Shear-enhanced compaction band identification at the laboratory scale using acoustic and full-field methods. *International Journal of Rock Mechanics & Mining Sciences*, 67:240–252, 2014a.
- E. Charalampidou, G. Kwieciek, S. Stanchits, and G. Dresen. Formation of compaction bands in a porous sandstone with high density inclusions. 5 2014b. 10th Euroconference on Rock Physics and Rock Mechanics 2014 ; Conference date: 12-05-2014 Through 15-05-2014.
- A. I. Chemenda, C. A. Wibberley, and E. Sallet. Evolution of compactive shear deformation bands: Numerical models and geological data. *Tectonophysics*, 526-529:56–66, 2012.
- L. Cheng, R. Cord-Ruwisch, and M. A. Shahin. Cementation of sand soil by microbially induced calcite precipitation at various degrees of saturation. *Canadian Geotechnical Journal*, 50(1):81–90, Jan 2013.
- A. Cilona, P. Baud, E. Tondi, F. Agosta, S. Vinciguerra, A. Rustichelli, and C. J. Spiers. Deformation bands in porous carbonate grainstones: Field and laboratory observations. *Journal of Structural Geology*, 45:137–157, 2012.
- A. Cilona, D. R. Faulkner, E. Tondi, F. Agosta, L. Mancini, A. Rustichelli, P. Baud, and S. Vinciguerra. The effects of rock heterogeneity on compaction localization in porous carbonates. *Journal of Structural Geology*, 67:75–93, 2014.
- T. T. Cladouhos. Shape preferred orientations of survivor grains in fault gouge. *Journal of Structural Geology*, 21:419–436, 1999.
- B. D. Collins and N. Sitar. Geotechnical properties of cemented sands in steep slopes. *Journal of Geotechnical and Geoenvironmental Engineering*, 135(Oct):1359–1366, 2009.
- N. Cruz, C. Rodrigues, and A. Viana da Fonseca. The influence of cementation in the critical state behaviour of artificial bonded soils. *International Symposium on Deformation Characteristics of Geomaterials*, (Jan):730–737, 2011.
- C. David, B. Menéndez, and Y. Bernabé. The mechanical behaviour of synthetic sandstone with varying brittle cement content. *International Journal of Rock Mechanics and Mining Sciences*, 35(6):759–770, 1998.

- J. Davidsen, G. Kwiatek, E. M. Charalampidou, T. Goebel, S. Stanchits, M. Rück, and G. Dresen. Triggering processes in rock fracture. *Physical Review Letters*, 119(6):1–6, 2017.
- L. F. De Ros, S. Morad, C. Broman, P. De Césero, and D. Gomez-Gras. Influence of uplift and magmatism on distribution of quartz and illite cementation: Evidence from siluro-devonian sandstones of the paraná basin, brazil. *Quartz Cementation in Sandstones - Special Publications of the International Association of Sedimentologists*, pages 231–252, 2009.
- J. T. Dejong, M. B. Fritzges, and K. Nüsslein. Microbially induced cementation to control sand response to undrained shear. *Journal of Geotechnical and Geoenvironmental Engineering*, pages 1381–1392, 2006.
- S. W. J. den Brok, C. David, and Y. Bernabé. Preparation of synthetic sandstones with variable cementation for studying the physical properties of granular rocks. *C. R. Académie des Sciences - Series IIA - Earth and Planetary Science*, 325(7):487–492, 1997.
- J. Desrues and E. Andò. Strain localisation in granular media. *Comptes Rendus Physique*, 16(1):26–36, 2015.
- J. Desrues and G. Viggiani. Strain localization in sand: An overview of the experimental results obtained in grenoble using stereophotogrammetry. *International Journal for Numerical and Analytical Methods in Geomechanics*, 28(4):279–321, 2004.
- J. Desrues, R. Chambon, M. Mokni, and F. Mazerolle. Void ratio evolution inside shear bands in triaxial sand specimens studied by computed tomography. *Géotechnique*, 46(3):529–546, 1996.
- J. Desrues, E. Andò, F. A. Mevoli, L. Debove, and G. Viggiani. How does strain localise in standard triaxial tests on sand: Revisiting the mechanism 20 years on. *Mechanics Research Communications*, 92(Aug):142–146, 2018.
- X. Du Bernard, P. Eichhubl, and A. Aydin. Dilation bands: A new form of localized failure in granular media. *Geophysical Research Letters*, 29(24):1–4, 2002.
- P. Dubois and J. Delfaud. Le bassin du sud-est. *Dynamique des bassins sédimentaires. Livre jubilaire BRGM, Orleans, France*, 1894.
- J. Dvorkin and H. Yin. Contact laws for cemented grains: Implications for grain and cement failure. *International Journal of Solids and Structures*, 32(17-18):2497–2510, Sep 1995.

- J. T. Engelder. Cataclasis and the generation of fault gouge. *Applied and Environmental Microbiology*, 85:1515–1522, 1974.
- U. Exner and C. Tschegg. Preferential cataclastic grain size reduction of feldspar in deformation bands in poorly consolidated arkosic sands. *Journal of Structural Geology*, 43:63–72, 2012.
- U. Exner, J. Kaiser, and S. Gier. Deformation bands evolving from dilation to cementation bands in a hydrocarbon reservoir (vienna basin, austria). *Marine and Petroleum Geology*, pages 504–515, 2013.
- L. A. Feldkamp, L. C. Davis, and J. W. Kress. Practical cone-beam algorithm. *Journal of the Optical Society of America*, 1(6):612, Jun 1984.
- Q. J. Fisher, R. J. Knipe, and R. H. Worden. Microstructures of deformed and non-deformed sandstones from the north sea: Implications for the origins of quartz cement in sandstones. 29:129–146, 2000.
- M. Ford and U. Stahel. The geometry of a deformed carbonate slope-basin transition: The ventoux-lure fault zone, se france. *Tectonics*, 14:1393–1410, 1995.
- H. Fossen, R. A. Schultz, Z. K. Shipton, and K. Mair. Deformation bands in sandstone: a review. *Journal of the Geological Society, London*, 164:755–769, 2007.
- H. Fossen, R. A. Schultz, and A. Torabi. Conditions and implications for compaction band formation in the navajo sandstone, utah. *Journal of Structural Geology*, 33(10):1477–1490, 2011.
- H. Fossen, R. Soliva, G. Ballas, B. Trzaskos, C. Cavalcante, and R. A. Schultz. A review of deformation bands in reservoir sandstones : geometries , mechanisms and distribution. *Geological Society of London Special Publication*, 459:9–33, 2017.
- R. H. Gabrielsen and R. Aarland. Characteristics of pre- and syn-consolidation structures and tectonic joints and microfaults in fine to medium-grained sandstones. *International Journal of Rock Mechanics and Mining Sciences & Geomechanics Abstracts*, 27(6):45–50, Dec 1990.
- J. I. Goldstein, C. E. Lyman, D. E. Newbury, E. Lifshin, P. Echlin, L. Sawyer, D. C. Joy, and J. R. Michael. *Scanning Electron Microscopy and X-Ray Microanalysis*. Kluwer Academic/Plenum Publishers, 2003.
- J. Griffiths, D. R. Faulkner, A. P. Edwards, and R. H. Worden. Deformation band development as a function of intrinsic host-rock properties in triassic sherwood sandstone. *Geological Society, London, Special Publications*, 435:1–16, Jan 2016.

- D. Griggs and J. Handin. Observations on fractures and a hypothesis of earthquakes. *Rock deformation - a symposium: Geological Society America Mem. 79*, pages 343–373, 1960.
- F. Guéguen. Mécanique des roches en géologie: des processus microscopiques au comportement macroscopique. pages 1–12, 2005.
- J. Hadamard. Leçons sur la propagation de ondes et les équations de l’hydrodynamique. *A. Hermann, Paris*, 1903.
- S. Haddad, R. H. Worden, D. Prior, and P. C. Smalley. Quartz cement in the fontainebleau sandstone, paris basin, france: Crystallography and implications for mechanisms of cement growth. *Journal of Sedimentary Research*, 76(2):244–256, 2006.
- S. M. Haeri, S. M. Hosseini, D. G. Toll, and S. S. Yasrebi. The behaviour of an artificially cemented sandy gravel. *Geotechnical and Geological Engineering*, 23(5):537–560, Sep 2005.
- S. A. Hall, N. Lenoir, and G. Viggiani. Strain localisation in sand under triaxial loading: characterisation by x-ray micro tomography and 3d digital image correlation. *Proceedings of the 1st Int. Symp. On Computational Geomechanics*, Mar 2009.
- S. A. Hall, M. Bornet, J. Desrues, Y. Pannier, N. Lenoir, G. Viggiani, and P. Bésuelle. Discrete and continuum analysis of localised deformation in sand using x-ray  $\mu$ ct and volumetric digital image correlation. *Géotechnique*, 60(5):315–322, 2010.
- I. Hara. Deformation of heterogeneously layered rocks in flexural folding. *Journal of the Geological Society of Japan*, 72(8):363–369, 1966.
- B. H. Hartmann, K. Juhsz-Bodnr, K. Ramseier, and A. Matter. Polyphased quartz cementation and its sources: A case study from the upper palaeozoic haushi group sandstones, sultanate of oman. *Quartz Cementation in Sandstones - Special Publications of the International Association of Sedimentologists*, pages 253–270, 2009.
- J. Harwood, a. C. Aplin, C. I. Fialips, J. E. Iliffe, R. Kozdon, T. Ushikubo, and J. W. Valley. Quartz cementation history of sandstones revealed by high-resolution sims oxygen isotope analysis. *Journal of Sedimentary Research*, 83(7):522–530, 2013.

- R. S. Haszeldine, A. J. Cavanagh, and G. L. England. Effects of oil charge on illite dates and stopping quartz cement: Calibration of basin models. *Journal of Geochemical Exploration*, 78-79:373–376, 2003.
- R. Hill. Acceleration waves in solids. *Journal of Mechanics Physics and Solids*, (10), 1961.
- K. Hoshino and H. Koide. Process of deformation of the sedimentary rocks. *Proc. 2nd Congr. Int. Soc. Rock Mech., Belgrade 1970*, I(13):353–359, 1970.
- M. A. Ismail, H. A. Joer, W. H. Sim, and M. F. Randolph. Effect of cement type on shear behavior of cemented calcareous soil. *Journal of Geotechnical and Geoenvironmental Engineering*, 128(6):520–529, Jun 2002.
- K. A. Issen and J. W. Rudnicki. Theory of compaction bands in porous rock. *Physics and Chemistry of the Earth, Part A: Solid Earth and Geodesy*, 26:95–100, 2001.
- K. A. Issen and J. W. Rudnicki. Conditions for compaction bands in porous rock. *Journal of Geophysical Research: Solid Earth*, 105(B9):21529–21536, Sep 2000.
- W. R. Jamison. Laramide deformation of the wingate sandstone, colorado national monument: a study of cataclastic flow. *PhD Thesis*, 1979.
- Y. Ji, S. A. Hall, P. Baud, and T.-f. Wong. Characterization of pore structure and strain localization in majella limestone by x-ray computed tomography and digital image correlation. *Geophysical Journal International*, 200(2):699–717, 2015.
- Z. Jiang, K. Wu, G. Couples, M. I. Van Dijke, K. S. Sorbie, and J. Ma. Efficient extraction of networks from three-dimensional porous media. *Water Resources Research*, 43(12):1–17, 2007.
- T. Jobe, S. Geiger, Z. Jiang, S. Zhang, and S. Agar. Micropore network modelling from 2d confocal imagery: impact on reservoir quality and hydrocarbon recovery. 24:323–334, 2017.
- M. E. Jones and M. A. Addis. The application of stress path and critical state analysis to sediment deformation. *Journal of Structural Geology*, 8(5):575–580, 1986.
- B. M. Kaproth, S. M. Cashman, and C. Marone. Deformation band formation and strength evolution in unlithified sand: The role of grain breakage. *Journal of Geophysical Research: Solid Earth*, 115(12):1–11, 2010.

- R. J. Knipe, G. Jones, and Q. J. Fisher. Faulting, fault sealing and fluid flow in hydrocarbon reservoirs: an introduction. *Geological Society, London, Special Publications*, 147(1):vii–xxi, 1998.
- H. Koide and K. Hoshino. Development of microfractures in experimentally deformed rocks (preliminary report). *Zisin (Journal of the Seismological Society of Japan. 2nd ser.)*, 20(2):85–97, 1967.
- G. Kraishan, M. Rezaee, and R. H. Worden. Significance of trace element composition of quartz cement as a key to reveal the origin of silica in sandstones: An example from the cretaceous of the barrow sub-basin, western australia. *Quartz Cementation in Sandstones - Special Publications of the International Association of Sedimentologists*, pages 317–331, 2009.
- W. T. Lambe and R. V. Whitman. *Soil Mechanics*. John Wiley & Sons, 1969.
- R. Lancellotta. *Geotechnical Engineering*. CRC Press, 1970.
- R. H. Lander and O. Walderhaug. Predicting porosity through simulating sandstone compaction and quartz cementation. *AAPG Bulletin*, 3(3):433–449, 1999.
- B. Lanson, D. Beaufort, G. Berger, A. Bauer, A. Cassagnabère, and A. Meunier. Authigenic kaolin and illitic minerals during burial diagenesis of sandstones: a review. *Clay Minerals*, 37:1–22, 2002.
- X. Le Pichon, C. Rangin, Y. Hamon, N. Loget, J. Y. Lin, L. Andreani, and N. Flotte. Geodynamics of the france south-east basin. *Bulletin de la Société Géologique de France*, 181:477–501, 2010.
- N. Lenoir, M. Bornert, J. Desrues, P. Bésuelle, and G. Viggiani. Volumetric digital image correlation applied to x-ray microtomography images from triaxial compression tests on argillaceous rock. *Strain*, 43:193–205, 2007.
- N. D. Lima, B. Trzaskos, and A. Pacheco. Influence of deformation bands on sandstone porosity : A case study using three-dimensional microtomography. *Journal of Structural Geology*, 72:96–110, 2015.
- E. F. Loughran. Micro fault indicators for built-in-test- equipment (microminiaturized systems for fault analysis and indication design and application to built-in test equipment. 1967.
- K. Mair and S. Abe. Breaking up: Comminution mechanisms in sheared simulated fault gouge. *Pure and Applied Geophysics*, 168:2277–2288, 2011.

- K. Mair, I. Main, and S. Elphick. Sequential growth of deformation bands in the laboratory. *Journal of Structural Geology*, 22(1):25–42, 2000.
- K. Mair, S. Elphick, and I. Main. Influence of confining pressure on the mechanical and structural evolution of laboratory deformation bands. *Geophysical Research Letters*, 29(10):49–1–49–4, May 2002.
- J. Mandel. Conditions de stabilité et postulat de drucker. *Rheology and Soil Mechanics*, pages 58–68, 1966.
- K. Marciniak and Z. Kuczyński. Limit strains in the processes of stretch-forming sheet metal. *Journal of Mechanical Sciences*, 9(9):609–612, 1967.
- E. F. McBride. Quartz cement in sandstones: a review. *Earth-Science Reviews*, 26(1-3):69–112, Jan 1989.
- B. Menéndez, W. Zhu, and T. F. Wong. Micromechanics of brittle faulting and cataclastic flow in berea sandstone. *Journal of Structural Geology*, 18(1):1–16, 1996.
- K. Milliken and R. M. Reed. Internal structure of deformation bands as revealed by cathodoluminescence imaging, hickory sandstone (cambrian), central texas. *Gulf Coast Association of Geological Societies and Gulf Coast Section SEPM; technical papers and abstracts*, 52:725–736, 2002.
- N. Molenaar and A. Venmans. Calcium carbonate cementation of sand: A method for producing artificially cemented samples for geotechnical testing and a comparison with natural cementation processes. *Engineering Geology*, 35(1-2):103–122, 1993.
- N. Molenaar, J. Cyziene, and S. Sliupa. Quartz cementation mechanisms and porosity variation in baltic cambrian sandstones. *Sedimentary Geology*, 195(3-4):135–159, 2007.
- P. N. Mollema and M. A. Antonellini. Compaction bands: A structural analog for anti-mode i cracks in aeolian sandstone. *Tectonophysics*, 267(1-4):209–228, 1996.
- M. B. E. Mørk and K. Moen. Compaction microstructures in quartz grains and quartz cement in deeply buried reservoir sandstones using combined petrography and ebsd analysis. *Journal of Structural Geology*, 29(11):1843–1854, 2007.
- R. Nova. *Soil Mechanics*. John Wiley & Sons, 2012.
- M. Oda. Deformation mechanism of sand in triaxial compression tests. *Soils and Foundations*, 12(4):45–63, 1972.

- S. Philit, R. Soliva, P. Labaume, C. Gout, and C. Wibberley. Relations between shallow cataclastic faulting and cementation in porous sandstones: First insight from a groundwater environmental context. *Journal of Structural Geology*, 81: 89–105, 2015.
- S. Philit, R. Soliva, R. Castilla, G. Ballas, and A. Taillefer. Clusters of cataclastic deformation bands in porous sandstones. *Journal of Structural Geology*, 114(Aug): 235–250, 2018.
- N. Prakongkep, A. Suddhiprakarn, I. Kheoruenromne, and R. J. Gilkes. Sem image analysis for characterization of sand grains in thai paddy soils. *Geoderma*, 156 (1-2):20–31, 2010.
- A. Rath, U. Exner, C. Tschegg, B. Grasemann, R. Laner, and E. Draganits. Diagenetic control of deformation mechanisms in deformation bands in a carbonate grainstone. *AAPG Bulletin*, 95(8):1369–1381, 2011.
- G. C. Rawling and L. B. Goodwin. Cataclasis and particulate flow in faulted, poorly lithified sediments. *Journal of Structural Geology*, 25(3):317–331, Mar 2003.
- G. C. Rawling and L. B. Goodwin. Structural record of the mechanical evolution of mixed zones in faulted poorly lithified sediments, rio grande rift, new mexico, usa. *Journal of Structural Geology*, 28(9):1623–1639, 2006.
- A. Rotevatn, A. Torabi, H. Fossen, and A. Braathen. Slipped deformation bands: A new type of cataclastic deformation bands in western sinai, sues rift, egypt. *Journal of Structural Geology*, 30(11):1317–1331, 2008.
- A. Rotevatn, T. H. Sandve, E. Keilegavlen, D. Kolyukhin, and H. Fossen. Deformation bands and their impact on fluid flow in sandstone reservoirs: The role of natural thickness variations. *Geofluids*, 13(3):359–371, 2013.
- A. Rotevatn, E. Thorsheim, E. Bastesen, H. S. S. Fossmark, A. Torabi, and G. Saelen. Sequential growth of deformation bands in carbonate grainstones in the hanging wall of an active growth fault: implications for deformation mechanisms in different tectonic regimes. *Journal of Structural Geology*, 90:27–47, 2016.
- G. Rotta, N. C. Consoli, P. D. Prietto, M. R. Coop, and J. Graham. Isotropic yielding in an artificially cemented soil cured under stress. *Géotechnique*, 53(5): 493–501, 2003.
- J. W. Rudnicki and J. R. Rice. Conditions for the localization of deformation in pressure-sensitive dilatant materials. *Journal of the Mechanics and Physics of Solids*, 23:371–394, 1975.



- E. Sallet. La localisation de la déformation dans les grès poreux : caractérisation d'un analogue de réservoir gréseux et faillé dans le bassin du sud-est, provence, france. *PhD Thesis*, 2009.
- E. Sallet and C. A. Wibberley. Evolution of cataclastic faulting in high-porosity sandstone, bassin du sud-est, provence, france. *Journal of Structural Geology*, 32: 1590–1608, 2010.
- E. Sallet and C. A. Wibberley. Permeability and flow impact of faults and deformation bands in high-porosity sand reservoirs: Southeast basin, france, analog. *AAPG Bulletin*, 97:437–464, 2013.
- J. Schindelin, I. Arganda-Carreras, E. Frise, V. Kaynig, M. Longair, T. Pietzsch, S. Preibisch, C. Rueden, B. Saalfeld, Schmid, J.-Y. Tinevez, D. J. White, V. Hartenstein, K. Eliceiri, P. Tomancak, and A. Cardona. Fiji: an open-source platform for biological-image analysis. *Nature methods*, 9(7):676–682, 2012.
- D. Schreiber, G. Giannerini, and J.-M. Lardeaux. The southeast france basin during late cretaceous times: The spatiotemporal link between pyrenean collision and alpine subduction. *Geodinamica Acta*, 24(1):21–35, 2011.
- S. Schueller, A. Braathen, H. Fossen, and J. Tveranger. Spatial distribution of deformation bands in damage zones of extensional faults in porous sandstones: Statistical analysis of field data. *Journal of Structural Geology*, 52(1):148–162, 2013.
- R. A. Schultz and R. V. Siddharthan. A general framework for the occurrence and faulting of deformation bands in porous granular rocks. *Tectonophysics*, 411(1-4): 1–18, 2005.
- R. A. Schultz and R. Soliva. Propagation energies inferred from deformation bands in sandstone. *International Journal of Fracture*, 176(2):135–149, 2012.
- Z. K. Shipton, J. P. Evans, and L. B. Thompson. The geometry and thickness of deformation-band fault core and its influence on sealing characteristics of deformation band fault zones. *Faults, fluid flow, and petroleum traps*, 85:181–195, 2005.
- R. H. Sibson. Fault rocks and fault mechanisms. *Journal of the Geological Society*, 133(3):191–213, 1977.
- R. H. Sibson. Rupture nucleation on unfavorably oriented faults. *Bulletin of the Seismological Society of America*, 80(6):1580–1604, 1990.

- E. Skurtveit, A. Torabi, R. H. Gabrielsen, and M. D. Zoback. Experimental investigation of deformation mechanisms during shear-enhanced compaction in poorly lithified sandstone and sand. *Journal of Geophysical Research: Solid Earth*, 118: 4083–4100, 2013.
- E. Skurtveit, G. Ballas, H. Fossen, A. Torabi, R. Soliva, and M. Peyret. Sand textural control on shear-enhanced compaction band development in poorly-lithified sandstone. *Journal of Geological Resource and Engineering*, 2(2), 2014.
- E. Skurtveit, A. Torabi, R. Alikarami, and A. Braathen. Fault baffle to conduit developments: reactivation and calcite cementation of deformation band fault in aeolian sandstone. *Petroleum Geoscience*, 21(1):3–16, Feb 2015.
- R. Soliva, R. A. Schultz, G. Ballas, A. Taboada, C. Wibberley, E. Sallet, and A. Benedicto. A model of strain localization in porous sandstone as a function of tectonic setting, burial and material properties; new insight from provence (southern france). *Journal of Structural Geology*, 49:50–63, 2013.
- R. Soliva, G. Ballas, H. Fossen, and S. Philit. Tectonic regime controls clustering of deformation bands in porous sandstone. *Geology*, 44(6):423–426, Jun 2016.
- I. Soriano, E.-M. Charalampidou, H. Lewis, G. Viggiani, J. Buckman, and G. Couples. Localised deformation of weakly cemented sands: A case study. *Bifurcation and Degradation of Geomaterials with Engineering Applications*, pages 381–389, 2017a.
- I. Soriano, E. Ibraim, E. Andò, A. Diambra, T. Laurencin, P. Moro, and G. Viggiani. 3d fibre architecture of fibre-reinforced sand. *Granular Matter*, 19(4), 2017b.
- K. R. Sternlof, M. Karimi-Fard, D. D. Pollard, and L. J. Durlofsky. Flow and transport effects of compaction bands in sandstone at scales relevant to aquifer and reservoir management. *Water Resources Research*, 42(7):1–16, Jul 2006.
- F. Tagliaferri, J. Waller, E. Andò, S. A. Hall, G. Viggiani, P. Bésuelle, and J. T. Dejong. Observing strain localisation processes in bio-cemented sand using x-ray imaging. *Granular Matter*, 13(3):247–250, 2011.
- D. Takano, N. Lenoir, J. Otani, and S. A. Hall. Localised deformation in a wide-grained sand under triaxial compression revealed by x-ray tomography and digital image correlation. *Soils and Foundations*, 55(4):906–915, 2015.
- S. Tavani, P. Granado, F. Balsamo, M. Pizzati, I. Cantarero, A. Corradetti, and J. Munoz. Shear-enhanced compaction-solution bands in quartz-rich calcarenites

- of the cotiella massif (spanish pyrenees). *Journal of Structural Geology*, pages 0–1, Jan 2018.
- S. Tembe, P. Baud, and T. F. Wong. Stress conditions for the propagation of discrete compaction bands in porous sandstone. *Journal of Geophysical Research: Solid Earth*, 113(9):1–16, 2008.
- C. Tempier. Modele nouveau de mise en place des structures provençales. *Bulletin de la Société Géologique de France*, 3:533–540, 1987.
- T. Y. Thomas. Plastic flow and fracture in solids. *Academic, San Diego, California*, 1961.
- A. Torabi and H. Fossen. Spatial variation of microstructure and petrophysical properties along deformation bands in reservoir sandstones. *AAPG Bulletin*, 93(7):919–938, 2009.
- A. Torabi, A. Braathen, F. Cuisiat, and H. Fossen. Shear zones in porous sand: Insights from ring-shear experiments and naturally deformed sandstones. *Tectonophysics*, 437(1-4):37–50, 2007.
- A. Torabi, H. Fossen, and A. Braathen. Insight into petrophysical properties of deformed sandstone reservoirs. *AAPG Bulletin*, 97(4):619–637, 2013.
- J.-M. Triat. Paléoaaltérations dans le crétacé supérieur de provence rhodanienne. pages 1–202, 1982.
- E. Tudisco, E. Andò, R. Cailletaud, and S. A. Hall. Tomowarp2: A local digital volume correlation code. *SoftwareX*, 6:267–270, Jan 2017.
- A. Tutuncu, J. Dvorkin, and A. Nur. Influence of cementation and permeability on wave velocities in poorly consolidated sands. *Journal of Rock Mechanics and Mining Science*, 34(313):3–4, 1997.
- P. H. Valvatne, M. Piri, X. Lopez, and M. J. Blunt. Predictive pore-scale modeling of single and multiphase flow. *Upscaling Multiphase Flow in Porous Media: From Pore to Core and Beyond*, pages 23–41, 2005.
- Y. Wang and S. Leung. A particulate-scale investigation of cemented sand behavior. *Canadian Geotechnical Journal*, 45(1):29–44, Jan 2008.
- C. A. J. Wibberley, J.-P. Petit, and T. Rives. The mechanics of fault distribution and localization in high-porosity sands, provence, france. *Geological Society, London, Special Publications*, 289:19–46, 2007.

- T.-F. Wong, C. David, and W. Zhu. The transition from brittle to cataclastic flow in porous sandstones: mechanical deformation. *Journal of Geophysical Research*, 102(B2):3009–3025, 1997.
- R. H. Worden and S. D. Burley. *Sandstone Diagenesis: The Evolution of Sand to Stone*. Number Feb. Wiley-Blackwell, 2003.
- R. H. Worden and S. Morad. Quartz cementation in oil field sandstones: a review of the key controversies. *Quartz Cementation in Sandstones - Special Publications of the International Association of Sedimentologists*, 29:1–20, Mar 2000.
- B. Zhang, J. Zhang, S. Yan, Z. Gu, and X. Wang. Detrital quartz and quartz cement in upper triassic reservoir sandstones of the sichuan basin: Characteristics and mechanisms of formation based on cathodoluminescence and electron backscatter diffraction analysis. *Sedimentary Geology*, 267-268:104–114, 2012.
- L. F. Zuluaga, H. Fossen, G. Ballas, and A. Rotevatn. Structural and petrophysical effects of overthrusting on highly porous sandstones: the aztec sandstone in the buffington window, se nevada, usa. *Geological Society, London, Special Publications*, Apr 2017.